AD-A216 882

Defense Nuclear Agency
Alexandria, VA 22310-3398

DNA-TR-89-108

Topics in HPM Generation, Coupling, and Interaction

K. F. Casey
JAYCOR
P.O. Box 7944
Fremont, CA 94537-7944

January 1990

Technical Report

DTIC
ELECTE
JAN 16 1990
S B D

90 01 12 014

DISTRIBUTION LIST UPDATE

This mailer is provided to enable DNA to maintain current distribution lists for reports. We would appreciate your providing the requested information.

☐ Add the individual listed to your distribution list.

☐ Delete the cited organization/individual.

☐ Change of address.

NAME: _____

ORGANIZATION: _____

OLD ADDRESS	**CURRENT ADDRESS**
_____	_____
_____	_____
_____	_____

TELEPHONE NUMBER: (____) _____

SUBJECT AREA(s) OF INTEREST:

_____ _____	_____
_____	_____
_____	_____

DNA OR OTHER GOVERNMENT CONTRACT NUMBER: _____ _____

CERTIFICATION OF NEED-TO-KNOW BY GOVERNMENT SPONSOR (if other than DNA):

SPONSORING ORGANIZATION: _____

CONTRACTING OFFICER OR REPRESENTATIVE: _____

SIGNATURE: _____

REPORT DOCUMENTATION PAGE

1a REPORT SECURITY CLASSIFICATION UNCLASSIFIED		1b RESTRICTIVE MARKINGS			
2a SECURITY CLASSIFICATION AUTHORITY N/A since Unclassified		3 DISTRIBUTION / AVAILABILITY OF REPORT Approved for public release; distribution is unlimited.			
2b. DECLASSIFICATION / DOWNGRADING SCHEDULE N/A since Unclassified					
4. PERFORMING ORGANIZATION REPORT NUMBER(S)		5 MONITORING ORGANIZATION REPORT NUMBER(S) DNA-TR-89-108			
6a NAME OF PERFORMING ORGANIZATION JAYCOR	6b OFFICE SYMBOL (If applicable)	7a NAME OF MONITORING ORGANIZATION Defense Nuclear Agency			
6c. ADDRESS (City, State, and ZIP Code) P.O. Box 7944 Fremont, CA 94537-7944		7b ADDRESS (City, State, and ZIP Code) 6801 Telegraph Road Alexandria, VA 22310-3398			
8a. NAME OF FUNDING / SPONSORING ORGANIZATION	8b OFFICE SYMBOL (If applicable) RAEV/Kwitkoski	9 PROCUREMENT INSTRUMENT IDENTIFICATION NUMBER DNA 001-86-C-0003			
8c. ADDRESS (City, State, and ZIP Code)		10 SOURCE OF FUNDING NUMBERS			

10 SOURCE OF FUNDING NUMBERS			
PROGRAM ELEMENT NO 63220C	PROJECT NO RX	TASK NO RF	WORK UNIT ACCESSION NO DH200895

11 TITLE (Include Security Classification)

Topics in HPM Generation, Coupling, and Interaction

12 PERSONAL AUTHOR(S)
Casey, Kendall F.

13a TYPE OF REPORT Technical	13b TIME COVERED FROM 830901 TO 860201	14 DATE OF REPORT (Year, Month, Day) 900101	15 PAGE COUNT 182

16 SUPPLEMENTARY NOTATION
This work was sponsored by the Defense Nuclear Agency under RDT&E RMC Code B3460867C64 RX RF 00022 25904D.

17.	COSATI CODES		18 SUBJECT TERMS (Continue on reverse if necessary and identify by block number)
FIELD	GROUP	SUB-GROUP	Coupling
20	15		High Power Microwave

19 ABSTRACT (Continue on reverse if necessary and identify by block number)

This document is a collection of technical notes on various aspects of high power microwave (HPM) generation, coupling and interaction.

20 DISTRIBUTION / AVAILABILITY OF ABSTRACT ☐ UNCLASSIFIED/UNLIMITED ☒ SAME AS RPT ☐ DTIC USERS	21 ABSTRACT SECURITY CLASSIFICATION UNCLASSIFIED	
22a NAME OF RESPONSIBLE INDIVIDUAL Bennie F. Maddox	22b TELEPHONE (Include Area Code) (703) 325-7043	22c OFFICE SYMBOL DNA/CSTI

DD Form 1473, JUN 86 *Previous editions are obsolete* SECURITY CLASSIFICATION OF THIS PAGE

Preface

This document comprises a collection of technical notes on various aspects of high-power microwave (HPM) generation, coupling, and interaction. The notes were written between October 1983 and February 1986, and were originally distributed rather informally as *Microwave Notes* to members of the HPM community. It has since seemed worthwhile to edit and transcribe them, and to publish them as a single report. Time and resources did not permit either as detailed an editing job as would have been desirable, or recalculation and plotting of the numerical results in a more elegant form. It is to be hoped, however, that this integrated document will prove useful to the community.

The selection of topics addressed in the *Microwave Notes* was influenced by questions which arose at various stages of the author's involvement in HPM-related activities. The subject of pulse radiation from aperture antennas subject to turn-on time errors (discussed in Note 1), for example, arose in the context of a proposed HPM generation scheme. Consideration of the scattering cross-section of a simple dipole and of its dual problem, the effective area of a thin slot (discussed in Note 2), was motivated by the need to understand the penetration of such slot apertures by HPM pulses. The slot-aperture penetration problem was considered further in *Note 5*, where a more complicated slot-to-internal-wire coupling configuration was addressed, and in *Note 7*, where the problem of coupling through a deep slot was considered. The "front-door" coupling problem was also of interest; hence the treatments of pulse propagation in waveguides (*Note 3*) and of coupling to a filamentary load in a waveguide (*Note 6*). Interest in estimating the HPM power that might be scattered into an antenna located over a rough surface by an incident field at which the antenna was not, in fact, "looking" motivated the study of that problem (*Note 4*).

The order of the chapters in this report follows that of the original *Notes*. It is perhaps worthwhile to point out that the analyses presented herein by no means represent original research. They were intended simply to make use of tried-and-true analytical methods for the study of problems of current interest. Thus the reader may be disappointed by the lack of *extensive references. Suffice it to say* that Harrington's *Time-Harmonic Electromagnetic Fields* and the *Handbook of Mathematical Functions* (M. Abramowitz and I. A. Stegun, eds.) were most useful during the preparation of the *Notes*.

iii

CONVERSION TABLE

Conversion factors for U.S. Customary to metric (SI) units of measurement

MULTIPLY $\longrightarrow$	BY $\longrightarrow$	TO GET
TO GET	$\longleftarrow$ BY	$\longleftarrow$ DIVIDE

angstrom	10^{-10}	meters (m)
British thermal unit (thermochemical)	1.054×10^3	joule (J)
calorie (thermochemical)	4.184	joule (J)
degree (angle)	1.745×10^{-2}	radian (rad)
electron volt	1.602×10^{-19}	joule (J)
erg	10^{-7}	joule (J)
erg/second	10^{-7}	watt (W)
foot	3.048×10^{-1}	meter (m)
inch	2.540×10^{-2}	meter (m)
micron	10^{-6}	meter (m)
mil	2.540×10^{-5}	meter (m)
mile (international)	1.609×10^3	meter (m)
statcoulombs	$1/3 \times 10^{-9}$	coulombs
statcoulombs/cm^3	$1/3 \times 10^{-3}$	coulombs/meter^3
statamperes	$1/3 \times 10^{-9}$	amperes (A)
statamperes/cm^2	$1/3 \times 10^{-5}$	amperes/meter^2
statvolts/cm	3×10^4	volts/meter
statvolts	300	volts (V)
gauss cm^2	10^{-8}	webers
gauss	10^{-4}	tesla
oersted	$1/4\pi \times 10^3$	amp-turn/meter
maxwell	10^{-8}	webers

Table of Contents

List of Illustrations

List of Illustrations (cont'd.)

List of Illustrations (cont'd.)

List of Illustrations (cont'd.)

List of Illustrations (cont'd.)

List of Illustrations (cont'd.)

List of Illustrations (cont'd.)

List of Illustrations (cont'd.)

List of Illustrations (cont'd.)

SECTION 1
PULSE RADIATION FROM APERTURES
WITH RANDOM-PHASE EXCITATION

Summary: We examine the field radiated by a circular aperture antenna which is excited by a pulsed field subject to turn-on time errors randomly distributed across the aperture. In particular, we calculate the expected value and the auto-correlation of the impulse response of the radiated field when the turn-on time is a random function of location in the aperture. It is assumed that this function is a stationary Gaussian random process with zero mean and an isotropic correlation. Analytical and numerical results are presented showing the pulse stretching that occurs as a result of the non-zero antenna fill time for off-axis observers and of the random turn-on time errors. We also present results showing the energy density radiated when the aperture field is a short cw pulse in the time domain.

In order to assess the potential threat posed by microwave directed-energy weapons one must first understand the characteristics of the signals which can be radiated by such weapons. These signals depend upon the microwave energy source and upon the antenna system.

In this section we examine the effect of the antenna itself on the radiation of a pulsed signal. In particular, we consider a circular aperture antenna excited by a field which is spatially uniform except for random variations caused by localized "turn-on time" errors. Using this model we investigate the effects of the finite antenna fill time, and of the turn-on time errors, on the impulse responses observed in the far field. Because of the assumed random character of the aperture field, we consider certain statistical descriptors of the far-zone radiated field: the expected value and the autocorrelation of the impulse response. These quantities can be combined by convolution with a given aperture field to yield the expected signal radiated by an aperture field of any specified time dependence.

Random-phase effects have been considered in the past for cw radiation from aperture antennas [1]. Such errors produce a reduction in the on-axis antenna gain and a broadening of the antenna's radiation pattern lobes. These phenomena can be understood on the basis of power transfer from the "coherent" or error-free radiation pattern into the "incoherent" pattern. The effect depends in detail on the variance and the correlation length of the phase errors.

1

We shall examine these effects in the time domain. The general formulation of the problem is given next, followed by analytical and numerical results for the field and energy density impulse responses. Implications of these results for microwave pulse radiation are discussed.

1.1 FORMULATION.

We consider a circular aperture antenna of radius a located in the plane $z = 0$, as shown in Figure 1. A scalar field $E_{xa}(\rho, \phi; t)$ is imposed over the aperture. This aperture field is taken to be of the form

$$E_{xa}(\rho, \phi; t) = E_{xa}[\rho, \phi; t - \tau(\rho, \phi)] \tag{1}$$

where $\tau(\rho, \phi)$ is assumed to be a two-dimensional Gaussian random process having zero mean, variance τ_0^2, and isotropic correlation function $r(\xi)$. Thus

$$< \tau(\vec{\rho}) > = 0 \tag{2}$$

$$< \tau(\vec{\rho})\tau(\vec{\rho}') > = \tau_0^2 r(| \vec{\rho} - \vec{\rho}' |) \tag{3}$$

with the brackets denoting the expected value; $\vec{\rho}$ and $\vec{\rho}'$ denote positions in the aperture.

In what follows we shall assume that the aperture field is spatially uniform except for the variation in turn-on time τ; thus

$$E_{xa}(\rho, \phi; t) = E_0[t - \tau(\rho, \phi)] \tag{4}$$

The Fourier transform of the aperture field is

$$
\begin{aligned}
\tilde{E}_{xa}(\rho, \phi) &= \int_{-\infty}^{\infty} E_0[t - \tau(\rho, \phi)]e^{-j\omega t}dt \\
&= e^{-j\omega\tau(\rho,\phi)} \int_{-\infty}^{\infty} E_0(t)e^{-j\omega t}dt \\
&= e^{-j\omega\tau(\rho,\phi)} \tilde{E}_0(j\omega) \tag{5}
\end{aligned}
$$

where $\tilde{E}_c$ denotes the Fourier transform of the aperture field in the absence of turn-on time errors. The far-zone radiated field corresponding to the assumed

2

aperture field is well known; it is given in the frequency domain by

$$\tilde{E}_x(r,\theta,\phi) \;=\; \frac{jk\tilde{E}_0(j\omega)}{2\pi r}e^{-jkr}\int_0^{2\pi}\int_0^a e^{jk\rho'\sin\theta\cos(\phi-\phi')}\cdot \tag{6}$$

$$e^{-j\omega\tau(\rho',\phi')}\rho'd\rho'd\phi'$$

wherein k is the free-space propagation constant[1] and $\tilde{E}_x$ is expressed in terms of the spherical coordinate system shown in Figure 1.
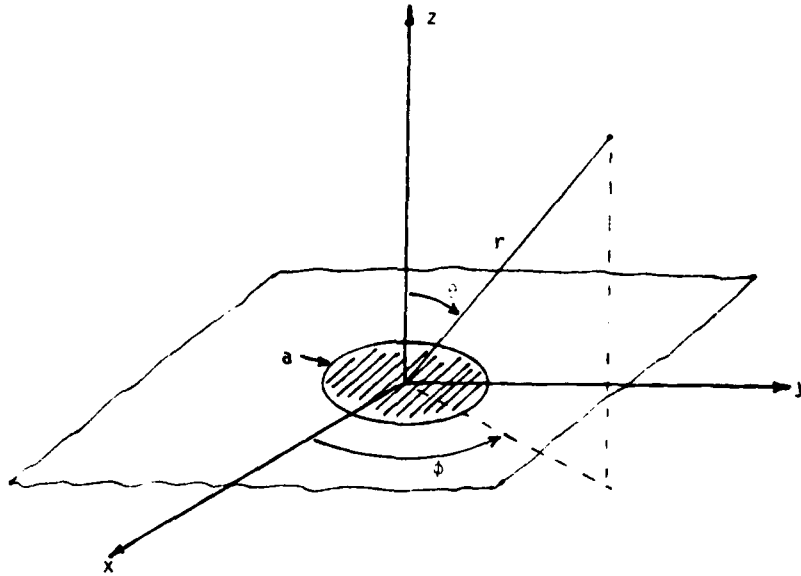
Figure 1.   Aperture geometry.

In what follows we shall make use of the mean and correlation functions

$$< e^{-j\omega\tau(\rho,\phi)} >= e^{-\omega^2\tau_0^2/2} \tag{7}$$

$$< e^{-j\omega\tau(\rho,\phi)+j\omega\tau(\rho',\phi')} >= e^{-\omega^2\tau_0^2[1-r(|\vec{\rho}-\vec{\rho}'|)]} \tag{8}$$

$$\equiv \left[1 - e^{-\omega^2\tau_0^2}\right]f(|\vec{\rho}-\vec{\rho}'|) + e^{-\omega^2\tau_0^2}$$

---

[1] $k = \omega\sqrt{\mu_0\epsilon_0}$, where μ_0 and ϵ_0 are respectively the permeability and the permittivity of free space.

wherein the function $f(\cdot)$ is defined by Equation (8). We shall calculate the expected value and the autocorrelation of the radiated field under the assumption that the aperture field in the absence of turn-on time errors is an impulse in the time domain.

1.2 IMPULSE RESPONSE OF THE RADIATED FIELD.

The time-domain radiated field is given by

$$E_x(r, \theta, \phi; t) = \frac{1}{2\pi} \int_{-\infty}^{\infty} \tilde{E}_x(r, \theta, \phi) e^{j\omega t} d\omega \qquad (9)$$

and the expected value of this field is

$$< E_x(r, \theta, \phi; t) > = \frac{1}{2\pi} \int_{-\infty}^{\infty} < \tilde{E}_x(r, \theta, \phi) > e^{j\omega t} d\omega \qquad (10)$$

by virtue of the linearity of the integration and expectation operations. Using Equations (6) and (7), we obtain

$$< E_x(r, \theta, \phi) > = \frac{jk\tilde{E}_0(j\omega)}{2\pi r} e^{-\omega^2 \tau_0^2/2} e^{-jkr} \ . \qquad (11)$$

$$\int_0^{2\pi} \int_0^a e^{jk\rho' \sin\theta \cos(\phi - \phi')} \rho' d\rho' d\phi'$$

The integral in Equation (11) can be readily expressed in terms of a Bessel function of the first kind, yielding

$$< \tilde{E}_x(r, \theta, \phi) > = \frac{ja\tilde{E}_0(j\omega)}{r \sin\theta} e^{-\omega^2 \tau_0^2/2} e^{-jkr} J_1(ka \sin\theta) \qquad (12)$$

We shall find it useful to employ the relation

$$J_1(x) = \frac{1}{j\pi} \int_{-1}^{1} e^{jxu} \frac{u \, du}{\sqrt{1 - u^2}} \qquad (13)$$

so that

$$< \tilde{E}_x(r, \theta, \phi) > = \frac{a\tilde{E}_0(j\omega)}{\pi r \sin\theta} e^{-jkr} e^{-\omega^2 \tau_0^2/2} \int_{-1}^{1} e^{jkau \sin\theta} \frac{u \, du}{\sqrt{1 - u^2}} \qquad (14)$$

4

Now if $E_0(t)$ is a delta function, $\tilde{E}_0(j\omega) = 1$ and we define

$$< h(t - r/c) > \; = \; \frac{a}{2\pi^2 r \sin\theta} \int_{-\infty}^{\infty} e^{j\omega(t-r/c)} e^{-\omega^2 \tau_0^2/2} d\omega \; . \tag{15}$$

$$\int_{-1}^{1} e^{jkau\sin\theta} \frac{udu}{\sqrt{1-u^2}}$$

as the expected value of the impulse response of the radiated field. Suppressing the time delay r/c, interchanging the order of integration, and performing the integration over ω, we obtain

$$< h(t) >= \frac{a}{\pi t_f r \sin\theta} \int_{-1}^{1} G\left(u + \frac{t}{t_f}; \frac{\tau_0}{t_f}\right) \frac{udu}{\sqrt{1-u^2}} \tag{16}$$

wherein we have defined the Gaussian function

$$G(x;\sigma) = \frac{1}{\sqrt{2\pi}\sigma} e^{-x^2/2\sigma^2} \tag{17}$$

and

$$t_f = \frac{a}{c}\sin\theta \tag{18}$$

denotes the radial "fill time" of the aperture for an observer at an angle θ with respect to the z-axis; $c = 1/\sqrt{\mu_0 \epsilon_0}$ denotes the speed of light in free space.

Now it is easy to show that $h(t)$ reduces, as it should, in the limit $\tau_0 \to 0$ to

$$\lim_{\tau_0 \to 0} < h(t) >= \frac{-a}{\pi r t_f \sin\theta} \frac{t/t_f}{\sqrt{1-(t/t_f)^2}} \quad (\mid t \mid < t_f) \tag{19}$$

and also that $< h(t) >$ is an odd function of t for any value of the parameter τ_0/t_f.[2] We have calculated the normalized impulse response

$$f(t) = -\frac{\pi r t_f \sin\theta}{a} < h(t) > \tag{20}$$

as a function of normalized time t/t_f, for various values of the parameter τ_0/t_f. The results are shown in Figure 2. It is evident from the curves shown that

---

[2]We remark that $< h(t) >$ is in general not causal. This is a consequence of our assumption that the turn-on time is a Gaussian random process.

the effect of increasing the value of τ_0 (the standard deviation of the turn-on time) smooths and broadens the expected value of the impulse response. It is not difficult to show that when τ_0/t_f becomes comparable to or exceeds unity,

$$\frac{-\pi r t_f \sin\theta}{a} < h(t) > \cong \frac{1}{2}\sqrt{\frac{\pi}{2}} \left[\frac{t_f}{\tau_0}\right]^2 \left[\frac{t}{\tau_0}\right] e^{-t^2/2\tau_0^2} \tag{21}$$

so that the width of the impulse response is ultimately controlled by τ_0, rather than by t_f. We show in Figure 3 a plot of $(\tau_0/t_f)^2 f(t)$ vs. normalized time t/τ_0 for the case where τ_0 dominates the impulse response.
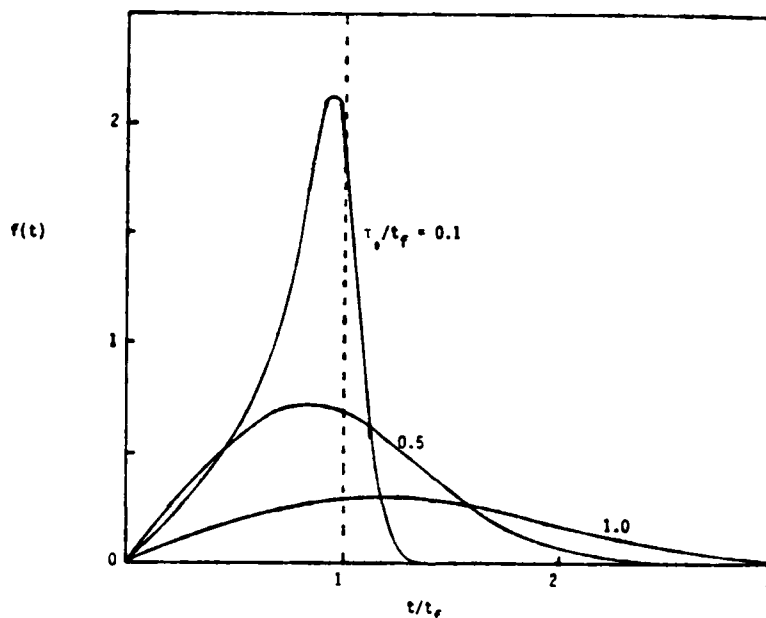
Figure 2. Normalized impulse response $f(t)$ vs. normalized time t/t_f, for $\tau_0/t_f =$ 0.1, 0.5, and 1.0, $0 \leq t/t_f \leq 3$; $f(-t) = -f(t)$.

It is evident that the effects of the random turn-on time are dominant for small observation angles θ. If we take as a maximum of t_f the value a/c, we see that turn-on time effects will dominate the impulse response for all observation angles if $c\tau_0/a$ is comparable to or greater than unity.

Since the impulse response, whether it is dominated by t_f or by τ_0, has a double peak, the radiated field will exhibit the same feature if the aperture field has a duration short compared to that of the impulse response. Thus a single short

6

pulse in the aperture can appear in the radiated field as a double pulse under certain conditions. The two components of the double pulse will be separated by a time of order $2t_f$ or $2\tau_0$, whichever is larger, and they will be opposite in sign. Under these conditions the antenna cannot be considered a "faithful" pulse radiator, because of the breakup of the radiated time-domain signal.

The expected value of the impulse response does not involve the spatial correlation of the turn-on time over the aperture. To show the effect of this descriptor of the aperture fields, we next consider the autocorrelation of the radiated field impulse response.
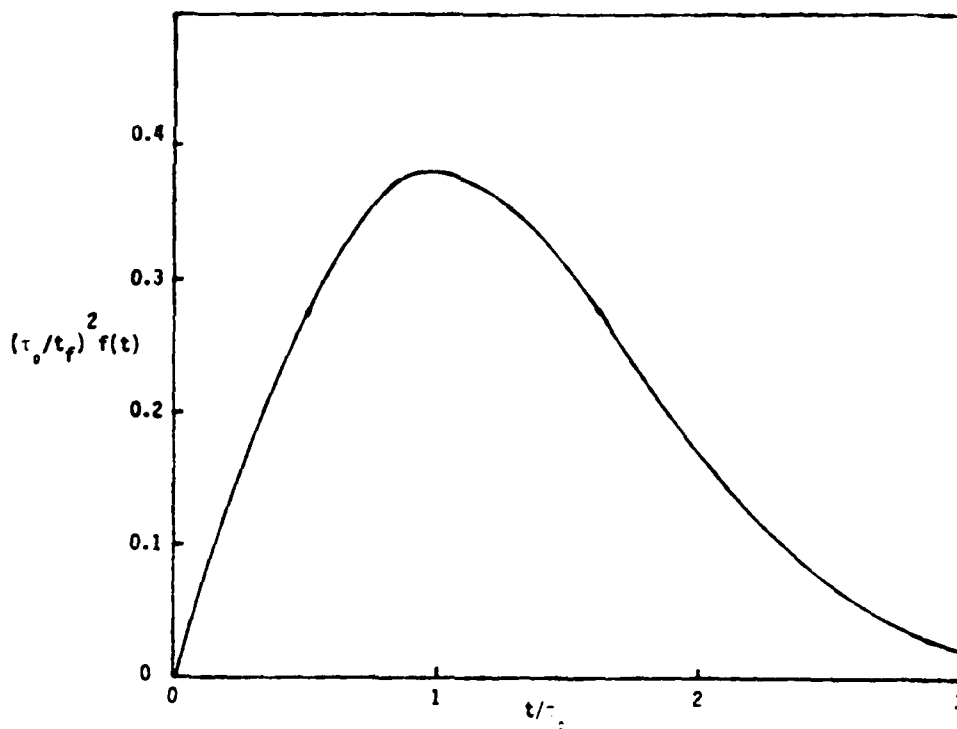
Figure 3. Normalized impulse response $(\tau_0/t_f)^2 f(t)$ vs normalized time t/τ_0 for the case where τ_0 dominates the response; $f(-t) = -f(t)$.

7

1.3 AUTOCORRELATION OF THE RADIATED FIELD IMPULSE RESPONSE.

The expected value of the energy spectral density in the radiated field is

$$\tilde{U}(\omega) = \frac{1}{Z_0} <\mid \tilde{E}_x(r,\theta,\phi) \mid^2> \tag{22}$$

where $Z_0 = \sqrt{\mu_0/\epsilon_0}$ denotes the intrinsic impedance of free space. Using equations (6) and (8), we have

$$\tilde{U}(\omega) = \frac{k^2 \mid \tilde{E}_0(j\omega) \mid^2}{4\pi^2 Z_0 r^2} \int_0^a \rho' d\rho' \int_0^{2\pi} d\phi' \int_0^a \rho'' d\rho'' \int_0^{2\pi} d\phi'' \cdot \tag{23}$$

$$e^{jk \sin\theta[\rho' \cos(\phi-\phi') - \rho'' \cos(\phi-\phi'')]} .$$

$$\left[e^{-\omega^2 \tau_0^2} + \left(1 - e^{-\omega^2 \tau_0^2}\right) f \left(\mid \vec{\rho}' - \vec{\rho}'' \mid\right) \right]$$

Now $\tilde{U}(\omega)$ as given by Equation (23) above can be expressed as

$$\tilde{U}(\omega) = \frac{\mid \tilde{E}_0(j\omega) \mid^2 a^2}{Z_0 r^2 \sin^2\theta} e^{-\omega^2 \tau_0^2} \ J_1^2(ka \sin\theta) \tag{24}$$

$$+ \ \frac{k^2 \mid \tilde{E}_0(j\omega) \mid^2}{Z_0 r^2} \left(1 - e^{-\omega^2 \tau_0^2}\right) \cdot$$

$$\left(\frac{1}{2\pi}\right)^2 \int_{A'} \int_{A''} e^{jk\hat{r}\cdot(\vec{\rho}'-\vec{\rho}'')} f(\mid \vec{\rho}' - \vec{\rho}'' \mid) d^2 s' d^2 s''$$

where $\hat{r}$ denotes the unit vector in the radial direction. If, as we shall assume, the correlation distance (i.e., the distance over which $f(\mid \vec{\rho}' - \vec{\rho}'' \mid)$ is close to unity) is small in comparison to the aperture radius a, the integral in Equation (24) may

be approximately evaluated, yielding for $\tilde{U}(\omega)$[3]

$$\tilde{U}(\omega) = \frac{|\tilde{E}_0(j\omega)|^2 a^2}{Z_0 r^2 \sin^2\theta} e^{-\omega^2 \tau_0^2} J_1^2(ka\sin\theta) \tag{25}$$

$$+ \frac{k^2 a^2 |E_0(j\omega)|^2}{2Z_0 r^2} \left(1 - e^{-\omega^2 \tau_0^2}\right) \int_0^\infty f(u) J_0(ku\sin\theta) u\, du$$

The autocorrelation of the radiated field impulse response, $H(t)$, is defined as the inverse Fourier transform of $Z_0 \tilde{U}(\omega) / |\tilde{E}_0(j\omega)|^2$:

$$H(t) \equiv \frac{a^2}{r^2 \sin^2\theta} \mathcal{F}^{-1} \left\{ e^{-\omega^2 \tau_0^2} J_1^2(ka\sin\theta) \right. \tag{26}$$

$$\left. + \frac{1}{2}(kl\sin\theta)^2 (1 - e^{-\omega^2 \tau_0^2}) \int_0^\infty f(lv) J_0(klv\sin\theta) v\, dv \right\}$$

where l denotes the characteristic correlation length. $H(t)$ thus comprises the sum of the autocorrelation of the expected value of the impulse response and an additional term which depends upon the spatial correlation of the aperture field turn-on time. To illustrate the behavior of the added term, consider the simple case where the aperture field turn-on times are perfectly correlated ($r = 1$) over circular regions of radius l ($l \ll a$) and uncorrelated outside these regions. Then defining

$$F_1(t) = \mathcal{F}^{-1} \left\{ e^{-\omega^2 \tau_0^2} J_1^2(ka\sin\theta) \right\} \tag{27}$$

$$F_2(t) = \mathcal{F}^{-1} \left\{ \frac{1}{2}(kl\sin\theta)^2 (1 - e^{-\omega^2 \tau_0^2}) \cdot \right. \tag{28}$$

$$\left. \int_0^\infty f(lv) J_0(klv\sin\theta) v\, dv \right\}$$

---

[3]In the event that the phase correlation distance is comparable to or larger than the aperture radius, $\tilde{U}(\omega)$ reduces to the simple result

$$\tilde{U}(\omega) = \frac{|\tilde{E}_0(j\omega)|^2 a^2}{Z_0 r^2 \sin^2\theta} J_1^2(ka\sin\theta)$$

which is not dependent on the statistical properties of the turn-on time.

9

so that

$$H(t) = \left(\frac{a}{r \sin \theta} \right)^2 [F_1(t) + F_2(t)] \tag{29}$$

we find [4]

$$F_1(t) = <h(t)> * <h(t)> \tag{30}$$

$$F_2(t) = \mathcal{F}^{-1} \left\{ \frac{1}{2} kl \sin \theta (1 - e^{-\omega^2 \tau_0^2}) J_1(kl \sin \theta) \right\} \tag{31}$$

When the correlation distance l is small (more precisely, if $kl \sin \theta << 1$ over the frequency range of interest),

$$F_2(t) \cong \mathcal{F}^{-1} \left\{ \left(\frac{1}{2} kl \sin \theta \right)^2 \left(1 - e^{-\omega^2 \tau_0^2} \right) \right\} \tag{32}$$

$$= -\left(\frac{l \sin \theta}{2c} \right)^2 \frac{d^2}{dt^2} \left[\delta(t) - \frac{1}{2\sqrt{\pi} \, \tau_0} e^{-t^2/4\tau_0^2} \right]$$

Furthermore, if τ_0 is comparable to or larger than t_f,

$$F_1(t) \cong -\left(\frac{a \sin \theta}{2c} \right)^2 \frac{d^2}{dt^2} \left(\frac{1}{2\sqrt{\pi} \, \tau_0} e^{-t^2/4\tau_0^2} \right) \tag{33}$$

so that

$$H(t) \cong -\left(\frac{a^2}{2rc} \right)^2 \frac{d^2}{dt^2} \left[\left(1 - \frac{l^2}{a_2} \right) \frac{1}{2\sqrt{\pi} \tau_0} e^{-t^2/4\tau_0^2} + \left(\frac{l}{a} \right)^2 \delta(t) \right] \tag{34}$$

$$\cong -\left(\frac{a^2}{2rc} \right)^2 \frac{d^2}{dt^2} \left[\frac{1}{2\sqrt{\pi} \, \tau_0} e^{-t^2/4\tau_0^2} + \left(\frac{l}{a} \right)^2 \delta(t) \right]$$

Thus the fact that the aperture field turn-on times are not highly correlated does not lengthen the duration of the autocorrelation function $H(t)$, and we conclude that

1. If the aperture field turn-on times are highly correlated, the autocorrelation duration is controlled by the fill time t_f, essentially independent of τ_0.

---

[4]The symbol * denotes the correlation operation.

2. If the aperture field turn-on time is not highly correlated, the autocorrelation duration is controlled by the larger of the fill time t_f or the standard deviation τ_0.

In the next section, we shall consider the effects of the fill time and the turn-on time errors on the radiated field when the aperture field is a cw pulse and the correlation function of the turn-on time is an exponential function:

$$r(u) = \exp(-u^2/l^2) \tag{35}$$

The function $\tilde{U}(\omega)$ for this case is

$$\tilde{U}(\omega) = \frac{\mid \tilde{E}_0(j\omega) \mid^2 a^2}{Z_0 r^2 \sin^2\theta} \left\{ e^{-\omega^2\tau_0^2} J_1^2(ka\sin\theta) \right. \tag{36}$$

$$\left. + \quad e^{-\omega^2\tau_0^2} \left(\frac{kl}{2}\sin\theta\right)^2 \sum_{n=1}^{\infty} \frac{(\omega\tau_0)^{2n}}{n(n!)} \exp\left[-\frac{1}{n}\left(\frac{kl}{2}\sin\theta\right)^2\right] \right\}$$

1.4   PULSED-CW RADIATED ENERGY DENSITY.

We have shown in the preceding sections that the impulse response duration is essentially the sum of the aperture fill time $t_f = (a/c)\sin\theta$ and the standard deviation of the turn-on time error τ_0. If the aperture field is a pulsed signal of duration $2T$, then the radiated field will be a "stretched" pulse of duration $2T + 2t_f + 2\tau_0$. In this section we consider the radiated energy density (J/m^2) when the aperture field is a Gaussian pulse of the form

$$E_0(t) = E_p e^{-t^2/2t_0^2} \cos\omega_0 t \tag{37}$$

E_p denotes the peak electric field strength in the aperture and t_0 is a measure of pulse width. The center frequency of the pulse is ω_0.

The total radiated-field energy density is readily shown to be

$$U = \frac{\pi E_p^2 t_0^2 a^2}{Z_0 r^2 \sin^2\theta} \int_{-\infty}^{\infty} e^{-(\omega-\omega_0)^2 t_0^2} \left[\tilde{F}_1(\omega) + \tilde{F}_2(\omega)\right] d\omega \tag{38}$$

11

with

$$\tilde{F}_1(\omega) = e^{-\omega^2 \tau_0^2} J_1^2(ka\sin\theta) \tag{39}$$

$$\tilde{F}_2(\omega) = e^{-\omega^2 \tau_0^2} \left(\frac{kl}{2}\sin\theta\right)^2 \sum_{n=1}^{\infty} \frac{(\omega\tau_0)^{2n}}{n(n!)} \exp\left[-\frac{1}{n}\left(\frac{kl}{2}\sin\theta\right)^2\right] \tag{40}$$

We shall consider the most important special case, that in which $t_0 \gg t_f$ and $t_0 \gg \tau_0$, so that the radiated pulse is a quasi-cw signal. The total energy radiated is readily found to be

$$U = U_0 \left\{ 4e^{-\omega_0^2 \tau_0^2} \frac{J_1^2(\omega_0 t_f)}{(\omega_0 t_f)^2} \tag{41} \right.$$

$$\left. + \left(\frac{l}{a}\right)^2 e^{-\omega_0^2 \tau_0^2} \sum_{n=1}^{\infty} \frac{(\omega_0 \tau_0)^{2n}}{n(n!)} \exp\left[-\frac{1}{n}\left(\omega_0 t_f \frac{l}{a}\right)^2\right] \right\}$$

where

$$U_0 = \frac{\pi^{3/2} k_0^2 a^4 E_p^2 t_0}{4 Z_0 r^2} \tag{42}$$

denotes the energy density radiated in the direction $\theta = 0$ when there is no turn-on time error.

Curves of U/U_0 as a function of $\omega_0 t_f$ are given in Figures 4 – 22 for various values of $\omega_0 \tau_0$ and l/a. We observe that as l/a (the normalized coherence length in the aperture) decreases, the effect of increasing the normalized standard deviation $\omega_0 \tau_0$ becomes more pronounced, appearing first at smaller values of $\omega_0 t_f$ (recall that turn-on time errors will dominate the impulse response if $\tau_0 > t_f$).

12
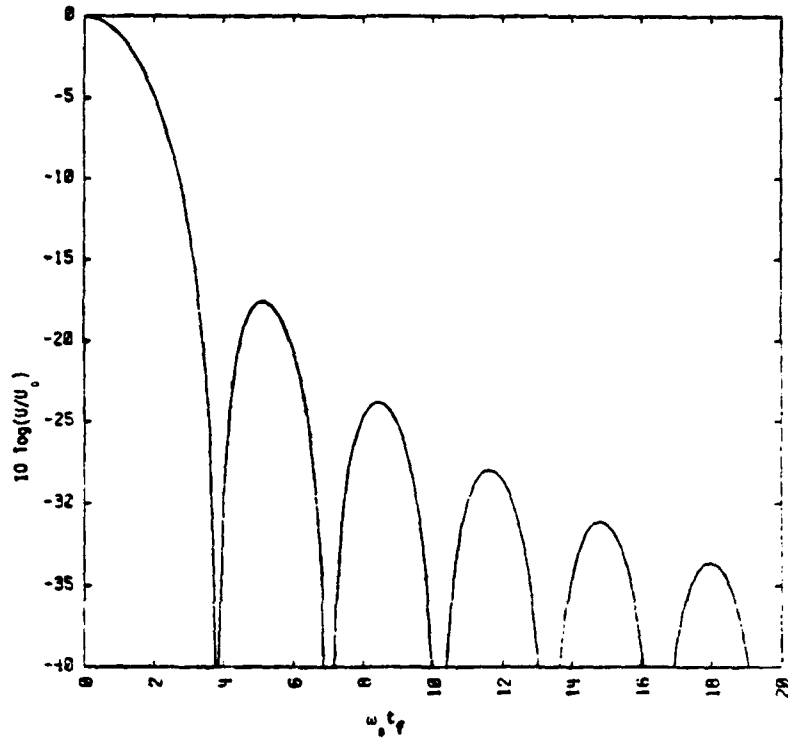
Figure 4. Normalized energy density U/U_0 vs. $\omega_0 t_f$: $\omega_0 \tau_0 = 0$ (perfectly coherent limit).
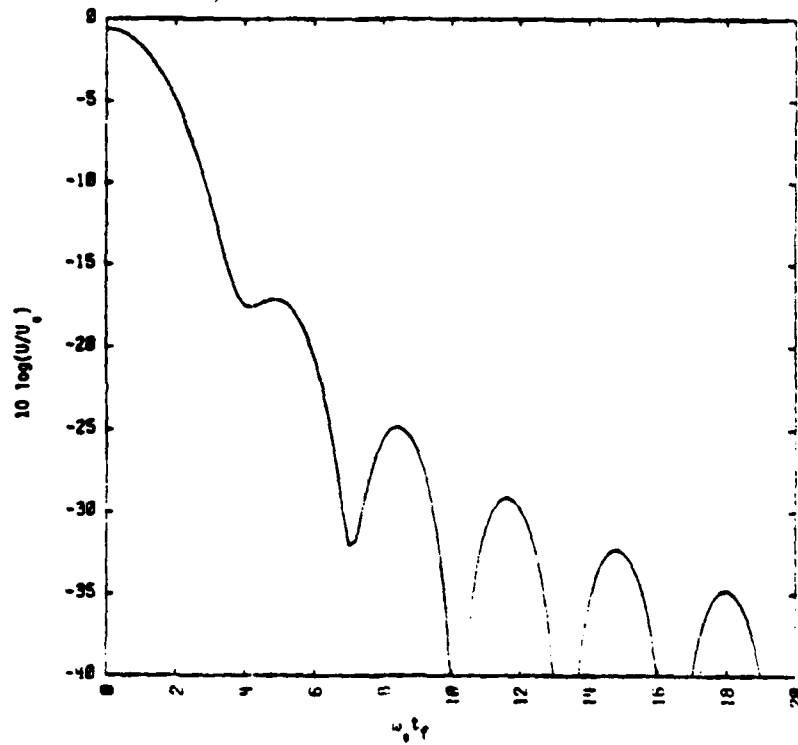
Figure 5. Normalized energy density U/U_0 vs. $\omega_0 t_f$: $l/a = 0.5$, $\omega_0 \tau_0 = \pi/6$.

13
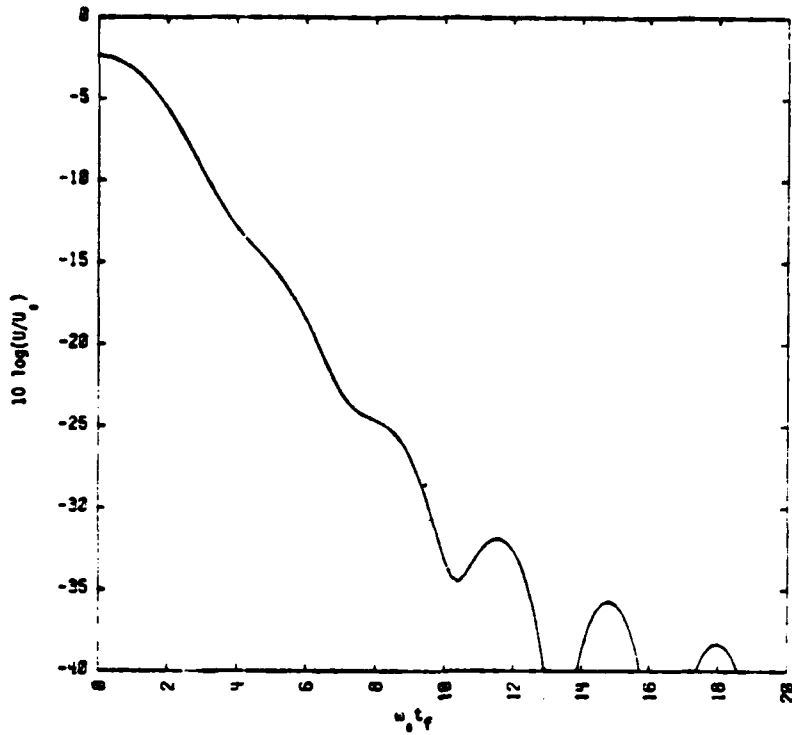
Figure 6. Normalized energy density U/U_0 vs. $\omega_0 t_f$: $l/a = 0.5$, $\omega_0 \tau_0 = \pi/3$.
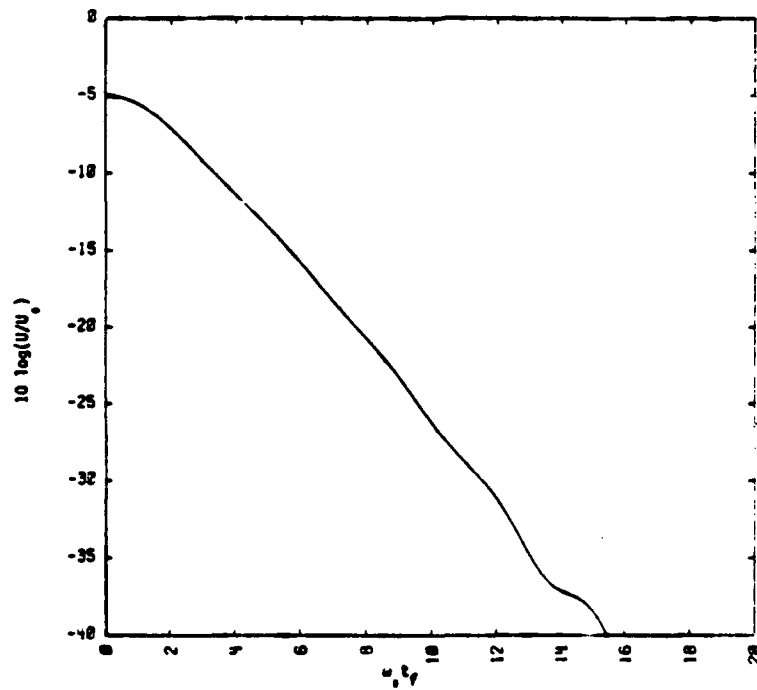
Figure 7. Normalized energy density U/U_0 vs. $\omega_0 t_f$: $l/a = 0.5$, $\omega_0 \tau_0 = \pi/2$.

14
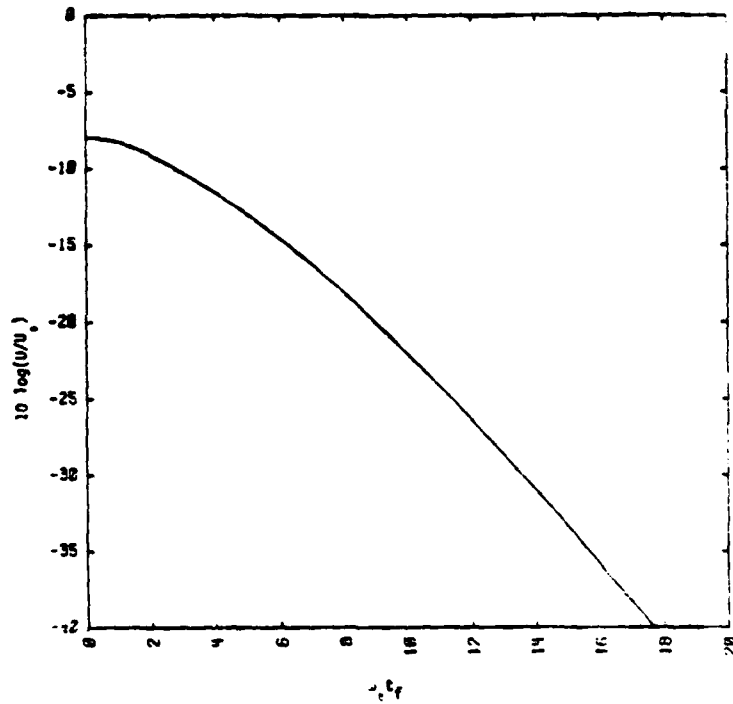
Figure 8.   Normalized energy density U/U_0 vs. $\omega_0 t_f$: $l/a = 0.5$, $\omega_0 \tau_0 = 2\pi/3$.
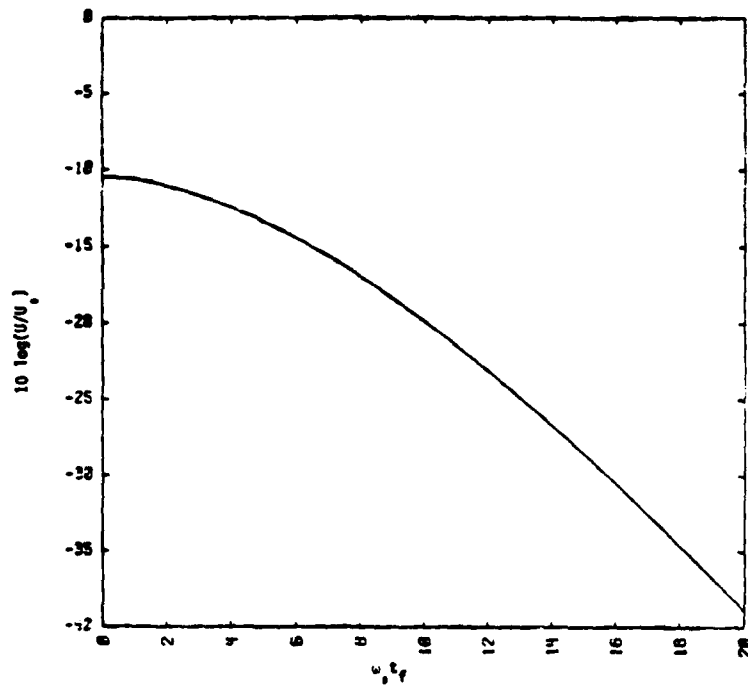
Figure 9.   Normalized energy density U/U_0 vs. $\omega_0 t_f$: $l/a = 0.5$, $\omega_0 \tau_0 = 5\pi/6$.
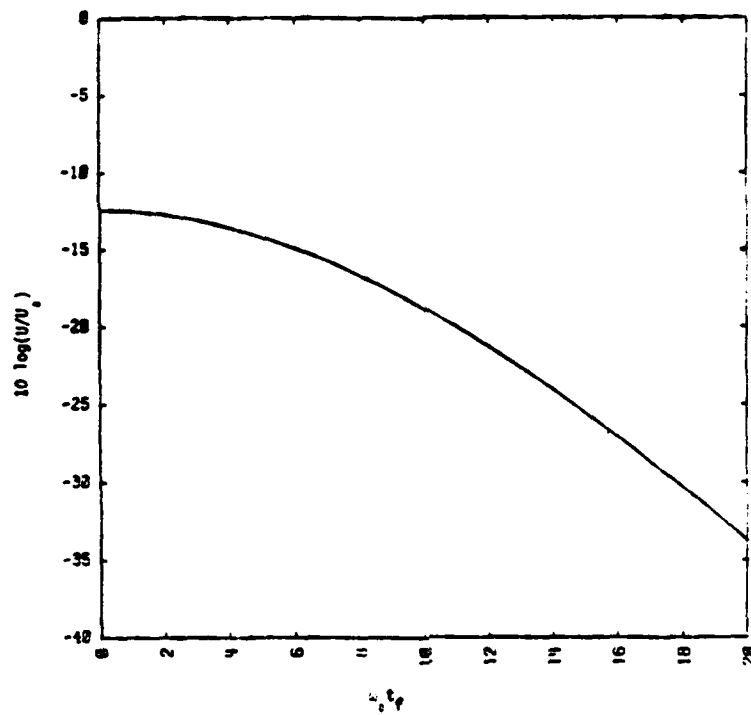
Figure 10. Normalized energy density U/U_0 vs. $\omega_0 t_f$: $l/a = 0.5$, $\omega_0 \tau_0 = \pi$.
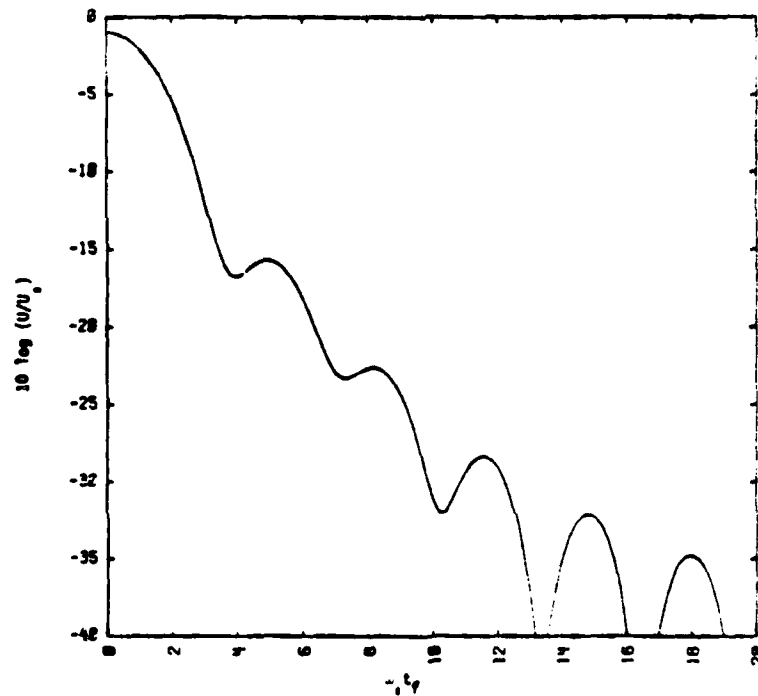
Figure 11. Normalized energy density U/U_0 vs. $\omega_0 t_f$: $l/a = 0.3$, $\omega_0 \tau_0 = \pi/6$.

16
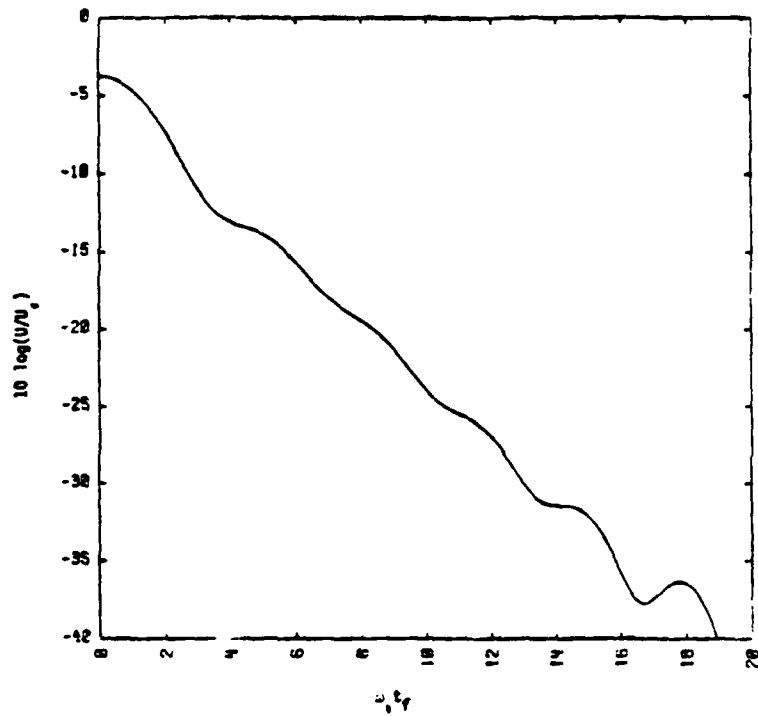
Figure 12. Normalized energy density U/U_0 vs. $\omega_0 t_f$: $l/a = 0.3$, $\omega_0 \tau_0 = \pi/3$.
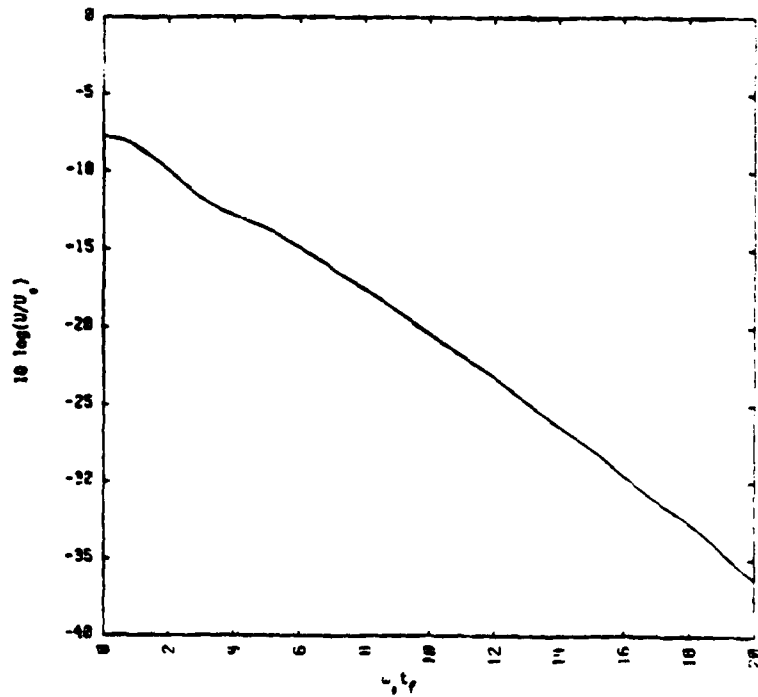
Figure 13. Normalized energy density U/U_0 vs. $\omega_0 t_f$: $l/a = 0.3$, $\omega_0 \tau_0 = \pi/2$.

17
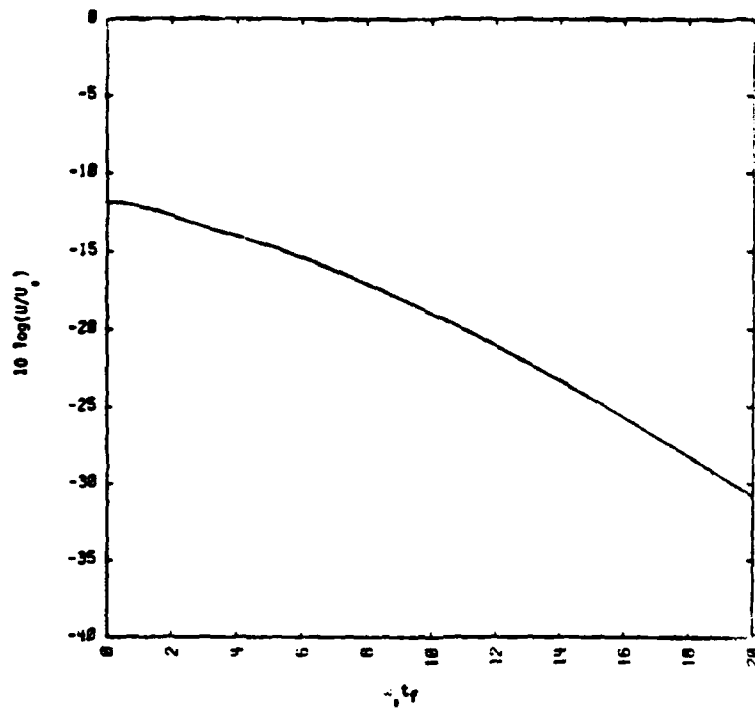
Figure 14. Normalized energy density U/U_0 vs. $\omega_0 t_f$: $l/a = 0.3$, $\omega_0 \tau_0 = 2\pi/3$.
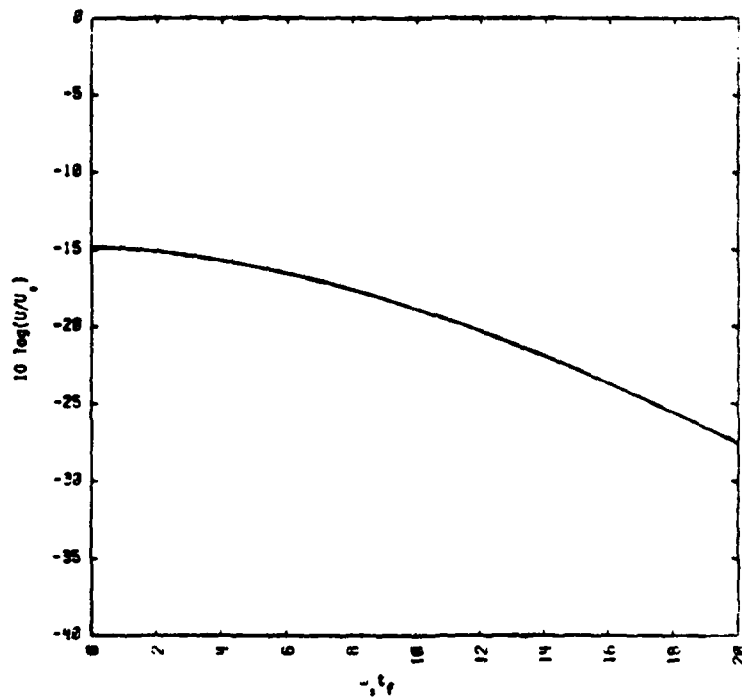
Figure 15. Normalized energy density U/U_0 vs. $\omega_0 t_f$: $l/a = 0.3$, $\omega_0 \tau_0 = 5\pi/6$.
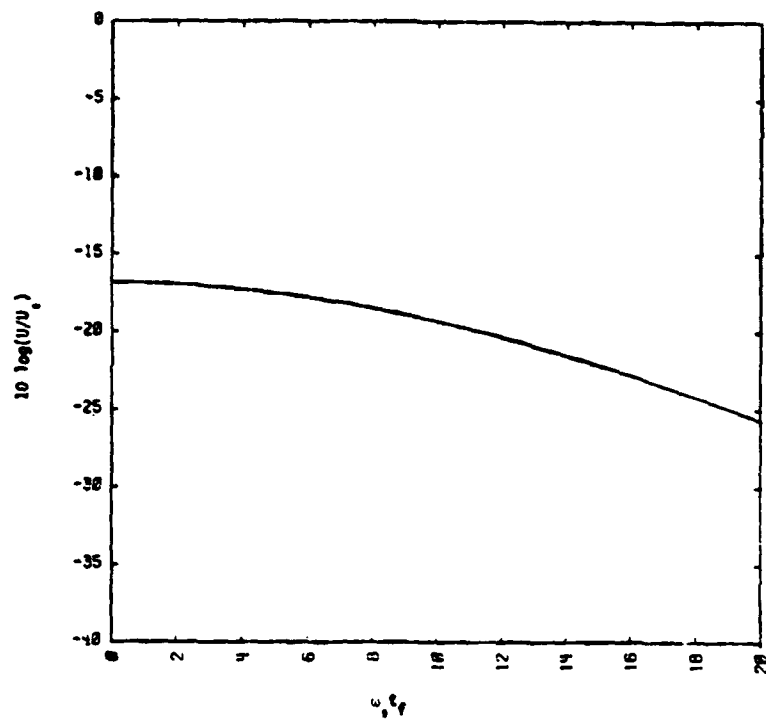
Figure 16. Normalized energy density U/U_0 vs. $\omega_0 t_f$: $l/a = 0.3$. $\omega_0 \tau_0 = \pi$.
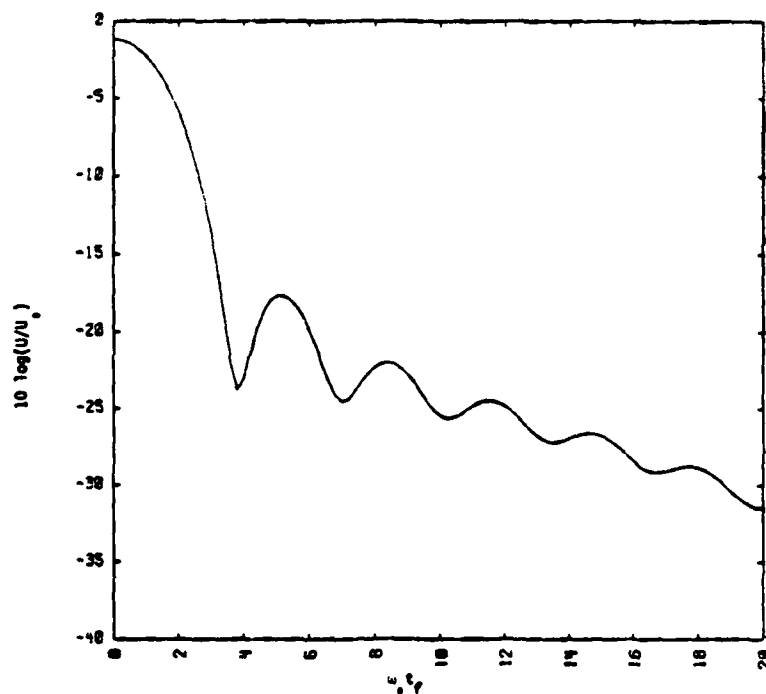
Figure 17. Normalized energy density U/U_0 vs. $\omega_0 t_f$: $l/a = 0.1$, $\omega_0 \tau_0 = \pi/6$.

19
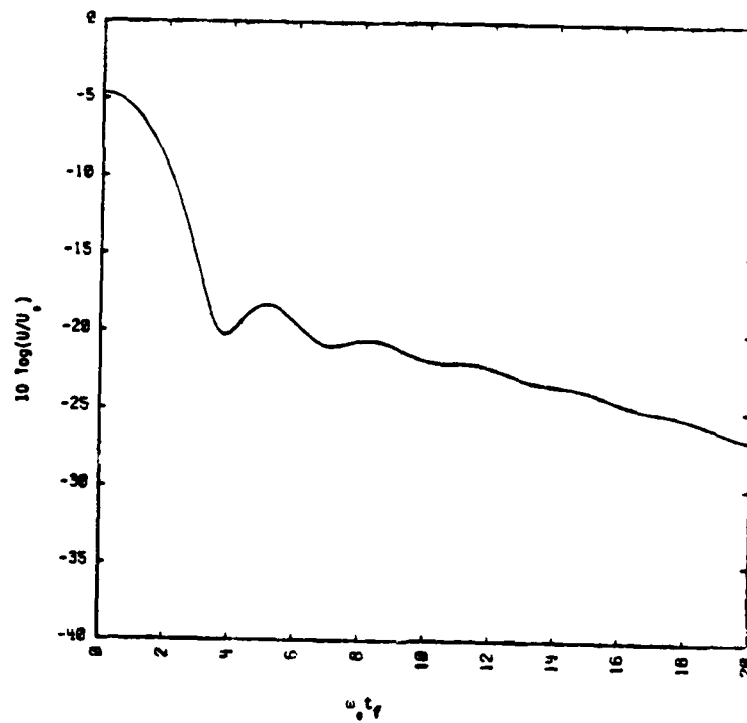
Figure 18.   Normalized energy density U/U_0 vs. $\omega_0 t_f$: $l/a = 0.1$, $\omega_0 \tau_0 = \pi/3$.
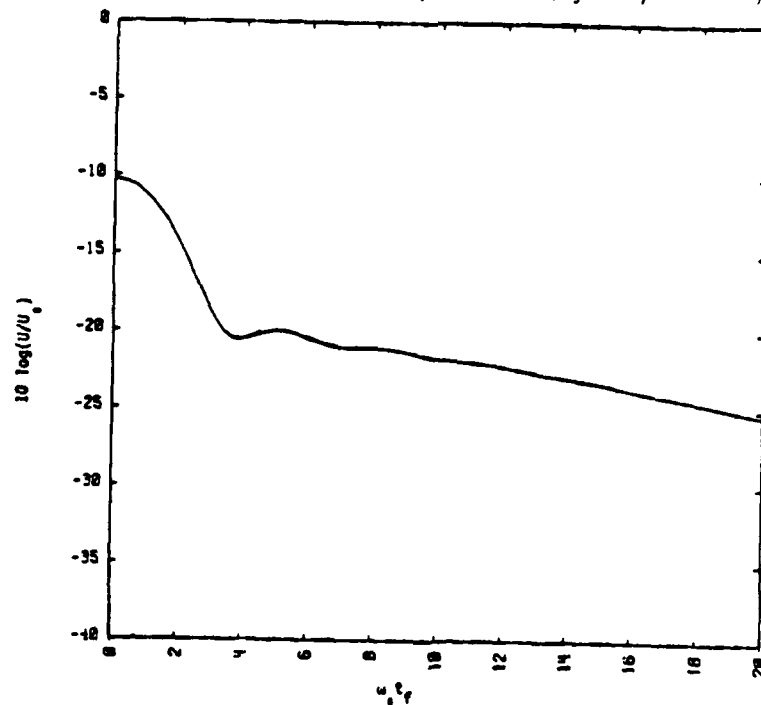
Figure 19.   Normalized energy density U/U_0 vs. $\omega_0 t_f$: $l/a = 0.1$, $\omega_0 \tau_0 = \pi/2$.

20
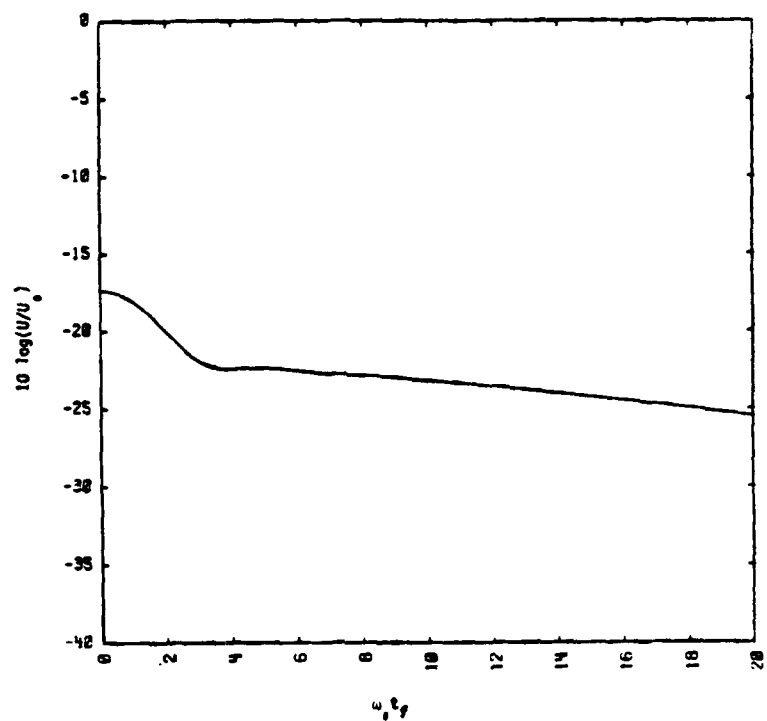
Figure 20. Normalized energy density U/U_0 vs. $\omega_0 t_f$: $l/a = 0.1$, $\omega_0 \tau_0 = 2\pi/3$.
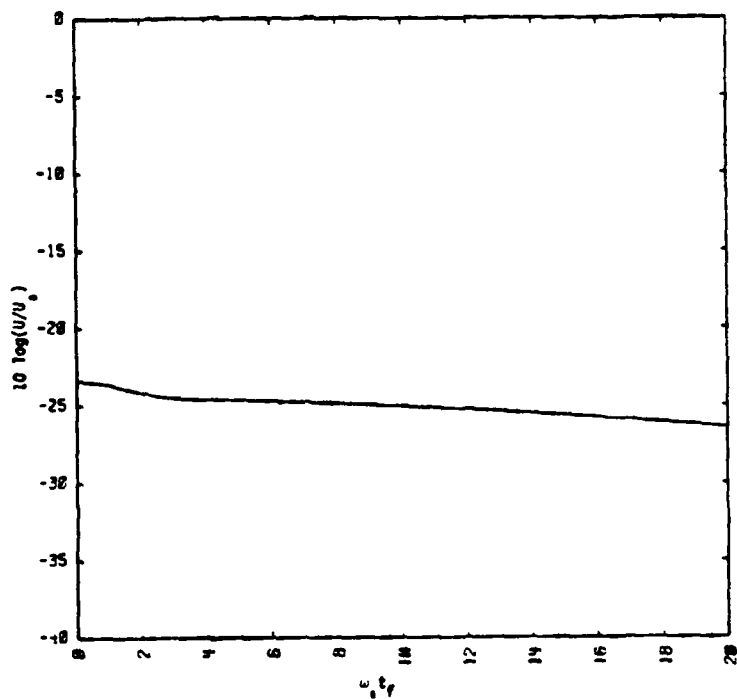
Figure 21. Normalized energy density U/U_0 vs. $\omega_0 t_f$: $l/a = 0.1$, $\omega_0 \tau_0 = 5\pi/6$.

21
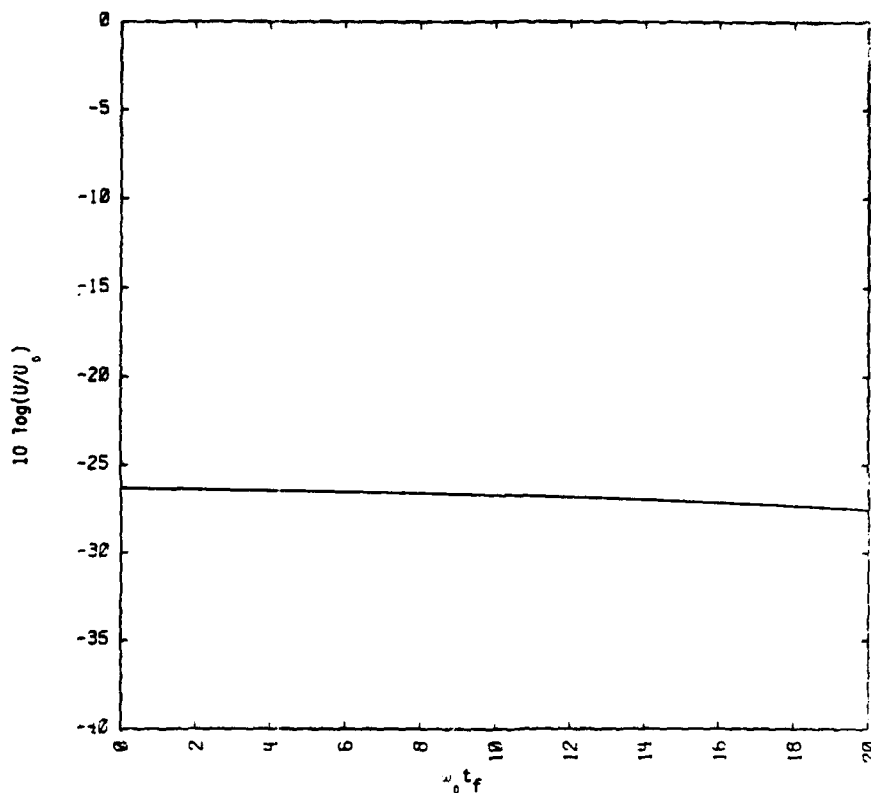
Figure 22. Normalized energy density U/U_0 vs. $\omega_0 t_f$: $l/a = 0.1$, $\omega_0 \tau_0 = \pi$.

1.5 CONCLUDING REMARKS.

We have considered the electromagnetic field radiated from a circular aperture excited by a field which is uniform except for randomly distributed turn-on time errors. We have found the expected value of the impulse response and of the autocorrelation of the radiated field, and have shown that the shape and the duration of these functions depend upon the aperture fill time $t_f = (a/c) \sin \theta$ and the standard deviation of the turn-on time τ_0. The fact that these functions possess two peaks separated by twice the sum of τ_0 and t_f means that the field radiated by a sufficiently short pulsed aperture field will comprise two more or less distinct components separated in time. Thus a pulse radiated from the aperture will "hang together" only if it is at least comparable in length to t_f and/or τ_0.

We have presented extensive numerical data for the pulse energy density radiated by a quasi-cw aperture-field pulse and have shown the influence of the standard deviation and of the correlation function of the turn-on time. In particular, for a fixed value of τ_0, decreasing the correlation distance causes a reduction in the energy radiated in the axial direction and an increase in that radiated in other directions: the source becomes, in effect, more nearly isotropic. A simular effect is seen as the standard deviation τ_0 is increased for a fixed correlation distance.

We also note that the effect of the nonuniformity in turn-on time can be quite

22

severe: the energy radiated in the axial direction decreases as $\exp(-\omega_0^2 \tau_0^2)$, where ω_0 is the pulse center frequency. Thus if $\omega_0 \tau_0 = \pi$ (corresponding to one-half cycle at frequency ω_0) the axial energy is reduced by over 40 dB if the turn-on time errors are not highly correlated over the aperture.

The value of $\omega_0 t_f$ associated with the edge of the main lobe of a circular aperture antenna pattern in the absence of turn-on time errors is 3.832, the first zero of $J_1(\cdot)$. For a short cw pulse to be radiated essentially as a single pulse over the corresponding angular range requires that $\omega_0 t_0 \gg 3.832$. If, for example, one chooses $\omega_0 t_0$ equal to 12π to satisfy this condition, then the aperture-field pulse contains six cycles. Thus an aperture-field pulse of few cycles will be radiated as a single pulse over the (cw) main antenna-pattern lobe. For angles greater than $\theta_m \cong \sin^{-1}(ct_0/a)$ the radiated pulse will be broken into two distinct pulses, [5] each of which will have a much lower amplitude than the single pulse radiated in the main lobe. The transition occurs over the angular range

$$\sin^{-1}\left[\frac{3.832}{\omega_0 t_0}\left(\frac{ct_0}{a}\right)\right] \le \theta \le \sin^{-1}\left(\frac{ct_0}{a}\right) \tag{43}$$

The implications of these results for microwave weapon threat analysis are that

- the principal threat comes from the main lobe of the transmitting antenna pattern and comprises a quasi-cw pulse which is stretched by an amount depending on the antenna fill time and the standard deviation of the turn-on time error. The energy density carried by this pulse can be estimated from results provided herein.

- the signal radiated well outside the main lobe of the transmitting antenna can be expected to be a "double pulse" of low amplitude.

- turn-on time errors in the aperture field of the transmitting antenna can drastically reduce the radiated energy density.

---

[5] Note that if $t_0 > a/c, \theta_m$ is a complex angle whose real part is $\pi/2$; thus a single pulse will be observed at any real angle θ if this condition is met.

SECTION 2
SCATTERING CROSS-SECTION OF A DIPOLE:
IMPLICATIONS FOR MICROWAVE COUPLING

Summary: We calculate the power scattering cross-section of an unloaded dipole antenna and estimate the equivalent source strength of a long thin slot illuminated by a plane-wave field. We also determine the impulse response of the s attered field in order to find the amount of pulse stretching caused by the scattering process. It is shown that under pulsed cw illumination, the peak power scattered by the wire or transmitted through the slot can be estimated on the basis of the cw cross-section in cases of practical interest.

A fundamental problem in the study of microwave interactions with systems is that of determining the amount of energy which could be coupled from the exterior to the interior of a shielded system by means of penetration through apertures in the "skin". In this section we investigate coupling through a narrow slot aperture, which may be of resonant length or longer, in a conducting surface. Our approach is an indirect one, in which we first treat the dual problem of scattering by a straight wire in free space and determine its equivalent power scattering cross-section for continuous-wave (cw) illumination. It is then a simple matter to obtain the equivalent transmission area of the thin slot.

The problem of electromagnetic-wave scattering by a wire has received a great deal of attention in the literature. We have elected to employ a primarily analytical, rather than numerical, approach to the problem based upon the Hallén integral equation for the wire current [2,3]. This approach has been used by Marin [4] to study the natural modes of various thin-wire structures and by Bedrosian [5] to find the natural resonances and modes of stick-model aircraft. In the present case, it leads to an (almost) closed-form expression for the scattering cross-section convenient for analytical and numerical exploration. This expression then can be carried over with minor modification to describe the electromagnetic penetration through a thin slot.

Our principal interest is actually in the pulsed cw response of the wire or slot. In order to estimate the total pulse energy scattered, we determine the impulse response of the scatterer. The temporal duration of this impulse response defines

24

the amount of pulse stretching which occurs in the scattering process. The peak power scattered can be estimated from the cw response of the scatterer when the illuminating pulse contains at least a few cycles of oscillation.

2.1 DIPOLE SCATTERING CROSS-SECTION.

The geometry of the dipole scattering problem is shown in Figure 23. A thin cylindrical conductor of radius a lies along the z-axis between $z = \pm l/2$. The conductor's radius is assumed to be small in comparison to its length l and to the free-space wavelength λ. The scatterer is illuminated by a plane electromagnetic wave polarized in the θ-direction and incident at an angle θ with respect to the z-axis.

Because the conductor is thin, the induced current and charge densities on it are essentially independent of angular position; and the current is predominantly in the axial direction. Thus the electromagnetic quantities of interest on the scatterer are its net axial current $I(z)$ and line charge density $\rho_l(z)$; these quantities are related by the continuity equation

$$\frac{dI}{dz} + j\omega\rho_l = 0 \tag{44}$$

We assume the time dependence $exp\ (j\omega t)$ for all field quantities.

The total power scattered by the cylindrical conductor can be expressed as [6]

$$P_s = \omega \int_{-l/2}^{l/2} \int_{-l/2}^{l/2} \left[\frac{\mu_0}{2} I^*(z)I(z') - \frac{1}{2\epsilon_0}\rho_l{}^*(z)\rho_l(z') \right] \frac{\sin k \mid z - z' \mid}{4\pi \mid z - z' \mid} dz dz' \tag{45}$$

where μ_0 and ϵ_0 denote, respectively, the permeability and permittivity of free space and $k = \omega\sqrt{\mu_0\epsilon_0}$. The incident power density S_{in} is expressed in terms of the incident electric field amplitude E_i as

$$S_{in} = \frac{\mid E_i \mid^2}{2Z_0} \tag{46}$$

where $Z_0 = \sqrt{\mu_0/\epsilon_0}$ denotes the instrinsic impedance of free space. The scattering cross-section is simply

$$A_e = \frac{P_s}{S_{in}} \tag{47}$$

25
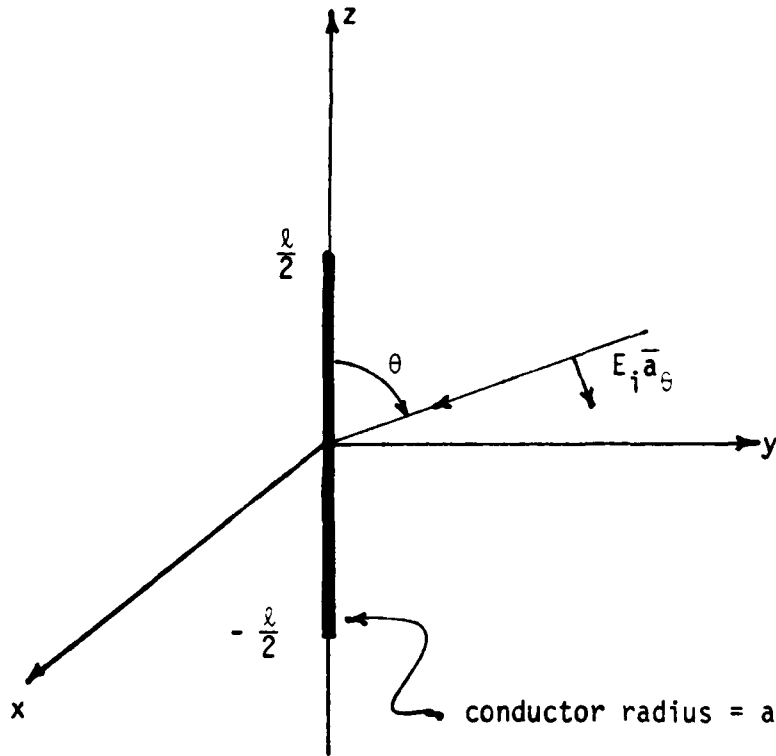
Figure 23.   Geometry of the dipole scattering problem. The radius of the dipole is a and the incident electric field is in the θ direction.

Therefore, anticipating that $I(z)$ must take the form

$$I(z) = \frac{E_i}{Z'} f(kz) \tag{48}$$

where Z' is an impedance per unit length and $f(\cdot)$ is a dimensionless function of kz, we find with Eqs. (44) - (47) that

$$A_e = \frac{Z_0{}^2}{4\pi \mid Z' \mid^2} \int_{-kl/2}^{kl/2} \int_{-kl/2}^{kl/2} \left[f^*(u)f(v) - \frac{df^*(u)}{du}\frac{df(v)}{dv} \right] \frac{\sin(u - v)}{u - v} du\, dv \tag{49}$$

The problem of determining the scattering cross-section A_e thus reduces to that of finding Z' and $f(\cdot)$.

The current induced on the scatterer is given approximately by the solution of the differential equation [3]

$$\frac{d^2 I}{dz^2} + k^2 I = \frac{-4\pi j\omega\epsilon_0 E_i}{\Omega} \sin\theta e^{jkz\cos\theta} \qquad \left(\mid z \mid \leq \frac{l}{2} \right) \tag{50}$$

26

subject to the end conditions $I(\pm l/2) = 0$. The "antenna parameter" Ω is defined

$$\Omega = 2\ln(l/a) \tag{51}$$

It is an elementary exercise to show that the solution of Eq. (50) which satisfies the end conditions is

$$I(z) = \frac{-4\pi j E_i l}{Z_0 \Omega \sin\theta(kl\sin kl)} \left[\sin kl \, e^{jkz\cos\theta} - 2j\cos\frac{kl}{2}\sin\left(\frac{kl}{2}\cos\theta\right)\sin kz \right. \tag{52}$$

$$\left. -2\sin\frac{kl}{2}\cos\left(\frac{kl}{2}\cos\theta\right)\cos kz \right]$$

The function in square brackets, which we shall identify as $f(kz)$, can also be written

$$f(u) = \sin kl \, e^{ju\cos\theta} - \sin\left[\frac{kl}{2}(1+\cos\theta)\right]e^{ju} \tag{53}$$

$$-\sin\left[\frac{kl}{2}(1-\cos\theta)\right]e^{-ju}$$

It is evident that $I(z)$ as given in Eq. (52) is singular at the antenna resonances $kl = n\pi$ ($|n| \geq 1$). To remove these unphysical singularities, we take the radiation damping into account by writing the factor $(kl\sin kl)^{-1}$ in the form of a Mittag-Leffler expansion [7] and then shifting its poles into the upper half of the complex k-plane. Thus

$$(kl\sin kl)^{-1} \rightarrow \frac{1}{D(kl)} \tag{54}$$

where

$$\frac{1}{D(kl)} = \frac{1}{(kl)^2} + \frac{1}{6} + \sum_{n=-\infty}^{\infty}{}' \frac{(-)^n}{n\pi}\left[\frac{1}{kl-n\pi-j\alpha_n} + \frac{1}{n\pi+j\alpha_n}\right] \tag{55}$$

The prime ($'$) on the summation indicates that the term for $n = 0$ is to be omitted. The constants α_n are calculated using a perturbation analysis [4] and can be written in closed form as

$$\alpha_n = \frac{1}{\Omega}\left[\gamma + \ln(2|n|\pi) - \text{Ci}(2|n|\pi)\right] \tag{56}$$

27

wherein $\gamma = 0.57721...$ is Euler's constant and $\text{Ci}(\cdot)$ denotes the cosine integral. Using Eqs. (48) and (52) with (54), we find that

$$\frac{1}{Z'} = \frac{-4\pi jl}{Z_0 \Omega \sin\theta D(kl)} \tag{57}$$

so the scattering cross-section A_e is written

$$A_e = \frac{4\pi l^2}{\Omega^2 \sin^2\theta \mid D(kl) \mid^2} \int_{-kl/2}^{kl/2} \int_{-kl/2}^{kl/2} \left[f^*(u)f(v) - \frac{df^*}{du}\frac{df}{dv} \right] \cdot \frac{\sin(u-v)}{u-v} du dv \tag{58}$$

where $f(u)$ is defined in Eq. (53) and $D(kl)$ in Eq. (54). The evaluation of the integral in Eq. (58) is tedious but straightforward. The real part of the function in square brackets can be written as

$$\Re[\cdot] = \sum_{n=1}^{4} a_n \cos\left[\alpha_n(u-v)\right] \cos\left[\beta_n(u+v)\right] \tag{59}$$

where

$$a_1 = \sin^2 kl \sin^2 \theta$$

$$a_2 = 4\sin\left[\frac{kl}{2}(1+\cos\theta)\right] \sin\left[\frac{kl}{2}(1-\cos\theta)\right]$$

$$a_3 = -2\sin kl \sin\left[\frac{kl}{2}(1+\cos\theta)\right](1-\cos\theta)$$

$$a_4 = -2\sin kl \sin\left[\frac{kl}{2}(1-\cos\theta)\right](1+\cos\theta) \tag{60}$$

$$\begin{array}{ll}
\alpha_1 = \cos\theta & \beta_1 = 0 \\
\alpha_2 = 0 & \beta_2 = 1 \\
\alpha_3 = \frac{1}{2}(1+\cos\theta) & \beta_3 = \frac{1}{2}(1-\cos\theta) \\
\alpha_4 = \frac{1}{2}(1-\cos\theta) & \beta_4 = \frac{1}{2}(1+\cos\theta)
\end{array}$$

An integral of the form

$$I_n = \int_{-kl/2}^{kl/2} \int_{-kl/2}^{kl/2} \cos\left[\alpha_n(u-v)\right] \cos\left[\beta_n(u+v)\right] \frac{\sin(u-v)}{u-v} du dv \tag{61}$$

28

can be expressed as

$$I_n = 2 \int_0^{kl} \frac{\sin \xi}{\xi} \cos \alpha_n \xi d\xi \int_0^{kl-\xi} \cos \beta_n \eta d\eta \qquad (62)$$

by means of a straightforward change of variables. The latter form for I_n is evaluated as

$$
\begin{aligned}
I_n \;=\; & \frac{1}{2\beta_n} \sin \beta_n kl \left\{ \mathrm{Si} \left[(1 + \alpha_n - \beta_n)kl \right] \right. \\[6pt]
& + \mathrm{Si} \left[(1 - \alpha_n - \beta_n)kl \right] + \mathrm{Si} \left[(1 - \alpha_n + \beta_n)kl \right] \\[6pt]
& \left. + \mathrm{Si} \left[(1 + \alpha_n + \beta_n)kl \right] \right\} \\[10pt]
& - \frac{1}{2\beta_n} \cos \beta_n kl \left\{ \ln \left[(1 + \beta_n - \alpha_n) kl \right] - \mathrm{Ci} \left[(1 + \beta_n - \alpha_n)kl \right] \right. \qquad (63) \\[6pt]
& - \ln \left[(1 - \alpha_n - \beta_n)kl \right] + \mathrm{Ci} \left[(1 - \alpha_n - \beta_n)kl \right] \\[6pt]
& - \ln \left[(1 + \alpha_n - \beta_n)kl \right] + \mathrm{Ci} \left[(1 + \alpha_n - \beta_n)kl \right] \\[6pt]
& \left. + \ln \left[(1 + \alpha_n + \beta_n)kl \right] - \mathrm{Ci} \left[(1 + \alpha_n + \beta_n)kl \right] \right\}
\end{aligned}
$$

When $\beta_n = 0$, we have

$$
\begin{aligned}
I_n(\beta_n = 0) \;=\; & kl \left\{ \mathrm{Si} \left[(1 + \alpha_n)kl \right] + \mathrm{Si} \left[(1 - \alpha_n)kl \right] \right\} \qquad (64) \\[8pt]
& - \left\{ \frac{1 - \cos \left[(1 + \alpha_n)kl \right]}{1 + \alpha_n} + \frac{1 - \cos \left[(1 - \alpha_n)kl \right]}{1 - \alpha_n} \right\}
\end{aligned}
$$

Thus,

$$
\begin{aligned}
I_1 \;=\; & kl \left\{ \mathrm{Si}[(1 + \cos \theta)kl] + \mathrm{Si}[(1 - \cos \theta)kl] \right\} \qquad (65) \\[8pt]
& - \left\{ \frac{1 - \cos[(1 + \cos \theta)kl]}{1 + \cos \theta} + \frac{1 - \cos[(1 - \cos \theta)kl]}{1 - \cos \theta} \right\}
\end{aligned}
$$

$$
\begin{aligned}
I_2 \;=\; & \sin kl \; \mathrm{Si}(2kl) \qquad (66) \\[8pt]
& - \cos kl \left[\alpha + \ln(2kl) - \mathrm{Ci}(2kl) \right]
\end{aligned}
$$

29

$$I_3 = \frac{\sin\left[\frac{kl}{2}(1-\cos\theta)\right]}{(1-\cos\theta)}\left\{\text{Si}\left[(1+\cos\theta)kl\right] + \text{Si}\left[(1-\cos\theta)kl\right] + \text{Si}(2kl)\right\} \tag{67}$$

$$- \frac{\cos\left[\frac{kl}{2}(1-\cos\theta)\right]}{(1-\cos\theta)}\left\{\ln\left[(1-\cos\theta)kl\right] - \text{Ci}\left[(1-\cos\theta)kl\right]\right.$$

$$- \ln\left[(1+\cos\theta)kl\right] + \text{Ci}\left[(1+\cos\theta)kl\right] + \ln(2kl) - \text{Ci}(2kl) + \gamma\}$$

$$I_4 = \frac{\sin\left[\frac{kl}{2}(1+\cos\theta)\right]}{(1+\cos\theta)}\left\{\text{Si}\left[(1+\cos\theta)kl\right] + \text{Si}\left[(1-\cos\theta)kl\right] + \text{Si}(2kl)\right\} \tag{68}$$

$$- \frac{\cos\left[\frac{kl}{2}(1+\cos\theta)\right]}{(1+\cos\theta)}\left\{\ln\left[(1+\cos\theta)kl\right] - \text{Ci}\left[(1+\cos\theta)kl\right]\right.$$

$$- \ln\left[(1-\cos\theta)kl\right] + \text{Ci}\left[(1-\cos\theta)kl\right] + \ln(2kl) - \text{Ci}(2kl) + \gamma\}$$

Assembling these results, we find that A_e is given by

$$A_e = \frac{4\pi l^2}{\Omega^2 \mid D(kl) \mid^2 \sin^2\theta}\left(f_1 + f_2 + f_3 + f_4\right) \tag{69}$$

where

$$f_1 = 2\left[1 - \cos kl \cos(kl\cos\theta)\right]\left[\gamma + \ln(2kl) - \text{Ci}(2kl)\right] \tag{70}$$

$$f_2 = 2\sin kl \sin(kl\cos\theta)\left\{2\log\left(\tan\frac{\theta}{2}\right) + \text{Ci}\left[(1+\cos\theta)kl\right] - \text{Ci}\left[(1-\cos\theta)kl\right]\right\} \tag{71}$$

$$f_3 = \left\{kl\sin^2\theta\sin^2 kl - 2\sin kl[\cos(kl\cos\theta) - \cos kl]\right\} \cdot \tag{72}$$

$$\left\{\text{Si}[(1+\cos\theta)kl] + \text{Si}[(1-\cos\theta)kl]\right\}$$

$$f_4 = -2\sin^2\theta\sin^2 kl\left\{\frac{\sin^2\left[\frac{kl}{2}(1+\cos\theta)\right]}{1+\cos\theta} + \frac{\sin^2\left[\frac{kl}{2}(1-\cos\theta)\right]}{1-\cos\theta}\right\} \tag{73}$$

When $\theta = \pi/2$, i.e., when the cylinder is illuminated at broadside, A_e simplifies to

$$A_e = \frac{4\pi l^2}{\Omega^2 \mid D(kl) \mid^2}g(kl) \tag{74}$$

30

with

$$g(kl) \;=\; 2(1 - \cos kl)(\gamma + \ln(2kl) - \text{Ci}(2kl)) \qquad (75)$$

$$+ \; 2\left[kl\sin^2 kl - 2\sin kl(1 - \cos kl)\right]\text{Si}(kl)$$

$$- \; 4\sin^2 kl \sin^2 \frac{kl}{2}$$

We have calculated the normalized scattering cross-section A_e/l^2 as a function of kl for various values of Ω and θ, and as a function of θ with Ω and kl as parameters. The results are shown in Figures 24 – 40.

The characteristic resonances are apparent in the plots of A_e/l^2 vs. kl, which also indicate the maximum value (approximately 2.1) attained by this quantity at the fundamental (half-wave) resonance. Thus the effective area of the unloaded dipole near its half-wave resonance is of the order of the square of its length, almost independent of its radius. The effect of changing the radius, and thus the antenna parameter Ω, is to alter the "Q" of the resonance.
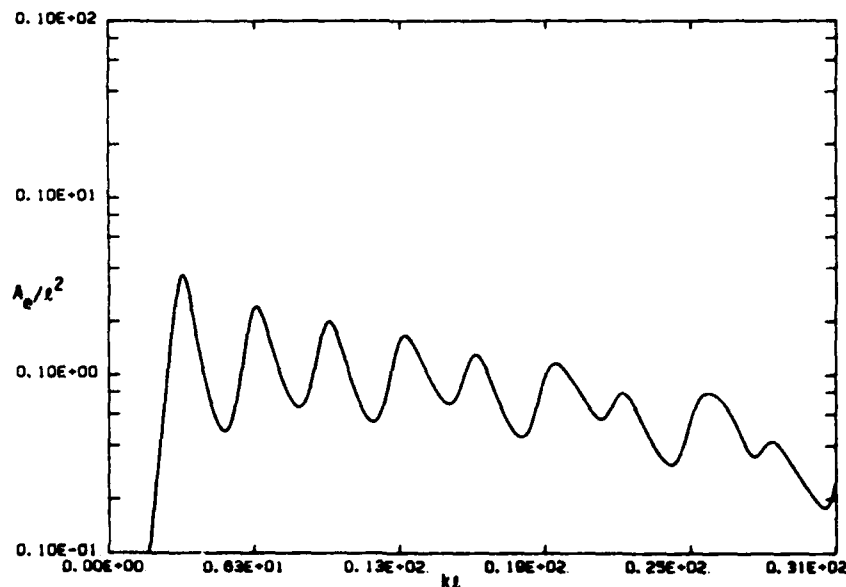
Figure 24. A_e/l^2 vs. kl; $\theta = 30°$, $\Omega = 5$.

31
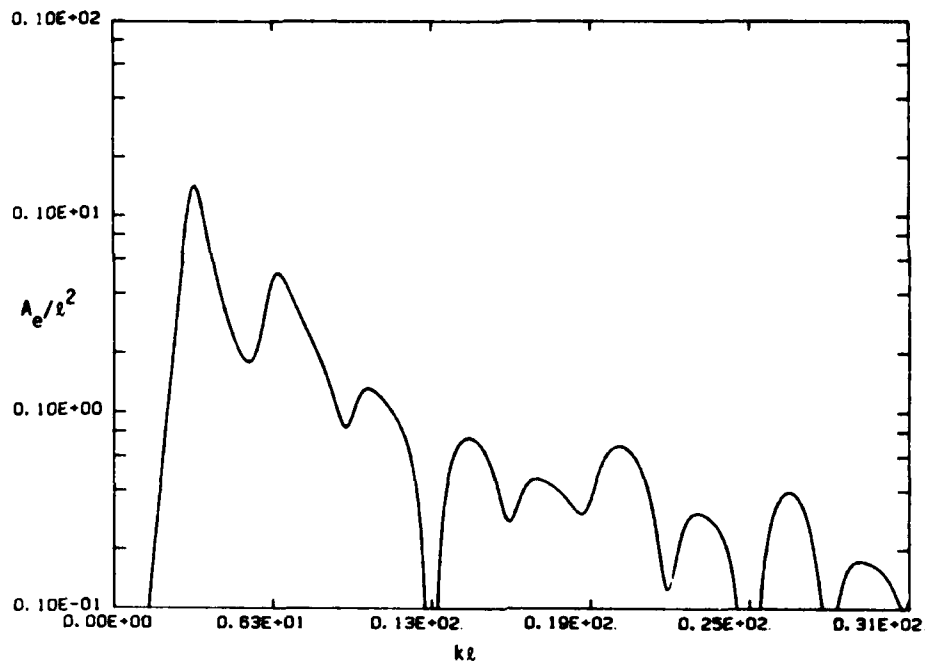
Figure 25. A_e/l^2 vs. kl; $\theta = 60°$, $\Omega = 5$.
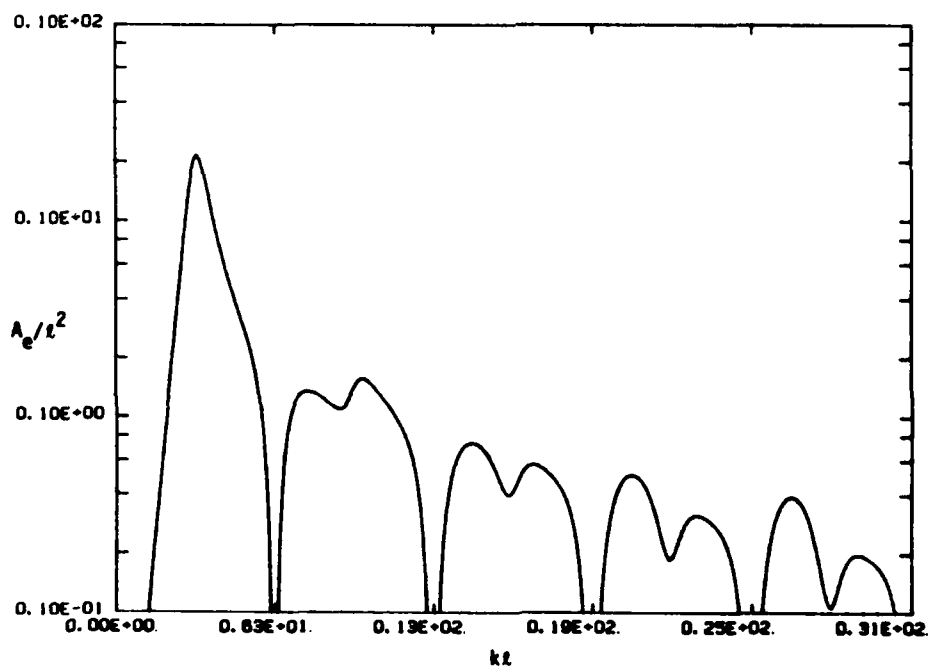
Figure 26. A_e/l^2 vs. kl; $\theta = 90°$, $\Omega = 5$.

32
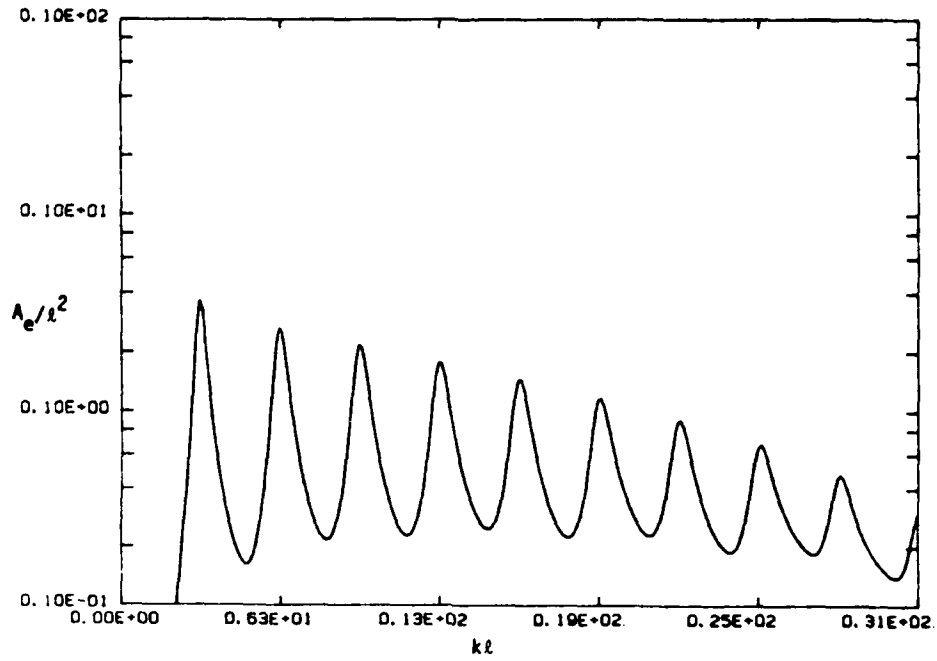
Figure 27. A_e/l^2 vs. kl; $\theta = 30°$, $\Omega = 10$.
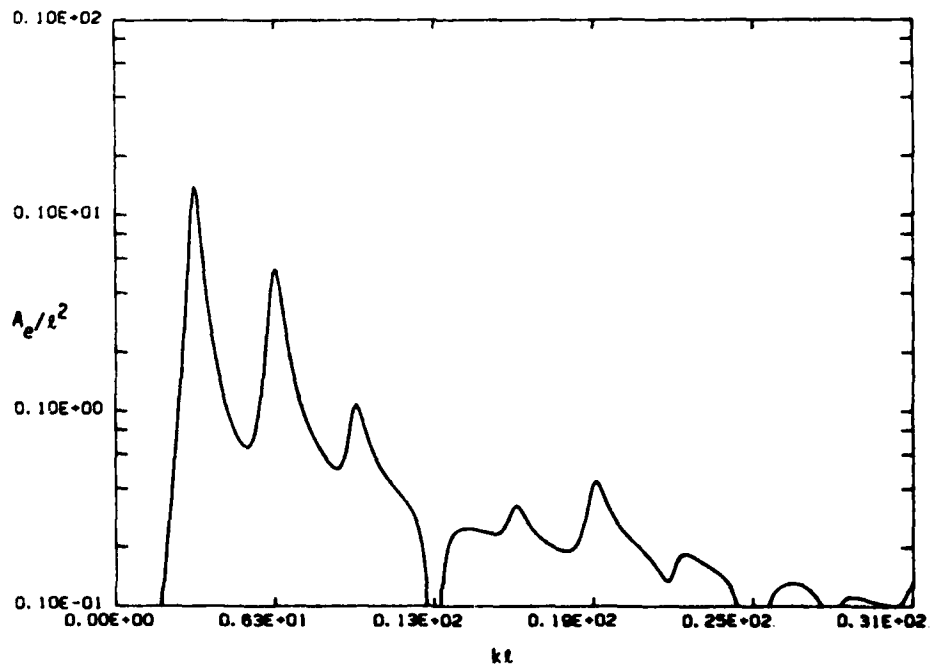
Figure 28. A_e/l^2 vs. kl; $\theta = 60°$, $\Omega = 10$.
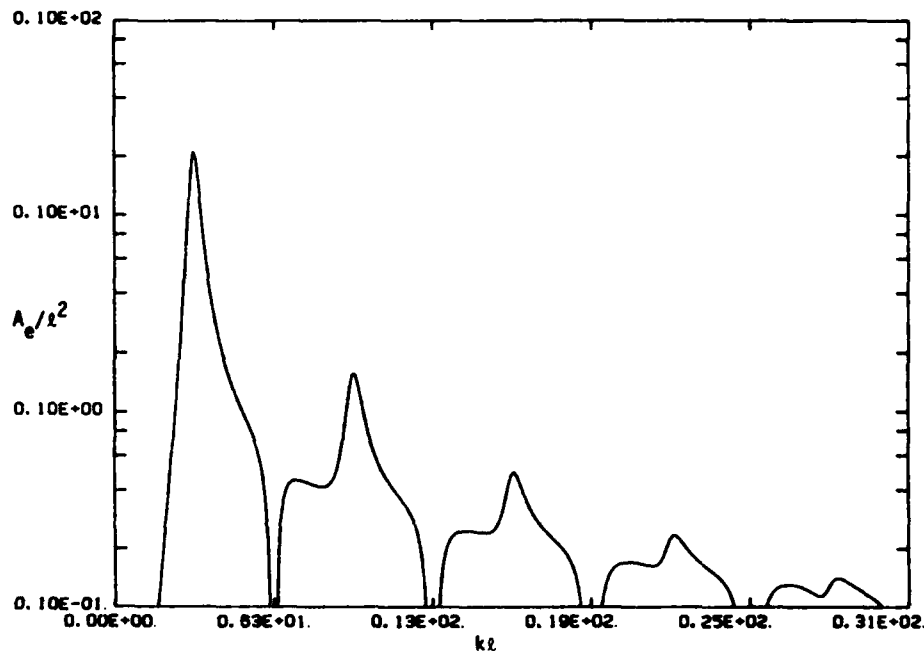
Figure 29. A_e/l^2 vs. kl; $\theta = 90°$, $\Omega = 10$.

The plots of A_e/l^2 vs. Ω in Figures 30 – 35 also show the resonant behavior of the structure and reproduce the features of the well-known radiation patterns of long-wire antennas. In general, the cross-section tends to decrease as frequency is increased from the fundamental resonance. The curves in Figures 30 – 35 are for cases where the antenna is an integral number of half-wavelengths long. When the frequency lies between the values shown, the curves are smoother. Examples are shown in Figures 36 – 40.

34
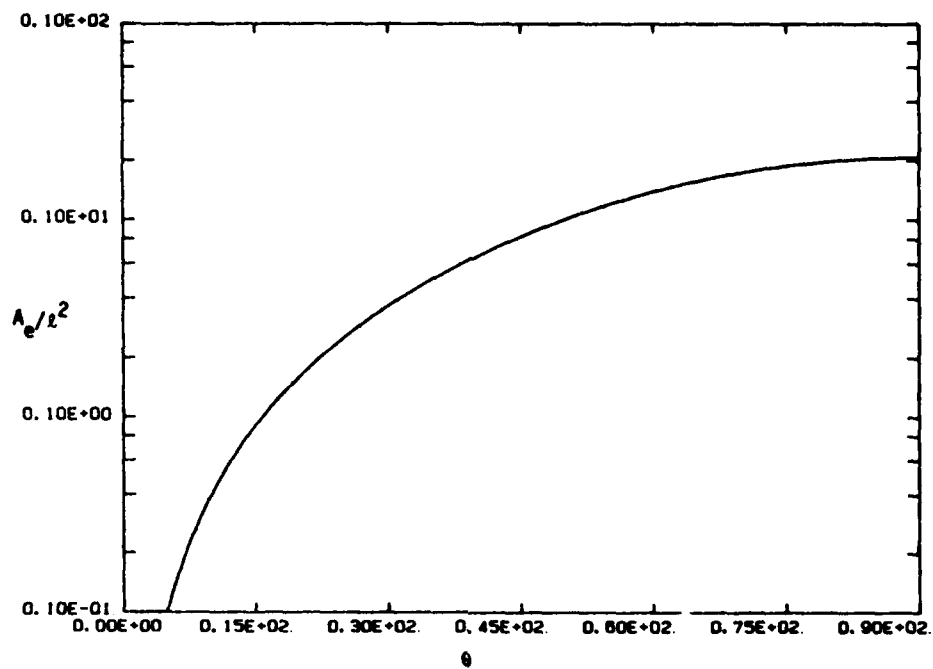
Figure 30. A_e/l^2 vs. θ; $kl = \pi$, $\Omega = 10$.

Figure 31. A_e/l^2 vs. θ; $kl = 2\pi$, $\Omega = 10$.

35
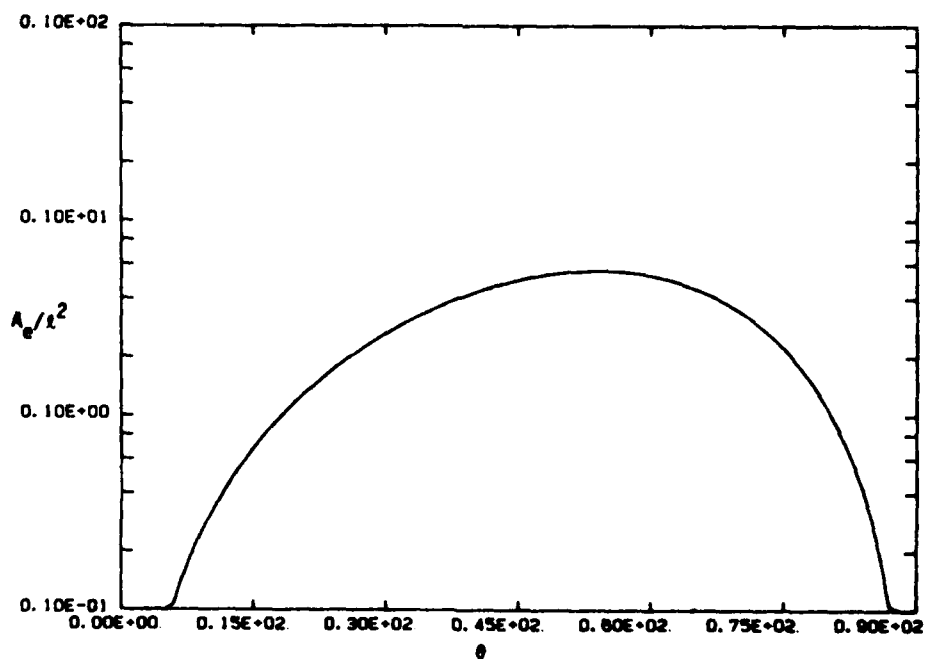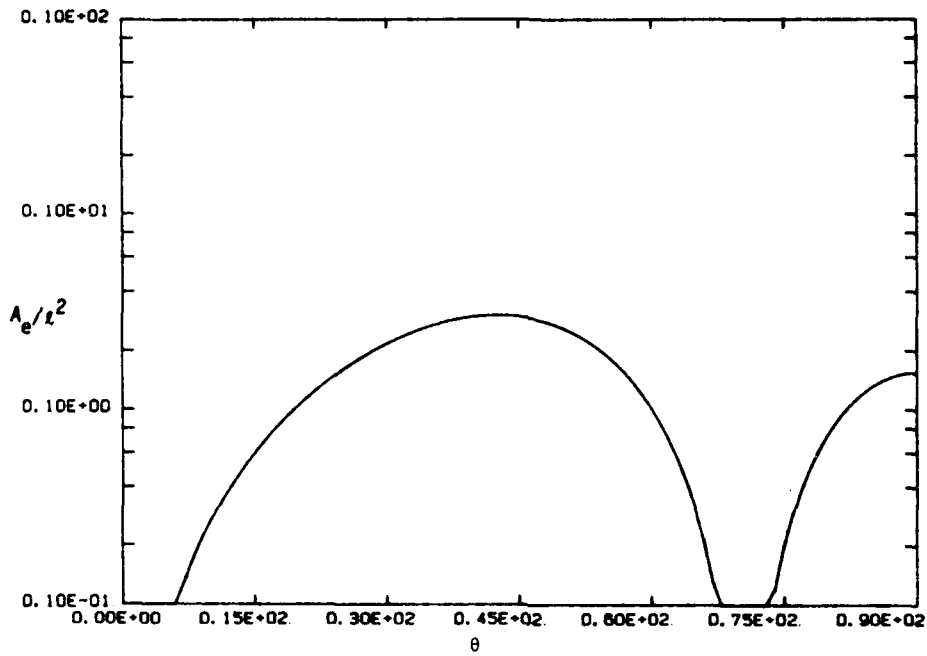
Figure 32. A_e/l^2 vs. θ; $kl = 3\pi$, $\Omega = 10$.

Figure 33. A_e/l^2 vs. θ; $kl = 4\pi$, $\Omega = 10$.

36
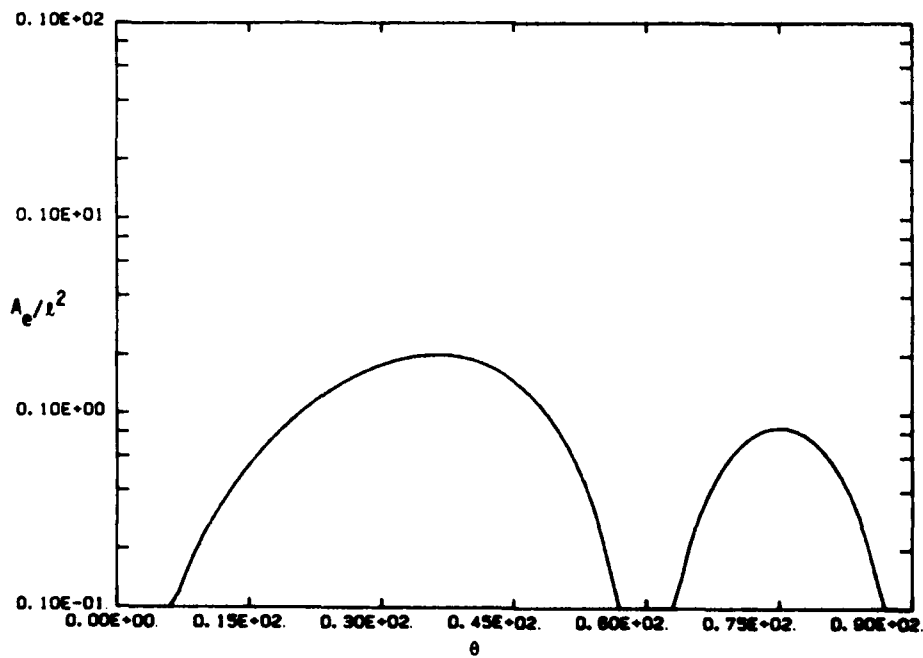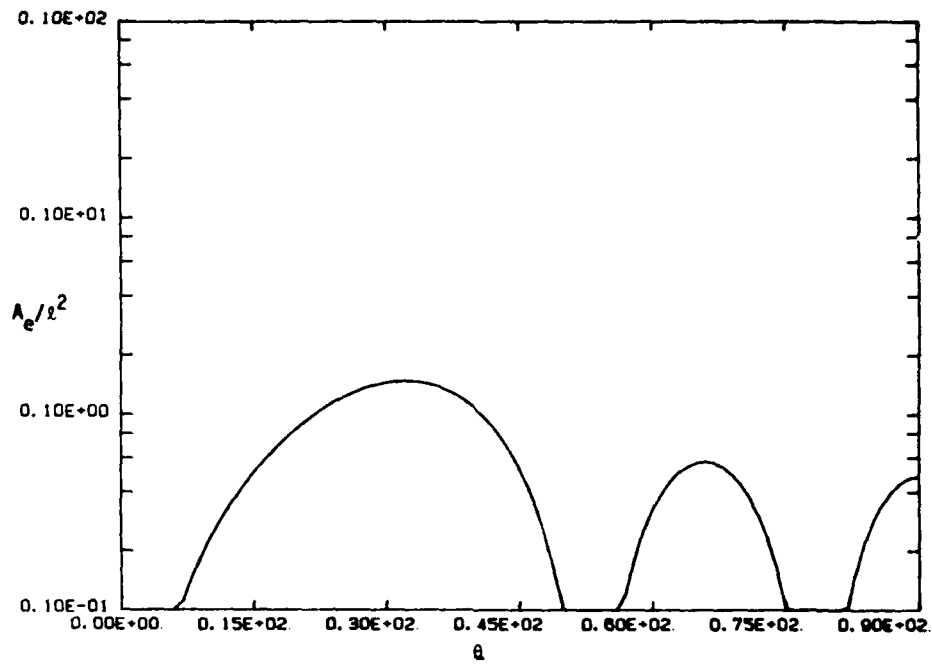
Figure 34. A_e/l^2 vs. θ; $kl = 5\pi$, $\Omega = 10$.

Figure 35. A_e/l^2 vs. θ; $kl = 6\pi$, $\Omega = 10$.

37
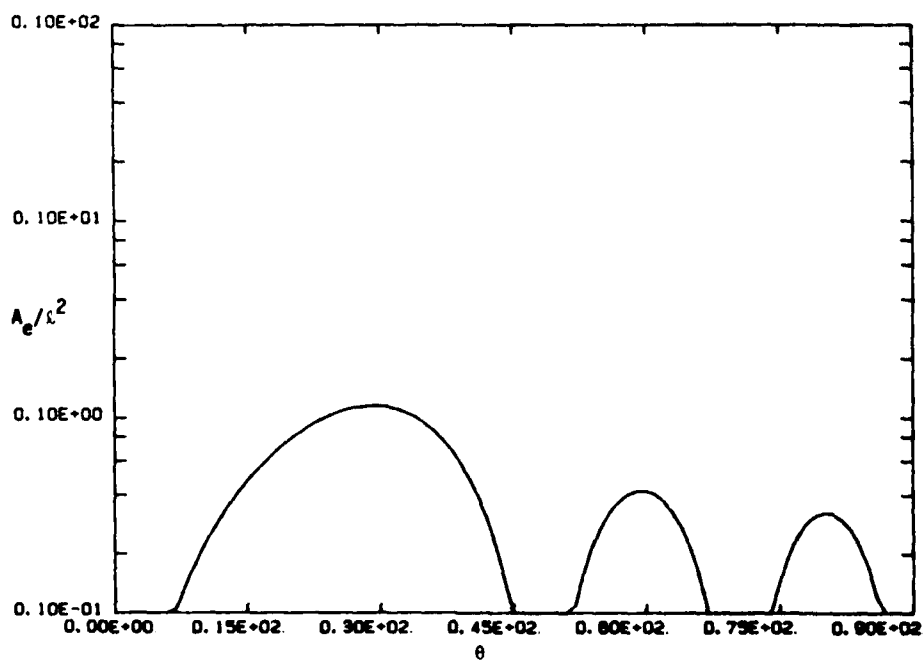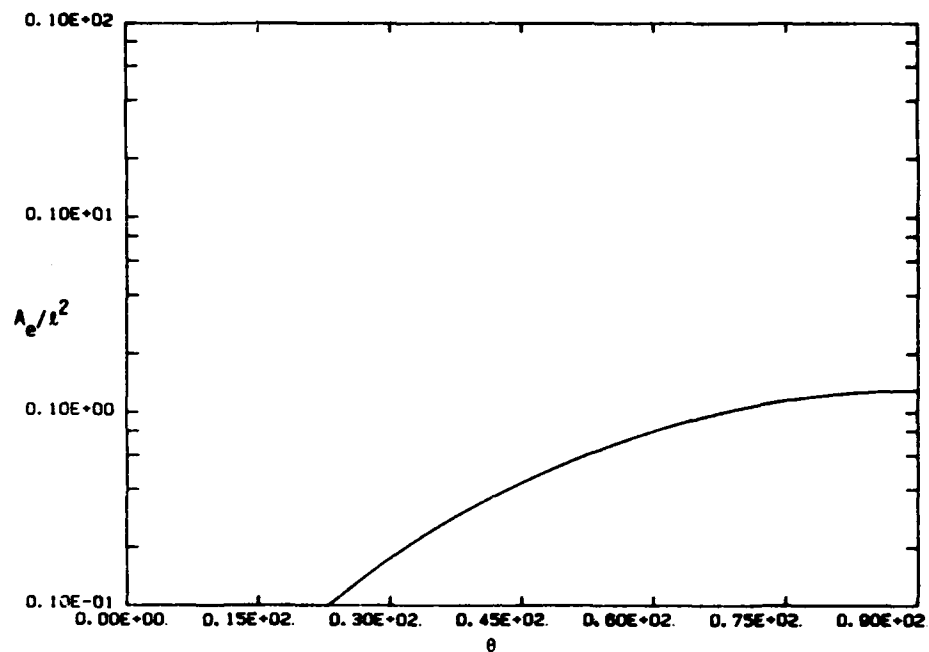
Figure 36. A_e/l^2 vs. θ; $kl = 3\pi/2$, $\Omega = 10$.
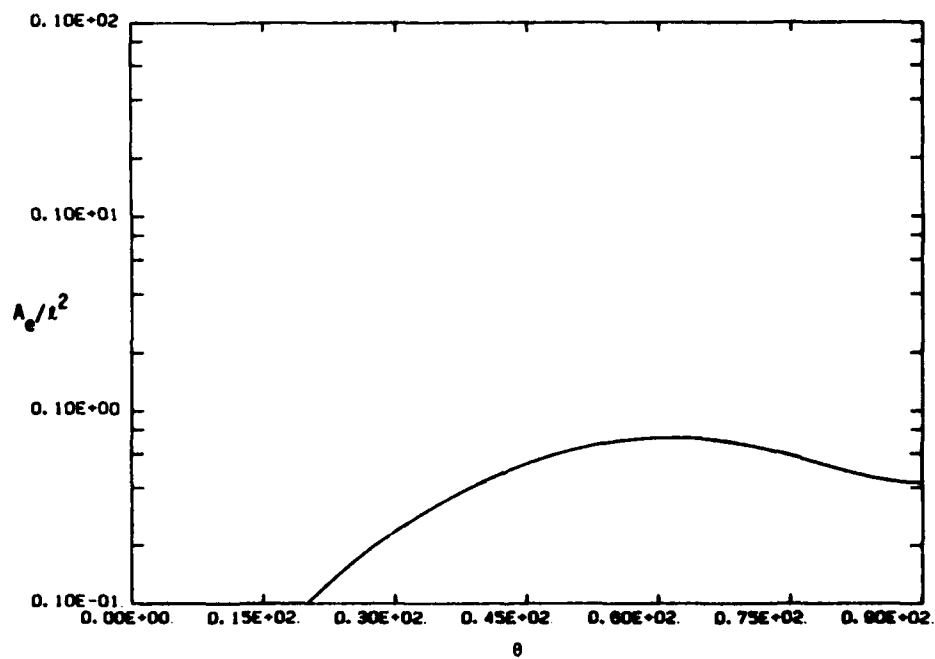
Figure 37. A_e/l^2 vs. θ; $kl = 5\pi/2$, $\Omega = 10$.
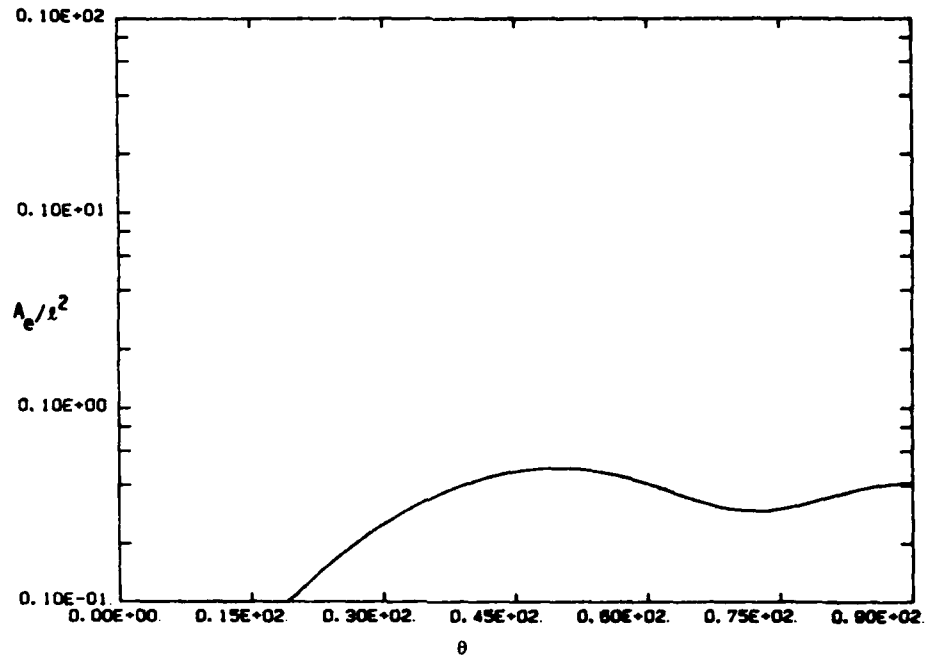
Figure 38. A_e/l^2 vs. θ; $kl = 7\pi/2$, $\Omega = 10$.
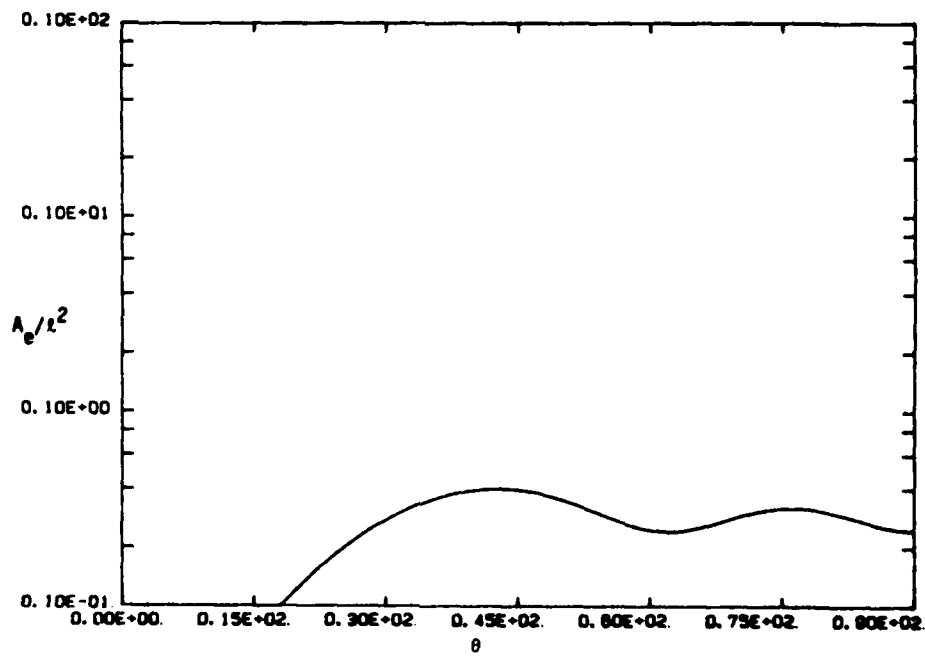
Figure 39. A_e/l^2 vs. θ; $kl = 9\pi/2$, $\Omega = 10$.
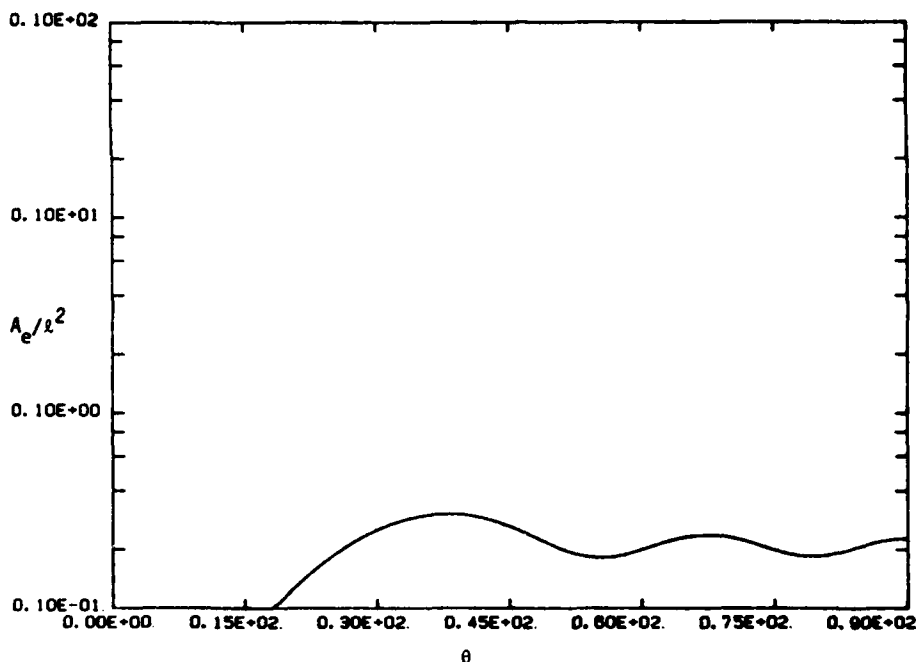
Figure 40. A_e/l^2 vs. θ; $kl = 11\pi/2$, $\Omega = 10$.

2.2 EQUIVALENT TRANSMISSION AREA OF A SLOT.

The scattering cross-section which was derived in the preceding section can be used to define an equivalent (power) source strength for a dipole. The equivalent transmission area of a thin slot can be readily obtained from the dipole scattering cross-sections.

The geometry of the slot-scattering problem is shown in Figure 41. The slot has width w and extends from $z = -l/2$ to $z = l/2$ in the $y = 0$ plane. The incident wave is ϕ-polarized, so that the short circuit magnetic field on the surface $y = 0+$ is

$$\vec{H}_{sc}(y = 0) = 2\frac{E_i}{Z_0}\sin\theta\vec{a}_z e^{jkz\cos\theta} \tag{76}$$

independent of ϕ for $0 \leq \phi < \pi$. This field induces a magnetic current K_z in the slot having a functional form identical to that given in Eq. (48), with the modification given in Eq. (49); but the parameter Ω is replaced by Ω_m, where [8]

$$\Omega_m = 2\ln(4l/w) \tag{77}$$

40

The total scattering cross-section of the slot is found to be identical to that of a thin wire of radius $w/4$. The scattered power is divided equally between the two sides of the conducting plane; thus the transmission cross-section is just half the total. Hence

$$A_t = \frac{\text{transmitted power}}{\text{incident power density}} \tag{78}$$

$$= \frac{1}{2} A_e \bigg|_{a \to w/4}$$
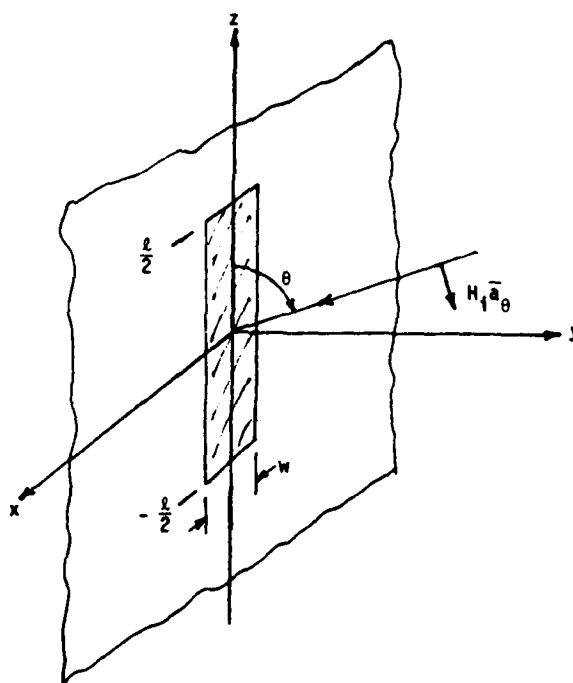
Figure 41.   Geometry of the slot-scattering problem. The width of the slot is w and the incident magnetic field is in the θ-direction.

It is implicit in the above that for the wire or the slot, the incident wave is polarized so as to yield maximum scattered power. For the wire scatterer along the z-axis, the electric vector of the incident wave is in the θ-direction. From the results in the previous section one is led to conclude that the equivalent transmission area of the slot is approximately 1.05 l^2 at the fundamental (half-wave) resonance.

41

2.3 TIME-DOMAIN SCATTERED FIELD.

We consider the dipole once again and find the scattered field in the time domain when the illuminating wave is a pulsed cw signal. In what follows, we determine the field scattered in the direction θ', denoting as before the direction of incidence of the illuminating field by θ. We have

$$E_\theta = jkZ_0 \sin\theta' \frac{e^{-jkr}}{4\pi r} \int_{-l/2}^{l/2} I(z')e^{jkz'\cos\theta'} dz' \tag{79}$$

Substituting for $I(z')$ from Eqs. (52) – (54) and carrying out the integration, we find

$$E_\theta = \frac{E_i l}{\Omega D(kl)} \frac{\sin\theta'}{\sin\theta} \frac{e^{-jkr}}{r} \left\{ \frac{2\sin kl \sin\left[\frac{kl}{2}(\cos\theta' + \cos\theta)\right]}{\cos\theta' + \cos\theta} \right. \tag{80}$$

$$- \frac{2\sin\left[\frac{kl}{2}(1 + \cos\theta)\right] \sin\left[\frac{kl}{2}(1 + \cos\theta')\right]}{1 + \cos\theta'}$$

$$\left. - \frac{2\sin\left[\frac{kl}{2}(1 - \cos\theta)\right] \sin\left[\frac{kl}{2}(1 - \cos\theta')\right]}{1 - \cos\theta'} \right\}$$

which may be written in the equivalent form

$$E_\theta = \frac{E_i l}{\Omega D(kl)} \frac{\sin\theta'}{\sin\theta} \frac{e^{-jkr}}{r} \left\{ \frac{(1 + \cos\theta)\cos\left[kl - \frac{kl}{2}(\cos\theta + \cos\theta')\right]}{(1 - \cos\theta')(\cos\theta + \cos\theta')} \right. \tag{81}$$

$$- \frac{(1 - \cos\theta)\cos\left[kl + \frac{kl}{2}(\cos\theta + \cos\theta')\right]}{(1 + \cos\theta')(\cos\theta + \cos\theta')}$$

$$\left. - \frac{2\cos\left[\frac{kl}{2}(\cos\theta - \cos\theta')\right]}{\sin^2\theta'} \right\}$$

In order to account properly for causality, we introduce two modifications to the frequency-domain result in Eq. (81). First, we multiply by the factor $\exp(-jkl\cos\theta/2)$ so that the wave incident upon the scatterer will have zero phase at the end of

the scatterer which is struck first. Second, we replace $D(kl)$ by $\hat{D}(kl)\exp(jkl)$, where $1/\hat{D}(kl)$ is the "pole-shifted" Mittag-Leffler expansion of the function

$$\frac{e^{jkl}}{kl \sin kl}$$

We have

$$\frac{1}{\hat{D}(kl)} = \frac{1}{(kl)^2} - \frac{1}{jkl} - 2\sum_{n=1}^{\infty}\frac{1}{(jkl + \alpha_n)^2 + (n\pi)^2} \tag{82}$$

wherein a contribution of order Ω^{-2} has been neglected. This latter modification ensures that the current at any point on the scatterer differs from zero only after that point has been illuminated.

The quantity in curly brackets in Eq. (81) is simply a weighted sum of exponential functions. Thus with the modifications discussed above, we see that the time-domain scattered field is

$$E_\theta(r,\theta',t;\theta) = \frac{l}{r\Omega}\frac{\sin\theta'}{\sin\theta}E_i(t) * f_0(t) * \left\{ w_1(\theta,\theta')\left[\delta(t - \frac{2l}{c} + \frac{l}{2c}\cos\theta' - r/c)\right.\right. \tag{83}$$

$$+ \delta(t - \frac{l}{c}\cos\theta - \frac{l}{2c}\cos\theta' - r/c)\bigg] + w_2(\theta,\theta')\left[\delta(t - \frac{2l}{c} - \frac{l}{c}\cos\theta - \frac{l}{2c}\cos\theta' - r/c)\right.$$

$$+ \delta(t + \frac{l}{2c}\cos\theta' - r/c)\bigg] - \csc^2\theta'\left[\delta(t - \frac{l}{c} - \frac{l}{c}\cos\theta + \frac{l}{2c}\cos\theta' - r/c)\right.$$

$$\left.\left. + \delta(t - \frac{l}{c} - \frac{l}{2c}\cos\theta' - r/c)\right]\right\}$$

where

$$w_1(\theta,\theta') = \frac{1 + \cos\theta}{2(1 - \cos\theta')(\cos\theta + \cos\theta')} \tag{84}$$

$$w_2(\theta,\theta') = \frac{1 - \cos\theta}{2(1 + \cos\theta')(\cos\theta + \cos\theta')} \tag{85}$$

and

$$f_0(t) = \mathcal{F}^{-1}\left\{\frac{1}{\hat{D}(kl)}\right\} = \left(\frac{c}{l}\right)\left\{\left(\frac{c}{l}\right)t + 1 + 2\sum_{n=1}^{\infty}\frac{1}{n\pi}e^{-\alpha_n ct/l}\sin\frac{n\pi ct}{l}\right\}\cdot U(t) \tag{86}$$

In order to illustrate the time-domain scattered field in a relatively simple way, we consider the "forward-scatter" case wherein $\theta' = \pi - \theta$. The forward-scattered time-domain field E_θ is given by

$$E_\theta(r, \pi - \theta, t; \theta) = \frac{l}{r\Omega} \frac{dE_i}{dt} * \left\{ \frac{l}{2c} f_0 \left(t - \frac{2l}{c} - \frac{l}{2c} \cos\theta \right) \right. \tag{87}$$

$$- \frac{l}{2c} f_0 \left(t - \frac{l}{2c} \cos\theta \right) + \csc^2\theta \left[F_0(t) + F_0 \left(t - \frac{2l}{c} \right) \right.$$

$$\left. \left. - F_0 \left(t - \frac{l}{c} + \frac{l}{c} \cos\theta \right) - F_0 \left(t - \frac{l}{c} - \frac{l}{c} \cos\theta \right) \right] \right\}$$

where

$$F_0(t) \equiv \int_0^t f_0(t) dt \tag{88}$$

and the propagation delay time r/c has been omitted. The function in curly brackets in Eq. (87) "turns on" at time $t = 0$; its final contribution begins at time $t = 2l/c$ and decays at a rate principally determined by the damping constant α_1, the characteristic decay time being $l/(\alpha_1 c)$. Typical values of α_1 are (a few)$^{-1}$, so the total duration of the function is a few to several transit times l/c. This behavior is illustrated in Figures 42 to 47, wherein we display the normalized step response (the function in curly brackets in Eq. (87)) as a function of normalized time ct/l for various values of θ and Ω.

We may make use of this result to determine under what conditions a quasi-steady state analysis of the problem can be applied. If $E_i(t)$ consists of n cycles of a cw signal at frequency f_0, then the incident pulse length is n/f_0 sec. A steady-state condition is reached in approximately $4l/c$ sec; thus $n \gg 4lf_0/c$,[1] the scattered field is essentially a cw pulse of amplitude

$$\tilde{E}_\theta = \frac{\tilde{E}_i(f_0)l}{\Omega D(k_0 l)} \left\{ k_0 l \sin k_0 l \right. \tag{89}$$

$$\left. - 4\csc^2\theta \sin\left[\frac{k_0 l}{2}(1 + \cos\theta) \right] \sin\left[\frac{k_0 l}{2}(1 - \cos\theta) \right] \right\}$$

[1]If the dipole (or slot) is excited near its half-wave resonance, the condition becomes $n \gg 2$, a condition likely to be met in practice.

44

where $k_0 = 2\pi f_0/c$ and $\tilde{E}_i(f_0)$ is the amplitude of the incident pulse. Furthermore, the total scattered energy can be accurately approximated by the product of the power scattered at frequency f_0 and the incident pulse width. Thus under conditions where the slot-transmitted or wire-scattered power is largest (i.e., near the fundamental resonance) a quasi-cw analysis would appear to be entirely appropriate.
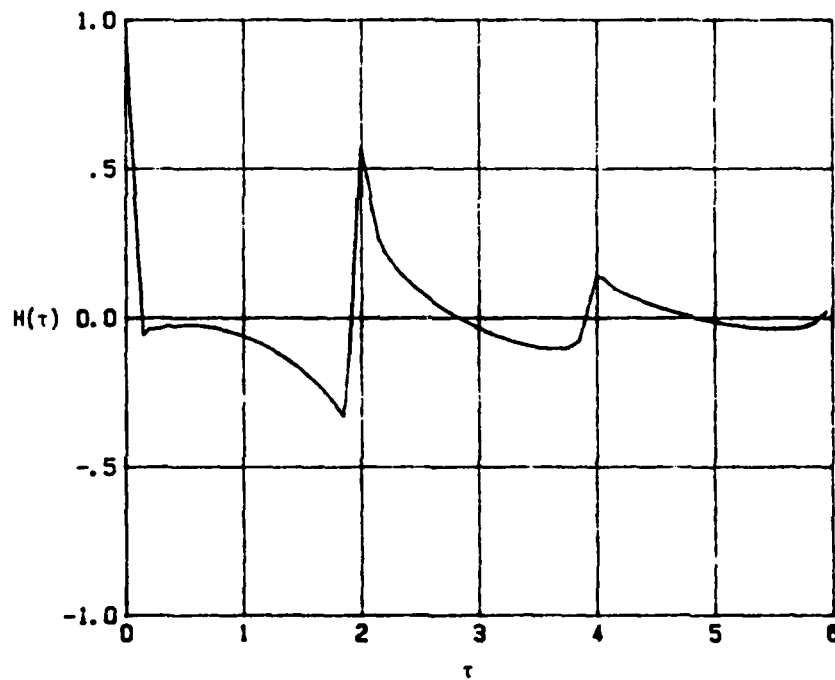
Figure 42.   Normalized step response $H(\tau)$ vs. normalized time τ; $\theta = 30°$, $\Omega = 5$.

45
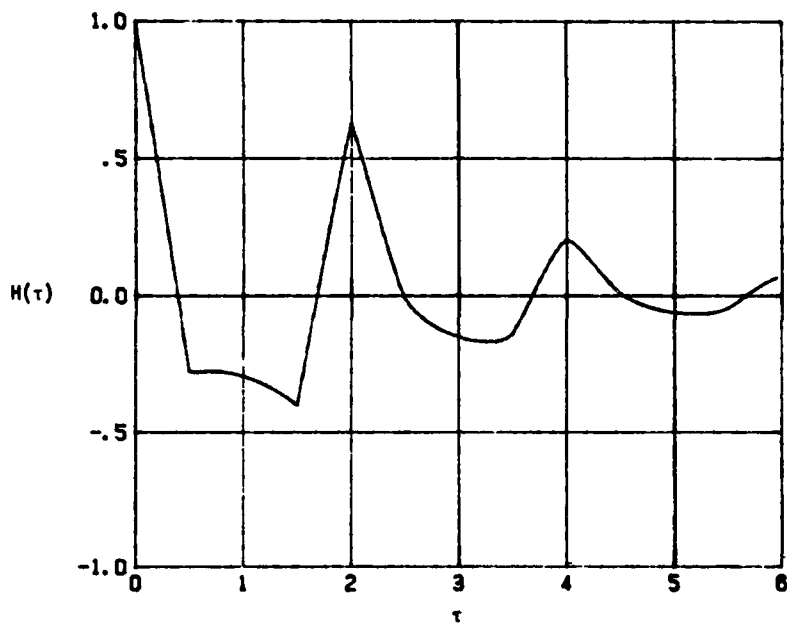
Figure 43. Normalized step response $H(\tau)$ vs. normalized time τ; $\theta = 60°$, $\Omega = 5$.
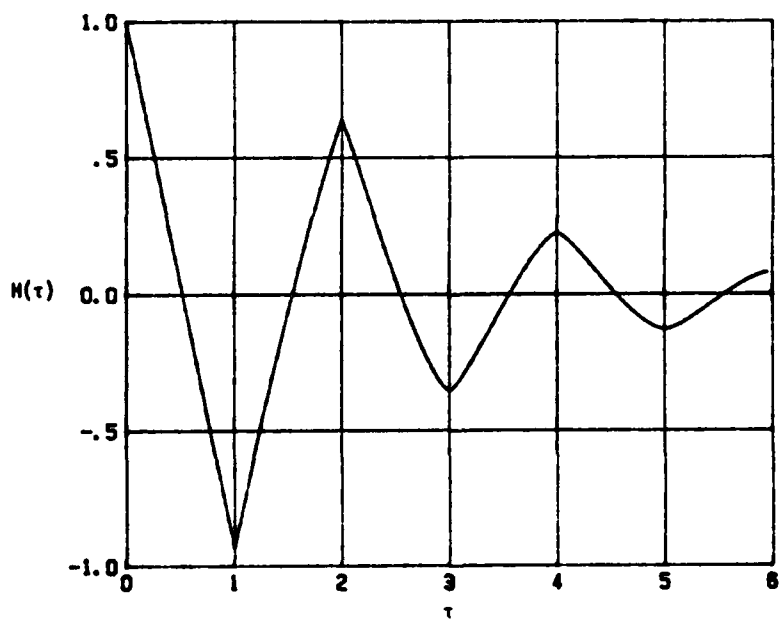
Figure 44. Normalized step response $H(\tau)$ vs. normalized time τ; $\theta = 90°$, $\Omega = 5$.

46
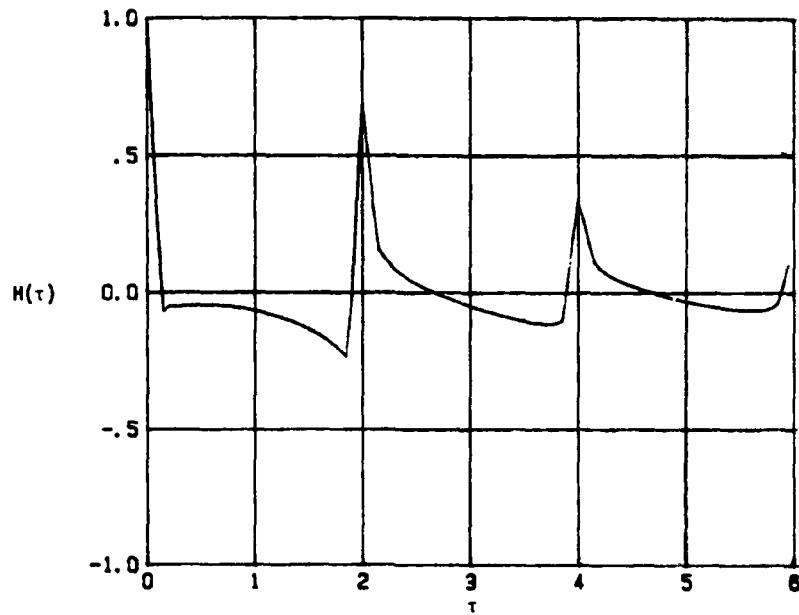
Figure 45. Normalized step response $H(\tau)$ vs. normalized time τ; $\theta = 30°$, $\Omega = 10$.
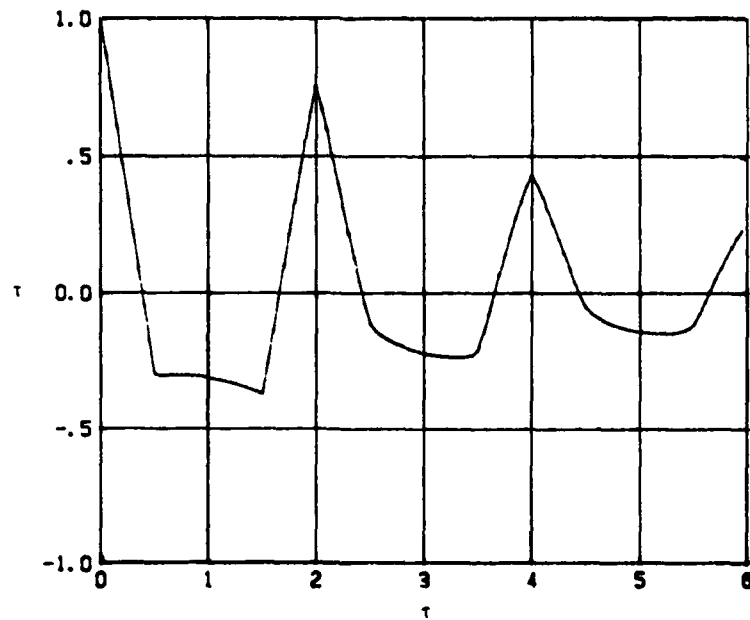
Figure 46. Normalized step response $H(\tau)$ vs. normalized time τ; $\theta = 60°$, $\Omega = 10$.
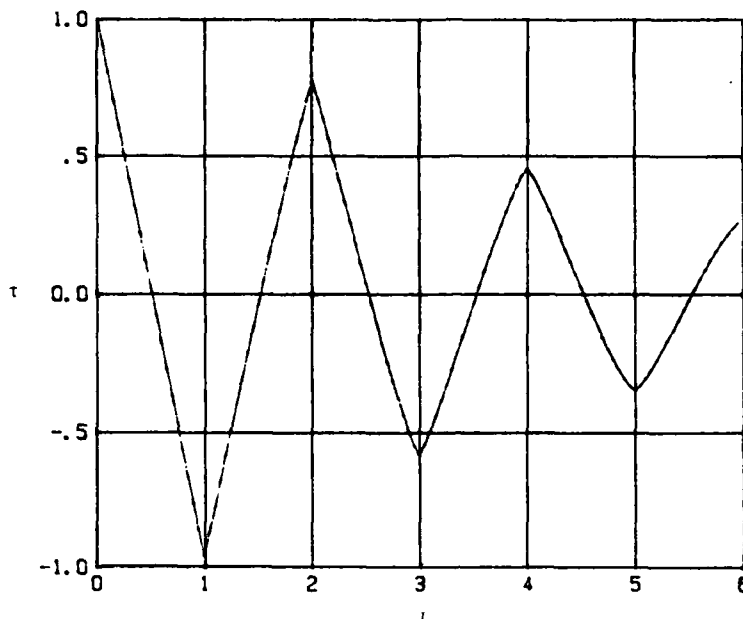
Figure 47. Normalized step response $H(\tau)$ vs. normalized time $\tau; \theta = 90°$,
$\Omega = 10$.

2.4 CONCLUDING REMARKS.

We have considered the power scattering cross-section of an unloaded wire and the transmission cross-section of a narrow slot in a conducting plane and have presented numerical results to illustrate the behavior of these quantities as the various problem parameters are varied. We have shown that the equivalent transmission area of a slot of length l can be as large as (approximately) 1.05 l^2, for frequencies near its fundamental resonance. We have also presented analytical and numerical results illustrating the impulse response of the scattered field and have derived the condition under which a steady-state analysis of the problem would be appropriate.

We conclude with a numerical example. Let the slot under consideration be 1.5 cm long. Then for illumination at normal incidence (and with proper polarization: E-field across the slot) and at a frequency of 10 GHz, the equivalent slot area will be approximately 2.4 cm^2. If the incident power density is 10 watts cm^{-2}, then 24 watts will penetrate the slot; for a pulse width of 10 ns (corresponding to 100 cycles in the incident pulse), the total penetrant energy will be 240 nJ. This energy will be radiated into the system interior.

48

SECTION 3
PULSE PROPAGATION IN WAVEGUIDES

Summary: We examine the propagation of transient signals in waveguides. By employing a saddle-point method of inverting the Laplace transform of the propagating signal, we display the various phases of this signal: the Sommerfeld precursor, the anterior transient leading to the main signal buildup, and the posterior transient. We consider single-mode propagation in some detail; multimode propagation can then be treated by superposition. As examples, we investigate the propagation of short cw pulses whose center frequency is above the dominant-mode cutoff frequency and whose envelopes are initially Gaussian or rectangular.

The propagation of pulsed signals in waveguides is a subject of critical importance for studying the potential effects of microwave weapons on systems. The subject is not a new one, especially in its general form wherein the mathematical problem is that of treating propagation in a dispersive medium. A waveguide constitutes a special case of the more general problem.

We shall address the problem with a view to demonstrating the principal features of the dispersed signal. We draw most heavily on the work of Sommerfeld [9] and Haskell and Case [10]; Sommerfeld investigated the percursor signal which propagates in a dispersive medium and which is the first signal component observed at early retarded times, while Haskell and Case considered transient signal propagation in a cold plasma. The latter problem has a mathematical form which corresponds to the waveguide propagation problem.

The propagation of a cw signal of frequency ω in a given waveguide mode gives rise to the simple relation

$$f(z,t) = A\cos(\omega t - \frac{z}{c}\sqrt{\omega^2 - \omega_c^2} + \phi) \qquad (90)$$

where $f(z,t)$ is the signal at a point z in the guide and A and ϕ are the amplitude and phase of the signal at $z = 0$. It is assumed in (90) that $\omega > \omega_c$, the cutoff frequency of the mode under consideration. In the event that $\omega < \omega_c$, we have

$$f(z,t) = A\cos(\omega t + \phi)\exp\left(-\frac{z}{c}\sqrt{\omega_c^2 - \omega^2}\right) \qquad (91)$$

and the signal does not propagate. The phase and group velocities of a monochromatic signal are defined

$$v_p = \frac{c}{\sqrt{1 - (\omega_c/\omega)^2}} \tag{92}$$

$$v_g = c\sqrt{1 - (\omega_c/\omega)^2} \tag{93}$$

where c denotes the speed of light. The fact that these velocities are not independent of the signal frequency indicates that the guide is dispersive: a pulsed signal will be spread, or dispersed, since its higher-frequency components travel with a greater group velocity than the lower-frequency components.

The signal dispersion can be illustrated by considering the propagation of a Gaussian pulse of center frequency ω_0 ($\omega_0 > \omega_c$) and width t_0:

$$f(0,t) = Ae^{-t^2/2t_0^2} \cos \omega_0 t \tag{94}$$

The signal at a point $z > 0$ in the guide can be written as a Fourier integral:

$$f(z,t) = \frac{1}{2\pi} \int_{-\infty}^{\infty} \tilde{F}_0(j\omega) e^{j\left(\omega t - \frac{z}{c}\sqrt{\omega^2 - \omega_c^2}\right)} d\omega \tag{95}$$

where

$$\tilde{F}_0(j\omega) = At_0\sqrt{\frac{\pi}{2}} \left[e^{-(\omega-\omega_0)^2 t_0^2/2} + e^{-(\omega+\omega_0)^2 t_0^2/2} \right] \tag{96}$$

By expanding the function

$$g(j\omega) = j\left(\omega t - \frac{z}{c}\sqrt{\omega^2 - \omega_c^2}\right) \tag{97}$$

near $\omega = \omega_0$ as

$$g(j\omega) \cong j\omega_0(t - z/v_{p0}) + j(\omega - \omega_0)(t - z/v_{g0}) + \frac{1}{2}j(\omega - \omega_0)^2 p \tag{98}$$

where v_{p0} and v_{g0} are as given in (92) and (93) with $\omega = \omega_0$,

$$p \equiv \frac{z}{c} \frac{\omega_c^2}{(\omega_0^2 - \omega_c^2)^{3/2}} \tag{99}$$

and similarly for $\omega = -\omega_0$ and evaluating the integral in (95), we find

$$f(z,t) \cong A\left(1 + \frac{p^2}{t_0^4}\right)^{-1/4} \exp\left[-\frac{(t - z/v_{g0})^2}{2t_0^2(1 + p^2/t_0^4)}\right] \cdot \tag{100}$$

$$\cos\left[\omega_0(t - z/v_{p0}) + \frac{1}{2}\tan^{-1}\frac{p}{t_0^2} - \frac{p(t - z/v_{g0})^2}{2t_0^4(1 + p^2/t_0^4)}\right]$$

We remark that if the term in (98) involving the parameter p were neglected, we would obtain

$$f(z,t) \cong Ae^{-(t-z/v_{g0})^2/2t_0^2}\cos\left[\omega_0(t - z/v_{p0})\right] \tag{101}$$

indicating that the pulse envelope travels at the group velocity v_{g0} and the points of constant phase travel at the phase velocity v_{p0}. Keeping the term involving p, we see that while the center of the pulse envelope travels at speed v_{g0}, the width of the envelope increases as it propagates, and its amplitude decreases. Furthermore, the phase changes in a complicated way as the pulse propagates.

We note that the governing parameter in this example is

$$\frac{p}{t_0^2} = \left(\frac{z}{ct_0}\right)\frac{1}{\omega_c t_0}\left(\omega_0^2/\omega_c^2 - 1\right)^{-1} \tag{102}$$

from which it is evident that pulse distortion will occur if any of the following conditions are met:

- the propagation distance (measured in units of ct_0) becomes large;

- the pulse width (measured in units of ω_c^{-1}) becomes small; or

- the center frequency of the pulse becomes close the the cutoff frequency.

We show in Figure 48 the variation in the pulse envelope as the pulse propagates as a function of normalized retarded time $(t - z/v_{g0})/t_0$ for different values of normalized propagation distance p/t_0^2.

Having demonstrated the phenomenon with this simple example, we turn in subsequent sections of this chapter to a more general treatment of pulse dispersion in waveguides. We examine single-mode transient propagation and then discuss a simple generalization to the multimode case.

51
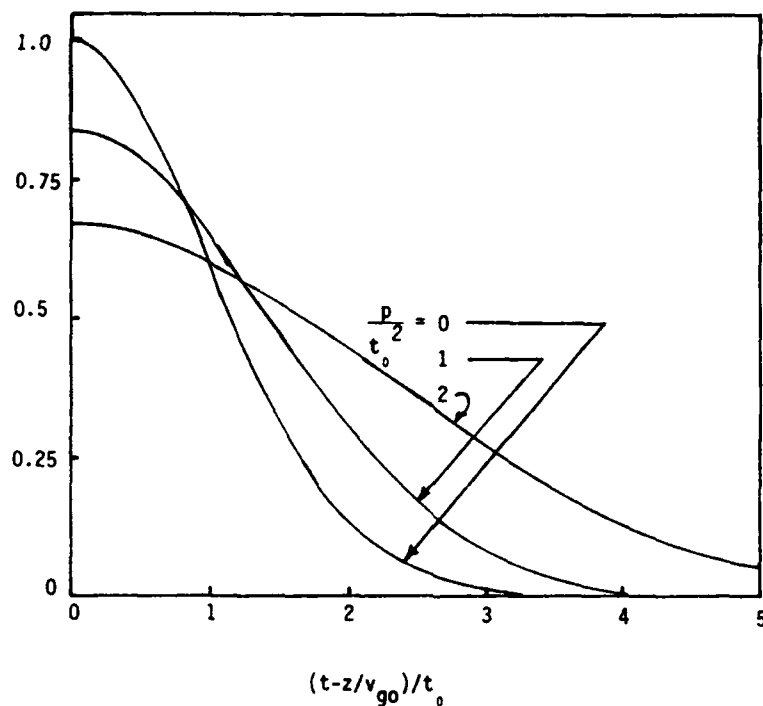
Figure 48. Gaussian pulse envelope vs. normalized time $(t - z/v_{g0})/t_0$ for various values of normalized distance p/t_0^2.

3.1 FORMULATION: SINGLE-MODE PROPAGATION.

The calculation of the dispersed signal associated with the propagation of a single waveguide mode of radian cutoff frequency ω_c reduces to the problem of evaluating the integral

$$f(z,t) = \frac{1}{2\pi j} \int_\Gamma \tilde{F}_0(s) e^{st - \frac{z}{c}\sqrt{s^2 + \omega_c^2}} ds \qquad (103)$$

where Γ is the Bromwich contour $(\sigma - j\infty$ to $\sigma + j\infty)$ in the complex s-plane and where $F_0(s)$ denotes the Laplace transform of $f(0,t)$:

$$\tilde{F}_0(s) = \int_0^\infty f(0,t) e^{-st} dt \qquad (104)$$

We shall assume in the following that the only singularities of $\tilde{F}_0(s)$ are poles in the left half-plane. The points $s = \pm j\omega_c$ are joined by a branch cut so that the

52

s-plane appears as shown in Figure 49. The cut is chosen so that on the upper Riemann sheet,

$$(s^2 + \omega_c^2)^{1/2} = \sqrt{R_1 R_2} \exp\left[j(\phi_1 + \phi_2)/2\right] \quad (-\pi/2 < \phi_1, \; \phi_2 < 3\pi/2) \tag{105}$$

We shall evaluate $f(z,t)$ approximately, using an appropriate set of analytical techniques. We shall show that in many cases of interest, the dispersed signal comprises three phases: first, the "Sommerfeld precursor" which appears at early times (t slightly greater than z/c); next, an anterior transient phase which precedes the main signal buildup at times near z/v_g, where v_g is the group velocity near the dominant frequency of $f(0,t)$; and finally, a posterior transient phase at late times.
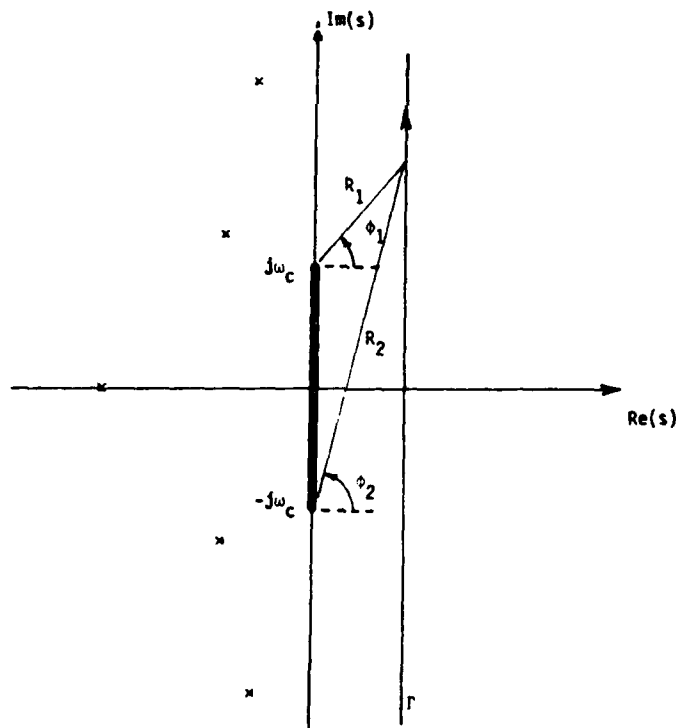
Figure 49. The complex s-plane. The ×'s indicate poles of the function $\tilde{F}_0(s)$.

3.1.1 The Sommerfeld Precursor.

We begin by deforming the Bromwich contour into a semicircle of (large) radius R in the right half-plane and adding its image in the left half-plane as shown in

53

Figure 50, so that

$$f(z,t) = \frac{1}{2\pi j} \int_{C_R} \tilde{F}_0(s) e^{st - \frac{z}{c}\sqrt{s^2 + \omega_c^2}} \, ds \qquad (106)$$

The contribution from the closure in the left half-plane is negligible for $t > z/c$; C_R denotes the circular integration path. On the path, we assume that

$$\tilde{F}_0(s) \cong \frac{A}{s^n} \qquad (n \geq 1) \qquad (107)$$

where A is a constant, and write

$$st - \frac{z}{c}\sqrt{s^2 + \omega_c^2} = s(t - z/c) - \frac{\omega_c^2 z}{2sc} + \cdots \qquad (108)$$

Thus

$$f(z,t) \cong \frac{A}{2\pi j} \int_{C_R} s^{-n} e^{\sqrt{\xi\tau}\left(s\sqrt{\frac{\tau}{\xi}} - \frac{1}{s}\sqrt{\frac{\xi}{\tau}}\right)} \, ds \qquad (109)$$

where $\tau = t - z/c$ is the retarded time and

$$\xi \equiv \frac{\omega_c^2 z}{2c} \qquad (110)$$

Now the integral in (109) can be evaluated by defining a new variable ϕ through

$$s = \frac{1}{j}\sqrt{\frac{\xi}{\tau}}\, e^{j\phi} \qquad (111)$$

and identifying $\sqrt{\xi/\tau}$ as the radius of the circular integration path. Then

$$\begin{aligned}
f(z,t) &\equiv \frac{A}{2\pi} j^{n-1} \left(\frac{\tau}{\xi}\right)^{(n-1)/2} \int_{-\pi}^{\pi} e^{-2j\sqrt{\xi\tau}\cos\phi - j(n-1)\phi} d\phi \qquad (112) \\
&= A\left(\frac{\tau}{\xi}\right)^{(n-1)/2} J_{n-1}\left(2\sqrt{\xi\tau}\right) \\
&= A\left[\frac{2(ct-z)}{\omega_c^2 z}\right]^{(n-1)/2} J_{n-1}\left[\sqrt{2}\,\omega_c\sqrt{\frac{z}{c}\left(t - \frac{z}{c}\right)}\right]
\end{aligned}$$

54
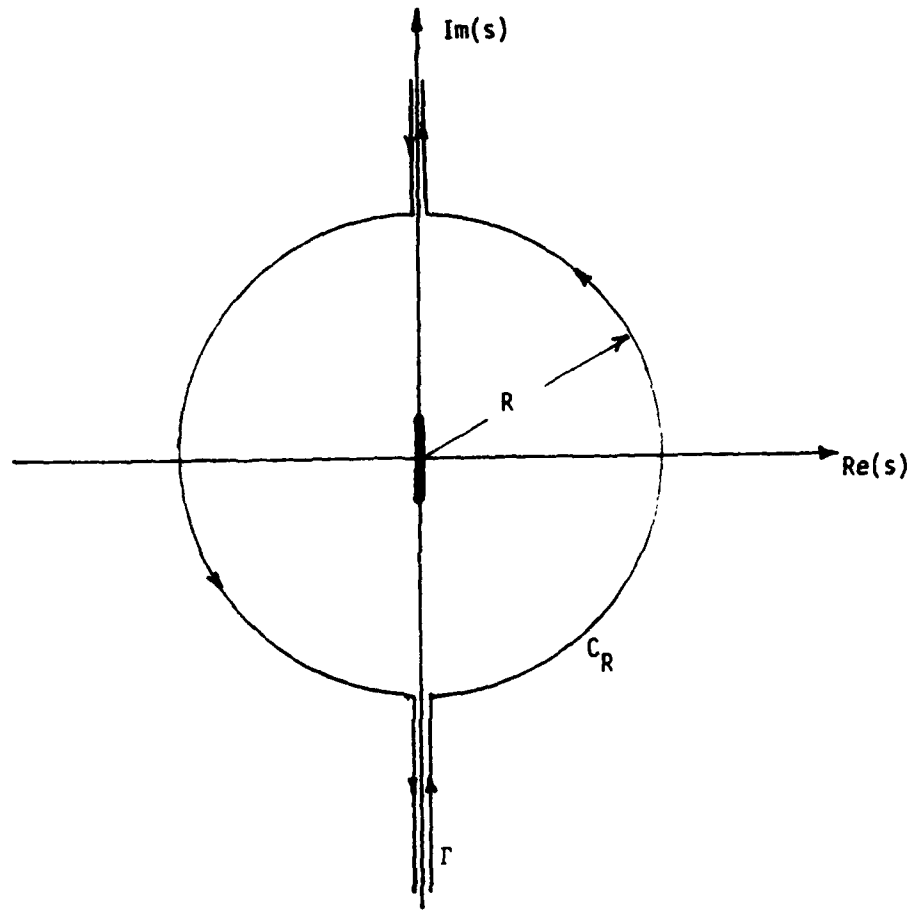
Figure 50. Deformation of Γ into a contour suitable for evaluating the Sommerfeld precursor. C_R denotes the circular contour.

where $J_{n-1}(\cdot)$ denotes a Bessel function. Evidently, if $\tilde{F}_0(s)$ can be expanded in a series of the form

$$\tilde{F}_0(s) = \sum_{l=1}^{\infty} \frac{A_l}{s^l} \quad (s \to \infty) \tag{113}$$

then the precursor signal can be expressed as

$$f(z,t) = \sum_{l=1}^{\infty} A_l \left[\frac{2(ct-z)}{\omega_c^2 z} \right]^{(l-1)/2} J_{l-1}\left[\sqrt{2}\, \omega_c \sqrt{\frac{z}{c}\left(t - \frac{z}{c}\right)} \right] \tag{114}$$

at early times.

To illustrate the application of this result, we consider a specific example. Let

$$f(0,t) = a_0 \sin \omega_0 t \; U(t) \tag{115}$$

so that

$$\tilde{F}_0(s) \;=\; \frac{\omega_0 a_0}{s^2 + \omega_0^2} \tag{116}$$

$$=\; \frac{\omega_0 a_0}{s^2} - \frac{\omega_0^3 a_0}{s^4} + \cdots$$

Thus the Sommerfeld precursor is

$$f(z,t) = a_0 \left[2 \left(\frac{\omega_0}{\omega_c} \right)^2 \left(\frac{ct}{z} - 1 \right) \right]^{1/2} J_1 \left(\sqrt{2} \, \frac{\omega_c}{c} \, z \sqrt{\frac{ct}{z} - 1} \right) + \cdots \tag{117}$$

which involves the frequency ω_0 only in the amplitude factor. The oscillatory character of this function depends only upon the cutoff frequency ω_c. We shall return to consider the Sommerfeld precursor after we examine the next phase of the dispersed signal, the *anterior transient*.

3.1.2 The Anterior and Posterior Transients.

To investigate the behavior of the dispersed signal after the earliest times, we employ a saddle point integration technique. Define

$$g(s) = st - \frac{z}{c}\sqrt{s^2 + \omega_c^2} \tag{118}$$

This function has two saddle points, located at

$$s_\pm = \pm j\omega_{sp} = \pm j\omega_c \frac{(ct/z)}{\sqrt{(ct/z)^2 - 1}} \tag{119}$$

We expand $g(s)$ about the saddle points in Taylor series, obtaining

$$g(s) = g(\pm j\omega_{sp}) + \frac{1}{2} \left(s \mp j\omega_{sp} \right)^2 \left. \frac{d^2 g}{ds^2} \right|_{s_\pm} + \cdots \tag{120}$$

56

where

$$\left.\frac{d^2 g}{ds^2}\right|_{s=\pm j\omega_{sp}} = \frac{\mp jz}{\omega_c c}\left[\left(\frac{ct}{z}\right)^2 - 1\right]^{3/2} \tag{121}$$

Now deform the original contour Γ into the steepest-descent path SDP, as shown in Figure 51. We have shown in the Figure the fact that the deformation of Γ into SDP can pick up some of the poles $\tilde{F}_0(s)$ lying in the left half of the s-plane. Thus

$$f(z,t) \cong \frac{1}{2\pi j}\int_{SDP}\tilde{F}_0(s)e^{g(s)}ds + \sum_n \text{Res } \tilde{F}_0(s)e^{g(s)}\bigg|_{s=s_n} \tag{122}$$

where s_n denotes a pole crossed by the deformation of the contour. By virtue of the fact that the poles crossed will occur in the complex-conjugate pairs ($s_n = -\sigma_n \pm j\omega_n$) and that $f(0,t)$ is a real function, we have for a typical pole-pair contribution

$$f_{pn}(t,z) = 2R_{pn}e^{-\sigma_n t + \alpha_n z}\cos(\omega_n t - \beta_n z + \varphi_n)U(t - t_n) \tag{123}$$

where

$$\text{Res } \tilde{F}_0(s)\big|_{-\sigma_n + j\omega_n} = R_{pn}e^{j\phi_n} \tag{124}$$

$$-\alpha_n + j\beta_n = \sqrt{\omega_c^2 - (\omega_n + j\sigma_n)^2} \tag{125}$$

$$t_n = \frac{z}{c}\frac{\omega_n - \sigma_n}{\sqrt{(\omega_n - \sigma_n)^2 - \omega_c^2}} \tag{126}$$

When the saddle points are not close to poles of $\tilde{F}_0(s)$, the contributions to $f(z,t)$ from the neighborhoods of the two saddle points are easily found. We obtain for $f_{sp}(z,t)$, the contribution to $f(z,t)$ from integration along SDP,

$$f_{sp}(z,t) = \left(\frac{2\omega_c c}{\pi z}\right)^{1/2}\left[\left(\frac{ct}{z}\right)^2 - 1\right]^{-3/4}\left|\tilde{F}_0(j\omega_{sp})\right| \cdot \tag{127}$$

$$\cos\left(\omega_c\frac{z}{c}\sqrt{\left(\frac{ct}{z}\right)^2 - 1} + \frac{\pi}{4} + \psi_{sp}\right)$$
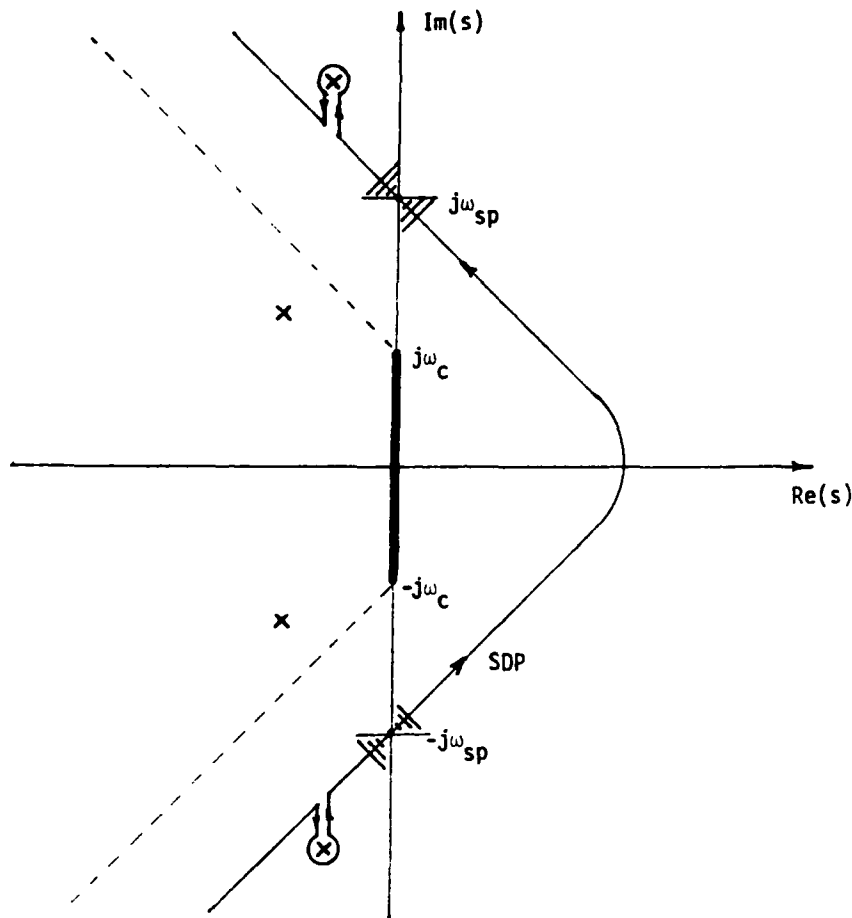
Figure 51. The steepest-descent contour in the s-plane. Poles in the region bounded by the dashed lines cannot be crossed by SDP.

where we have written

$$\tilde{F}_0\left(j\omega_{sp}\right) = \left|\tilde{F}_0(j\omega_{sp})\right| e^{j\psi_{sp}} \tag{128}$$

The above result applies when the saddle points are neither too close to poles of $\tilde{F}_0(s)$ which might lie close to the $j\omega$-axis nor too close to the branch points at $s = \pm j\omega_c$, which are the points approached by the saddle points at very late times. Before proceeding to the investigation of these situations, however, we observe that if $\tilde{F}_0(s)$ as given in our example for the Sommerfeld precursor is applied to the calculation of $f_{sp}(z,t)$ at early times, we find

$$f_{sp}(z,t) \;\rightarrow\; a_0 \left(\frac{\omega_0}{\omega_c}\right) \left(\frac{z}{ct}\right)^2 \left(\frac{2c}{\pi\omega_c z}\right)^{1/2} \left[\left(\frac{ct}{z}\right)^2 - 1\right]^{1/4} \cdot \tag{129}$$

$$\cos\left(\omega_c\frac{z}{c}\sqrt{\left(\frac{ct}{z}\right)^2 - 1} - \frac{3\pi}{4}\right)$$

58

$$\cong \ a_0 \left(\frac{\omega_0}{\omega_c}\right) \left(\frac{2c}{\pi \omega_c z}\right)^{1/2} \left(\frac{ct}{z} - 1\right)^{1/4} 2^{1/4} \ .$$

$$\cos\left(\sqrt{2} \ \omega_c \frac{z}{c}\sqrt{\frac{ct}{z} - 1} - \frac{3\pi}{4}\right)$$

when ct/z is only slightly greater than unity. One immediately observes that the result in (129) is identical to that obtained if one uses (117) with the usual asymptotic approximation for $J_1(\cdot)$. Thus the early-time saddle point integral expression for $f(z,t)$ matches the Sommerfeld precursor expression when $ct/z - 1 \ll 1$ and

$$\sqrt{2} \ \frac{\omega_c z}{c}\sqrt{\frac{ct}{z} - 1} \ \gg \ 1 \tag{130}$$

The required conditions can be simultaneously met if z is at least a few wavelengths at the cutoff frequency. We shall assume that z is always at least this large, and we identify the transition between the Sommerfeld precursor and the early-time saddle-point expression as the onset of the anterior transient.

When the saddle points pass close to a complex-conjugate pole pair the expression for $f_{sp}(z,t)$ given in (127) must be modified. We remark parenthetically that if the poles are located at $s = -\sigma_p \pm j\omega_p$ where σ_p is small and $\omega_p > \omega_c$, the saddle points and the poles are closest when $\omega_{sp} = \omega_p$, or when

$$z \ = \ ct\sqrt{1 - (\omega_c/\omega_p)^2} \tag{131}$$

$$= \ v_g(\omega_p)t$$

where $v_g(\omega_p)$ is simply the group velocity for a signal at frequency ω_p.

When a pole is close to a saddle point, we write for $\tilde{F}_0(s)$

$$\tilde{F}_0(s) = \frac{\mathrm{Res} \ \tilde{F}_0(s_p)}{s - s_p} + \tilde{G}_0(s) \tag{132}$$

where $\tilde{G}_0(s)$ is analytic at $s = s_p$. Then the contribution to $f(z,t)$ from the integration over SDP can be written

$$\frac{1}{2\pi j}\int_{SDP} \tilde{F}_0(s)e^{g(s)}ds \ = \ \frac{1}{2\pi j}\mathrm{Res} \ \tilde{F}_0(s_p)\int_{SDP} e^{g(s)}\frac{ds}{s - s_p} \tag{133}$$

59

$$+ \frac{1}{2\pi j} \int_{SDP} \tilde{G}_0(s)e^{g(s)}ds$$

The second integral on the right-hand side of (133) yields a contribution of the form given in (127) and (128) with $\tilde{F}_0$ replaced by $\tilde{G}_0$. The first integral can be expressed in terms of the complementary error function; and we find that the contribution to the integral over SDP made by poles near the saddle points before SDP crosses over the poles is

$$f_{sp}(z,t) \cong \qquad\qquad\qquad\qquad\qquad\qquad\qquad (134)$$

$$\frac{1}{2}\text{Res }\tilde{F}_0(s_p^+)e^{j\left(\omega_0 t - \frac{z}{c}\sqrt{\omega_0^2 - \omega_c^2}\right)}\text{erfc}\left[e^{j\pi/4}\sqrt{\frac{p}{2}}\left(\omega_{sp} + js_p^+\right)\right]$$

$$+\frac{1}{2}\text{Res }\tilde{F}_0(s_p^-)e^{-j\left(\omega_0 t - \frac{z}{c}\sqrt{\omega_0^2 - \omega_c^2}\right)}\text{erfc}\left[e^{-j\pi/4}\sqrt{\frac{p}{2}}\left(\omega_{sp} - js_p^-\right)\right]$$

where $s_p^{\pm} = -\sigma_p \pm j\omega_p$ and

$$p \equiv \left(\frac{z}{\omega_c c}\right)\left[\left(\frac{ct}{z}\right)^2 - 1\right]^{3/2} \qquad\qquad (135)$$

After SDP has passed over the poles, we include the pole contributions to obtain

$$f(z,t) \cong \frac{1}{2}\text{Res }\tilde{F}_0(s_p^+)e^{j\left(\omega_0 t - \frac{z}{c}\sqrt{\omega_0^2 - \omega_c^2}\right)} . \qquad\qquad (136)$$

$$\left\{2 - \text{erfc}\left[e^{j\pi/4}\sqrt{\frac{p}{2}}\left(-js_p^+ - \omega_{sp}\right)\right]\right\}$$

$$+ \frac{1}{2}\text{Res }\tilde{F}(s_p^-)e^{-j\left(\omega_0 t - \frac{z}{c}\sqrt{\omega_0^2 - \omega_c^2}\right)} .$$

$$\left\{2 - \text{erfc}\left[e^{-j\pi/4}\sqrt{\frac{p}{2}}\left(js_p^- - \omega_{sp}\right)\right]\right\}$$

We observe that $f(z,t)$ as given in (134) and (136) above is continuous as SDP picks up the pole contributions; this is a consequence of the symmetry property of the complementary error function [11]:

$$\text{erfc}(-iz) = 2 - \text{erfc}(iz) \qquad\qquad (137)$$

60

At very late times, the saddle points approach the branch points. It is, however, not necessary to modify the result in (127) in the limiting case, since the magnitude of $g''(s)$ becomes very large as the branch points are approached. Thus

$$f_{sp}(z,t) \sim \left(\frac{2\omega_c c}{\pi z}\right)^{1/2} \left(\frac{z}{ct}\right)^{3/2} \left|\tilde{F}_0(j\omega_c)\right| \cos\left(\omega_c t + \frac{\pi}{4} + \psi_c\right) \qquad (138)$$

as $t \to \infty$.

We now consider our example once again, where $f(0,t)$ is a sine wave of frequency ω_0 turned on at $t = 0$. The precursor signal which appears at the earliest times is

$$f(z,t) = \sqrt{2}\, a_0 \frac{\omega_0}{\omega_c} \sqrt{\frac{ct}{z} - 1}\; J_1\left(\sqrt{2}\, \frac{\omega_c z}{c} \sqrt{\frac{ct}{z} - 1}\right) \qquad (139)$$

The anterior transient signal before the saddle points approach the poles at $\pm j\omega_0$ is

$$f(z,t) = \left(\frac{2\omega_c}{\pi z}\right)^{1/2} a_0 \omega_0 \left[\left(\frac{ct}{z}\right)^2 - 1\right]^{1/4} \left[\left(\frac{ct}{z}\right)^2 \left(\omega_c^2 - \omega_0^2\right) + \omega_0^2\right]^{-1} \cdot \quad (140)$$

$$\cos\left(\omega_c \frac{z}{c}\sqrt{\left(\frac{ct}{z}\right)^2 - 1} - \frac{3\pi}{4}\right)$$

When the saddle points approach and pass through the poles, we have for $\omega_{sp} > \omega_s$ (i.e., before the crossing occurs)

$$f(z,t) = \frac{a_0}{4j}\left\{e^{j\left(\omega_0 t - \frac{z}{c}\sqrt{\omega_0^2 - \omega_c^2}\right)} \operatorname{erfc}\left[e^{j\pi/4}\sqrt{\frac{p}{2}}(\omega_{sp} - \omega_0)\right] \right. \qquad (141)$$

$$\left. - e^{-j\left(\omega_0 t - \frac{z}{c}\sqrt{\omega_0^2 - \omega_c^2}\right)} \operatorname{erfc}\left[e^{-j\pi/4}\sqrt{\frac{p}{2}}(\omega_{sp} - \omega_0)\right]\right\}$$

After the poles are crossed,

$$f(z,t) = \frac{a_0}{4j}\left\{e^{j\left(\omega_0 t - \frac{z}{c}\sqrt{\omega_0^2 - \omega_c^2}\right)} \left[2 - \operatorname{erfc}\left(e^{j\pi/4}\sqrt{\frac{p}{2}}(\omega_0 - \omega_{sp})\right)\right] \right. \qquad (142)$$

$$\left. - e^{-j\left(\omega_0 t - \frac{z}{c}\sqrt{\omega_0^2 - \omega_c^2}\right)} \left[2 - \operatorname{erfc}\left(e^{-j\pi/4}\sqrt{\frac{p}{2}}(\omega_0 - \omega_{sp})\right)\right]\right\}$$

Finally, after the saddle points have moved away from the poles, we have

$$
f(z,t) \;=\; \left(\frac{2\omega_c c}{\pi z}\right)^{1/2} a_0 \omega_0 \left[\left(\frac{ct}{2}\right)^2 - 1\right]^{1/4} \left[\left(\frac{ct}{2}\right)^2 \left(\omega_0^2 - \omega_c^2\right) - \omega_0^2\right]^{-1} \cdot (143)
$$

$$
\cos\left(\omega_c \frac{z}{c}\sqrt{\left(\frac{ct}{z}\right)^2 - 1} + \frac{\pi}{4}\right) + a_0 \sin\left(\omega_0 t - \frac{z}{c}\sqrt{\omega_0^2 - \omega_c^2}\,\right)
$$

which comprises the posterior transient and the steady-state signal at frequency ω_0.

Near the time of the main signal buildup, the function $f(z,t)$ in (141) can be written in the form

$$
f(z,t) = \frac{1}{2}\sin\omega_0(t - z/v_{p0}) \tag{144}
$$

$$
+\; \frac{1}{\sqrt{\pi}}\sum_{n=0}^{\infty}\frac{(-)^n q^{2n+1}}{(2n+1)n!}\sin\left[\omega_0(t - z/v_{p0}) + \frac{n\pi}{2} + \frac{\pi}{4}\right]
$$

wherein v_{p0} denotes the phase velocity at frequency ω_0:

$$
v_{p0} = c(1 - \omega_c^2/\omega_0^2)^{-1/2} \tag{145}
$$

and

$$
q = \left(\frac{\omega_c z}{2c}\right)^{1/2}\left[\left(\frac{ct}{z}\right)^2 - 1\right]^{1/4}\left[-\frac{ct}{z} + \frac{\omega_0}{\omega_c}\sqrt{\left(\frac{ct}{z}\right)^2 - 1}\,\right] \tag{146}
$$

One notes that q passes through zero when $t = z/v_{g0}$, where v_{g0} is the group velocity at frequency ω_0

$$
v_{g0} = c\left(1 - \omega_c^2/\omega_0^2\right)^{1/2} \tag{147}
$$

If we write

$$
f(z,t) = A(z,t)\sin\left[\omega_0(t - z/v_{p0}) + \phi(z,t)\right] \tag{148}
$$

where $A(z,t)$ is an amplitude and $\phi(z,t)$ a phase function, we can readily show that the amplitude function $A(z,t)$ is given by

$$
A(z,t) = \left[\left(\frac{1}{2} + S_1\right)^2 + S_2^2\right]^{1/2} \tag{149}
$$

62

where

$$S_{\frac{1}{2}} = \frac{1}{\sqrt{\pi}} \sum_{n=0}^{\infty} \frac{(-)^n q^{2n+1}}{(2n+1)n!} \frac{\cos}{\sin} \left(\frac{n\pi}{2} + \frac{\pi}{4}\right) \qquad (150)$$

When $q \cong 0$, we have

$$A(z,t) \cong \frac{1}{2} + \frac{\omega_c}{2\omega_0} \left(\frac{\omega_0^2}{\omega_c^2} - 1\right)^{3/4} \left(\frac{c}{\pi\omega_c z}\right)^{1/2} \omega_0 \left(t - z/v_{g0}\right) \qquad (151)$$

whence the rate of rise of the signal amplitude near the time of the main signal buildup is clearly

$$\left.\frac{dA}{dt}\right| \cong \frac{\omega_c}{2} \left(\frac{\omega_0^2}{\omega_c^2} - 1\right)^{3/4} \left(\frac{c}{\pi\omega_c z}\right)^{1/2} \qquad (152)$$

$$t = z/v_{g0}$$

The decrease in the rate of rise as $k_c z$ increases or as ω_0 approaches ω_c is apparent.

We show in Figure 52 a plot of $f(z,t)$ as a function of normalized retarded time $\tau_r = \omega_0(t - z/c)$ for the case $\omega_0/\omega_c = 1.5$, $k_c z = 60\pi$. The saddle point crosses the pole at $\tau_r = 96.6$ for this parameter choice. One observes that the precursor and anterior transient signals build continuously in amplitude from $\tau_r = 0$ and that the sum of the pole contribution and the posterior transient produce a slow "beat" in the envelope of the signal after the pole has been crossed. The amplitude of the signal gradually approaches unity at late times, the beat amplitude decreasing as $t^{-3/2}$.

3.2   A PULSE-PROPAGATION EXAMPLE.

We now consider the application of the foregoing analysis to a practically interesting problem of pulse propagation. Specifically, we assume that

$$f(0,t) = a_0 \sin \omega_0 t \left[U(t) - U(t - t_0)\right] \qquad (153)$$

where $\omega_0 t_0/\pi$ is equal to an even integer.

Turn-On Sine Wave
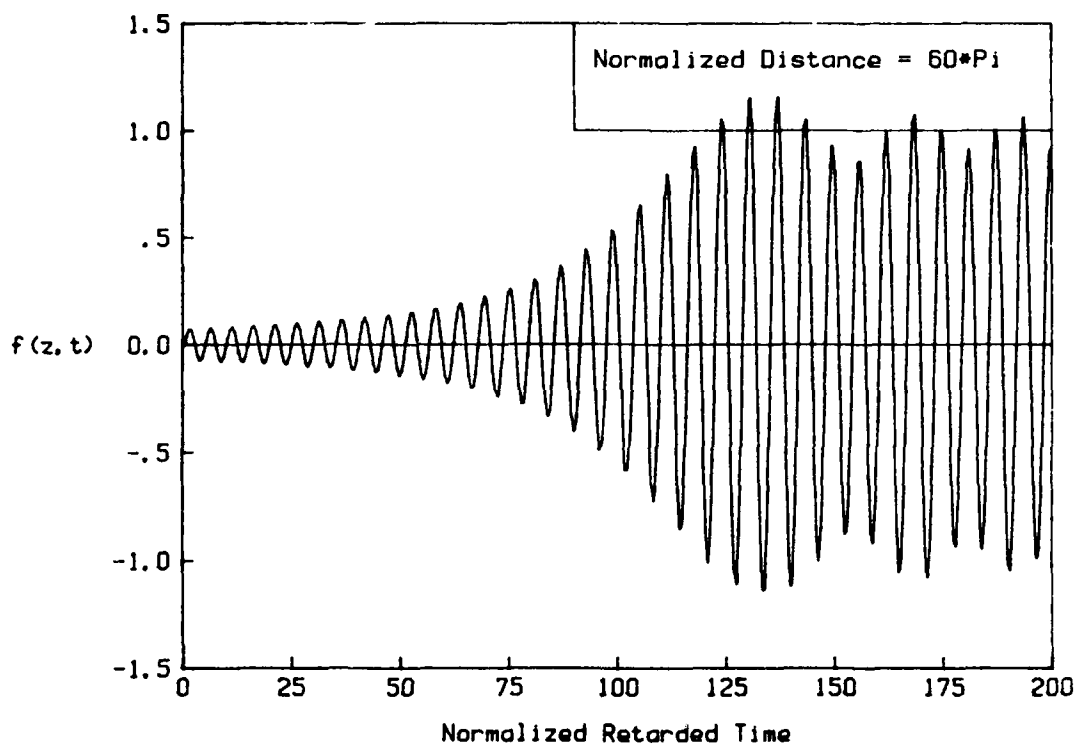
Figure 52. Turn-on sine wave of frequency ω_0 as a function of normalized retarded time $\omega_0(t - z/c)$ for $\omega_0/\omega_c=1.5$; normalized propagation distance $k_c z = 60\pi$.

By virtue of the fact that this signal is simply the difference of two turn-on sine waves separated by an interval t_0, we have immediately

$$f(z,t) = f_0(z,t) - f_0(z,t - t_0) \qquad (154)$$

where $f_0(z,t)$ now denotes the function given in (139) to (143) above.

We show in Figures 53 – 58 the (pulse) function $f(z,t)$ as a function of normalized retarded time $\omega_0(t - z/c)$ for $\omega_0/\omega_c =1.5$, $\omega_0 t = 8\pi$ and various values of $k_c z$. The results show the dispersion of the pulse as a function of propagation distance. We note that when $k_c z$ is not large, the peak value of the propagated signal can exceed its value at $z = 0$. This is related to the "beat" phenomenon mentioned earlier in connection with the turn-on sine wave.

64
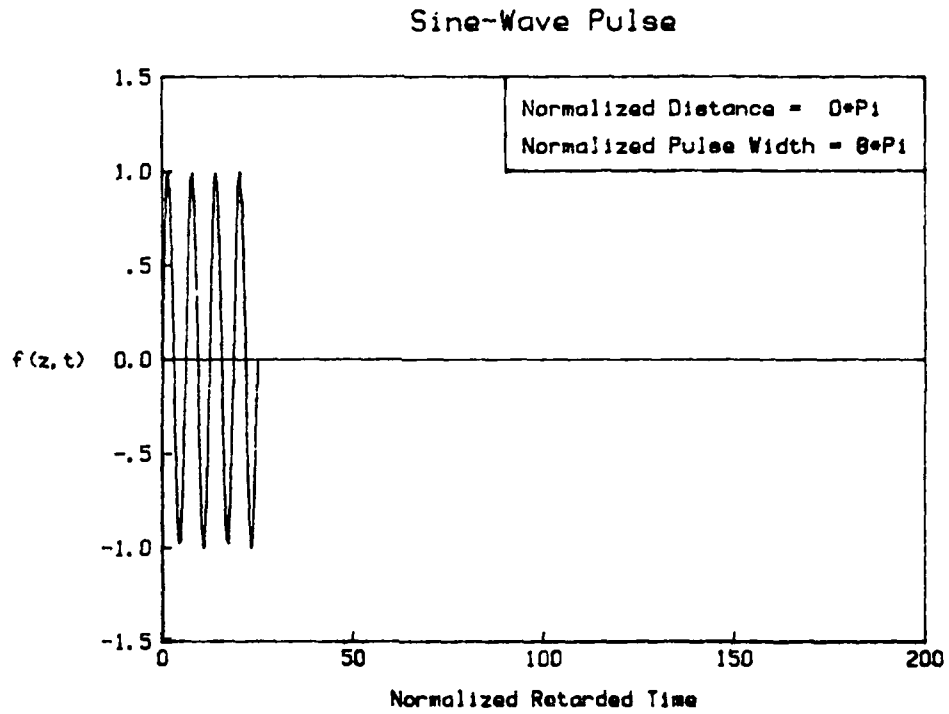
Sine-Wave Pulse

Figure 53. Sine-wave pulse vs. normalized retarded time $\omega_0(t - z/c)$ for $k_c z = 0$; $\omega_0 t_0 = 8\pi$.
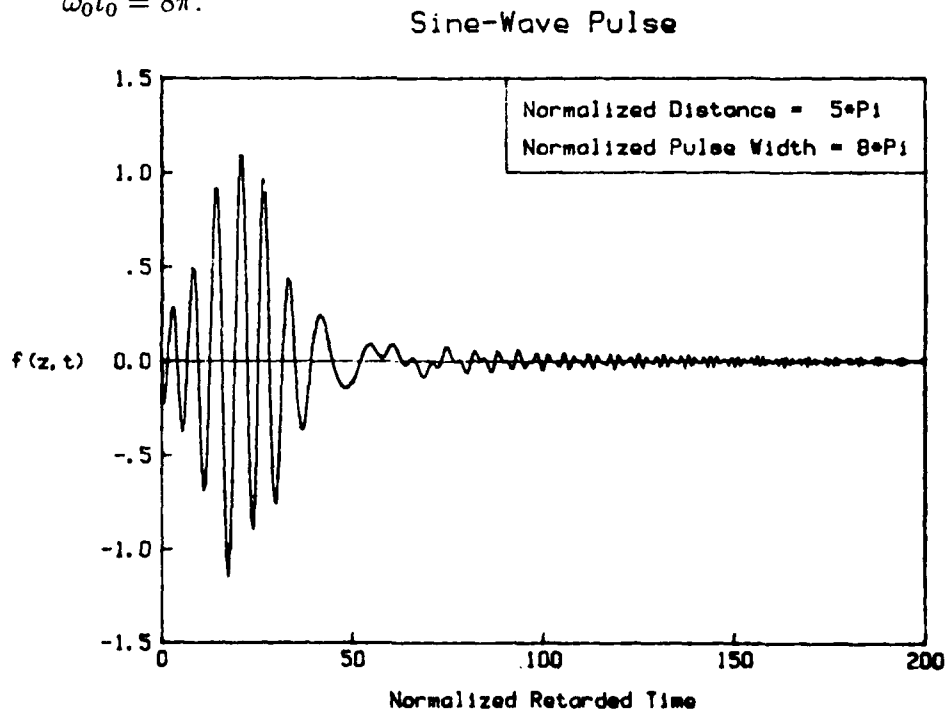
Sine-Wave Pulse

Figure 54. Sine-wave pulse vs. normalized retarded time $\omega_0(t - z/c)$ for $k_c z = 5\pi$; $\omega_0 t_0 = 8\pi$.

65
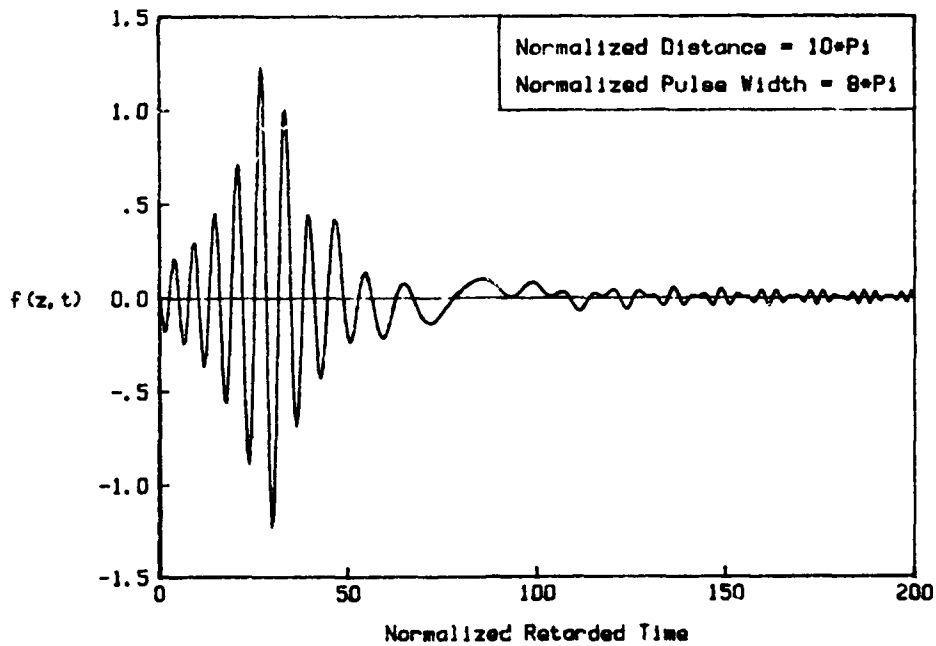
Sine-Wave Pulse

Figure 55. Sine-wave pulse vs. normalized retarded time $\omega_0(t - z/c)$ for $k_c z = 10\pi; \omega_0 t_0 = 8\pi$.

Sine-Wave Pulse
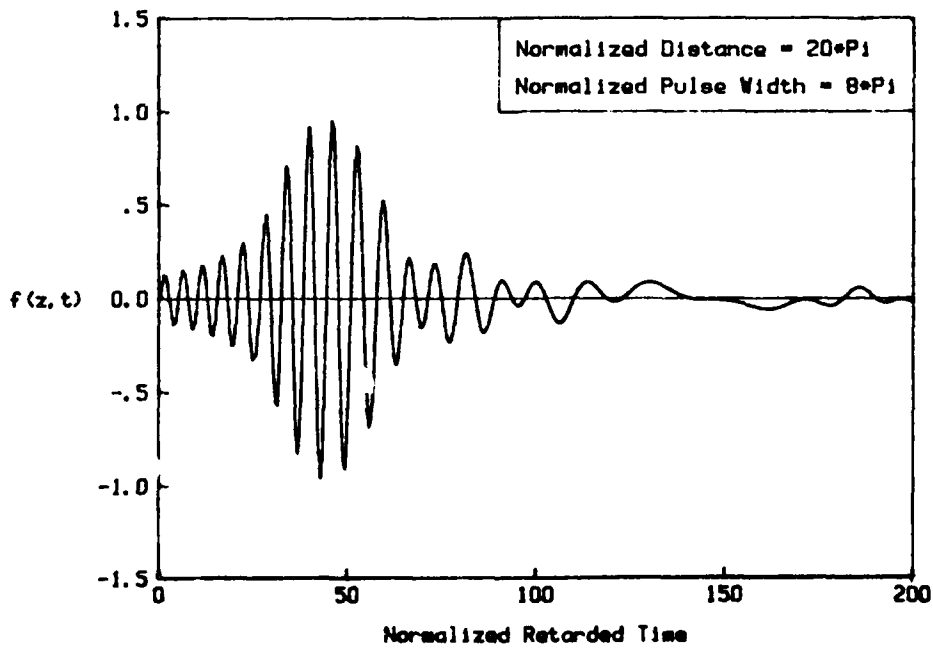
Figure 56. Sine-wave pulse vs. normalized retarded time $\omega_0(i - z/c)$ for $k_c z = 20\pi; \omega_0 t_0 = 8\pi$.

66
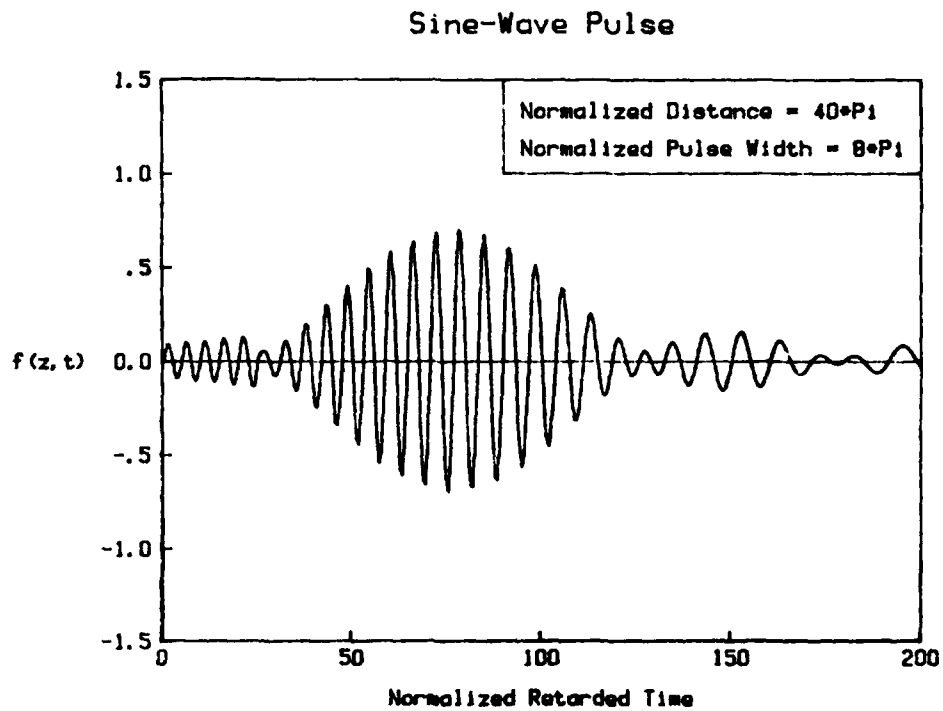
Sine-Wave Pulse

Figure 57.   Sine-wave pulse vs. normalized retarded time $\omega_0(t - z/c)$ for $k_c z = 40\pi$; $\omega_0 t_0 = 8\pi$.
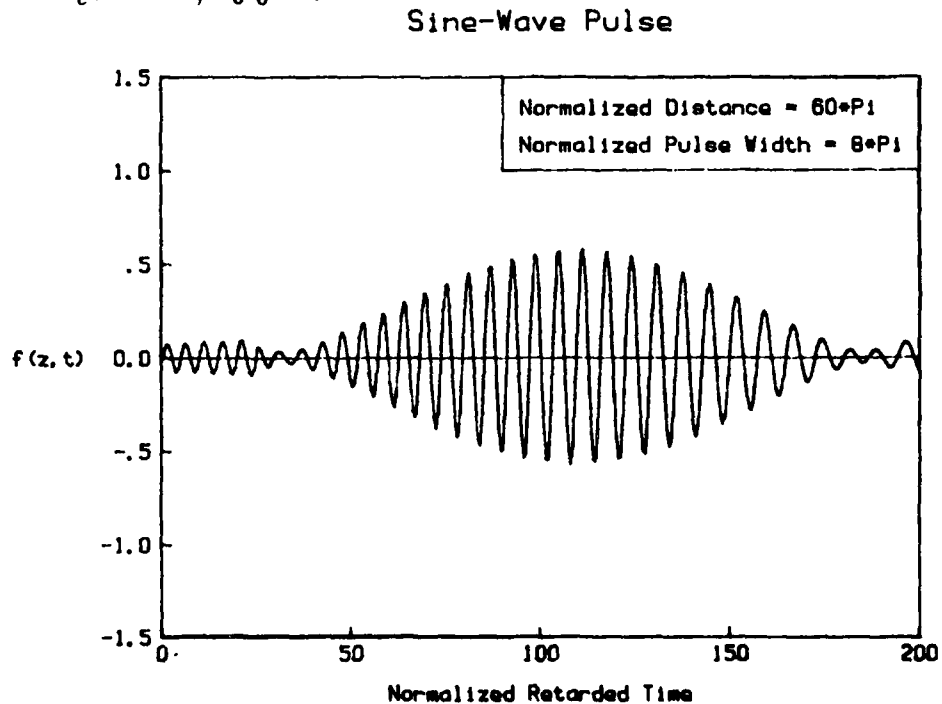
Sine-Wave Pulse

Figure 58.   Sine-wave pulse vs. normalized retarded time $\omega_0(t - z/c)$ for $k_c z = 60\pi$; $\omega_0 t_0 = 8\pi$.

3.3 MULTIMODE PROPAGATION.

The transverse electric field inside a conducting waveguide of general cross-section can be expressed in terms of the individual modal field distributions $\vec{e}_{mn}(\xi, \eta)$ in the form

$$\vec{E}_t(\xi, \eta, z; t) = \sum_{m,n} a_{mn} \vec{e}_{mn}(\xi, \eta) f_{mn}(z, t) \tag{155}$$

where a_{mn} is the amplitude of the $(m, n)^{th}$ mode and

$$f_{mn}(z, t) = \frac{1}{2\pi j} \int_\Gamma \tilde{F}_0(s) \exp\left(st - \frac{z}{c}\sqrt{s^2 + \omega_{cmn}^2}\right) ds \tag{156}$$

The frequency ω_{cmn} is the cutoff frequency of the $(m, n)^{th}$ mode and ξ and η are the transverse coordinates. It is assumed that the time dependence $f(0, t)$ is the same for each mode. Each of the integrals (156) can be treated as in the foregoing and the results superposed to yield the total transverse electric field at any point in the guide.

We consider a simple example to illustrate the multimode propagation problem. Let the waveguide be rectangular in cross-section such that the interior is defined by $0 \leq x \leq a$, $0 \leq y \leq b$, and let the electric field at $z = 0$ be $E_0 f(t)\vec{a}_y$. Then in the guide, the electric field E_y for any position $z > 0$ is

$$E_y(x, y, z; t) = \sum_{\substack{n=1 \\ (odd)}}^{\infty} \frac{4E_0}{n\pi} \sin\frac{n\pi x}{a} \cdot \tag{157}$$

$$\frac{1}{2\pi j} \int_\Gamma \tilde{F}_0(s) \exp\left(st - \frac{z}{c}\sqrt{s^2 + \omega_{cn}^2}\right) ds$$

where $\omega_{cn} = n\pi c/a$. Consider the field across the center of the guide ($x = a/2$) when $f(t)$ is a sinusoidal pulse with a Gaussian envelope. Then from results obtained earlier in this section, we obtain

$$E_y\left(\frac{a}{2}, y, z; t\right) = \sum_{\substack{n=1 \\ (odd)}}^{n_{max}} \frac{4E_0}{n\pi} \sin\frac{n\pi}{2} \left(1 + \frac{p_n^2}{t_0^4}\right)^{-1/4} \cdot \tag{158}$$

$$\exp\left[\frac{-(t - z/v_{gn})^2}{2t_0^2\left(1 + p_n^2/t_0^4\right)}\right] \cos\left[\omega_0\left(t - z/v_{pn}\right) + \phi_n(z, t)\right]$$

where t_0 is a measure of the pulse width at $t = 0$ and

$$p_n = \frac{z}{c} \frac{\omega_{cn}^2}{\left(\omega_0^2 - \omega_{cn}^2\right)^{3/2}} \tag{159}$$

$$v_{gn} = c\sqrt{1 - \omega_{cn}^2/\omega_0^2}$$

$$v_{pn} = c^2/v_{gn}$$

$$\phi_n(z,t) = \frac{1}{2}\tan^{-1}\frac{p_n}{t_0^2} - \frac{p_n\left(t - z/v_{gn}\right)^2}{2t_0^4\left(1 + p_n^2/t_0^4\right)}$$

and $n_{\max}$ is the largest value of n such that $\omega_{cn} < \omega_0$.

We have computed E_y/E_0 as a function of normalized retarded time $\omega_0(t - z/c)$ for various values of normalized z-position, for the case $\omega_0 t_0 = 4\pi$, $\omega_0 = 5.5\pi c/a$. The normalized distance is taken to be $k_{c1}z = \omega_{c1}z/c$. Three propagating modes ($n = 1,\ 3,\ 5$) are excited in the waveguide. Numerical results are presented in Figures 59 to 64.
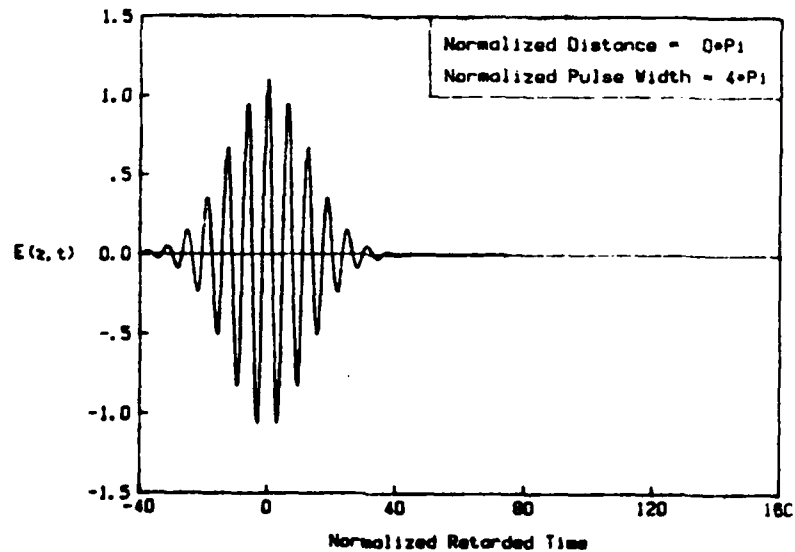
Figure 59. Mode sum E_y/E_0 vs. normalized retarded time $\omega_0(t - z/c)$ for Gaussian-envelope pulse. Normalized propagation distance $k_{c1}z = 0$; $\omega_0 t_0 = 4\pi$.

69

Multimode Gaussian Pulse
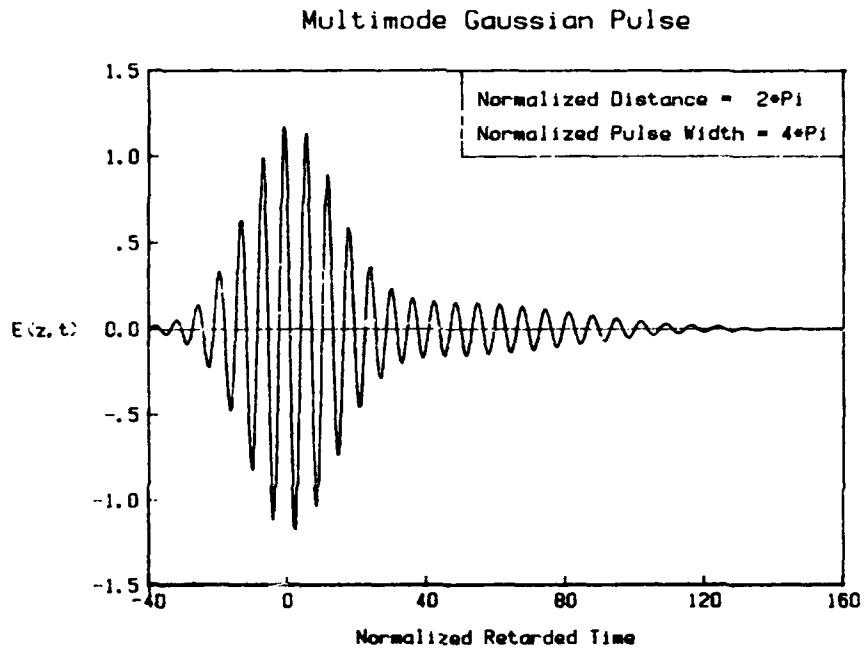
Figure 60. Mode sum E_y/E_0 vs. normalized retarded time $\omega_0(t - z/c)$ for
Gaussian-envelope pulse. Normalized propagation distance
$k_{c1}z = 2\pi$; $\omega_0 t_0 = 4\pi$.

Multimode Gaussian Pulse
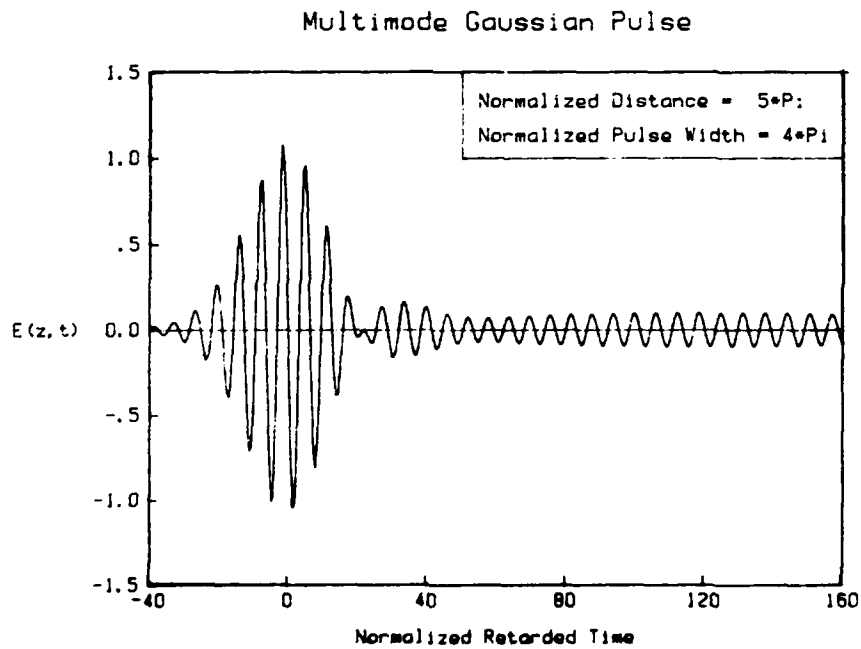
Figure 61. Mode sum E_y/E_0 vs. normalized retarded time $\omega_0(t - z/c)$ for
Gaussian-envelope pulse. Normalized propagation distance
$k_{c1}z = 5\pi$; $\omega_0 t_0 = 4\pi$.

70

Multimode Gaussian Pulse
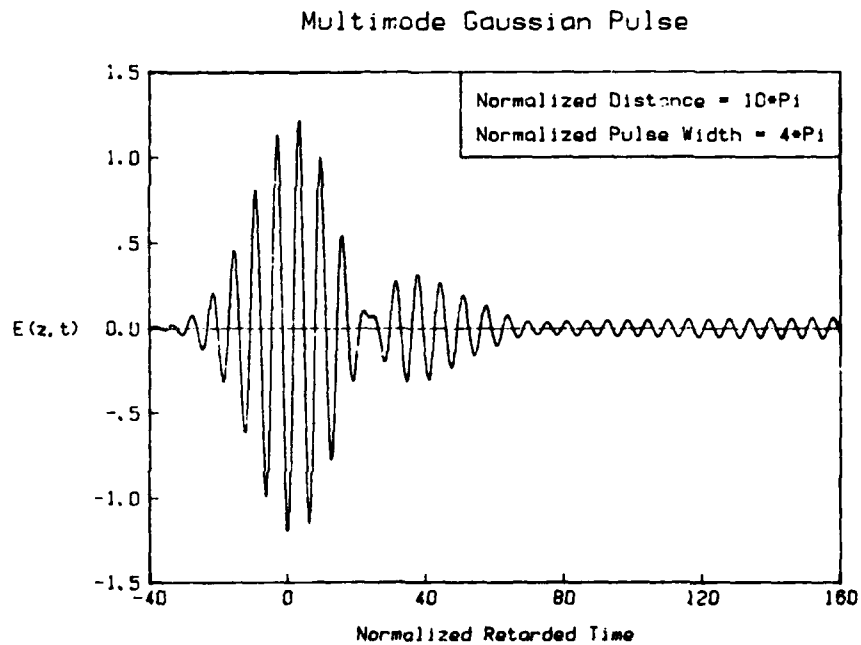
Figure 62. Mode sum E_y/E_0 vs. normalized retarded time $\omega_0(t - z/c)$ for Gaussian-envelope pulse. Normalized propagation distance $k_{c1}z = 10\pi$; $\omega_0 t_0 = 4\pi$.

Multimode Gaussian Pulse
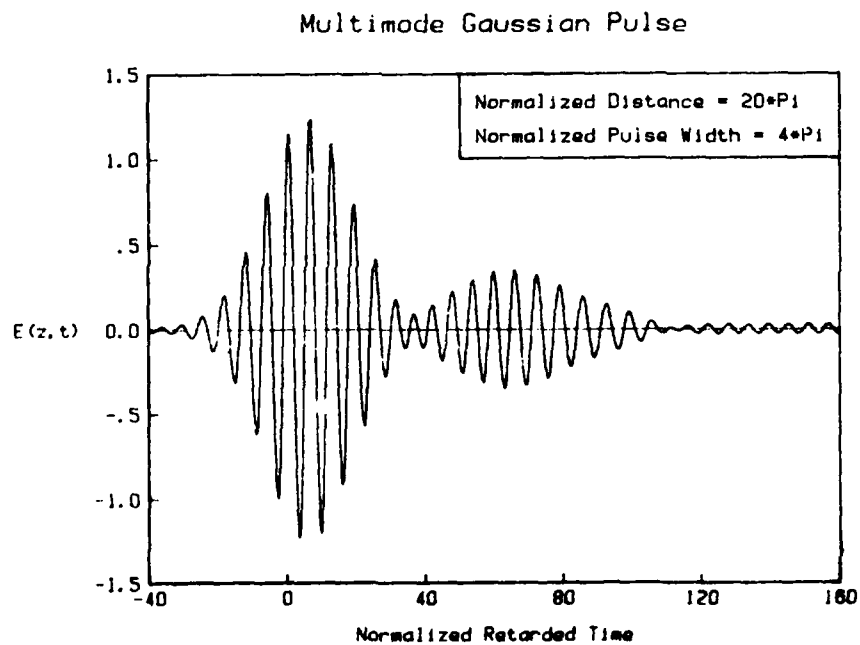
Figure 63. Mode sum E_y/E_0 vs. normalized retarded time $\omega_0(t - z/c)$ for Gaussian-envelope pulse. Normalized propagation distance $k_{c1}z = 20\pi$; $\omega_0 t_0 = 4\pi$.

71

Multimode Gaussian Pulse

Normalized Distance = 30*Pi
Normalized Pulse Width = 4*Pi
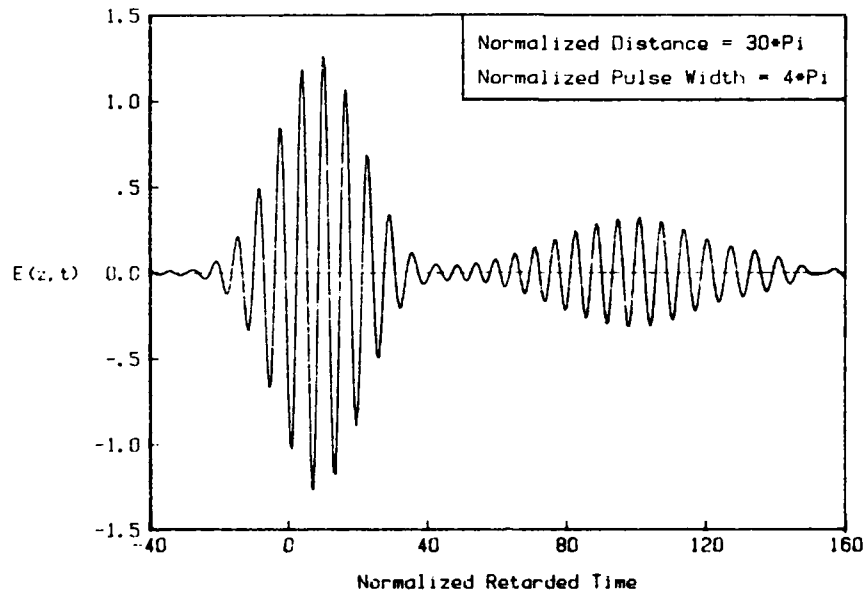
Figure 64.   Mode sum E_y/E_0 vs. normalized retarded time $\omega_0(t - z/c)$ for Gaussian-envelope pulse. Normalized propagation distance $k_{c1}z = 30\pi$; $\omega_0 t_0 = 4\pi$.

Figure 59 shows the sum of the three modes at $z = 0$. The peak amplitude exceeds unity because the non-propagating modes have not been included in the sum. In Figures 60 to 64 we show the signal at different positions in the guide. One will note that as the distance $k_{c1}z$ increases the TE_{50} mode contribution separates first, followed by the TE_{30} contribution. When $k_{c1}z = 5\pi$, the TE_{50} contribution is already very highly dispersed, while the TE_{30} contribution is just beginning to appear. The development and separation of this contribution is evident in the remainder of the plots. It is interesting to note that after the higher-order mode contributions have been separated, the dominant-mode contribution exceeds the three-mode sum at $z = 0$. This is a consequence of the fact that the TE_{10} mode amplitude coefficient is $4/\pi = 1.27$; when this modal contribution is separated from the higher-order modes by the dispersion, the total signal amplitude displays the peak value of the TE_{10} mode alone.

Figures 65 – 70 display the three-mode sum for the case $\omega_0 t_0 = 2\pi$. The increased dispersion associated with the broader bandwith of this pulse is apparent.

72
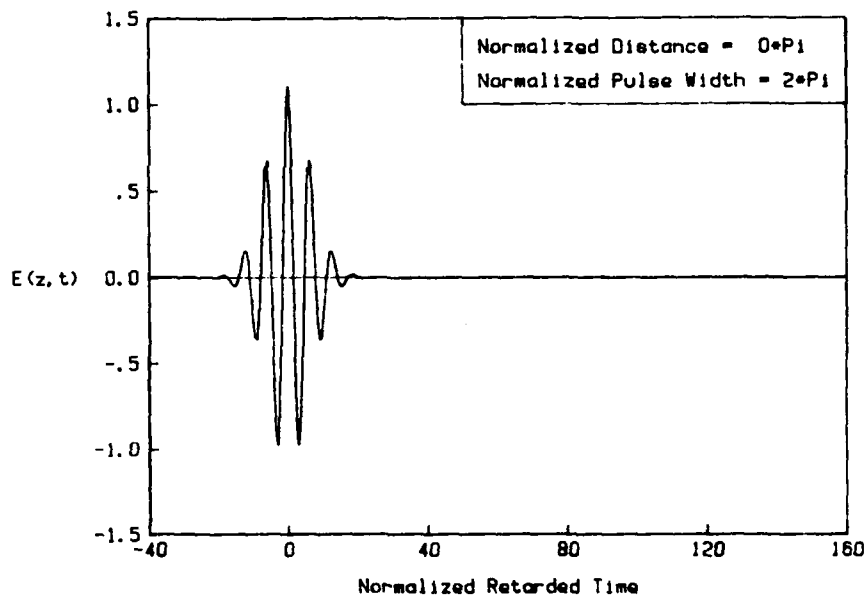
Figure 65. Mode sum E_y/E_0 vs. normalized retarded time $\omega_0(t - z/c)$ for
Gaussian-envelope pulse. Normalized propagation distance
$k_{c1}z = 0$; $\omega_0 t_0 = 2\pi$.
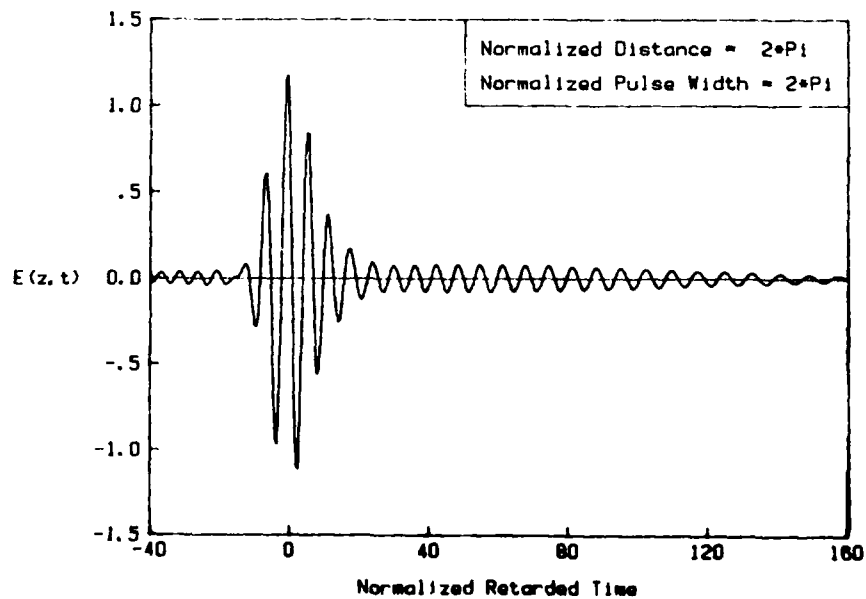
Figure 66. Mode sum E_y/E_0 vs. normalized retarded time $\omega_0(t - z/c)$ for
Gaussian-envelope pulse. Normalized propagation distance
$k_{c1}z = 2\pi$; $\omega_0 t_0 = 2\pi$.

Multimode Gaussian Pulse
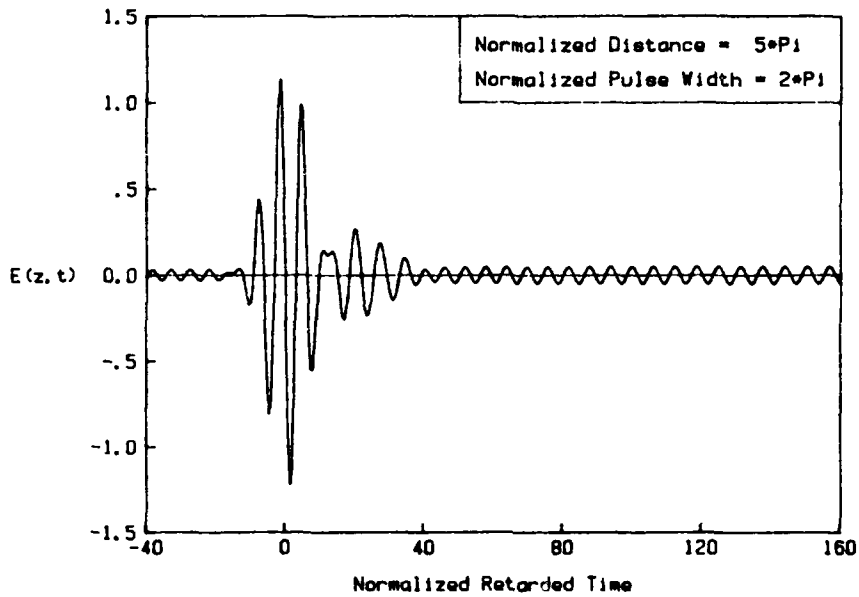
Figure 67. Mode sum E_y/E_0 vs. normalized retarded time $\omega_0(t - z/c)$ for Gaussian-envelope pulse. Normalized propagation distance $k_{c1}z = 5\pi$; $\omega_0 t_0 = 2\pi$.

Multimode Gaussian Pulse
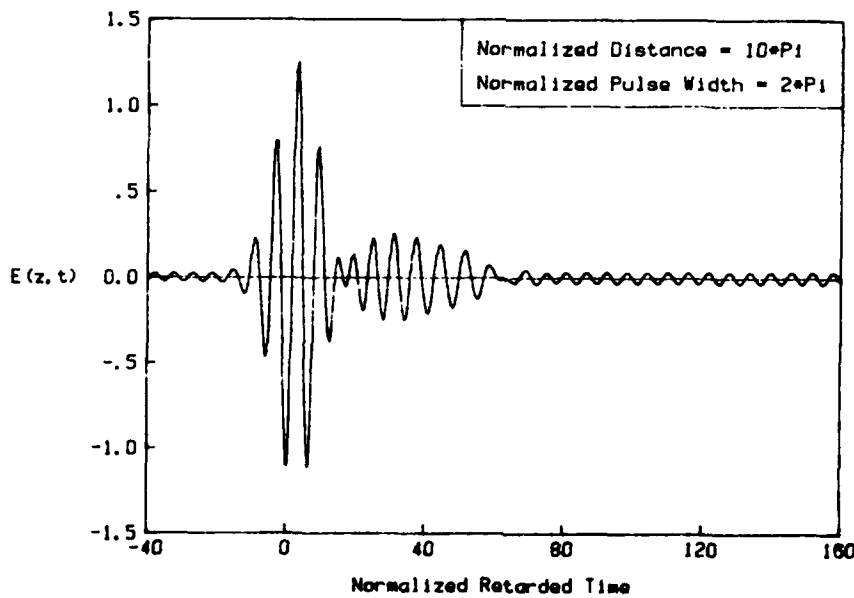
Figure 68. Mode sum E_y/E_0 vs. normalized retarded time $\omega_0(t - z/c)$ for Gaussian-envelope pulse. Normalized propagation distance $k_{c1}z = 10\pi$; $\omega_0 t_0 = 2\pi$.

74

Multimode Gaussian Pulse
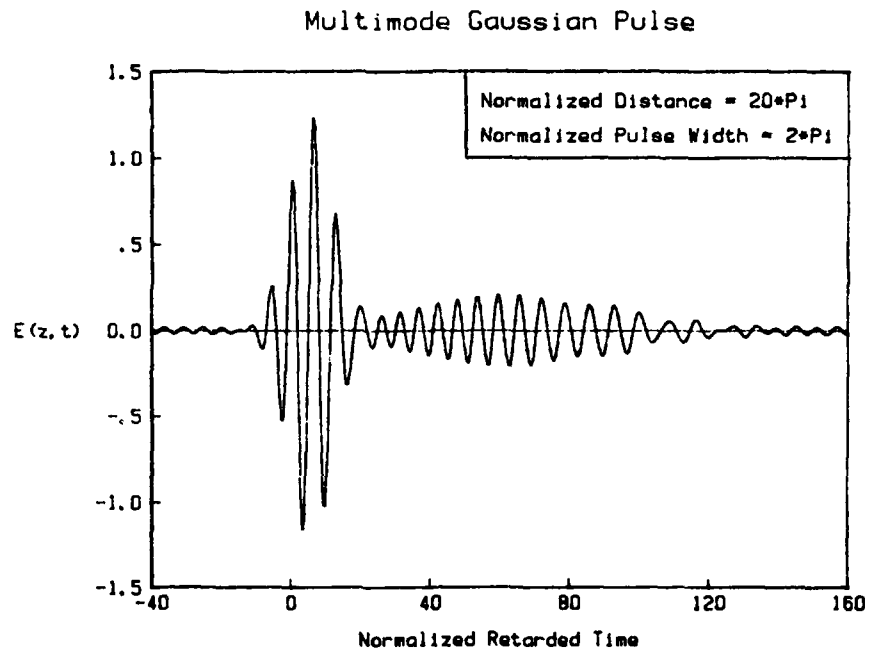
Figure 69.   Mode sum E_y/E_0 vs. normalized retarded time $\omega_0(t - z/c)$ for Gaussian-envelope pulse. Normalized propagation distance $k_{c1}z = 20\pi$; $\omega_0 t_0 = 2\pi$.

Multimode Gaussian Pulse
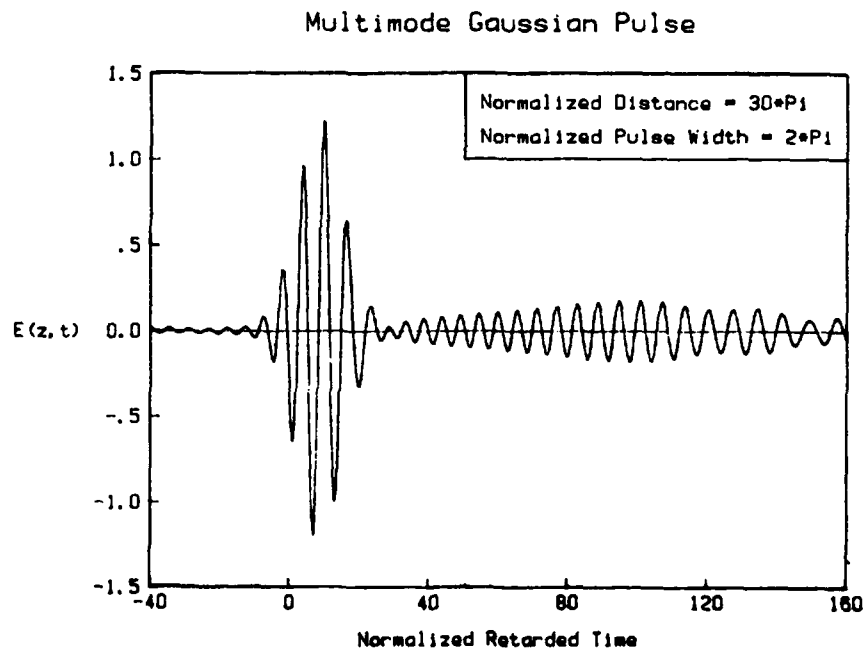
Figure 70.   Mode sum E_y/E_0 vs. normalized retarded time $\omega_0(t - z/c)$ for Gaussian-envelope pulse. Normalized propagation distance $k_{c1}z = 30\pi$; $\omega_0 t_0 = 2\pi$.

3.4 CONCLUDING REMARKS.

In this chapter we have considered the approximate analytical evaluation of transient signals propagating in waveguides. Both Gaussian and rectangular pulses have been used as examples. The multimode problem was also discussed and illustrated by example.

The propagation of a pulse whose center frequency is not much greater than the fundamental mode cutoff frequency is characterized by substantial dispersion. The peak amplitude and the rate of rise of the pulse decrease as it propagates, while the apparent pulse length increases. A pulse whose center frequency greatly exceeds the cutoff frequency propagates with little distortion; but several modes would typically exist simultaneously in such a situation. It was shown in an example that the dominant mode propagated almost undistorted and that the appearance of the total signal was essentially that of the dominant mode followed by a "tail" comprising the higher-order mode contributions. Thus when the center frequency of the pulse is well above the dominant-mode cutoff frequency, the dominant-mode contribution to the total field will be the first to arrive at a given point and will likely be the largest-amplitude portion of the total signal. Multimode propagation *per se* would not appear to be an issue in microwave interactions with systems; the important point would seem to be simply that a signal well above the dominant-mode cutoff frequency can propagate essentially undistorted in the system waveguides.

SECTION 4
POWER COLLECTED BY AN ANTENNA OVER A LOSSY
ROUGH SURFACE

Summary: We develop an expression for the power received by an antenna over a lossy rough surface. We perform representative calculations for the case where the illumination is randomly polarized and normally incident, and where the rough-surface height is a two-dimensional stationary random process with isotropic correlation.

A receiving antenna situated over a rough surface which is illuminated by a remote transmitter will receive power both directly from the illuminating field and indirectly from the field reflected by the surface. The reflected field will comprise both coherent and incoherent contributions, the latter resulting solely from the roughness of the surface. The coherent contribution arises from reflection from the "average" surface. If the surface height variations are of the order of the incident wavelength or larger, the coherent contribution is very small and the reflected field is dominated by the incoherently scattered contribution.

We consider the power received from the incoherently scattered field. Although rigorous theories of scattering from very rough surfaces do not exist, an approximate theory based on first-order perturbation methods does exist and can be used to address the problem. The approximate theory is strictly valid only when the surface height variations are small in comparison to the wavelength, but it provides a phenomenological framework within which the more general case can be studied. We employ the first-order perturbation theory in this section and remark as appropriate on the use, for example, of experimentally derived scattering data in the theoretical framework.

In the following we review the rough-surface scattering problem as it applies to a rough interface between free space and a lossy medium. Then we consider the power collected by an antenna over such an interface when the illumination is normally incident from above. We end the section with an example calculation.

4.1 ELECTROMAGNETIC SCATTERING FROM A LOSSY ROUGH SURFACE.

Consider a monochromatic plane electromagnetic wave incident at an angle θ_i on a rough surface, as shown in Figure 71. The incident wave carries power densities

- S_{inc}^h in horizontal polarization

- S_{inc}^v in vertical polarization

The power densities in each polarization which are incoherently scattered by an area ΔA on the rough surface in the direction θ_s, ϕ_s are given by

$$
\begin{bmatrix} \Delta S_{sc}^h \\ \Delta S_{sc}^v \end{bmatrix} = \frac{\Delta A}{4\pi r^2} \begin{bmatrix} \sigma_{hh} & \sigma_{hv} \\ \sigma_{vh} & \sigma_{vv} \end{bmatrix} \begin{bmatrix} S_{\text{inc}}^h \\ S_{\text{inc}}^v \end{bmatrix}
\tag{160}
$$

where $\sigma_{hh}, \ldots$ denote the scattering cross-sections per unit area of the rough surface and R is the distance from the area ΔA. Each of these cross-sections depends on the angles θ_i, θ_s, and ϕ_s; the (complex) relative permittivity ϵ_r of the scattering medium; the frequency; and the statistical properties of the rough-surface height. Specifically, the first-order perturbation theory yields [12]

$$
\sigma = 4\pi k^4 \cos^2 \theta_i \cos^2 \theta_s W(k \sin \theta_s \cos \phi_s - k \sin \theta_i, \; k \sin \theta_s \sin \phi_s) \mid \alpha \mid^2
\tag{161}
$$

where k is the propagation constant of a plane wave in free space and where

$$
\alpha_{hh} = \frac{-(\epsilon_r - 1) \cos \phi_s}{\left(\cos \theta_i + \sqrt{\epsilon_r - \sin^2 \theta_i} \right) \left(\cos \theta_s + \sqrt{\epsilon_r - \sin^2 \theta_s} \right)}
\tag{162}
$$

$$
\alpha_{hv} = \frac{(\epsilon_r - 1) \sin \phi_s \sqrt{\epsilon_r - \sin^2 \theta_i}}{\left(\epsilon_r \cos \theta_i + \sqrt{\epsilon_r - \sin^2 \theta_i} \right) \left(\cos \theta_s + \sqrt{\epsilon_r - \sin^2 \theta_s} \right)}
\tag{163}
$$

$$
\alpha_{vh} = \frac{-(\epsilon_r - 1) \sin \phi_s \sqrt{\epsilon_r - \sin^2 \theta_s}}{\left(\cos \theta_i + \sqrt{\epsilon_r - \sin^2 \theta_i} \right) \left(\epsilon_r \cos \theta_s + \sqrt{\epsilon_r - \sin^2 \theta_s} \right)}
\tag{164}
$$

78
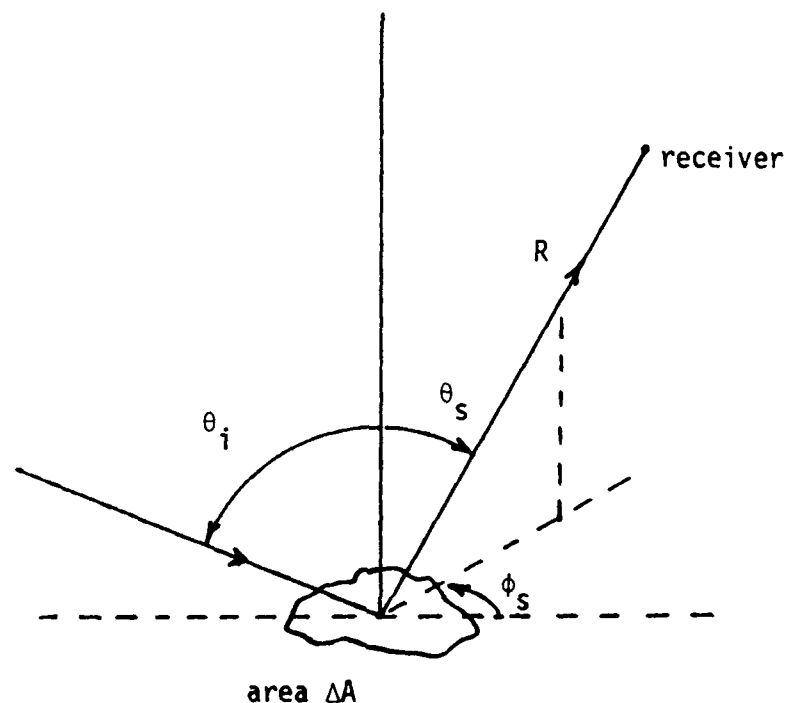
Figure 71. Geometry of the rough-surface scattering problem.

$$\alpha_{vv} = \frac{(\epsilon_r - 1)\left(\epsilon_r \sin\theta_i \sin\theta_s - \cos\phi_s\sqrt{\epsilon_r - \sin^2\theta_i}\sqrt{\epsilon_r - \sin^2\theta_s}\right)}{\left(\epsilon_r \cos\theta_i + \sqrt{\epsilon_r - \sin^2\theta_i}\right)\left(\epsilon_r \cos\theta_s + \sqrt{\epsilon_r - \sin^2\theta_s}\right)} \qquad (165)$$

The function $W(p,q)$ is the spatial-frequency power spectrum of the height of the rough surface:

$$W(p,q) = \frac{1}{\pi^2} \int_{-\infty}^{\infty} \int_{-\infty}^{\infty} e^{-ipx - iqy} R(x,y)\,dx\,dy \qquad (166)$$

where $R(x,y) = < \zeta(x',y')\zeta(x'-x,\ y'-y) >$ is the autocorrelation function of the rough-surface height $\zeta(x',\ y')$. The brackets $<>$ denote the expected value; and it is assumed that the height ζ is a stationary, zero-mean random process in two dimensions.

We shall examine the special case in which

- the incident wave is randomly polarized;

79

- the angle of incidence $\theta_i = 0$; and

- the autocorrelation $R(x,y)$ is isotropic.

When the incident wave is randomly polarized, $S_{\text{inc}}^h = S_{\text{inc}}^v = \frac{1}{2}S_{\text{inc}}$. Thus

$$\Delta S_{sc}^h = \frac{\Delta A}{4\pi R^2}\sigma_h S_{\text{inc}} \tag{167}$$

$$\Delta S_{sc}^v = \frac{\Delta A}{4\pi R^2}\sigma_v S_{\text{inc}} \tag{168}$$

where

$$\sigma_h = \frac{1}{2}(\sigma_{hh} + \sigma_{hv}) \tag{169}$$

$$\sigma_v = \frac{1}{2}(\sigma_{vh} + \sigma_{vv}) \tag{170}$$

Furthermore, when $\theta_i = 0$ we find

$$\alpha_{hh} = -\alpha_h \cos\phi_s \tag{171}$$

$$\alpha_{hv} = \alpha_h \sin\phi_s \tag{172}$$

$$\alpha_{vh} = -\alpha_v \sin\phi_s \tag{173}$$

$$\alpha_{vv} = -\alpha_v \cos\phi_s \tag{174}$$

where

$$\alpha_h = \frac{\sqrt{\epsilon_r} - 1}{\cos\theta_s + \sqrt{\epsilon_r - \sin^2\theta_s}} \tag{175}$$

$$\alpha_v = \frac{\left(\sqrt{\epsilon_r} - 1\right)\sqrt{\epsilon_r - \sin^2\theta_s}}{\epsilon_r\cos\theta_s + \sqrt{\epsilon_r - \sin^2\theta_s}} \tag{176}$$

Finally, when the autocorrelation function can be written in the form

$$R(x,y) = \overline{h^2}f\left(\sqrt{x^2 + y^2}/l\right) \tag{177}$$

80

where l is a characteristic correlation distance and $\overline{h^2}$ is the variance of the rough-surface height, we find that

$$W(\cdot) \;=\; \frac{2l^2\overline{h^2}}{\pi} \int_0^\infty f(u) J_0(klu\sin\theta_s)u\,du \tag{178}$$

$$\;=\; l^2\overline{h^2}\tilde{F}(kl\sin\theta_s)$$

where $J_0(\cdot)$ denotes the Bessel function of order zero. Thus

$$\sigma_h = 2\pi k^4 l^2\overline{h^2}\cos^2\theta_s\tilde{F}(kl\sin\theta_s)\mid\alpha_h\mid^2 \tag{179}$$

$$\sigma_v = 2\pi k^4 l^2\overline{h^2}\cos^2\theta_s\tilde{F}(kl\sin\theta_s)\mid\alpha_v\mid^2 \tag{180}$$

We next consider the power received by an antenna situated over the rough surface.

4.2 POWER COLLECTED BY AN ANTENNA OVER A ROUGH SURFACE.

Let the antenna be located at height h over the rough surface and let its axial direction be defined by angles θ_B, ϕ_B, as shown in Figure 72. The effective aperture of the antenna is denoted $A_e(\theta',\phi')$ where θ' and ϕ' are defined with respect to the antenna axis.

The power density scattered in the direction of the antenna by a small area ΔA in the $z = 0$ plane is

$$\Delta S_{sc}^{h,v} = \frac{\Delta A}{4\pi R^2}\sigma_{h,v}S_{\text{inc}} \tag{181}$$

and the power ΔP received from this small area is

$$\Delta P^{h,v} = \frac{S_{\text{inc}}A_e(\theta',\phi')\sigma_{h,v}}{4\pi\cos\theta_s}\frac{\Delta A\cos\theta_s}{R^2} \tag{182}$$

Now $\Delta A\cos\theta_s/R^2$ is just $\Delta\Omega$, the solid angle subtended by the area ΔA. Thus the total power received by the antenna is simply

$$P^{h,v} = \frac{S_{\text{inc}}}{4\pi}\int_{\Omega_0}\frac{A_e(\theta',\phi')\sigma_{h,v}(\theta_s)}{\cos\theta_s}d\Omega \tag{183}$$

81

where Ω_0 denotes the total solid angle (of 2π steradians) subtended by the rough surface.

We consider the special case where the axis of the antenna is parallel to the x-axis, so that

$$\cos\theta_s = \sin\theta'\cos\phi' \tag{184}$$

$$\sin\theta_s\sin\phi_s = \sin\theta'\sin\phi' \tag{185}$$
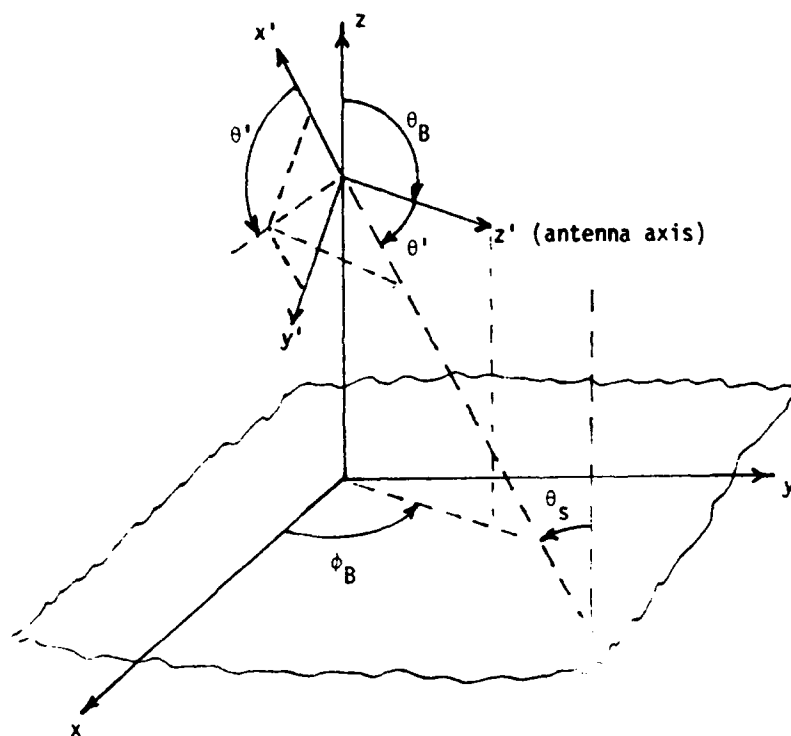
Figure 72. Antenna over a rough surface: geometry.

Furthermore, $d\Omega = \sin\theta' d\theta' d\phi'$ in the antenna coordinates with $-\pi/2 \le \phi' \le \pi/2$, $0 \le \theta' \le \pi$. Thus

$$P^{h,v} = \frac{S_{inc}}{4\pi} \int_{-\pi/2}^{\pi/2} \sec\phi' d\phi' \int_0^\pi A_e(\theta',\phi')\sigma_{h,v}(\theta_s)d\theta' \tag{186}$$

Substituting eqs. (179), (180), (184), and (185) into eq. (186), we obtain

$$P^{h,v} = \frac{1}{2}S_{inc}k^4 l^2 \overline{h^2} \int_{-\pi/2}^{\pi/2} \cos\phi' d\phi' \int_0^\pi \sin^2\theta' d\theta' \cdot \tag{187}$$

82

$$\tilde{F}\left(kl\sqrt{1 - \sin^2\theta'\cos^2\phi'}\right) A_e(\theta', \phi') \mid \alpha_{h,v}(\theta', \phi') \mid^2$$

where

$$\alpha_h = \frac{\sqrt{\epsilon_r} - 1}{\sin\theta'\cos' + \sqrt{\epsilon_r - 1 + \sin^2\theta'\cos^2\phi'}} \tag{188}$$

$$\alpha_v = \frac{\left(\sqrt{\epsilon_r} - 1\right)\sqrt{\epsilon_r - 1 + \sin^2\theta'\cos^2\phi'}}{\epsilon_r \sin\theta'\cos\phi' + \sqrt{\epsilon_r - 1 + \sin^2\theta'\cos^2\phi'}} \tag{189}$$

$$\tilde{F}(\xi) = \frac{2}{\pi}\int_0^\infty f(u)J_0(u\xi)u\,du \tag{190}$$

In eqs. (186) and (187) above, $P^{h,v}$ has been expressed in terms of an integral over the antenna coordinates θ', ϕ'. It may also be written in terms of the coordinates θ_s and ϕ_s. Specifically, defining

$$\hat{A}_e(\theta_s, \phi_s) = A_e(\theta', \phi') \tag{191}$$

we obtain

$$P^{h,v} = \frac{S_{\text{inc}}}{4\pi}\int_0^{\pi/2}\tan\theta_s\sigma_{h,v}(\theta_s)d\theta_s\int_{-\pi}^{\pi}\hat{A}_e(\theta_s, \phi_s)d\phi_s \tag{192}$$

$$= \frac{S_{\text{inc}}}{2}k^4l^2\overline{h^2}\int_0^{\pi/2}\mid\alpha_{h,v}(\theta_s)\mid^2\tilde{F}(kl\sin\theta_s)\sin\theta_s\cos\theta_s d\theta_s \cdot$$

$$\int_{-\pi}^{\pi}\hat{A}_e(\theta_s, \phi_s)d\phi_s$$

This latter expression may be more suitable than that given in eq. (187) for a given application.

4.3 EXAMPLE CALCULATIONS.

It is evident that except under conditions which allow many simplifying approximations to be made, $P^{h,v}$ must be evaluated numerically. We shall confine our attention to a specific antenna configuration, the rectangular aperture with uniform illumination. For such an antenna,

$$A_e(\theta', \phi') = ab\,\text{sinc}^2\left(\frac{ka}{2}\sin\theta'\cos\phi'\right)\text{sinc}^2\left(\frac{kb}{2}\sin\theta'\sin\phi'\right) \tag{193}$$

83

$$\hat{A}_e(\theta_s, \phi_s) = ab \operatorname{sinc}^2\left(\frac{ka}{2}\cos\theta_s\right)\operatorname{sinc}^2\left(\frac{kb}{2}\sin\theta_s\sin\phi_s\right) \tag{194}$$

where a and b are the aperture dimensions and the sides of length a are taken to be parallel to the z-axis. Furthermore, $\operatorname{sinc}(x) \equiv (\sin x)/x$.

We shall also consider that $\tilde{F}(\xi)$ is of the form appropriate for a Gaussian correlation function (cf. eq. (177))

$$R(x, y) = \overline{h^2}e^{-(x^2+y^2)/l^2} \tag{195}$$

Thus

$$\tilde{F}(\xi) = \frac{1}{\pi}e^{-\xi^2/4} \tag{196}$$

Substituting eqs. (194) and (196) into eq. (192), we obtain

$$P^{h,v} = \frac{S_{\text{inc}}ab}{2\pi}k^4l^2\overline{h^2}\int_0^{\pi/2}|\alpha_{h,v}(\theta_s)|^2 \ e^{-\left(\frac{kl}{2}\sin\theta_s\right)^2}\operatorname{sinc}^2\left(\frac{ka}{2}\cos\theta_s\right)\cdot \tag{197}$$

$$\sin\theta_s\cos\theta_s d\theta_s\int_{-\pi/2}^{\pi/2}\operatorname{sinc}^2\left(\frac{kb}{2}\sin\theta_s\sin\phi_s\right)d\phi_s$$

wherein we have altered the limits of the integral over ϕ_s to include only the "forward-looking" portion of the antenna pattern.

The integral over ϕ_s can be expressed in terms of a function $G(\xi)$ defined as follows:

$$G(\xi) = \frac{2}{\pi}\int_0^{\pi/2}\operatorname{sinc}^2(\xi\sin\phi)d\phi \tag{198}$$

$$= \sum_{k=0}^{\infty}\frac{(-)^k\xi^{2k}}{(2k+1)k!(k+1)!}$$

with

$$G(\xi) \to \frac{1}{\xi} \quad (\xi \to \infty) \tag{199}$$

Thus

$$P^{h,v} = \frac{S_{\text{inc}}ab}{2}k^4l^2\overline{h^2}\int_0^{\pi/2}|\alpha_{h,v}(\theta_s)|^2 \ e^{-\left(\frac{kl}{2}\sin\theta_s\right)^2}\cdot \tag{200}$$

$$\operatorname{sinc}^2\left(\frac{ka}{2}\cos\theta_s\right)G\left(\frac{kb}{2}\sin\theta_s\right)\sin\theta_s\cos\theta_s d\theta_s$$

84

A plot of the function $G(\xi)$ vs. ξ is shown in Figure 73.

We have performed sample calculations of the expression for P^h given in eq. (200) for the case in which $|\epsilon_r| \gg 1$. In this case, $\alpha_h \cong 1$; and we have evaluated the normalized quantity

$$p_h = \frac{P^h}{abS_{\text{inc}}} \tag{201}$$

$$= \frac{1}{2}k^4 l^2 \overline{h^2} \int_0^{\pi/2} e^{-\left(\frac{kl}{2}\sin\theta_s\right)^2} \text{sinc}^2\left(\frac{ka}{2}\cos\theta_s\right) \cdot$$

$$G\left(\frac{kb}{2}\sin\theta_s\right) \sin\theta_s \cos\theta_s d\theta_s$$

which is the ratio of the power received from rough-surface scattering to the total power which is available to the antenna.

It is evident from eq. (201) that the parameters on which p_h depends are the electrical dimensions of the antenna, ka and kb; the electrical correlation length kl; and the electrical rough-surface height variance $k^2\overline{h^2}$. The factor $k^2\overline{h^2}$ can be considered as the limiting form for small height variances of the factor

$$1 - \exp\left(-k^2\overline{h^2}\right)$$

whose maximum value is unity. In order to bound the collected power we shall assume this factor to be unity in the computational results. Thus

$$p_h \leq \hat{p}_h = \frac{1}{2}k^2 l^2 \int_0^1 e^{-(klu/2)^2} \text{sinc}^2\left(\frac{ka}{2}\sqrt{1-u^2}\right) G\left(\frac{kbu}{2}\right) u\,du \tag{202}$$

It is easy to show that $\hat{p}_h$ becomes, in the limit of long correlation lengths l,

$$\lim_{l\to\infty} \hat{p}_h = \text{sinc}^2\frac{ka}{2} \tag{203}$$
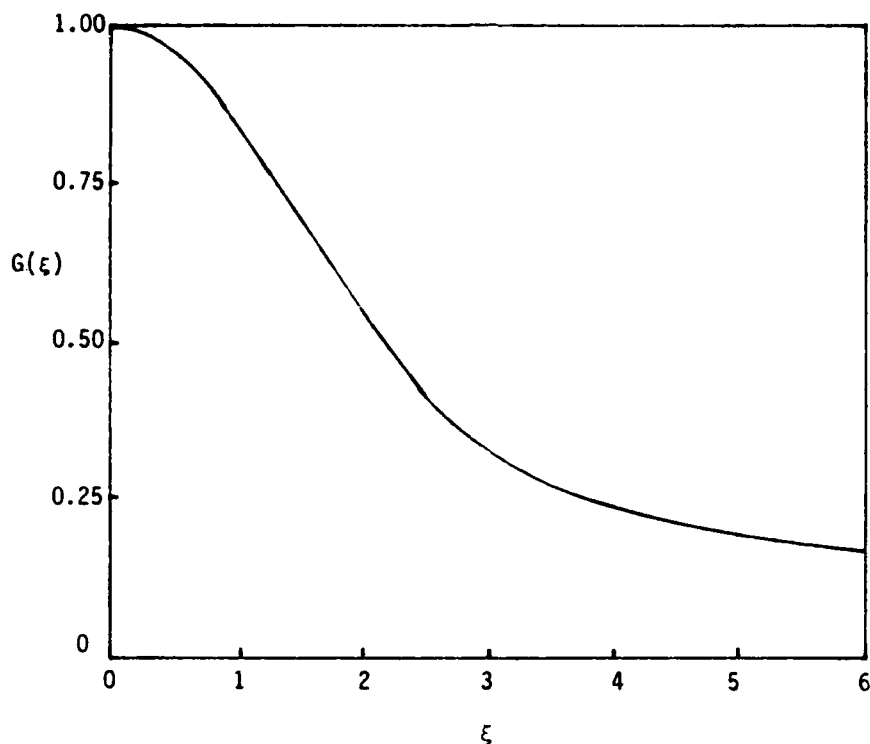
Figure 73. $G(\xi)$ vs. ξ. The function differs significantly from $1/\xi$ only for
$0 \le \xi \le 3$.

This limit is obviously related to the effective area of the aperture antenna at grazing incidence (scattering angle $\theta_s = 0$). For simplicity in the numerical results to follow we shall take $ka = 2n\pi$ $(n > 1)$. Thus the limit of $\hat{p}_h$ for large l will be zero in every case which we consider. The maximum gain G_0 of the aperture is

$$G_0 = \frac{1}{\pi}\frac{b}{a}(ka)^2 = \frac{4n^2\pi b}{a} \tag{204}$$

We shall choose ratios b/a such that (204) is satisfied for a given value of G_0. Thus $\hat{p}_h$ can be written

$$\hat{p}_h = 2\left(\frac{n\pi l}{a}\right)^2 \int_0^1 \exp\left[-\left(\frac{n\pi l}{a}u\right)^2\right] \text{sinc}^2\left(n\pi\sqrt{1 - u^2}\right) G\left(\frac{G_0}{4n}u\right)\ u\,du \tag{205}$$

wherein G_0, n and l/a are parameters. We have evaluated $\hat{p}_h$ as a function of l/a for the cases listed below:

$G_0 = 10$ dB,	$n = 1$	$(b/a = 0.80)$
$G_0 = 15$ dB,	$n = 1$	$(b/a = 2.52)$
	$n = 2$	$(b/a = 0.63)$
$G_0 = 20$ dB,	$n = 2$	$(b/a = 1.99)$
	$n = 3$	$(b/a = 0.88)$
	$n = 4$	$(b/a = 0.50)$
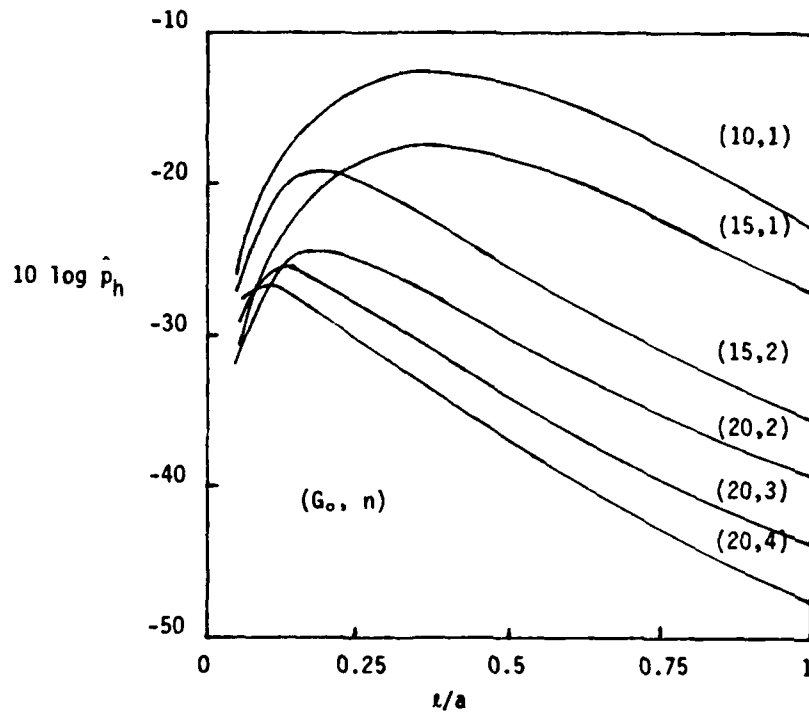
Figure 74. Normalized received power $\hat{p}_h$ vs. normalized correlation length l/a. G_0 is given in dB.

87

The results are shown in Figure 74. It is evident from the curves shown there that

1. The peak value of $\hat{p}_h$ as a function of l/a decreases as the antenna gain is increased and as n is increased.

2. The value of l/a at which the peak occurs decreases as the gain is increased and as n is increased, and is less than 0.5 in all curves considered.

3. The peak value of $\hat{p}_h$ in dB is less than the negative of the antenna gain in dB.

4. The peak value of $\hat{p}_h$ is not a strong function of n.

Results 3 and 4 indicate that at least for the configuration considered here, the maximum power collected from rough surface scattering is easily estimated and that it is not a strong function of the antenna pattern.

4.4   CONCLUDING REMARKS.

We have considered the scattered power collected by an antenna over a rough surface and have calculated some representative results for a rectangular aperture antenna whose axis is directed parallel to the surface. It has been shown that the collected power decreases as the antenna gain increases and that this power is maximized when the coherence length of the scattering surface is less than the antenna's vertical dimension. The peak value of the collected power, normalized to the power available to the antenna, is roughly equal to the negative of the antenna gain in dB and does not depend strongly on the details of the antenna pattern.

Our treatment of this problem has been based upon an analytical model derived from a first-order perturbation theory. This theory provides the scattering cross-sections $\sigma_{hh}, \ldots$ in terms of the properties of the scattering medium and its rough surface. If experimental data for these quantities are used, the framework of the analysis given herein remains unchanged. The result given in (183) would simply employ experimentally derived expressions for σ_h and σ_v rather than those used here.

88

SECTION 5
APERTURE COUPLING TO A WIRE IN A CYLINDRICAL CAVITY

Summary: We examine the electromagnetic coupling to a thin wire on the axis of a circular cylindrical cavity through a thin azimuthal slot aperture on the cavity side wall. The wire is shorted to a cavity end wall at one end and it becomes the center conductor of a coaxial cable at the other end. The coupling is described in terms of the Thévenin equivalent circuit driving the feed point of the coaxial cable, so that an arbitrary load may be considered. The source is specified in terms of the voltage across the slot aperture in the outer wall, so that the exterior-to-interior coupling problem may be approximately decoupled. Representative numerical data are presented to illustrate the results.

In this section we examine a relatively simple and analytically tractable approximate treatment of electromagnetic coupling through an aperture in a cavity wall to a wire inside the cavity. Our purpose is to develop the transfer function which relates the incident electromagnetic field on the exterior of the cavity to the current induced in an internal load.

The geometry of the problem is shown in Figure 75. The cavity itself is a right circular cylinder of radius b and length l. A wire radius of a is coaxial with the cavity and shorted to the cavity wall at $z = 0$. It leaves the cavity at $z = l$, forming the center conductor of a coaxial line whose outer radius is c. We assume that $a << b$ and $c << b$. The cavity is excited by a thin circumferentially-oriented slot of width w and angular extent $\Delta\phi$, located at $z = z_0$ in the cavity side wall.

In our analysis of the exterior problem the slot is treated as if it were located in an infinitely extended conducting plane. Use is made of results in Section 2 to estimate the voltage across the slot. This slot voltage is then used to drive the interior problem. Thus the transfer function from the incident field to the internal wire current is the product of

- the transfer function relating the incident field to the slot voltage, derived in Section 2; and

- the transfer function relating the slot voltage to the internal wire current, derived herein.

The approximation employed herein obviously does not take into account the effect of the cavity itself on the fields in the slot. This approximation will cause the cavity Q to appear higher than it actually is, because reradiation from the slot is not accounted for.
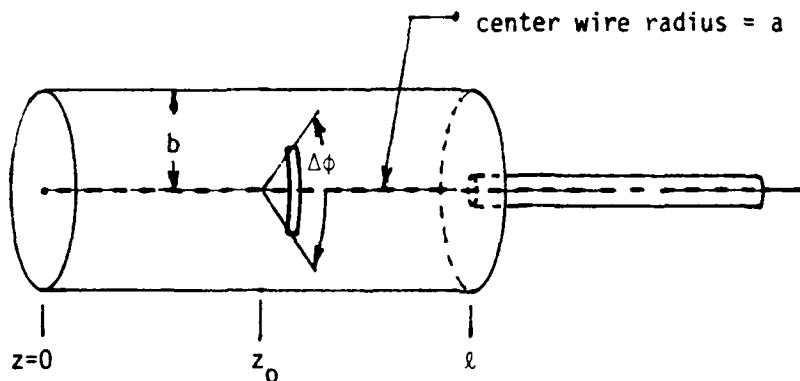
Figure 75.   Geometry of the problem. The slot width is w and the outer radius of the coax leaving the cavity is c.

5.1   FORMULATION.

The electromagnetic field which excites axial currents on the center conductor in the cavity is the axially symmetric TM_z portion of the total field, expressed in terms of a scalar function ψ by the relations

$$E_\rho = \frac{1}{j\omega\epsilon_0} \frac{\partial^2\psi}{\partial\rho\partial z} \qquad (206)$$

$$E_z = \frac{1}{j\omega\epsilon_0} \left(\frac{\partial^2}{\partial z^2} + k^2 \right) \psi$$

$$H_\phi = -\frac{\partial\psi}{\partial\rho}$$

90

The function ψ is a solution of the scalar Helmholtz equation in circular-cylindrical coordinates

$$\frac{1}{\rho}\frac{\partial}{\partial\rho}\left(\rho\frac{\partial\psi}{\partial\rho}\right) + \frac{\partial^2\psi}{\partial z^2} + k^2\psi = 0 \tag{207}$$

wherein $k^2 = \omega^2\mu_0\epsilon_0$ with μ_0 and ϵ_0 denoting the permeability and permittivity of free space respectively. The time dependence $\exp(j\omega t)$ is assumed and suppressed.

Our approach to solving the problem of electromagnetic coupling from a slot aperture on the outer side wall of the cavity to a transmission line which leaves the center of an end wall is as follows: first, the current I_0 on the center conductor due to the excitation of the outer slot is determined as a function of the average slot voltage $\overline{V_0}$ and written in the form

$$I_0 = Y_0\overline{V_0} \qquad (V_1 = 0) \tag{208}$$

In the calculation of I_0 it is assumed that the coupling aperture to the transmission line is closed. Next, the current I_1 due to voltage V_1 across the transmission-line aperture is determined, assuming that the outer-wall slot is closed, so that

$$I_1 = Y_1 V_1 \qquad (\overline{V_0} = 0) \tag{209}$$

The total current, $I_0 + I_1$, is then related to the voltage V_1 by the input admittance to the transmission line Y_i:

$$I_0 + I_1 = Y_i V_1 \tag{210}$$

The relation (210) is used to solve for V_1 in terms of $\overline{V_0}$. Thus

$$V_1 = Y_0\overline{V_0}(Y_i - Y_1)^{-1} \tag{211}$$

and the solution is complete. Knowledge of the external excitation ($\overline{V_0}$) and the line input admittance (Y_i) yields the line excitation (V_1). In the following, we carry out each of the steps leading to the result (211).

5.1.1   Coupling through the Outer Slot.

The electric field E_z at the outer slot at $\rho = b$, $| \phi | \leq \Delta\phi/2$, $z = z_0$ is presumed known:

$$E_{zs} = V_0(\phi)\delta(z - z_0) \qquad (\rho = b) \tag{212}$$

91

We assume that $E_\phi \equiv 0$ over the slot. The function ψ is conveniently represented in the form

$$\psi = \psi_0 = j\omega\epsilon_0 \sum_{n=0}^{\infty} A_n \cos\left(\frac{n\pi z}{l}\right) \frac{1}{\lambda_n^2} C_0(\lambda_n \rho, \lambda_n a) \tag{213}$$

where the coefficients A_n are to be determined and

$$C_0(x, y) = J_0(x)N_0(y) - J_0(y)N_0(x) \tag{214}$$

$$\lambda_n^2 = k^2 - (n\pi/l)^2 \tag{215}$$

The form for ψ_0 given by (213) and (214) above ensures that E_ρ vanishes at $z = 0$ and $z = l$ and that E_z vanishes at $\rho = a$; E_ϕ is identically zero throughout the cavity.

Matching the boundary condition (212) in the least-squares sense, we readily obtain for A_n

$$A_0 = \frac{\overline{V_0}}{lC_0(kb, ka)} \tag{216}$$

$$A_n = \frac{2\overline{V_0}\cos(n\pi z_0/l)}{lC_0(\lambda_n b, \lambda_n a)} \quad (n \geq 1)$$

where

$$\overline{V_0} \equiv \frac{1}{2\pi} \int_{-\Delta\phi/2}^{\Delta\phi/2} V_0(\phi) d\phi \tag{217}$$

The current on the center wire at the endpoint $z = l$ is given by

$$I_0 = 4j\omega\epsilon_0 l \overline{V_0} \left\{ \frac{1}{k^2 l^2 C_0(kb, ka)} \right. \tag{218}$$

$$+ \left. 2 \sum_{n=1}^{\infty} \frac{(-)^n \cos(n\pi z_0/l)}{\lambda_n^2 l^2 C_0(\lambda_n b, \lambda_n a)} \right\}$$

$$\equiv Y_0 \overline{V_0}$$

which completes the solution of the first part of the problem.

5.1.2 Current Due to End-Slot Excitation.

A suitable representation for the function ψ is

$$\psi = \psi_1 = j\omega\epsilon_0 B_0 \ln\frac{\rho}{a}\cos kz \tag{219}$$

$$+ \ 2j\omega\epsilon_0 \sum_{n=1}^{\infty} B_n \cos\left(\sqrt{k^2 - h_n^2}\ z\right) C_0(h_n\rho, h_na)$$

where the coefficients h_n are obtained from the roots of the equation

$$C_0(h_nb,\ h_na) = 0 \tag{220}$$

The form chosen for ψ_1 ensures that E_z vanishes at $\rho = a$ and $\rho = b$ and that E_ρ vanishes at $z = 0$.

The radial electric field E_ρ at $z = l$ is given by

$$E_\rho(z = l) = \frac{V_1}{\rho\ln(c/a)} \quad (a \leq \rho \leq c) \tag{221}$$

where $c < b$. V_1 is the voltage across the coaxial line leaving the cavity. Imposing the boundary condition (221) leads to the relation

$$- \ \frac{kB_0}{\rho}\sin kl - 2\sum_{n=1}^{\infty} B_n\sqrt{k^2 - h_n^2}\sin\left(\sqrt{k^2 - h_n^2}\ l\right) \cdot \tag{222}$$

$$h_n C_0'(h_n\rho, h_na) = \frac{V_1}{\rho\ln(c/a)} \quad (a \leq \rho \leq c)$$

wherein

$$C_0'(x, y) = J_0'(x)N_0(y) - J_0(y)N_0'(x) \tag{223}$$

$$= \ J_0(y)N_1(x) - J_1(x)N_0(y)$$

$$\equiv \ -C_1(x, y)$$

Integrating (222) with respect to ρ from $\rho = a$ to $\rho = b$ and using (220) yields

$$B_0 = \frac{-V_1}{k\sin kl\ln(b/a)} \tag{224}$$

93

Then multiplying (222) through by $\rho C_0'(h_m\rho,\ h_m a)$ and integrating with respect to ρ, we obtain

$$B_m = \frac{-V_1 C_0(h_m c,\ h_m a)}{2\sqrt{k^2 - h_m^2}\ \sin\left(\sqrt{k^2 - h_m^2}\, l\right) \ln(c/a) N_m} \tag{225}$$

with

$$N_m = \int_{h_m a}^{h_m b} u \left[C_0'(u,\ h_m a)\right]^2 du \tag{226}$$

$$= \frac{h_m^2 b^2}{2} C_1^2(h_m b,\ h_m a) - \frac{2}{\pi^2}$$

Now the current I_1 on the center conductor at $z = l$ is given by

$$I_1 = 4j\omega\epsilon_0 l V_1 \left\{ \frac{\pi \cot kl}{2kl \ln(b/a)} \right. \tag{227}$$

$$\left. - 2 \sum_{n=1}^{\infty} \frac{\cot\left(\sqrt{k^2 - h_n^2}\ l\right) C_0(h_n c,\ h_n a)}{2\sqrt{k^2 - h_n^2}\ l N_n \ln(c/a)} \right\}$$

$$\equiv Y_1 V_1$$

We shall assume that both c and a are small and make use of the fact that in this limit

$$C_0(h_n c,\ h_n a) \cong -\frac{2}{\pi} \ln \frac{c}{a} \tag{228}$$

Thus

$$Y_1 \cong 2\pi j\omega\epsilon_0 l \left\{ \frac{\cot kl}{kl \ln(b/a)} \right. \tag{229}$$

$$\left. + \sum_{n=1}^{\infty} \frac{\cot\left(\sqrt{k^2 - h_n^2}\ l\right)}{\left(\sqrt{k^2 - h_n^2}\ l\right) \left[\left(\pi h_n b/2\right)^2 C_1^2(h_n b,\ h_n a) - 1\right]} \right\}$$

5.1.3 Exterior to Coaxial Line Coupling.

The total current on the center conductor at the feed point of the coaxial cable is just $I_0 + I_1$. The two current components are now related by imposing the condition that the coaxial cable leaving the cavity presents an impedance Z_i at the point $z = l$. Thus, with $Y_i = 1/Z_i$, we have

$$I_0 + I_1 = Y_i V_1 \qquad (230)$$

Using (218) and (227) and solving for V_1, we obtain

$$V_1 = Y_0(Y_i - Y_1)^{-1} \overline{V_0} \qquad (231)$$

which is the desired relation between the "external" excitation represented by $\overline{V_0}$ and the "internal" excitation V_1.

We may also construct an equivalent circuit representing the source at the feed point of the coaxial cable. The open-circuit voltage at the feed point is

$$V_{oc} = -Y_0\overline{V_0}/Y_1 \qquad (232)$$

and the short-circuit current is

$$I_{sc} = I_0 = Y_0\overline{V_0} \qquad (233)$$

Thus the equivalent circuit takes either of the forms shown in Figure 76. Such equivalent circuits can be used to determine the voltages and currents induced in an arbitrary load.

5.2 REPRESENTATIVE NUMERICAL RESULTS.

We present numerical results for the transfer functions relating the current or voltage induced in a 50 Ω load to the average slot voltage $\overline{V_0}$ and to an incident electric field.

(a) Thévenin   (b) Norton
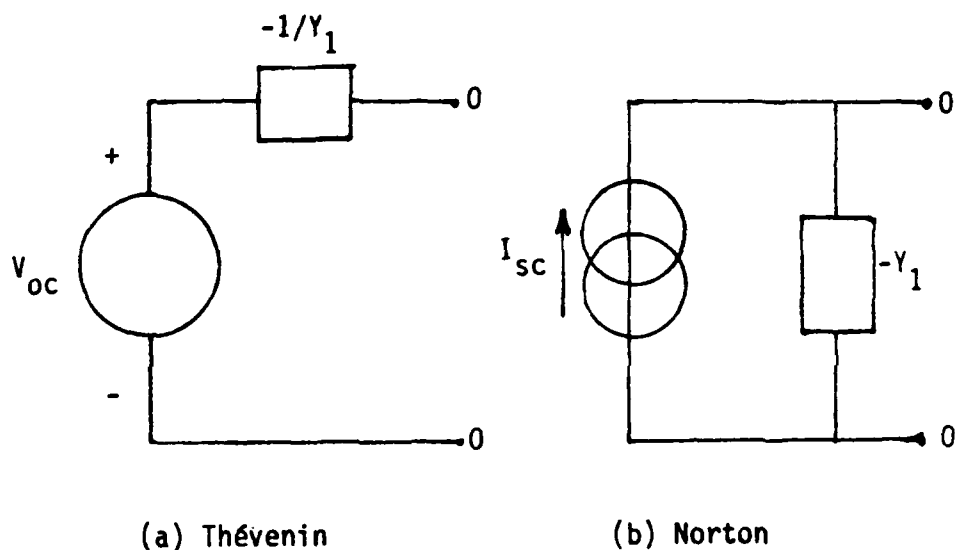
Figure 76.   Equivalent circuits for the feed point of the coaxial line.

The current in a resistive load R_L connected across the terminals of either of the equivalent circuits shown in Figure 76 is easily shown to be

$$I_L = \frac{\overline{V_0}Y_0}{R_L Y_1 - 1} \tag{234}$$

We define a transfer admittance Y_T as

$$Y_T = \frac{I_L}{\overline{V_0}} = \frac{Y_0}{R_L Y_1 - 1} \tag{235}$$

We have calculated Y_T as a function of frequency for the "baseline" configuration:

$$R_L = 50\ \Omega \qquad \text{(load resistance)}$$
$$l\ \ = 40\ \text{cm} \qquad \text{(cylinder length)}$$
$$z_0 = 20\ \text{cm} \qquad \text{(aperture position)}$$
$$b\ \ = 10\ \text{cm} \qquad \text{(cylinder radius)}$$
$$a\ \ = 0.5\ \text{mm} \qquad \text{(wire radius)}$$

as well as excursions from this baseline, over the frequency range 0-6 GHz. Plots of the magnitude of Y_T are shown in Figures 77 to 84.

96
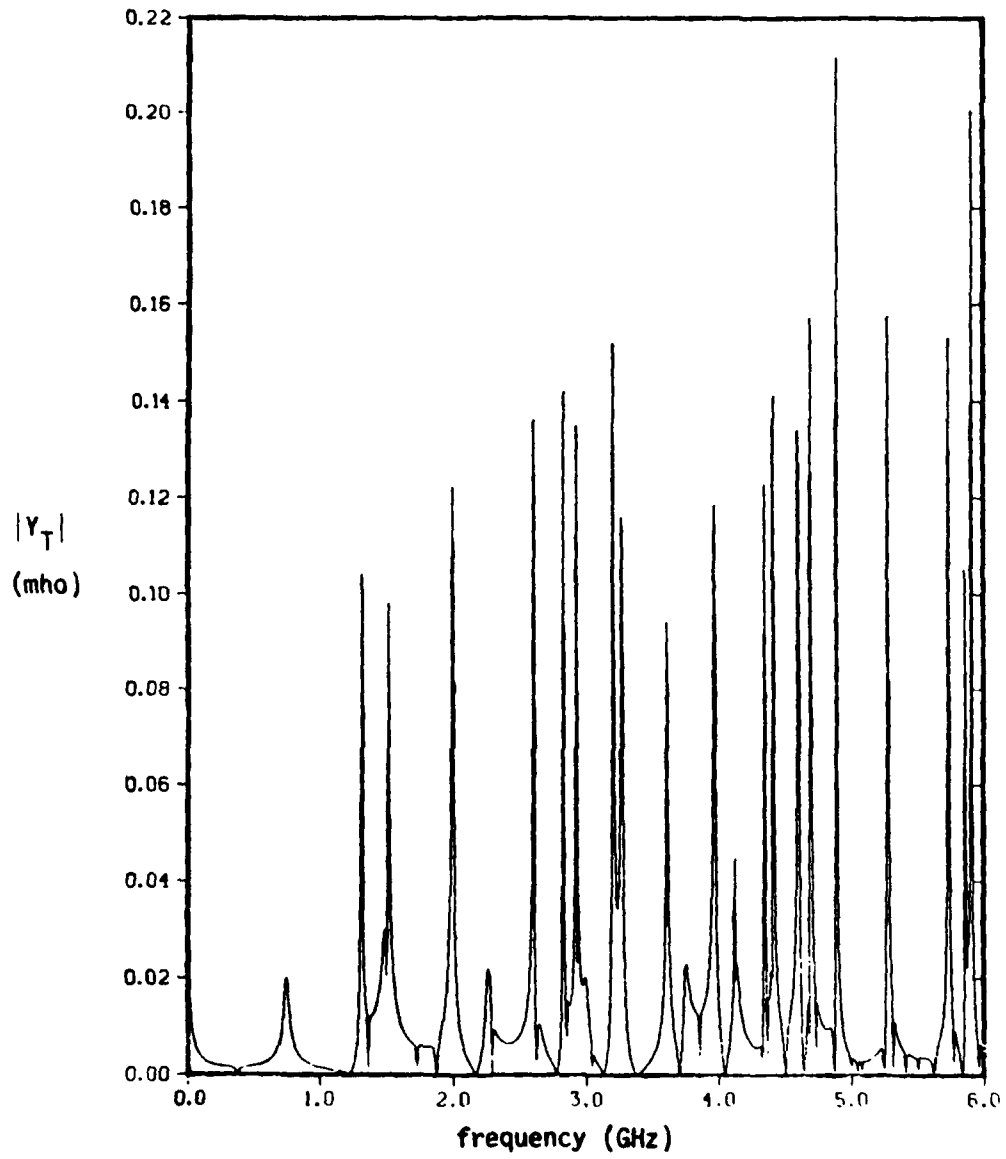
Figure 77.   Magnitude of Y_T vs. frequency for baseline configuration: $l = 40$ cm, $b = 10$ cm, $z_0 = 20$ cm, $a = 0.5$ mm, $R_L = 50$ Ω; $0 \leq f \leq 6$ GHz.
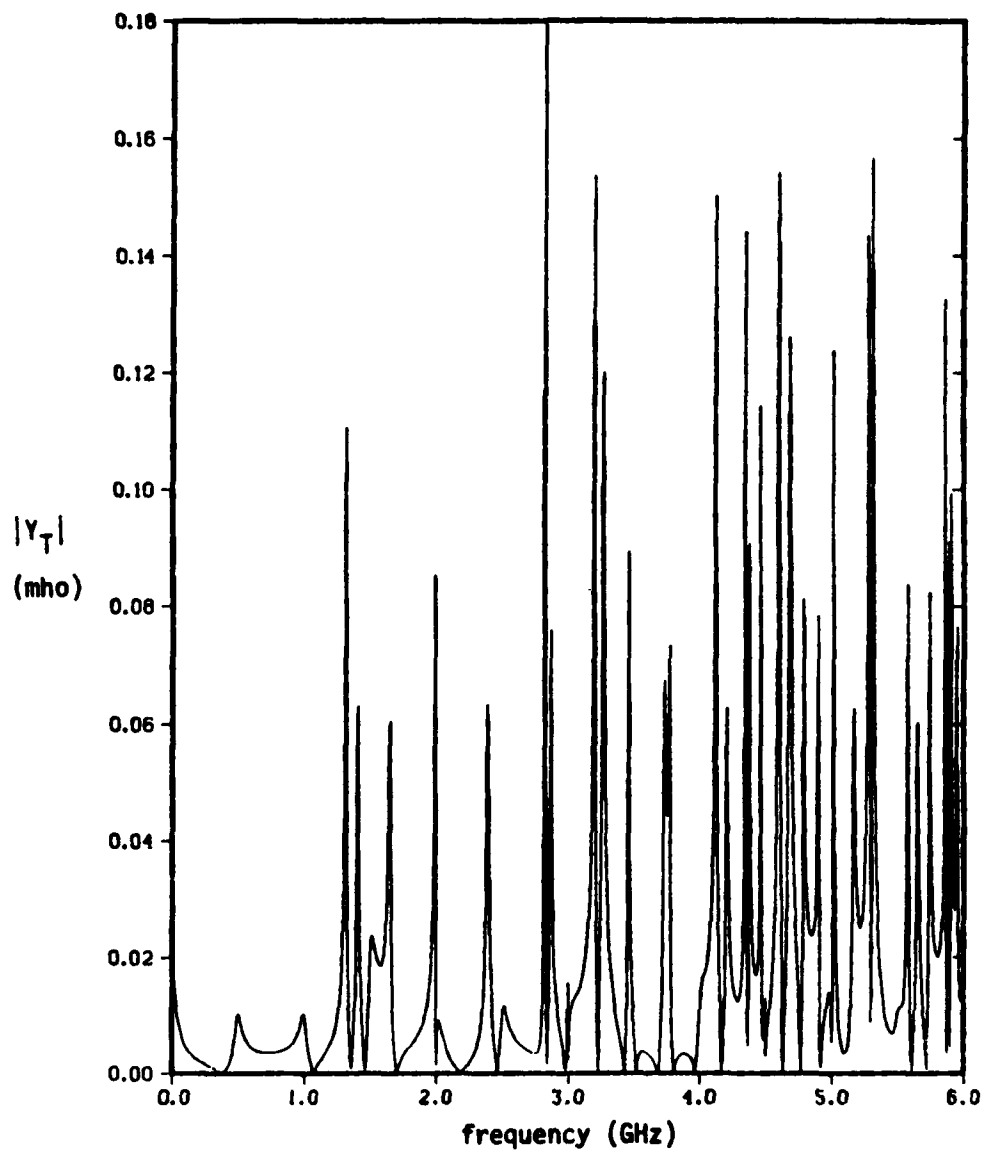
Figure 78.   Magnitude of Y_T vs. frequency for altered configuration: $l = 30$ cm, $b = 10$ cm, $z_0 = 20$ cm, $a = 0.5$ mm, $R_L = 50 \ \Omega$; $0 \leq f \leq 6$ GHz.
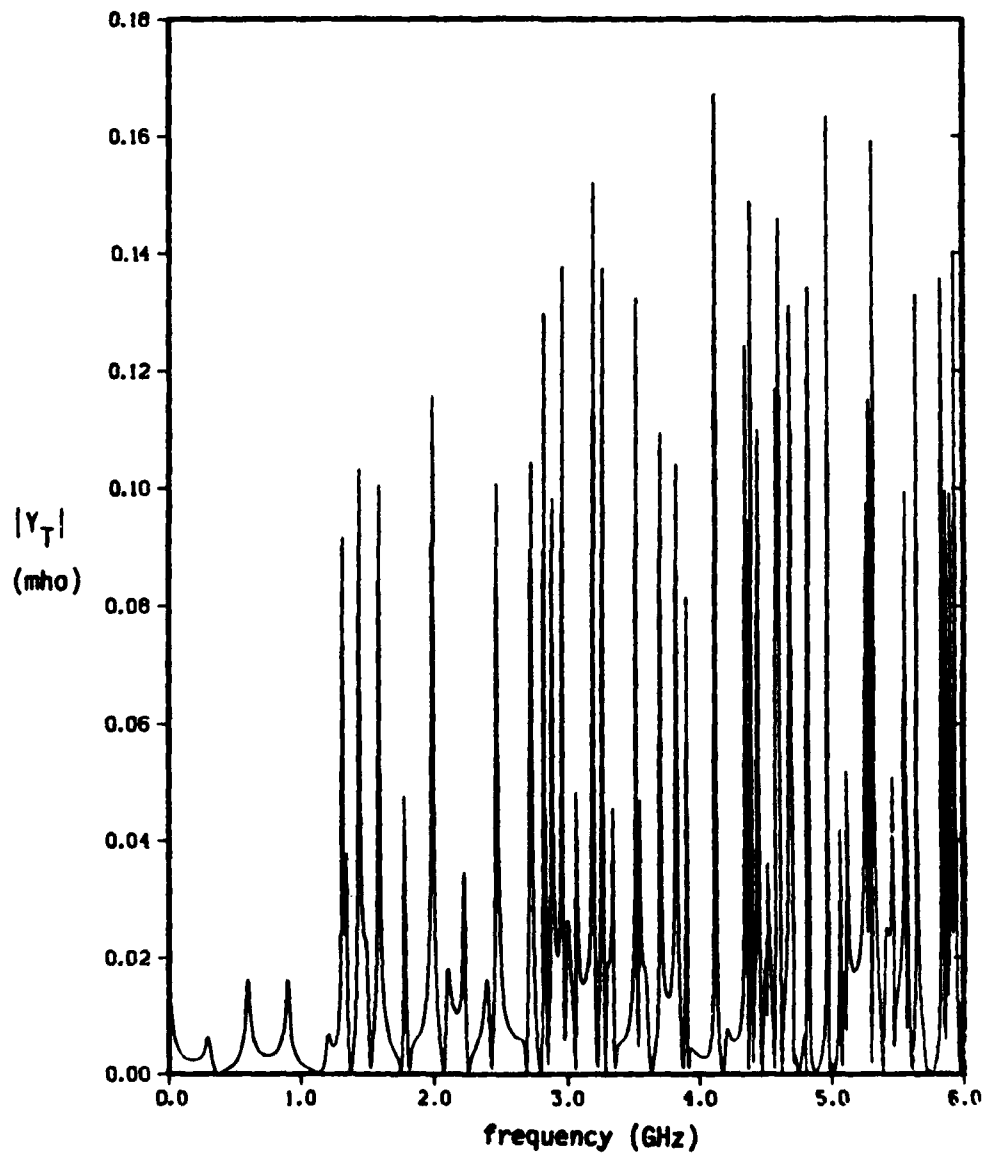
Figure 79. Magnitude of Y_T vs. frequency for altered configuration: $l =$ 50 cm, $b = 10$ cm, $z_0 = 20$ cm, $a = 0.5$ mm, $R_L = 50$ Ω; $0 \leq f \leq 6$ GHz.

99
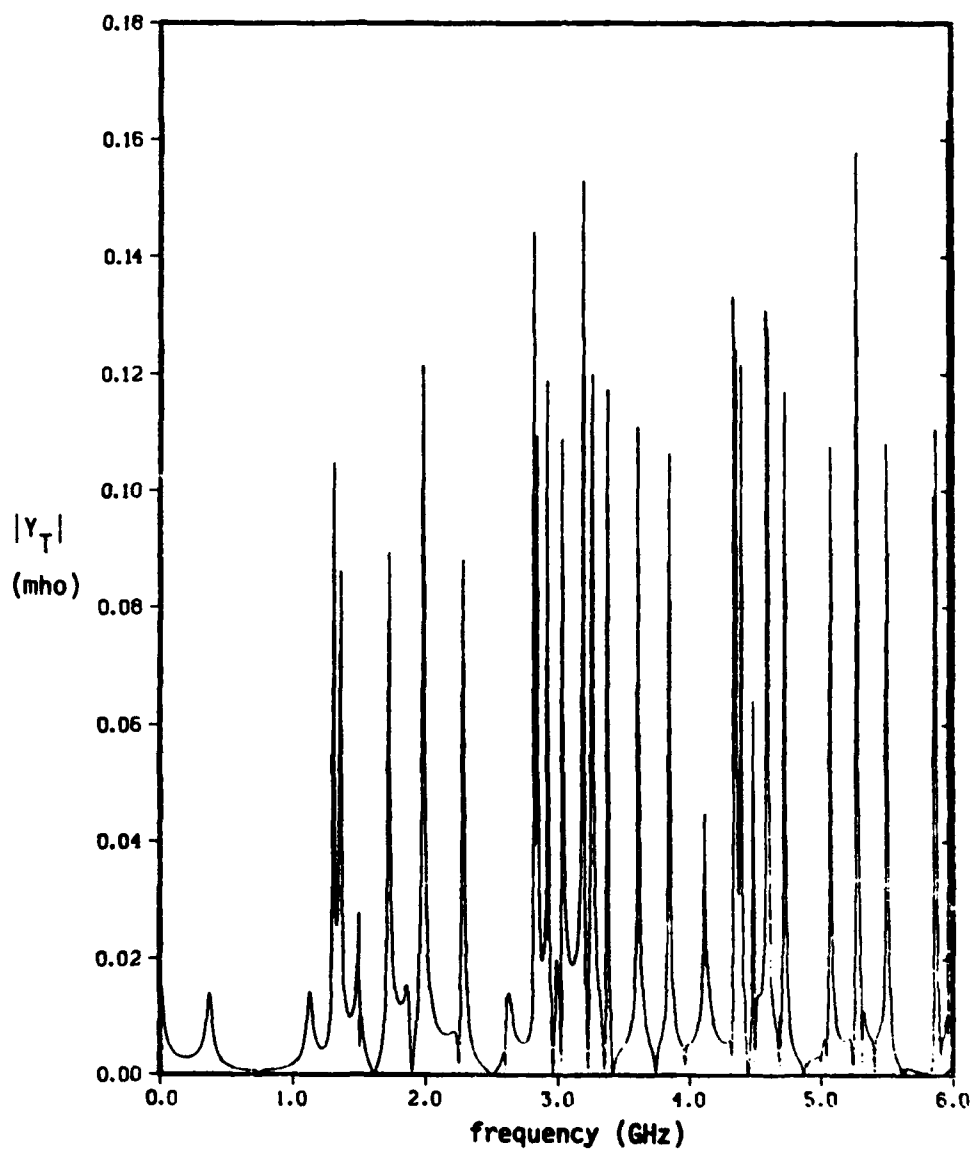
Figure 80. Magnitude of Y_T vs. frequency for altered configuration: $l = 40$ cm, $b = 10$ cm, $z_0 = 10$ cm, $a = 0.5$ mm, $R_L = 50$ Ω; $0 \le f \le$ ¡ GHz.

100
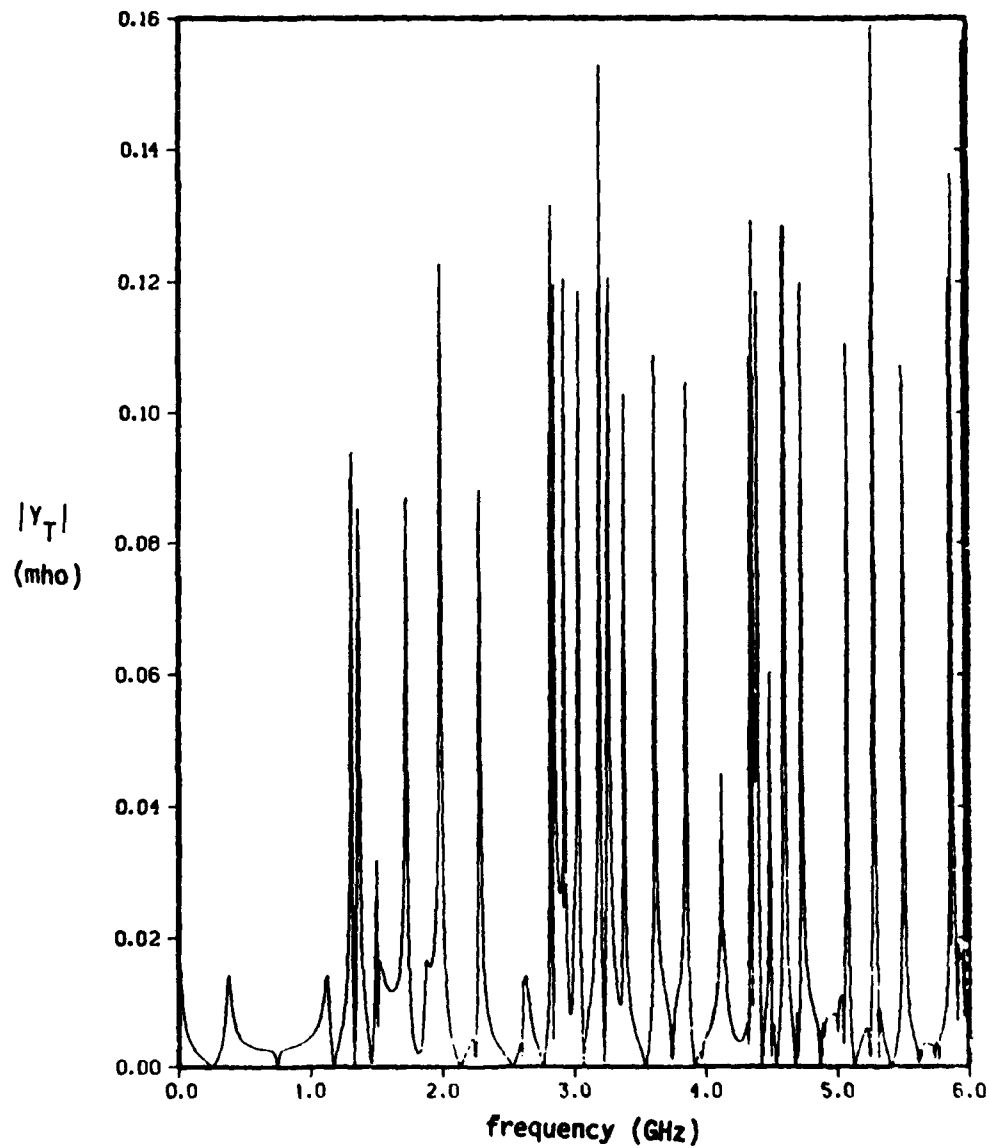
Figure 81.   Magnitude of Y_T vs. frequency for altered configuration: $l = 40$ cm, $b = 10$ cm, $z_0 = 30$ cm, $a = 0.5$ mm, $R_L = 50\ \Omega$; $0 \leq f \leq 6$ GHz.
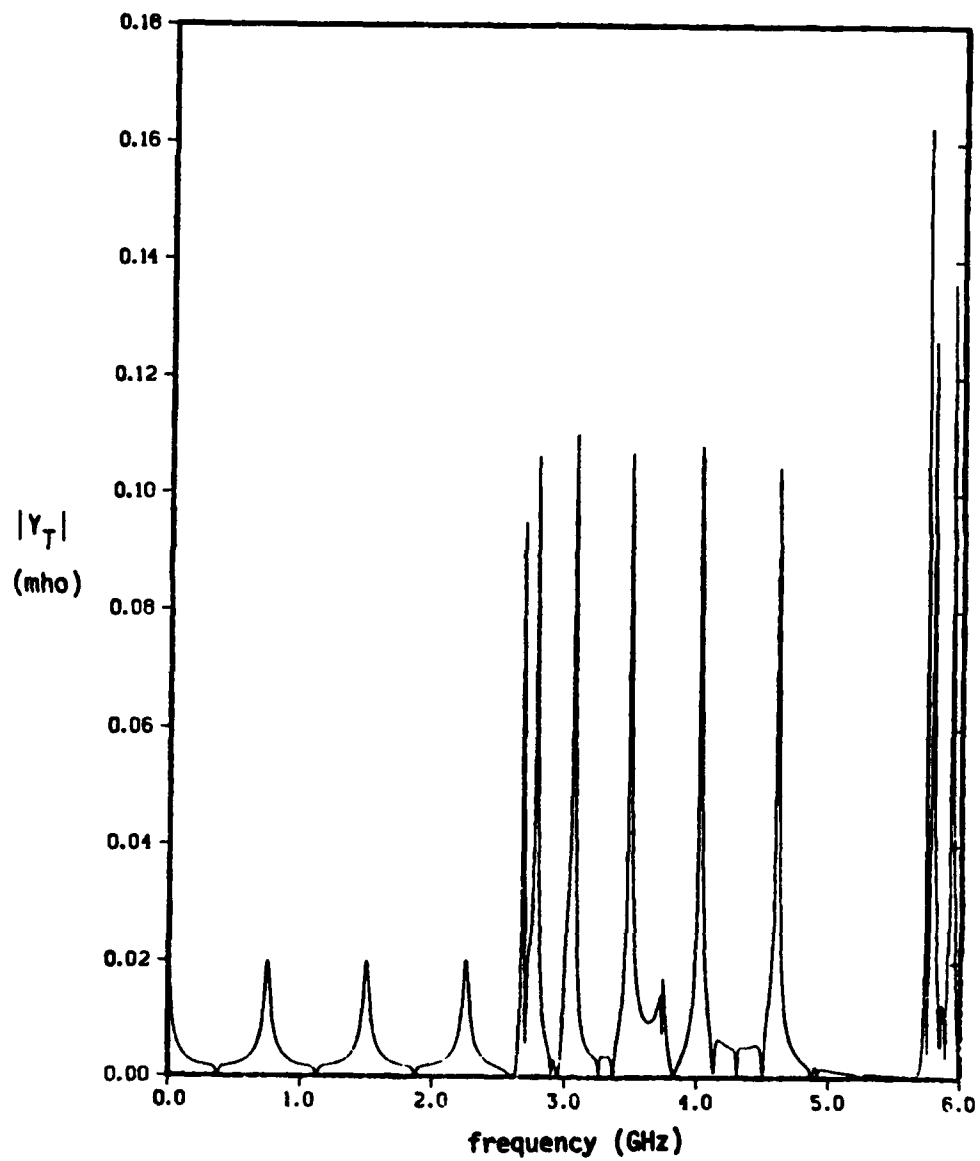
Figure 82.   Magnitude of Y_T vs. frequency for altered configuration:
$l = 40$ cm, $b = 5$ cm, $z_0 = 20$ cm, $a = 0.5$ mm, $R_L = 50$ Ω;
$0 \leq f \leq 6$ GHz.

102
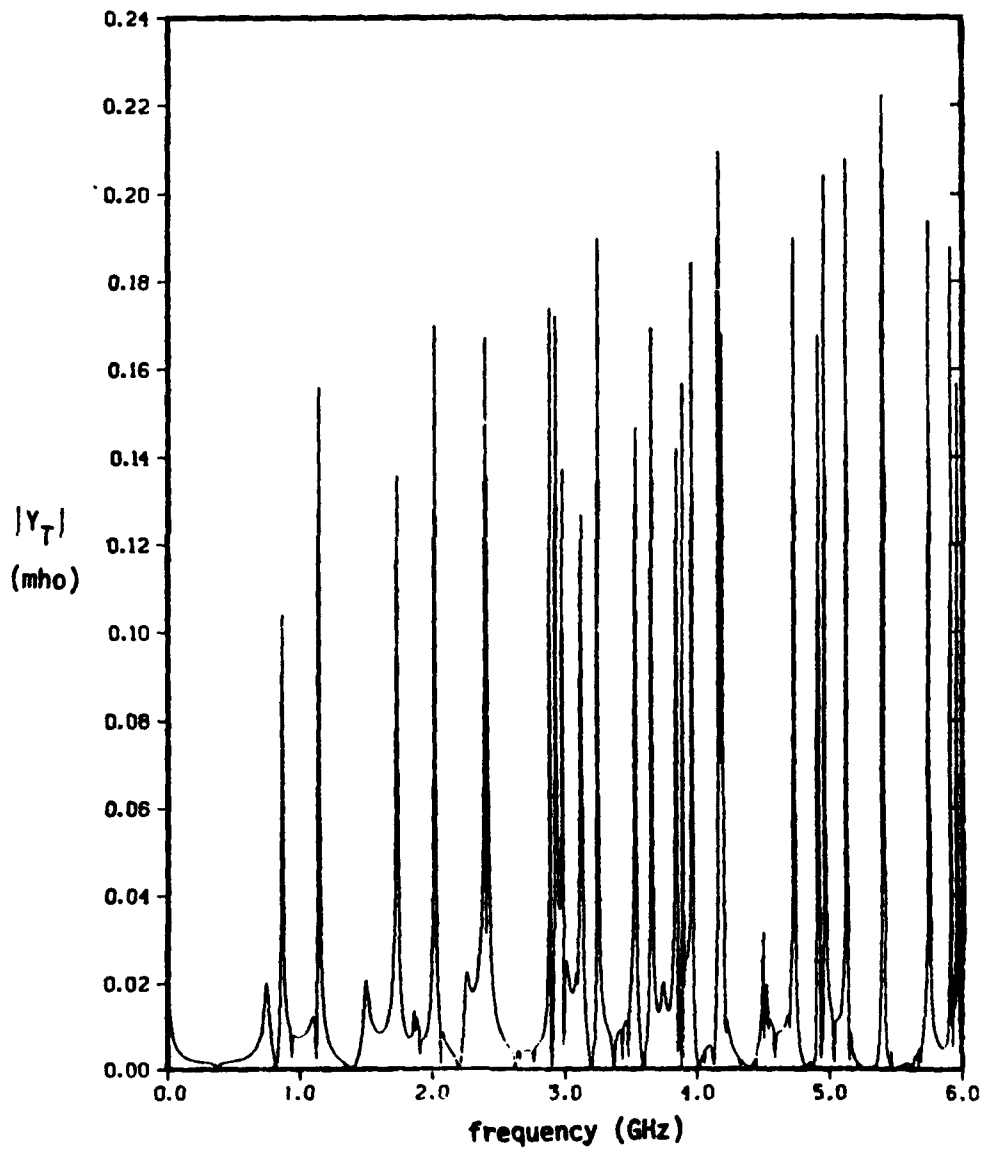
Figure 83. Magnitude of Y_T vs. frequency for altered configuration: $l = 40$ cm, $b = 15$ cm, $z_0 = 20$ cm, $a = 0.5$ mm, $R_L = 50$ Ω; $0 \leq f \leq 6$ GHz.
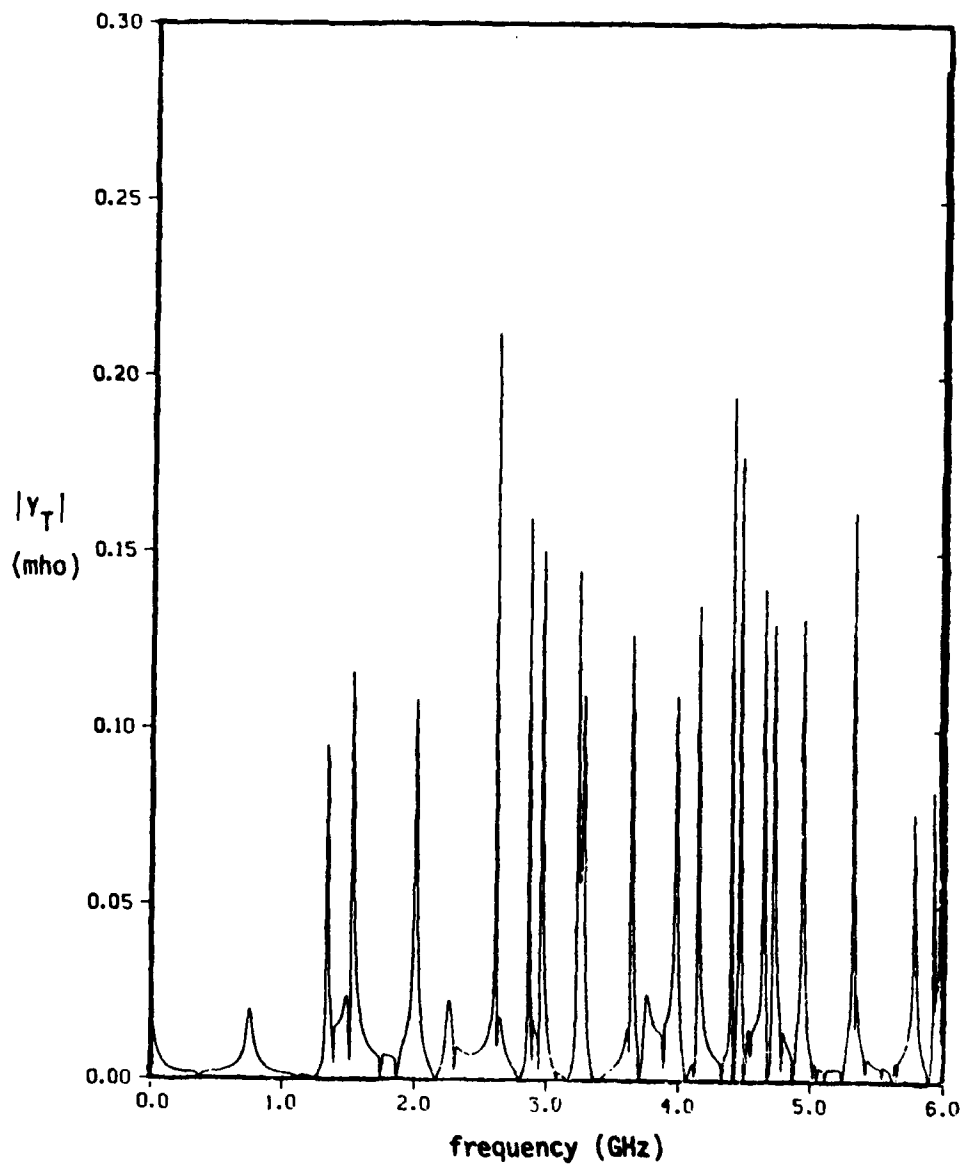
Figure 84. Magnitude of Y_T vs. frequency for altered configuration:
$l = 40$ cm, $b = 10$ cm, $z_0 = 20$ cm, $a = 1$ mm, $R_L = 50$ Ω;
$0 \leq f \leq 6$ GHz.

The highly resonant character of the configuration is evident in each of these plots. The TEM mode resonances are seen at the lowest frequencies and are especially clear in Figure 82, where the cavity radius was chosen to be 5 cm. The higher-order mode resonances generally cause $|Y_T|$ to peak at higher values than the TEM mode resonances and the Q of the higher-order modes is also higher. The peak values of $|Y_T|$ in every case are a few tenths of a mho. For a load impedance of 50 Ω, therefore, the load voltage at the resonant peaks is of the order of 5 to 10 times $\overline{V_0}$, the average slot voltage. Away from the resonances, the load voltage is of the order of the average slot voltage or less.

It is of greater practical interest to consider the exterior-to-interior coupling problem in its entirety. To do so, we need to the average slot voltage $\overline{V_0}$ in terms of the field incident upon the cylinder from the outside. We may use the results of Section 2 to show that the voltage across a slot of width w in an infinitely extended conducting plane illuminated by a normally incident plane electromagnetic wave whose electric vector is directed across the slot is given by

$$V(z') = \frac{2\pi j E_i \hat{l}}{\Omega D(k\hat{l})} \left(\sin k\hat{l} - 2\sin \frac{k\hat{l}}{2} \cos kz' \right) \quad \left(| z' | \le \hat{l}/2 \right) \tag{236}$$

wherein $\hat{l}$ denotes the slot length, z' is a coordinate along the long dimension of the slot, Ω is the antenna parameter

$$\Omega = 2\ln\left(\frac{4\hat{l}}{w}\right) \tag{237}$$

and

$$\frac{1}{D(k\hat{l})} = \frac{1}{(k\hat{l})^2} + \frac{1}{6} + \sum_{n=-\infty}^{\infty}{}' \frac{(-)^n}{n\pi} \left[\frac{1}{k\hat{l} - n\pi - j\alpha_n} + \frac{1}{n\pi + j\alpha_n} \right] {}^1 \tag{238}$$

The damping constants α_n are given by

$$\alpha_n = \frac{1}{\Omega} \left[\gamma + \ln(2|n|\pi) - \mathrm{Ci}(2|n|\pi) \right] \tag{239}$$

wherein $\gamma = 0.57721\ldots$ (Euler's constant) and $\mathrm{Ci}(\cdot)$ denotes the cosine integral function [13].

---

[1]The prime on the summation sign indicates that the $n = 0$ term is to be omitted.

We shall use the expression (236) to describe the voltage across the slot in the cylindrical surface, assuming that the total angular extent of the slot $\Delta\phi$ is less, say, than one radian. The average slot voltage is easily shown to be

$$\overline{V_0} = \frac{jE_i\hat{l}^2}{b\Omega D(k\hat{l})}\left[\sin k\hat{l} - \frac{4}{k\hat{l}}\sin^2\frac{k\hat{l}}{2}\right] \tag{240}$$

We show in Figures 85 and 86 plots of the magnitude of the quantity

$$\frac{2\pi b}{E_i\hat{l}^2}\overline{V_0} = \frac{2\pi j}{\Omega D(k\hat{l})}\left(\sin k\hat{l} - \frac{4}{k\hat{l}}\sin^2\frac{k\hat{l}}{2}\right) \tag{241}$$

as a function of $k\hat{l}$ ($0 \le k\hat{l} \le 2\pi$) for $\Omega = 5$ and $\Omega = 10$.

The voltage V_L across a load resistance R_L driven by the equivalent sources in Figure 76 can be expressed in terms of $\overline{V_0}$ and the transfer admittance Y_T as

$$V_L = \overline{V_0}Y_T R_L \tag{242}$$

$$= \frac{jE_i\hat{l}^2}{b\Omega D(k\hat{l})}\left(\sin k\hat{l} - \frac{4}{k\hat{l}}\sin^2\frac{k\hat{l}}{2}\right)\frac{Y_0 R_L}{Y_1 R_L - 1}$$

We have calculated the transfer function $V_L/(E_i\hat{l})$ as a function of frequency for the baseline configuration and excursions described earlier in this section, under the assumption that the slot length $\hat{l} = 5$ cm. The fundamental slot resonance occurs at 3 GHz. Plots of the magnitude of this transfer function as a function of frequency are shown in Figures 87 – 94 for $\Omega = 5$ and 95 – 102 for $\Omega = 10$.

The broadly resonant character of the average slot voltage as a function of $k\hat{l}$ is evident in the curves shown in Figures 85 and 86. The peak value of the quantity plotted there is almost unaffected by the slot width w, but the sharpness of the resonance is increased slightly as w is decreased. The overall effect of the slot response on the normalized load voltage $V_L/(E_i\hat{l})$ is simply to "envelope" the many cavity resonances, as shown in Figures 87 – 102. The peak values of the magnitude of the load voltage are in every case less than $E_i\hat{l}$ and are typically only a few tenths of $E_i\hat{l}$. It is easy to show that the effective area of the slot penetration is thus of order $\hat{l}^2$ at a resonance of the interior cavity and considerably less away from resonance.
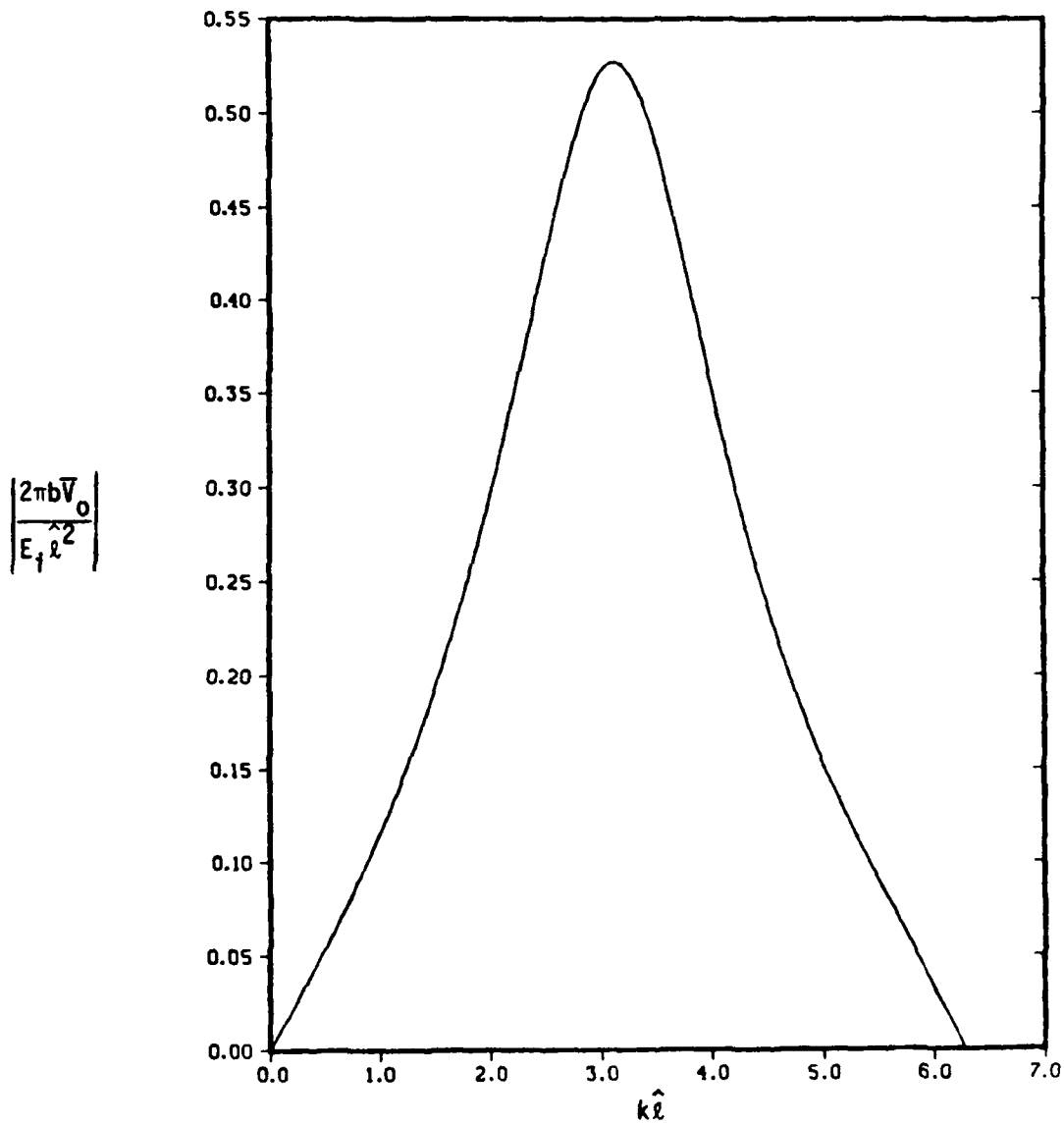
Figure 85. Normalized average slot voltage vs. $k\hat{l}$ for $\Omega = 5$.
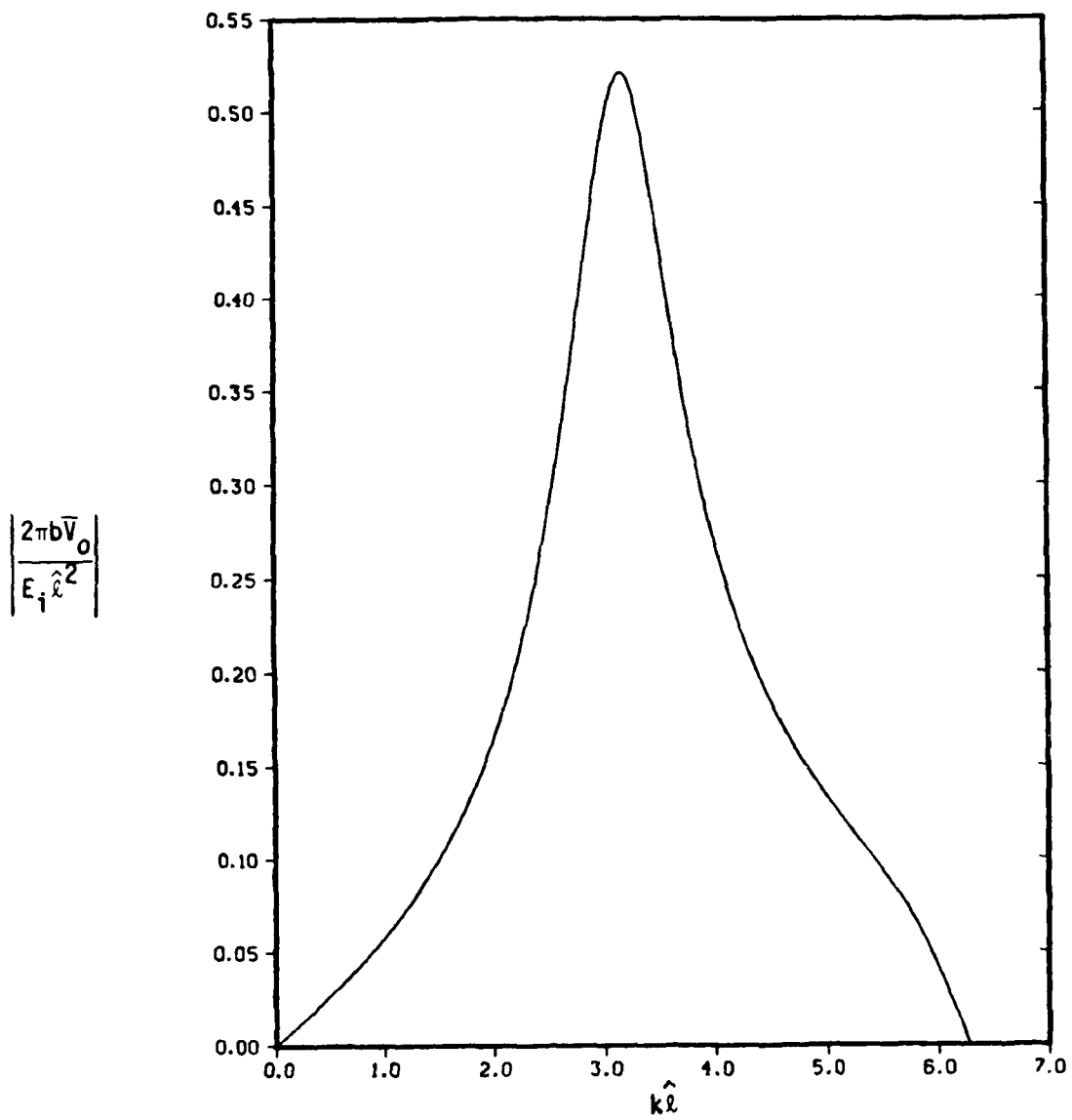
Figure 86.   Normalized average slot voltage vs. $k\hat{l}$ for $\Omega = 10$.

108
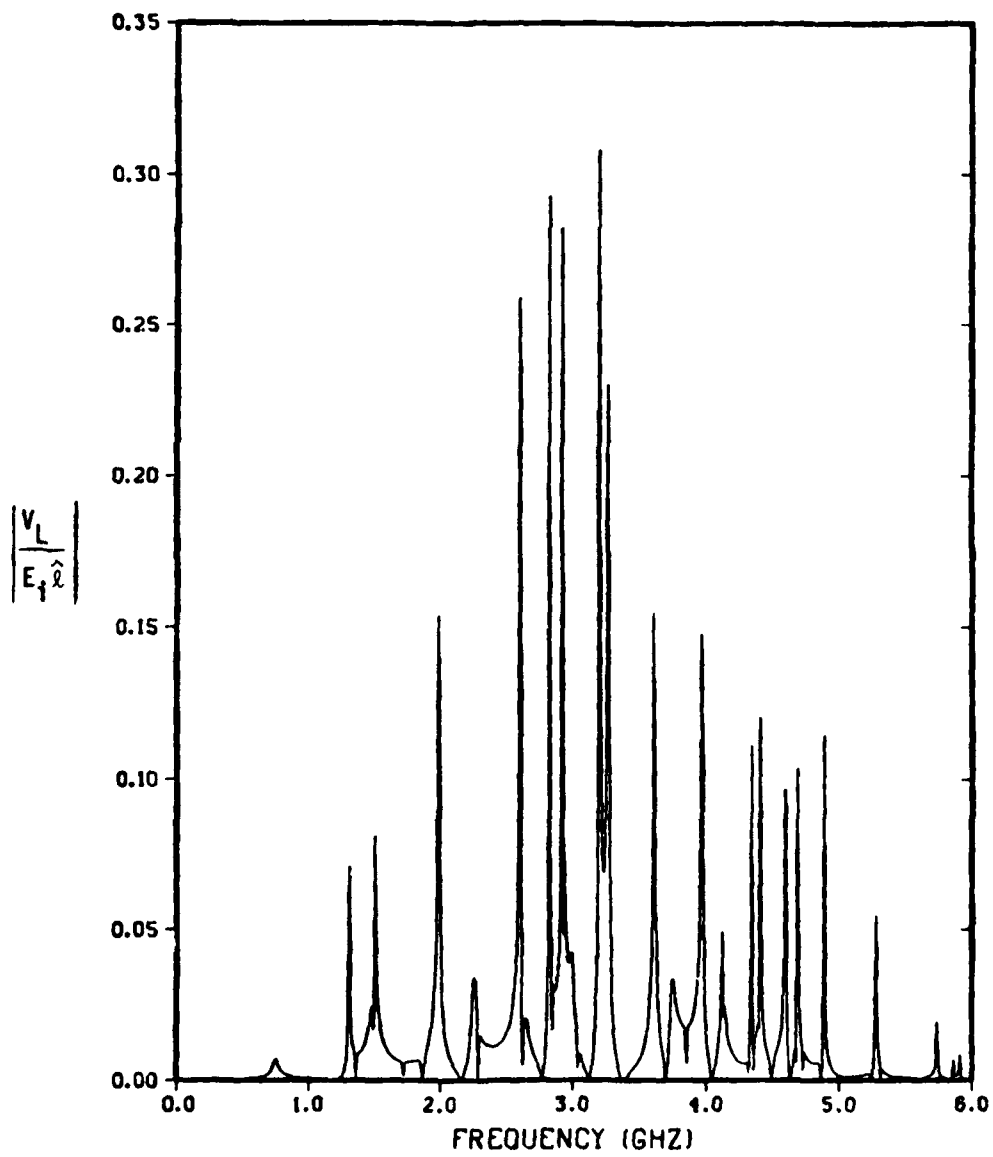
Figure 87.   Magnitude of $V_L/(E_i\hat{l})$ vs. frequency for baseline configuration:
$l = 40$ cm, $b = 10$ cm, $z_0 = 20$ cm, $a = 0.5$ mm, $R_L = 50$ Ω,
$\hat{l} = 5$ cm; $\Omega = 5$.
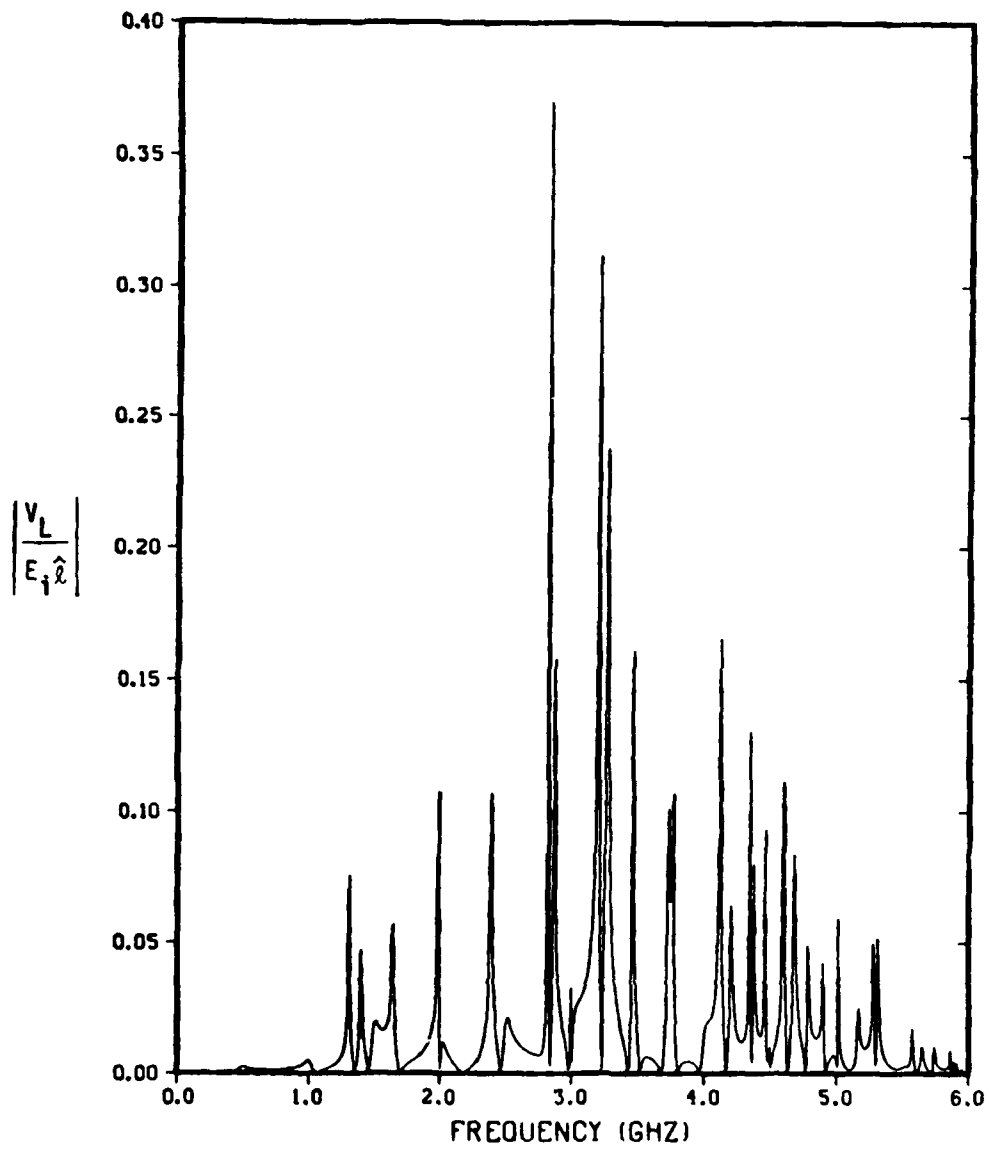
Figure 88. Magnitude of $V_L/(E_i\hat{l})$ vs. frequency for baseline configuration, except $l = 30$ cm; $\Omega = 5$.
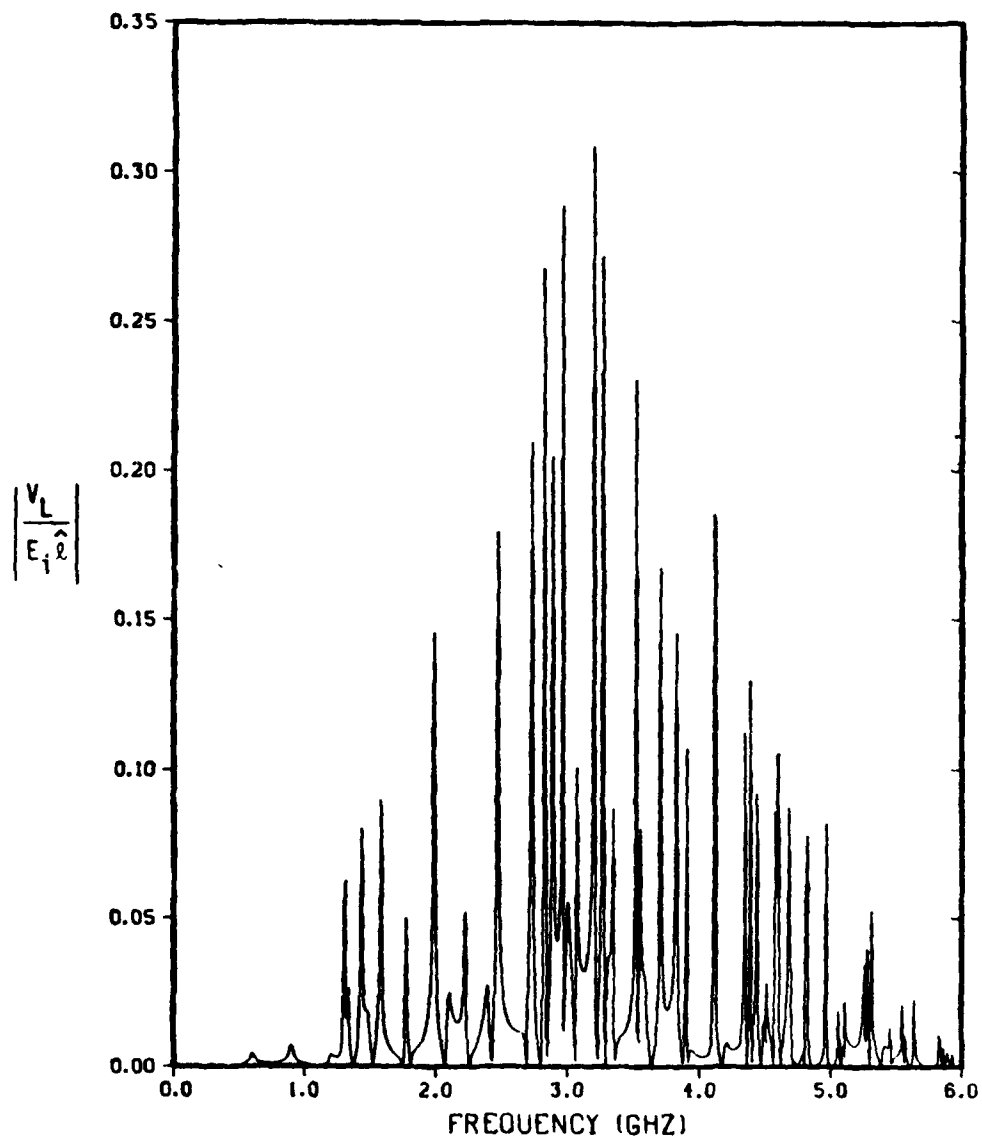
Figure 89.   Magnitude of $V_L/(E_i \hat{l})$ vs. frequency for baseline configuration, except $l = 50$ cm; $\Omega = 5$.
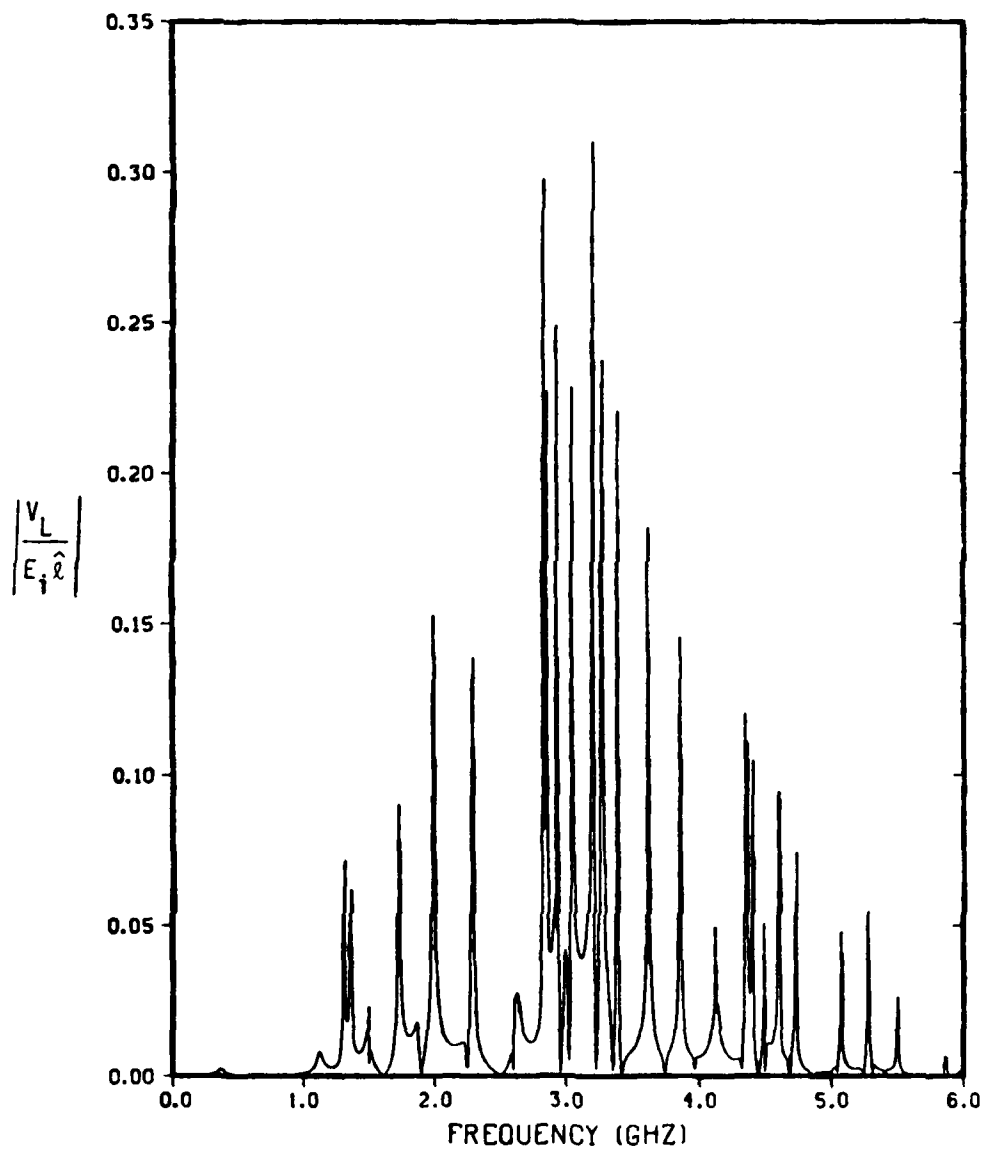
Figure 90.   Magnitude of $V_L/(E_i\hat{l})$ vs. frequency for baseline configuration, except $z_0 = 10$ cm; $\Omega = 5$.
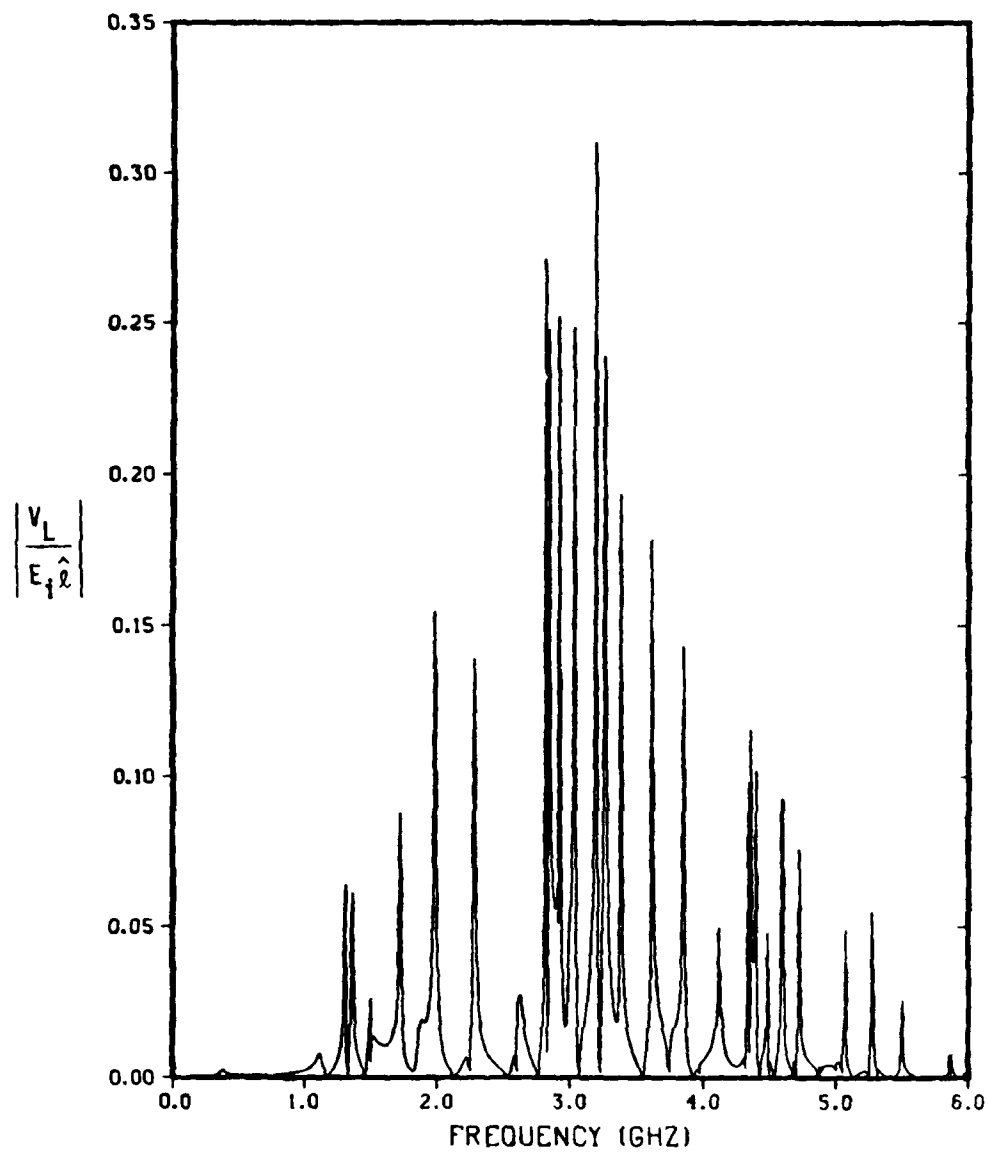
Figure 91. Magnitude of $V_L/(E_i\hat{l})$ vs. frequency for baseline configuration, except $z_0 = 30$ cm; $\Omega = 5$.
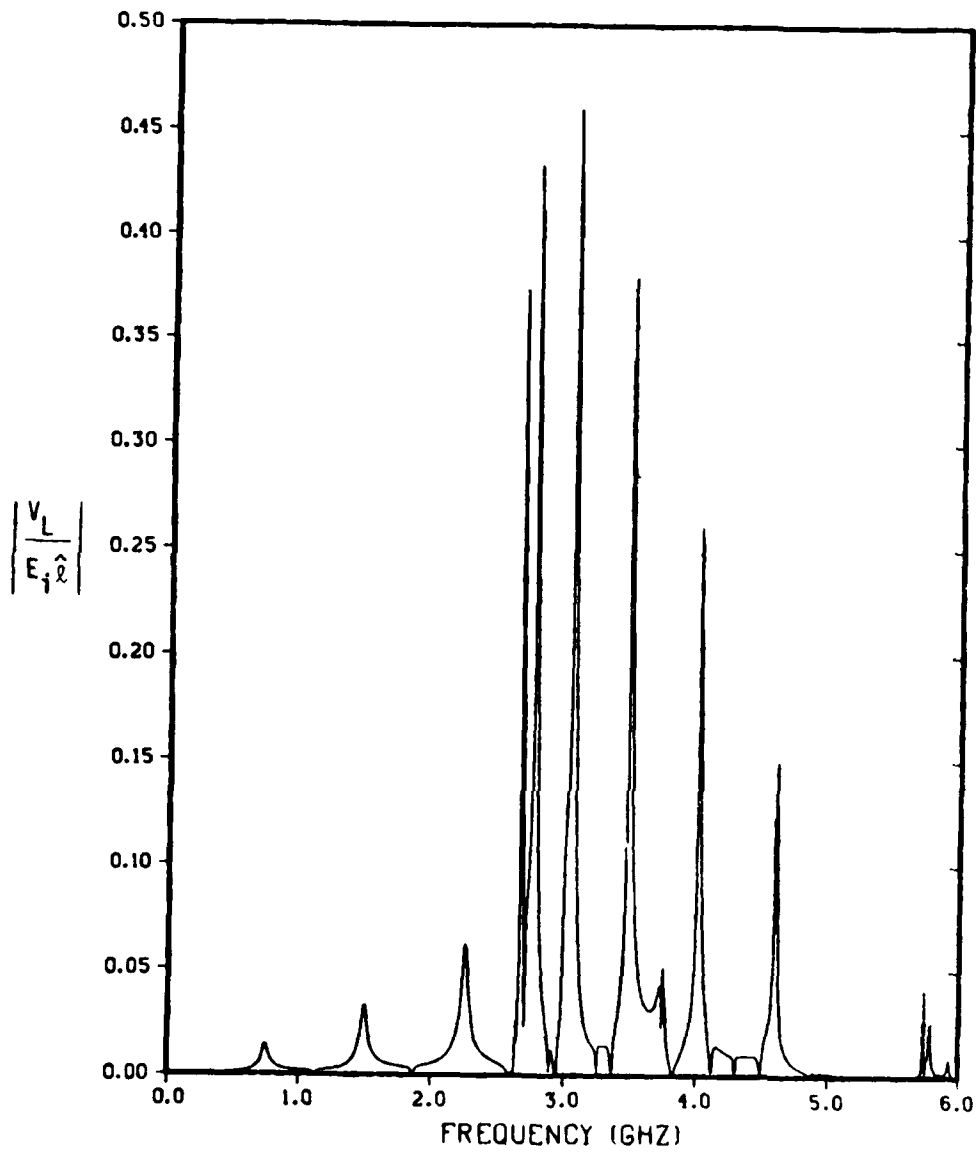
Figure 92. Magnitude of $V_L/(E_i\hat{l})$ vs. frequency for baseline configuration, except $b = 5$ cm; $\Omega = 5$.

114
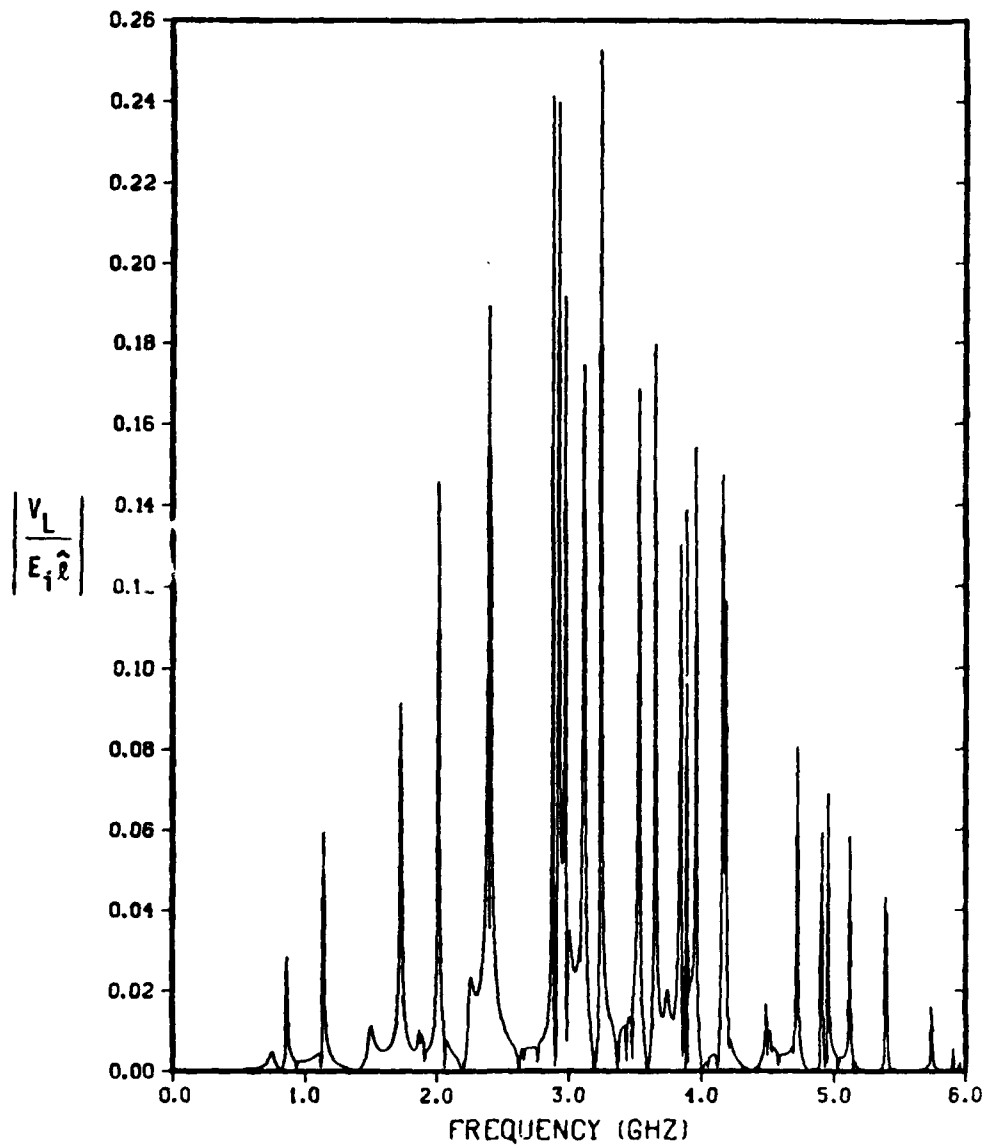
Figure 93. Magnitude of $V_L/(E_i\hat{l})$ vs. frequency for baseline configuration, except $b = 15$ cm; $\Omega = 5$.
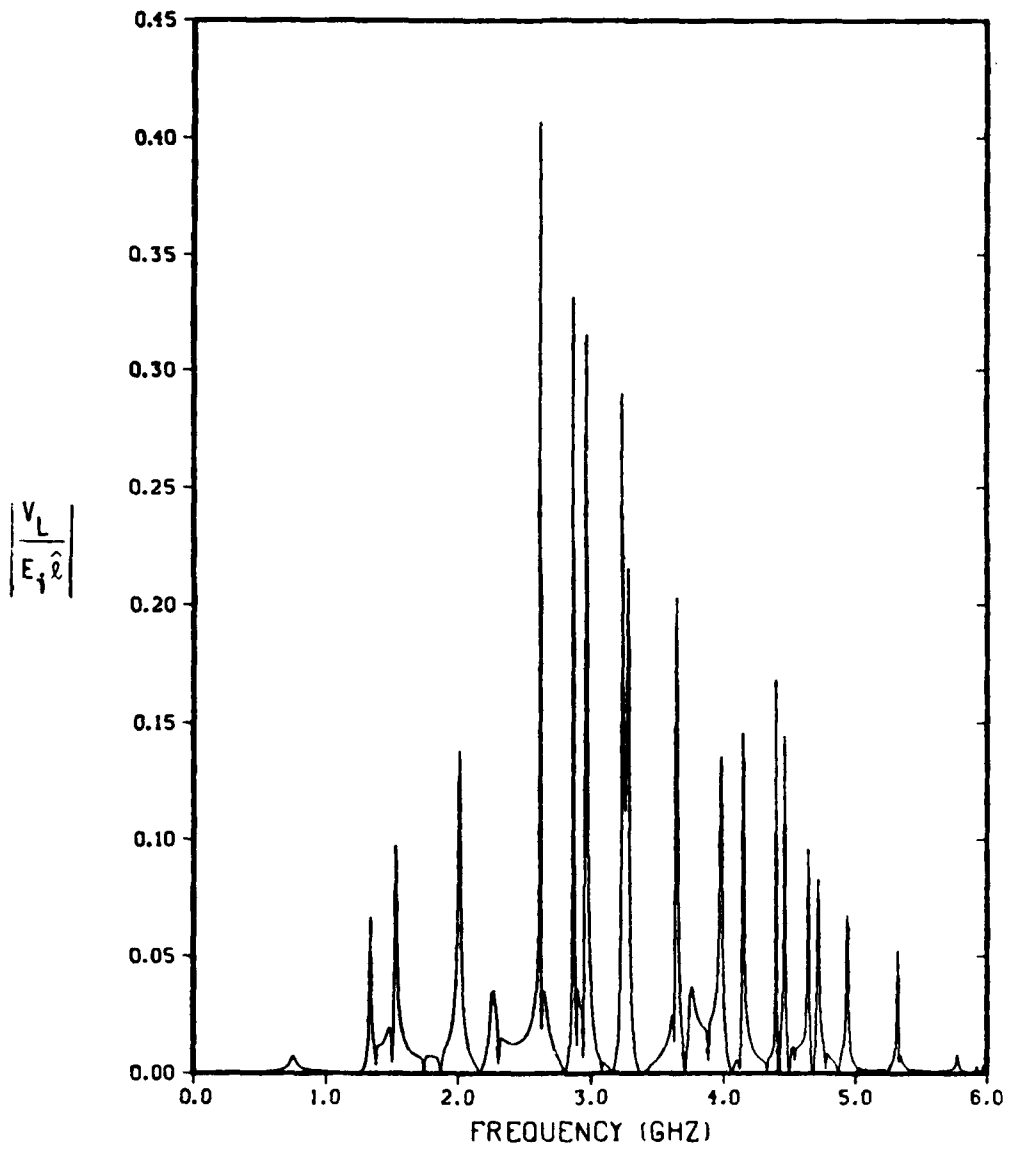
Figure 94. Magnitude of $V_L/(E_i \hat{l})$ vs. frequency for baseline configuration, except $a = 1$ mm; $\Omega = 5$.

116
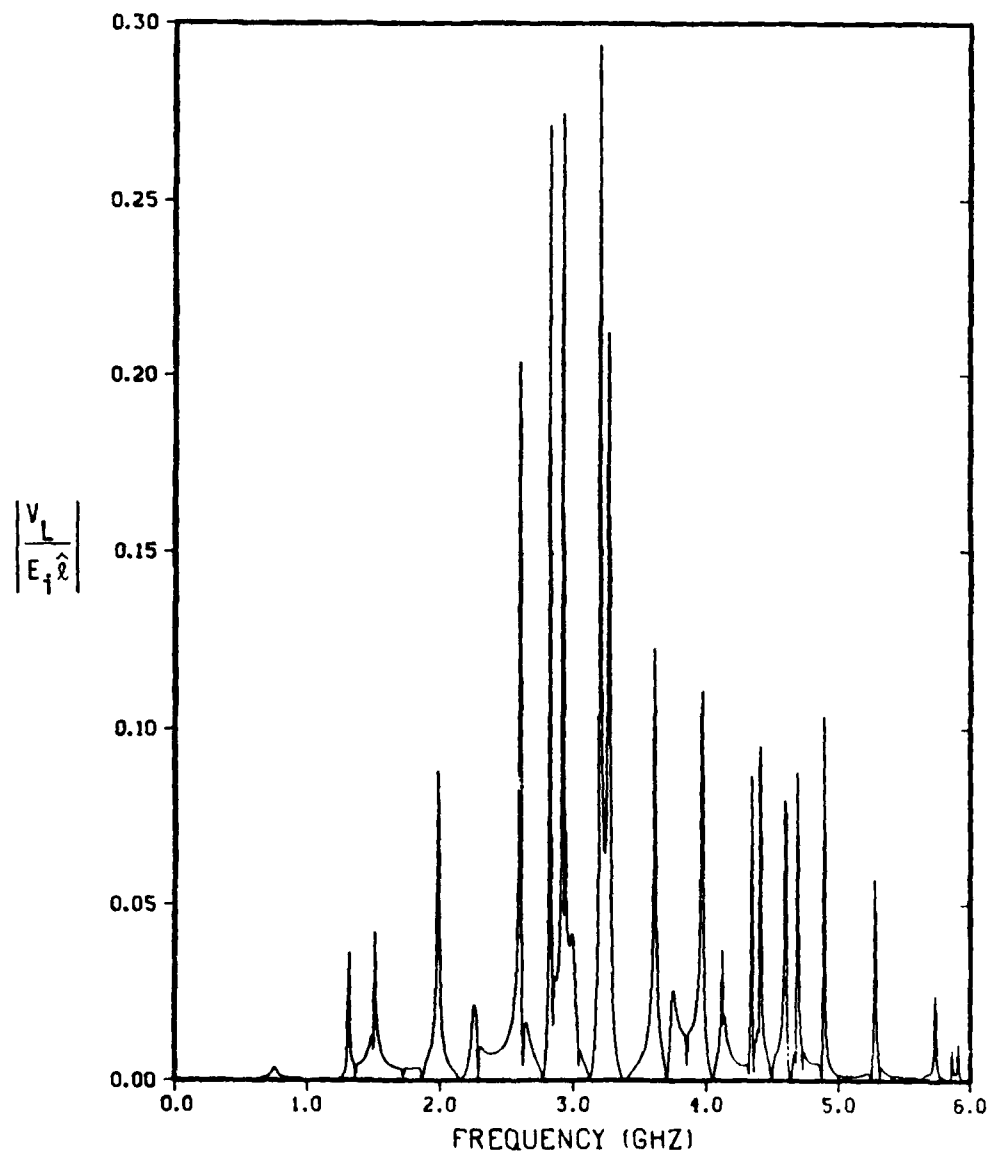
Figure 95.   Magnitude of $V_L/(E_i \hat{l})$ vs. frequency for baseline configuration: $l = 40$ cm, $b = 10$ cm, $z_0 = 20$ cm, $a = 0.5$ mm, $R_L = 50$ Ω, $\hat{l} = 5$ cm; $\Omega = 10$.

117
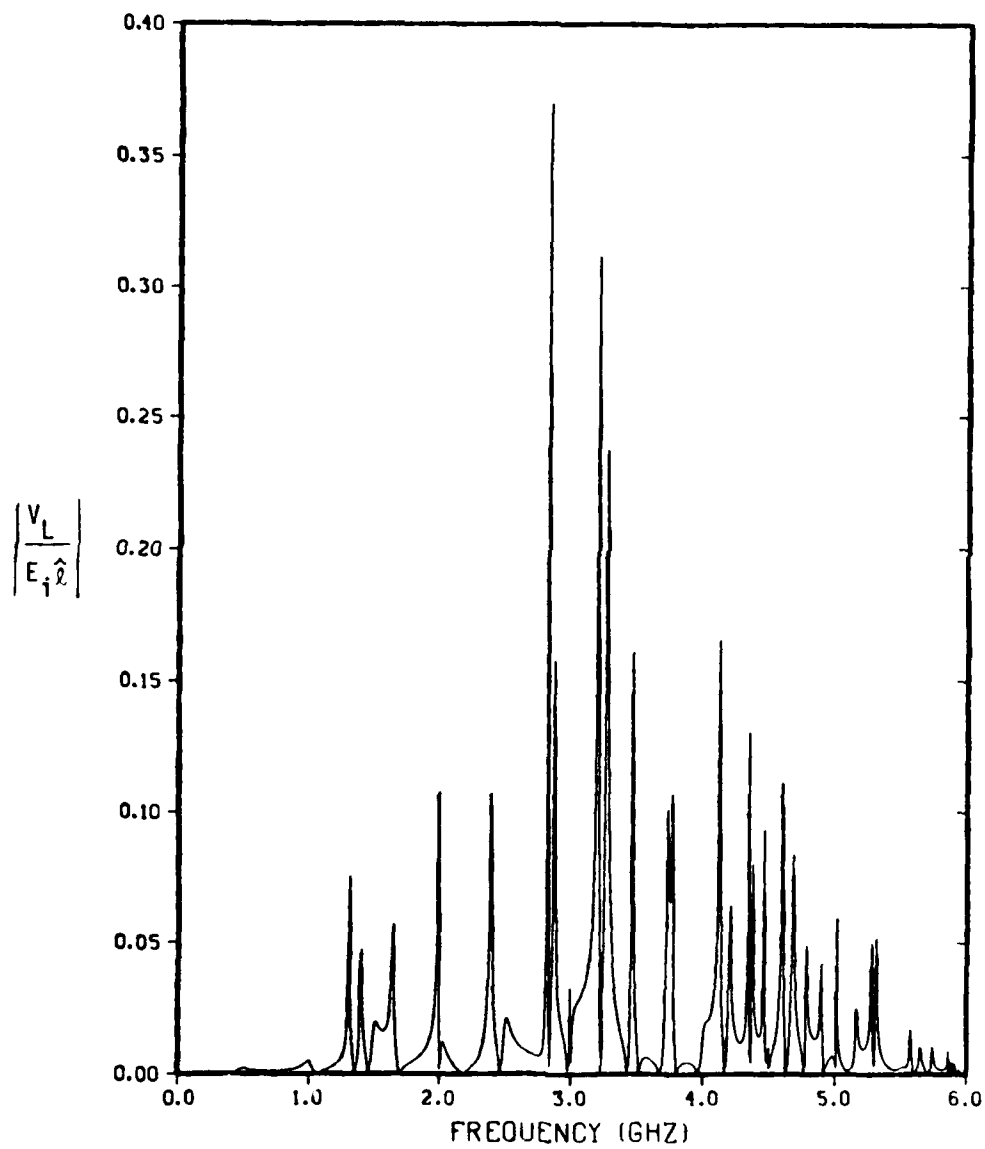
Figure 96. Magnitude of $V_L/(E_i\hat{l})$ vs. frequency for baseline configuration, except $l = 30$ cm; $\Omega = 10$.

118
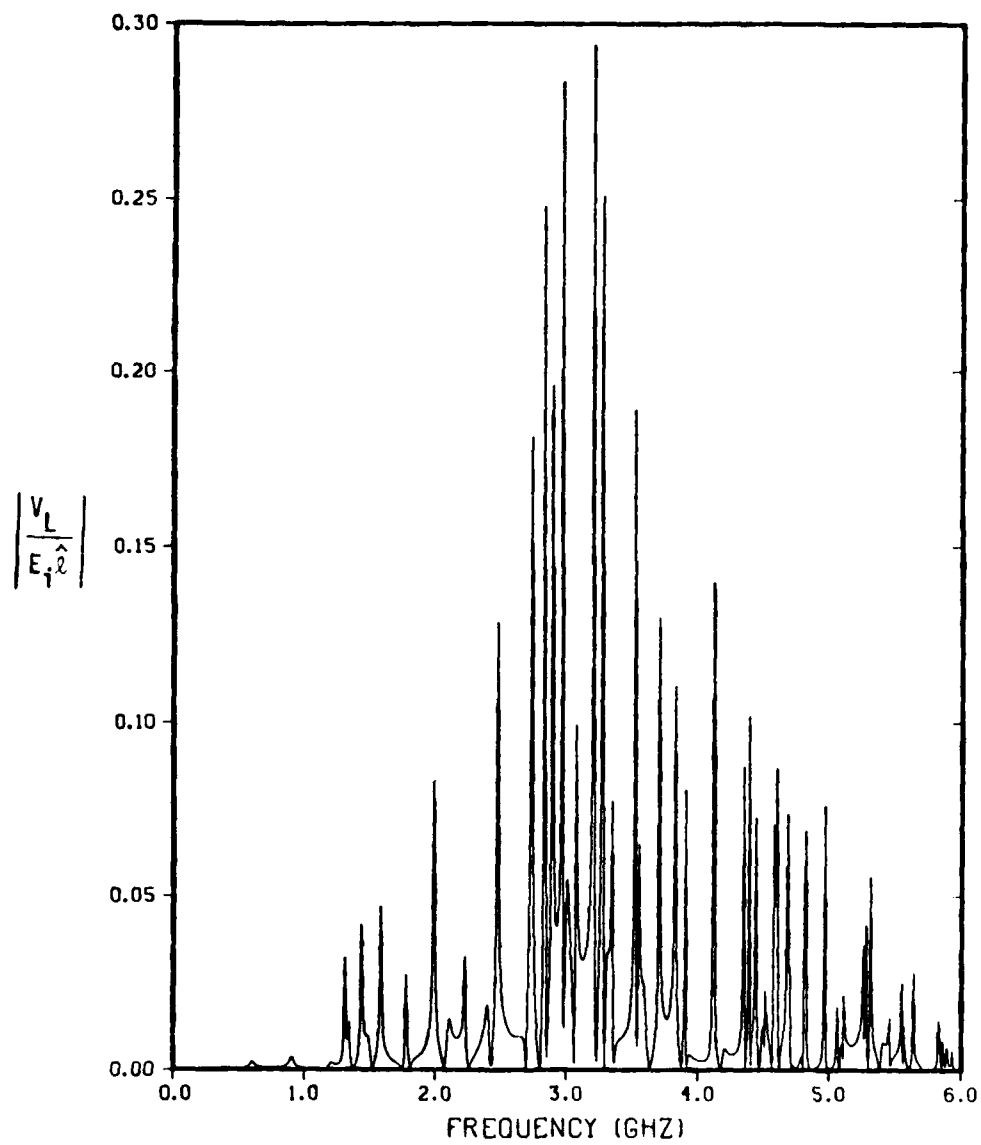
Figure 97.   Magnitude of $V_L/(E_i\hat{l})$ vs. frequency for baseline configuration, except $l = 50$ cm; $\Omega = 10$.
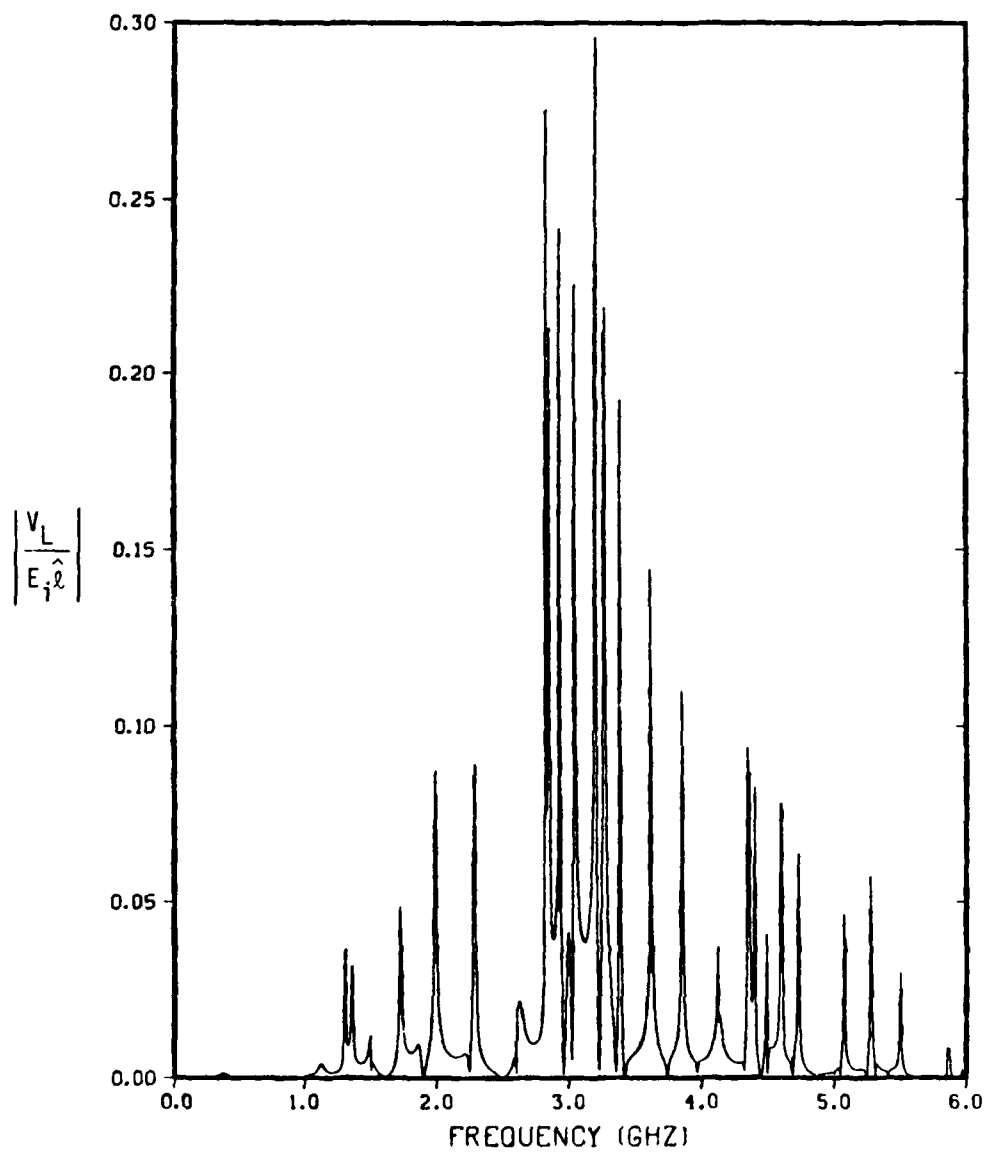
Figure 98. Magnitude of $V_L/(E_i\hat{l})$ vs. frequency for baseline configuration, except $z_0 = 10$ cm; $\Omega = 10$.
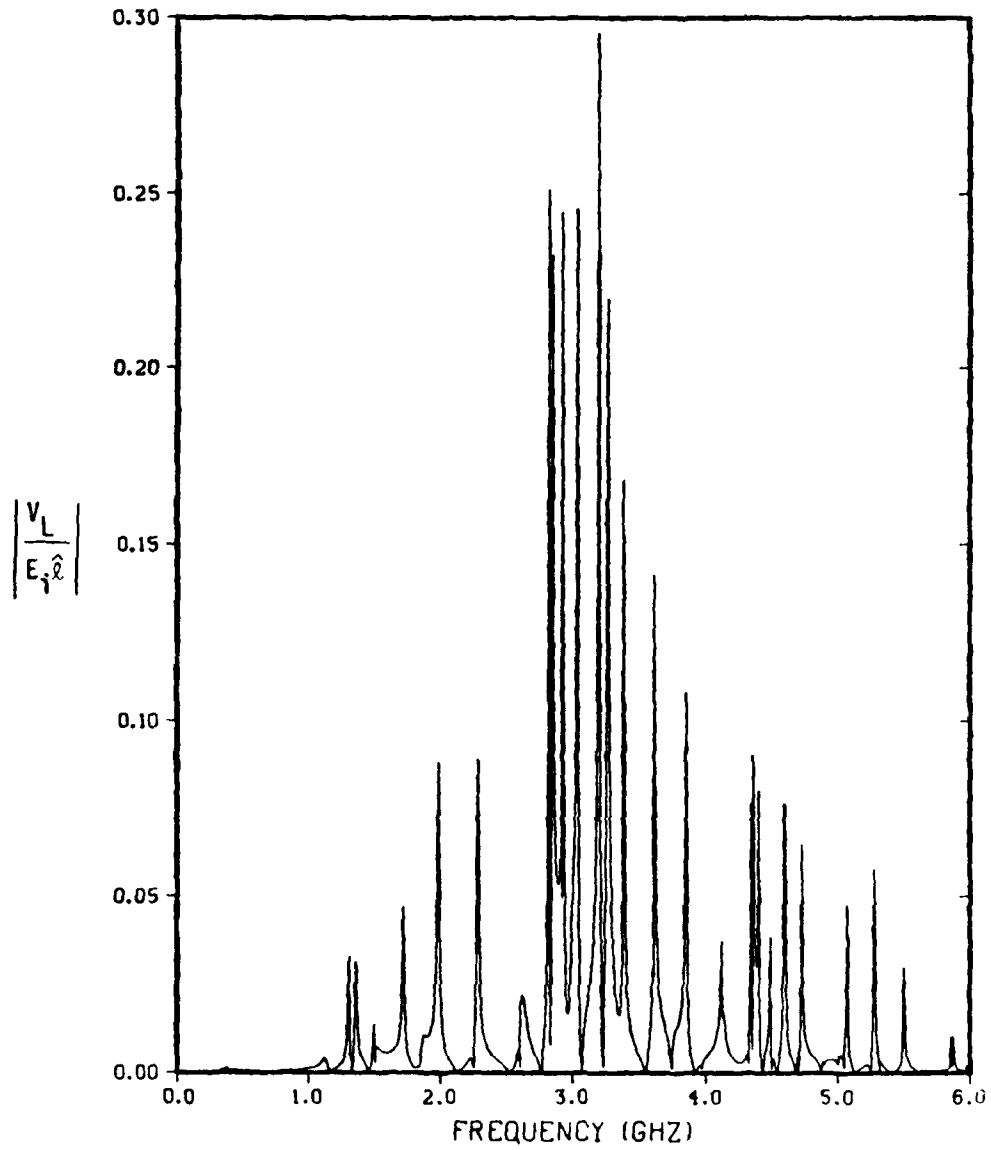
Figure 99.   Magnitude of $V_L/(E_i\hat{l})$ vs. frequency for baseline configuration, except $z_0 = 30$ cm; $\Omega = 1\mathrm{C}$.

121
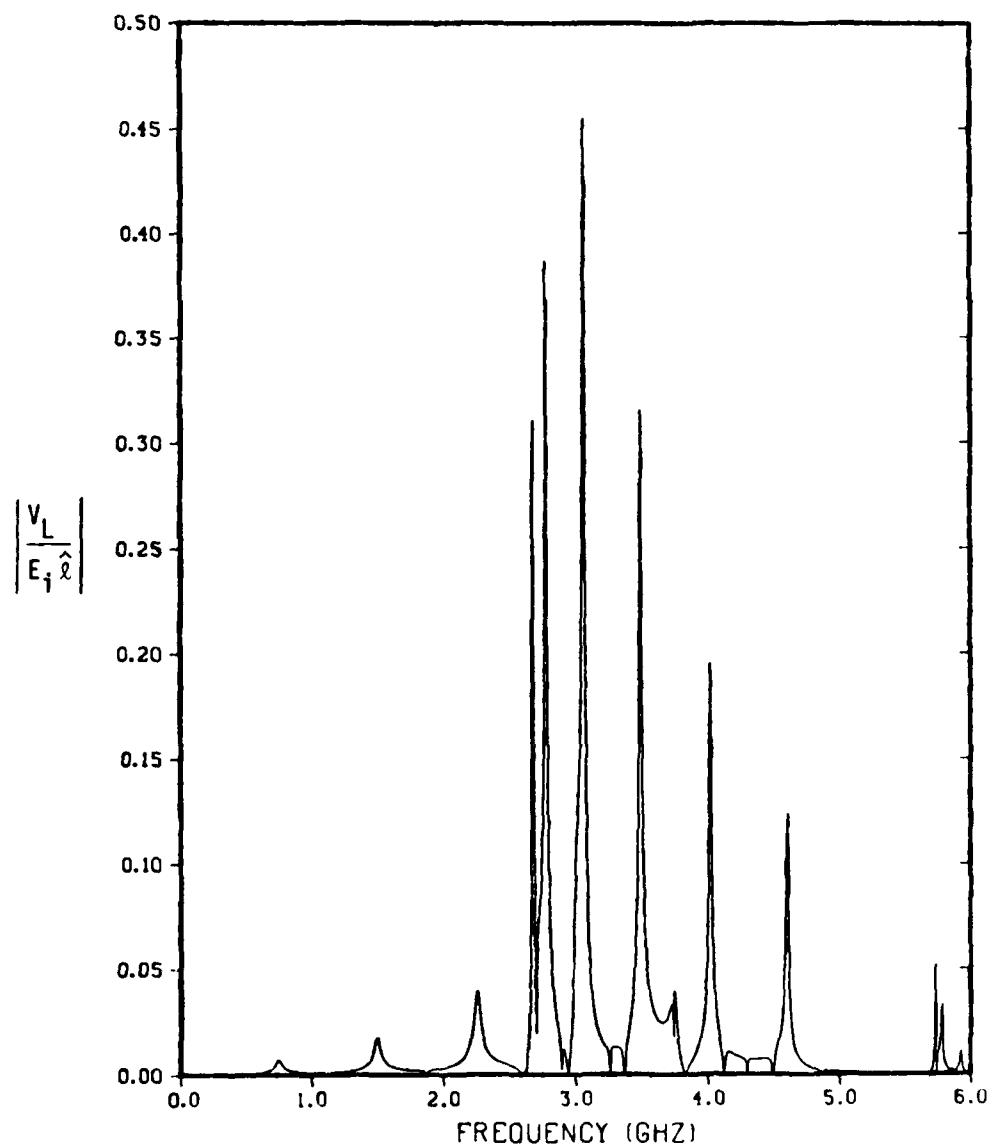
Figure 100. Magnitude of $V_L/(E_i\hat{l})$ vs. frequency for baseline configuration, except $b = 5$ cm; $\Omega = 10$.
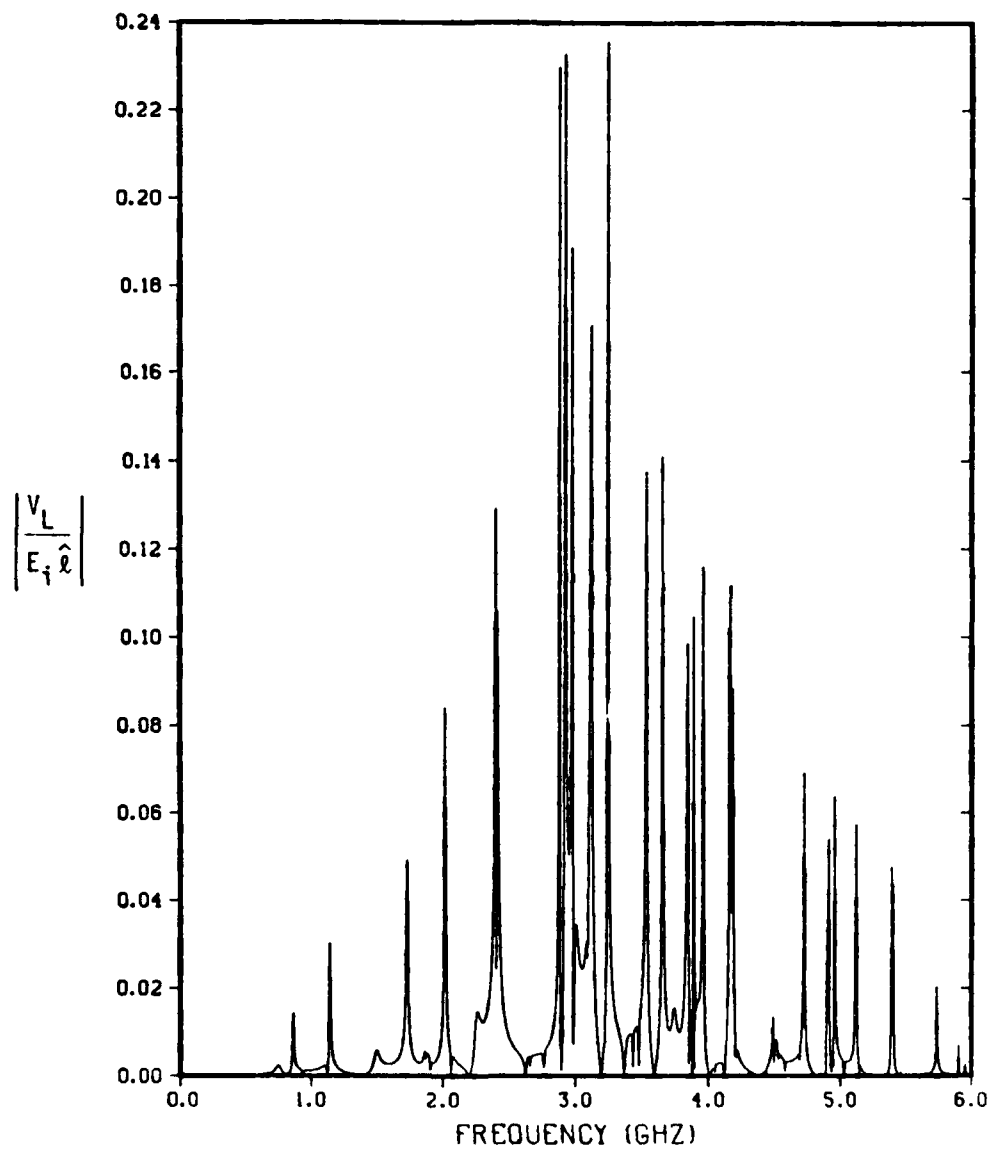
Figure 101. Magnitude of $V_L/(E_i \hat{l})$ vs. frequency for baseline configuration, except $b = 15$ cm; $\Omega = 10$.
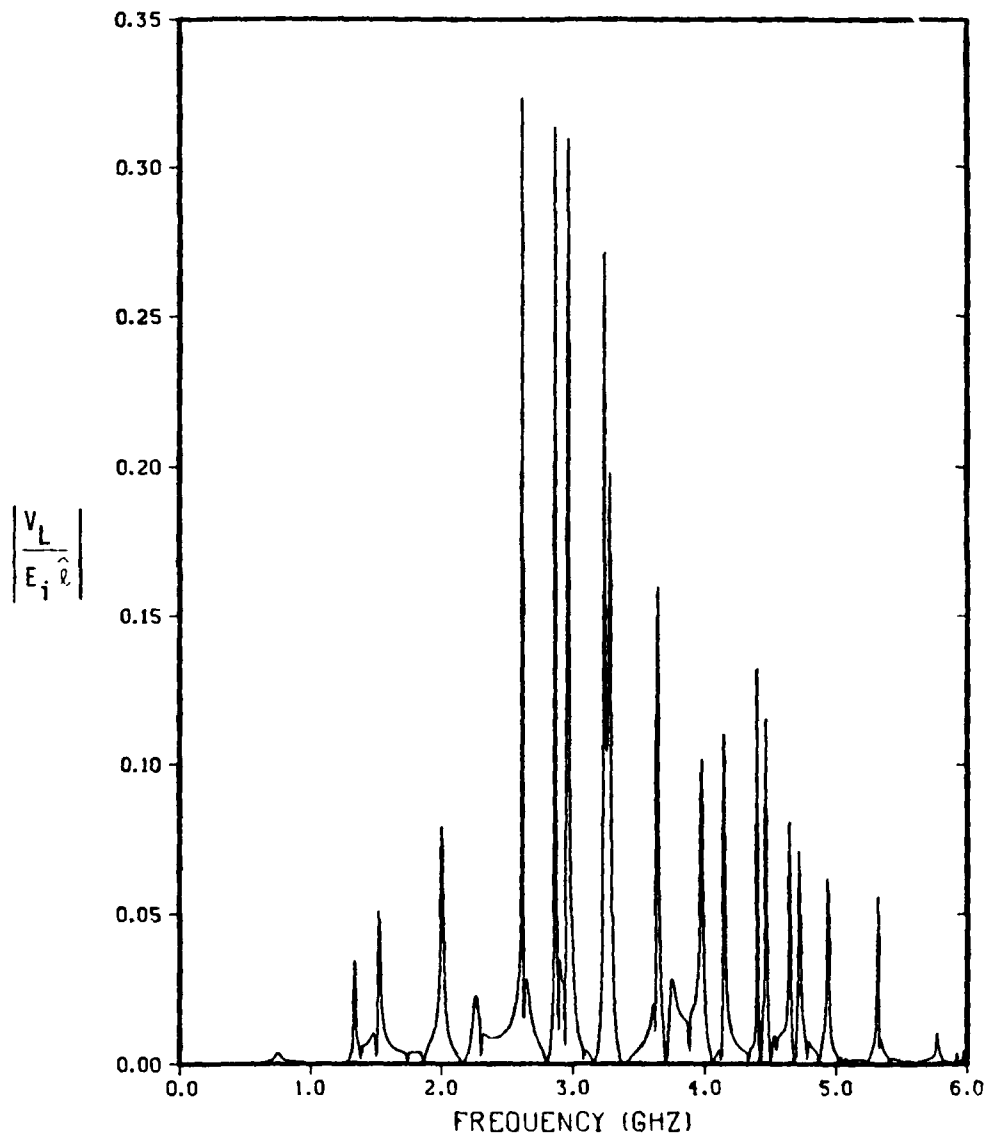
Figure 102.   Magnitude of $V_L/(E_i\hat{l})$ vs. frequency for baseline configuration, except $a = 1$ mm; $\Omega = 10$.

124

5.3 CONCLUDING REMARKS.

We have considered a simple problem of microwave coupling to a load in the interior of a shielded region, the penetration occurring via a thin slot aperture oriented and excited so as to yield the maximum coupling to the load. The treatment of the problem was approximate in the sense that the effects of the cavity on the average slot voltage were not taken into account. This approximation causes the cavity resonances to appear sharper than they actually are, because the reradiation of the cavity fields out of the slot is not accounted for.

For the configuration which was explored numerically, the cavity resonances were much sharper than that of the slot aperture, so that the frequency-domain magnitude of the load voltage (normalized to an incident voltage $E_i\hat{l}$) was dominated in its structure by the sharp cavity resonances. The effective area of the slot aperture was of the order of the square of the slot length at a resonance of the cavity, decreasing to zero at anti-resonances. The effective area for a pulsed signal will depend upon the center frequency and bandwidth of the pulse.

Several extensions and variants of the present problem would be of interest for microwave applications. One such variant would be the problem of coupling to a cavity homogeneously filled with an absorptive material representing, say, circuit boards and other electronic components. One would compute the total energy absorbed by the lossy material under pulse excitation of the cavity. It would also be a worthwhile exercise to refine the treatment of the problem treated herein to include the effects of the cavity fields upon the slot voltage.

Microwave coupling applications of interest at the present time will tend to involve cavities which are reasonably large in comparison to the wavelength, and coupling apertures which are comparable to the wavelength in size. Thus the number of cavity resonances "spanned" by the aperture response will, as in the case treated in this section, be large.

It is an interesting exercise to estimate the total power or energy coupled to a load inside a general slot-excited cavity. It is easily shown that the number of cavity modes having resonance frequencies between f and $f + \Delta f$ is approximately

$$\Delta N = \frac{8\pi V}{c^3} f^2 \Delta f \tag{243}$$

where V is the cavity volume and c denotes the speed of light. A signal of center

frequency f_0 and bandwidth Δf_0 will thus excite approximately

$$\Delta N_0 = \frac{8\pi V}{c^3} f_0^2 \Delta f_0 \tag{244}$$

modes. Denote the quality factor of these (loaded) resonant modes by Q^2. Thus the width Δf_r of a given resonance will be approximately

$$\Delta f_r = \frac{f_0}{Q} \tag{245}$$

and the power absorbed in a single resonance will be

$$P_r \cong \tilde{S}_{\text{inc}} A_e \frac{f_0}{Q} \tag{246}$$

where $\tilde{S}_{\text{inc}}$ denotes the incident power density spectrum (watts per square meter per Hz) and A_e is an effective area. The total power absorbed P_a is thus

$$
\begin{aligned}
P_a &\cong P_r \Delta N_0 \tag{247} \\[2ex]
&= \tilde{S}_{\text{inc}} \Delta f_0 A_e \frac{8\pi V f_0^3}{c^3 Q} \\[2ex]
&= S_{\text{inc}} A_e \frac{8\pi V f_0^3}{c^3 Q}
\end{aligned}
$$

where $S_{\text{inc}} = \tilde{S}_{\text{inc}} \Delta f_0$ is the incident power density (watts per square meter).

Now if the center frequency f_0 is that of the (broad) slot resonance, we have

$$f_0 = \frac{c}{2\hat{l}} \tag{248}$$

Furthermore, if A_e at a cavity resonance can be written as

$$A_e = \alpha \hat{l}^2 \tag{249}$$

where α is a constant, we have

$$P_a \cong \frac{\alpha \pi V}{Q \hat{l}} S_{\text{inc}} \tag{250}$$

---

[2]It is, of course, an approximation to ascribe the same value for Q to each of the (many) modes under consideration.

126

Thus the effective area for power absorbed from the incident signal is

$$A_{\text{eff}} \cong \frac{\alpha \pi V}{Q \hat{l}} \qquad (251)$$

where the center frequency is close to that of the slot resonance and when the bandwidth of the incident signal includes several cavity resonances. For the geometry considered in this chapter, and estimating $Q \cong 50$ and $\alpha \cong 1/\pi$, we find $A_{\text{eff}} \cong 16\pi$ cm^2.

SECTION 6
WAVEGUIDE FIELD COUPLING TO A FILAMENTARY LOAD

Summary: A model is constructed to represent the Thévenin equivalent circuit which drives a thin coaxial probe in a rectangular waveguide. The model is intended to represent the drive on a detector/mixer diode in a microwave receiver. Representative numerical results are presented which display the coupling to a linear resistive load as a function of the various problem parameters, over the frequency band in which only the dominant mode can propagate in the waveguide. It is found that even when the probe reactance is uncompensated, the absorbed power can still reach within 3 dB of the incident power for the example cases considered.

An important problem in microwave system vulnerability analysis is that of determining the coupling of energy which has entered the system to a potentially vulnerable detector or mixer – typically a very sensitive diode. The diode is typically coupled to the electromagnetic field in the waveguide by a thin coaxial probe which extends into the guide. The detected signal is then observed across the diode. We consider a model for the equivalent circuit which drives the diode. We assume that the waveguide is terminated beyond the coaxial probe location by a short circuit. This configuration is typical; the position of the short is adjusted to maximize the signal at the probe position, at the center of the operating frequency band.

In the remainder of this section we set up an equivalent circuit at the probe terminals and evaluate the elements in this circuit. We present numerical results which show the power coupled to a linear load representing the small-signal diode impedance. In particular, we explore the frequency dependence of the absorbed power over the operating frequency band. Implications for vulnerability assessment are discussed.

6.1 EQUIVALENT CIRCUIT FOR A WAVEGUIDE PROBE.

The geometry of the waveguide/probe configuration is shown in Figure 103. The waveguide is rectangular in cross-section, of dimensions $a \times b$ ($a > b$), and extends from $z = -\infty$ to $z = l$, where it is terminated in a short circuit. The probe is the center conductor of a coaxial connector on the bottom ($y = 0$) wall of the

waveguide; its radius is denoted r and it is centered at $x = x_0$, $z = 0$. It is assumed that $r \ll a$ and that the frequency of operation is such that only the dominant TE_{10} mode can propagate in the waveguide.

A transmission-line equivalent circuit for this configuration is shown in Figure 104 [14]. The purpose of the analysis of the next subsection is to evaluate the transformer ratio N and the reactance X_p. Before proceeding, however, we reduce the transmission-line model of Figure 104 to a Thévenin equivalent circuit at the terminals of the coaxial connector.

We assume that a TE_{10} mode field is incident on the probe and the waveguide termination from $z = -\infty$. The incident electric field across the center of the guide will be denoted E_0, so that the incident signal voltage $V_0 = E_0 b$ (recall that b is the height of the waveguide). The characteristic impedance of the TE_{10} mode will be denoted Z_0. Transforming the source and termination to the probe location yields the equivalent circuit shown in Figure 105. The transformed termination impedance Z_T' is

$$Z_T' = jZ_0 \tan \beta_{10} l = jX_T \tag{252}$$

where β_{10} denotes the propagation constant of the dominant mode.

side view   end view
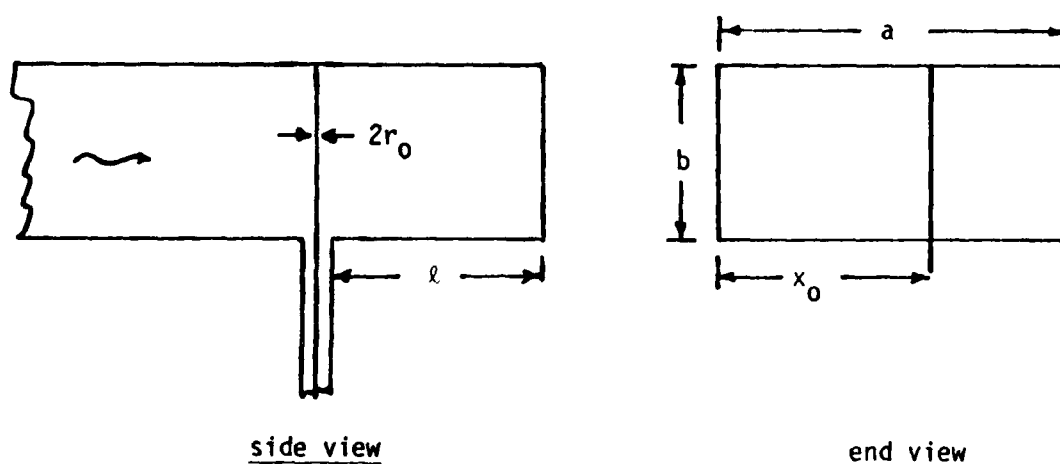
Figure 103. Geometry of the waveguide and probe configuration.

129
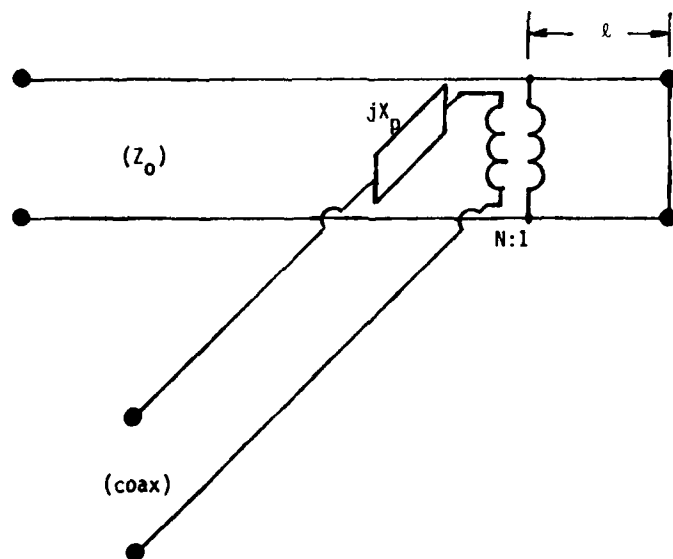
Figure 104. Transmission-line equivalent circuit for the waveguide and probe. Z_0 denotes the characteristic impedance of the TE_{10} waveguide mode.
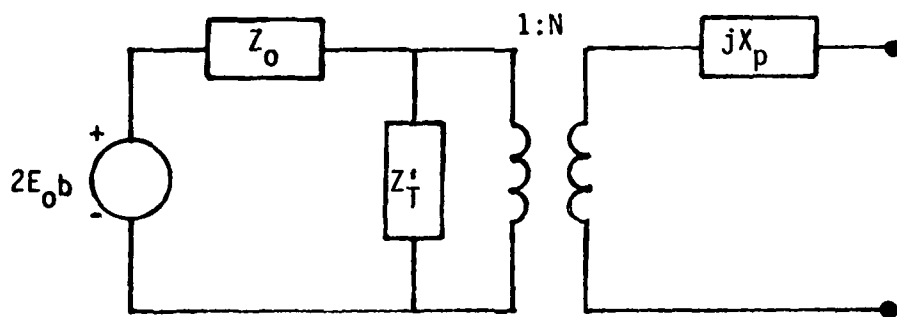
Figure 105. Thévenin equivalent circuit at the probe connector terminals.

130

Once the parameters N and X_p have been determined, the circuit model can be exercised with an arbitrary load. A diode load will, of course, be nonlinear; in that situation a circuit-analysis code would be used for accurate computation of the diode voltage and the power dissipated in the diode. However, it is instructive to consider a linearized diode model. We describe the diode as a pure resistance R_d. Then the power absorbed in the diode, normalized to the incident power, is given by the expression

$$\frac{P_{abs}}{P_{inc}} = 4N^2 R_d Z_0 \left| \frac{jX_T}{jX_T(R_d + jX_p) + Z_0(R_d + jX_p + jN^2 X_T)} \right|^2 \tag{253}$$

where the incident power is expressed as [1]

$$P_{inc} = \frac{b^2}{2Z_0} \mid E_0 \mid^2 \tag{254}$$

We shall numerically explore this normalized power later. We turn now to the evaluation of the transformer ratio N and the reactance X_p.

6.2 PROBE INPUT IMPEDANCE.

Since the parameters N and X_p are independent of the details of the waveguide termination (a shorting plate at $z = l$) we address the computation of the probe input impedance by considering the waveguide to be matched at $z = \pm\infty$. Furthermore, although we can choose a variety of probe configurations in the waveguide, we consider only the case where the probe runs all the way across the waveguide and is connected to the wall at $y = b$. The modeling of other probe configurations can be carried out using methods employed in this section.

We assume that the current on the probe is of the approximate functional form

$$I(y) = I_0 \sec kb \cos k(y - b) \tag{255}$$

The electromagnetic field in the waveguide is TM_y and derivable from a scalar function ψ via the relations

$$\vec{H} = \nabla \times \psi \vec{a}_y \tag{256}$$

---

[1] This expression for the incident power results from the choice $V_0 = E_0 b$ in the Thévenin equivalent circuit.

131

$$\vec{E} = \frac{1}{j\omega\epsilon_0}\nabla \times \nabla \times \psi\vec{a}_y \tag{257}$$

where ψ satisfies the scalar Helmholtz equation

$$\nabla^2\psi + k^2\psi = 0 \tag{258}$$

The propagation constant $k = \omega/c$, where ω denotes the frequency (the frequency dependence $\exp(j\omega t)$ is assumed and suppressed) and c is the speed of light.

We first model the surface density $\vec{J}_s$ in the plane $z = 0$ as resulting from a zero-thickness filament. Thus

$$\vec{J}_s = I_0 \sec kb \cos k(y - b)\delta(x - x_0)\vec{a}_y \tag{259}$$

Writing the function ψ as

$$\psi = \sum_{m=1}^{\infty}\sum_{n=0}^{\infty} a_{mn}\sin\frac{m\pi x}{a}\cos\frac{n\pi y}{b}\exp(-j\beta_{mn}\mid z \mid) \tag{260}$$

wherein

$$\beta_{mn}^2 = k^2 - (m\pi/a)^2 - (n\pi/b)^2 \tag{261}$$

and employing (256) and (259), we write the boundary condition at $z = 0$ as

$$2j\sum_{m=1}^{\infty}\sum_{n=0}^{\infty}\beta_{mn}a_{mn}\sin\frac{m\pi x}{a}\cos\frac{n\pi y}{b} = I_0\sec kb\cos k(y - b)\delta(x - x_0) \tag{262}$$

The coefficients a_{mn} are then easily shown to be

$$a_{mn} = \frac{I_0\epsilon_n}{j\beta_{mn}ab\cos kb}\sin\frac{m\pi x_0}{a}\int_0^b\cos k(y - b)\cos\frac{n\pi y}{b}dy \tag{263}$$

$$= \frac{kI_0\epsilon_n\tan kb}{j\beta_{mn}ab}\frac{\sin(m\pi x_0/a)}{[k^2 - (n\pi/b)^2]}$$

where Neumann's number $\epsilon_n = 1$ if $n = 0$ and $\epsilon_n = 2$ if $n \geq 1$.

We evaluate the complex power supplied by the probe current by performing the integral

$$P = -\frac{1}{2}\int_{S_p} E_y\frac{1}{2\pi r}I_0^*\sec kb\cos k(y - b)dS_p \tag{264}$$

132

where S_p denotes the probe surface. Since we have assumed that the probe radius is small, E_y will be essentially uniform around the probe so that P is given approximately by

$$P \cong -\frac{I_0^*}{2} \int_0^b E_y(x_0, y, r) \sec kb \cos k(y - b) dy \qquad (265)$$

Now since P can also be written in terms of the input impedance Z_{in} seen at the probe terminals from the coaxial connector side, we have

$$P = \frac{1}{2} Z_{in} \mid I_0 \mid^2 \qquad (266)$$

Thus using (265) and (266), we find

$$Z_{in} = j\omega\mu_0 b \left(\frac{\tan kb}{kb}\right)^2 \sum_{m=1}^{\infty} \sum_{n=0}^{\infty} \frac{\epsilon_n \sin^2(m\pi x_0/a)e^{-j\beta_{mn}r}}{j\beta_{mn}a\left[1 - (n\pi/kb)^2\right]} \qquad (267)$$

On the waveguide side of the transformer in Figure 104, the input impedance is, by inspection, $Z_0/2$. [2] The real part of Z_{in} in (267) must transform to $Z_0/2$; thus

$$N^2 = \frac{2}{Z_0} \Re(Z_{in}) \qquad (268)$$

$$= \frac{2b}{a} \left(\frac{\tan kb}{kb}\right)^2 \sin^2 \frac{\pi x_0}{a}$$

where we have used the fact that $Z_0 = \omega\mu_0/\beta_{10}$.

Furthermore, it is evident that

$$X_p = \Im(Z_{in}) \qquad (269)$$

$$= \omega\mu_0 b \left(\frac{\tan kb}{kb}\right)^2 \sum_{\substack{m=1 \\ (m,n)\neq(1,0)}}^{\infty} \sum_{n=0}^{\infty} \frac{\epsilon_n \sin^2(m\pi x_0/a)e^{-\alpha_{mn}r}}{\alpha_{mn}a\left[1 - (n\pi/kb)^2\right]}$$

where

$$\alpha_{mn}^2 = (m\pi/a)^2 + (n\pi/b)^2 - k^2 \qquad (270)$$

---

[2] Recall that for the purpose of evaluating Z_{in} we have taken the guide to be matched at $z = \pm\infty$.

133

This completes the formal evaluation of the parameters necessary to specify the equivalent circuit of Figure 105. We now reduce the expression in (269) for X_p to a simpler and more easily computed form. First write X_p as

$$X_p = \omega\mu_0 b \left(\frac{\tan kb}{kb}\right)^2 \left\{ 2 \sum_{n=1}^{\infty} \frac{e^{-\alpha_{1n}r}\sin^2(\pi x_0/a)}{\alpha_{1n}a\left[1 - (n\pi/kb)^2\right]} \right. \tag{271}$$

$$+ \sum_{n=0}^{\infty} \frac{\epsilon_n}{1 - (n\pi/kb)^2} \sum_{m=2}^{\infty} \sin^2 \frac{m\pi x_0}{a} \left[\frac{e^{-\alpha_{mn}r}}{\alpha_{mn}a} - \frac{e^{-m\pi r/a}}{m\pi}\right]$$

$$\left. + \sum_{n=0}^{\infty} \frac{\epsilon_n}{1 - (n\pi/kb)^2} \sum_{m=2}^{\infty} \sin^2 \frac{m\pi x_0}{a} \frac{1}{m\pi} e^{-m\pi r/a} \right\}$$

In what follows, we set $x_0 = a/2$; this is the situation of practical interest. Now [15]

$$\sum_{n=0}^{\infty} \frac{\epsilon_n}{1 - (n\pi/kb)^2} = kb \cot kb \tag{272}$$

$$\sum_{\substack{m=3 \\ (odd\ m)}}^{\infty} \frac{1}{m\pi} e^{-m\pi r/a} = \frac{1}{2\pi} \ln\left(\coth \frac{\pi r}{2a}\right) - \frac{1}{\pi} e^{-\pi r/a} \tag{273}$$

so that

$$X_p = \omega\mu_0 b \left(\frac{\tan kb}{kb}\right) \left\{ \frac{1}{2\pi} \ln\left(\coth \frac{\pi r}{2a}\right) - \frac{e^{-\pi r/a}}{\pi} \right. \tag{274}$$

$$+ 2\left(\frac{\tan kb}{kb}\right) \sum_{n=1}^{\infty} \frac{e^{-\alpha_{1n}r}}{\alpha_{1n}a\left[1 - (n\pi/kb)^2\right]}$$

$$\left. + \left(\frac{\tan kb}{kb}\right) \sum_{n=0}^{\infty} \frac{\epsilon_n}{1 - (n\pi/kb)^2} \sum_{\substack{m=3 \\ (odd\ m)}}^{\infty} \left[\frac{e^{-\alpha_{mn}r}}{\alpha_{mn}a} - \frac{e^{-m\pi r/a}}{m\pi}\right] \right\}$$

The infinite series in this representation for X_p are rapidly convergent and the numerical evaluation of X_p is straightforward. Curves of X_p, normalized by the free-space intrinsic impedance $\eta_0 = 120\pi\ \Omega$, are shown in Figure 106 as a function of normalized frequency ka/π for $b/a = 0.5$ and $r/a = 0.01$, 0.03, and 0.1. We

134

note that X_p is negative, indicating that the probe impedance is capacitive over this frequency range.
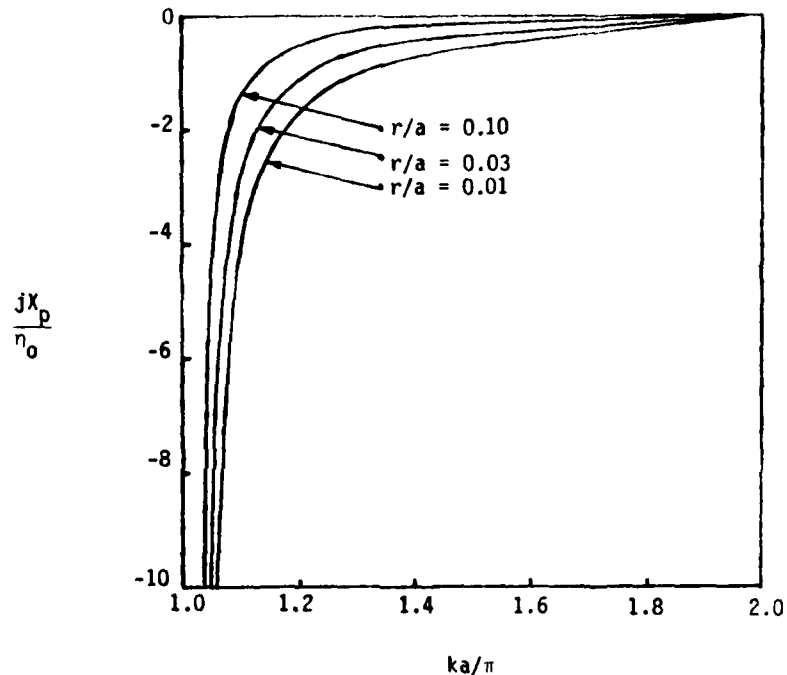
Figure 106. Normalized probe reactance vs. normalized frequency for $b/a = 1/2$; $r/a = 0.01, 0.03, 0.1$.

6.3 NUMERICAL RESULTS FOR ABSORBED POWER.

In this section we present numerical results for the normalized absorbed power of Eq. (253) as a function of normalized frequency ka/π. The waveguide and termination dimensions are chosen such that

$$b = a/2 \tag{275}$$

$$l = a/2 \tag{276}$$

This choice for l makes $X_T = \infty$ at $ka/\pi = \sqrt{2}$. The normalized absorbed power can be written

$$\frac{P_{abs}}{P_{inc}} = \frac{4N^2 R_d Z_0}{(R_d \cot \beta_{10} l - X_p)^2 + (R_d + N^2 Z_0 + X_p \cot \beta_{10} l)^2} \tag{277}$$

135

where R_d is the small-signal diode resistance, X_p is given in (274), N is given in (268), and

$$Z_0 = \eta_0 \left[1 - \left(\frac{\pi}{ka} \right)^2 \right]^{-1/2} \tag{278}$$

$$\beta_{10}l = \frac{\pi l}{a} \left[\left(\frac{ka}{\pi} \right)^2 - 1 \right]^{-1/2} \tag{279}$$

We have performed numerical calculations of P_{abs}/P_{inc} as a function of ka/π for a variety of cases. First, in Figure 107 we plot P_{abs}/P_{inc} vs. ka/π when the probe reactance $X_p \equiv 0$. In this case, we assume that the reactance is tuned out at every frequency; P_{abs}/P_{inc} becomes

$$P_{abs}/P_{inc} \Big|_{X_p \equiv 0} = \frac{4N^2 R_d Z_0}{R_d^2 \cot^2 \beta_{10}l + (R_d + N^2 Z_0)^2}. \tag{280}$$
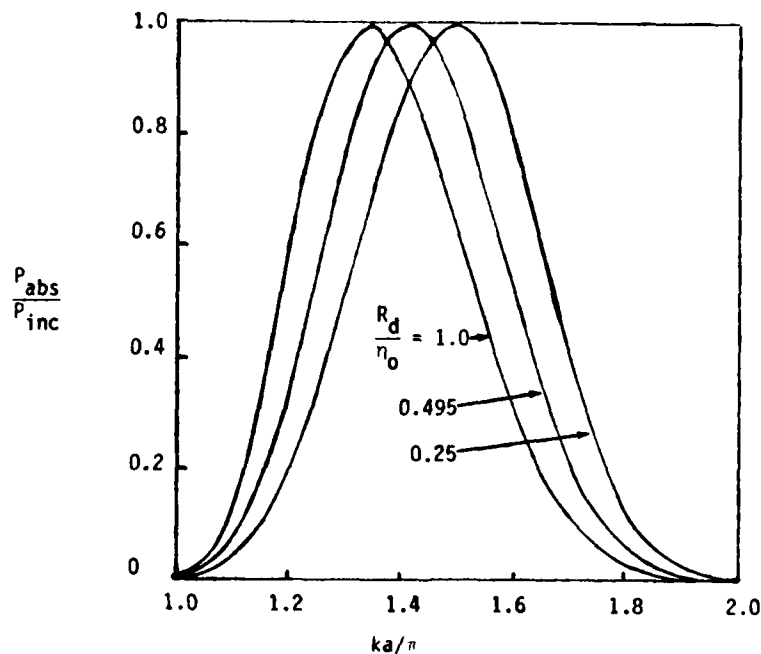
Figure 107. Normalized absorbed power vs. normalized frequency for $X_p = 0$; $R_d/\eta_0 = 0.25, 0.495, 1.0$.

136

This quantity has a maximum with respect to R_d occurring at

$$R_d = N^2 Z_0 \sin \beta_{10} l \qquad (281)$$

The value of the maximum is

$$P_{abs}/P_{inc} \bigg|_{\substack{\text{max;} \\ X_p \equiv 0}} = \frac{2 \sin \beta_{10} l}{1 + \sin \beta_{10} l} \qquad (282)$$

When $\beta_{10} l = \pi/2$, a condition that would denote the design point, the maximum value of P_{abs}/P_{inc} is unity. A value of $R_d = 0.495\eta_0$ meets the condition of Eq. (281) at the design point.

We observe from Figure 107 that changing R_d from this value still permits P_{abs}/P_{inc} to approach unity; the frequency at which this occurs decreases if $R_d > 0.495\eta_0$ and increases if $R_d < 0.495\eta_0$. This is a consequence of the frequency dependence of $N^2 Z_0$ and of $\cot \beta_{10} l$. We conclude from this result that if the probe reactance can be tuned out (as it certainly can, at least at a given frequency), essentially all of the power incident upon the diode can be absorbed by it, at some frequency in the band.

We show curves of P_{abs}/P_{inc} vs. ka/π for various uncompensated probe inductances (determined by different ratios r/a) and various values of R_d/η_0 in Figures 108 – 110. The trends are adequately shown by the curves in Figure 109 for $r/a = 0.03$. P_{abs}/P_{inc} reaches a higher maximum value at a lower frequency as R_d/η_o is increased. The differences in peak values become more pronounced as r/a decreases, that is, as the probe inductance increases. However, the decrease in peak value of P_{abs}/P_{inc} when $R_d/\eta_0 = 0.25$ and $r/a = 0.01$ is only a factor of two, or 3 dB. We conclude that even when the probe reactance is uncompensated, the fractional power absorbed in the load can be substantial. We remark also that the half-power width of these curves is nearly $ka/2\pi$ – half of the TF_{10} operating band.
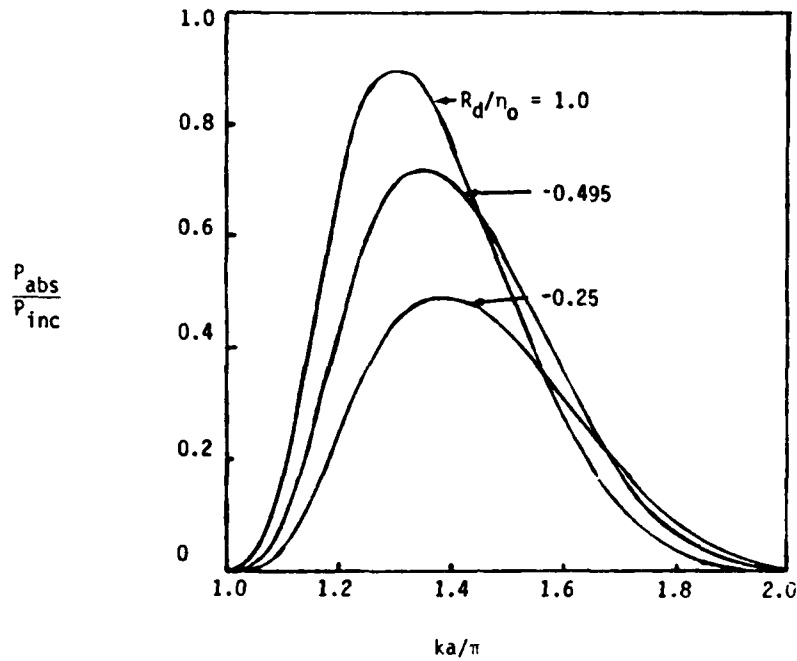
Figure 108. Normalized absorbed power vs. normalized frequency for $r/a = 0.01$; $R_d/\eta_0 = 0.25, 0.495, 1.0$.
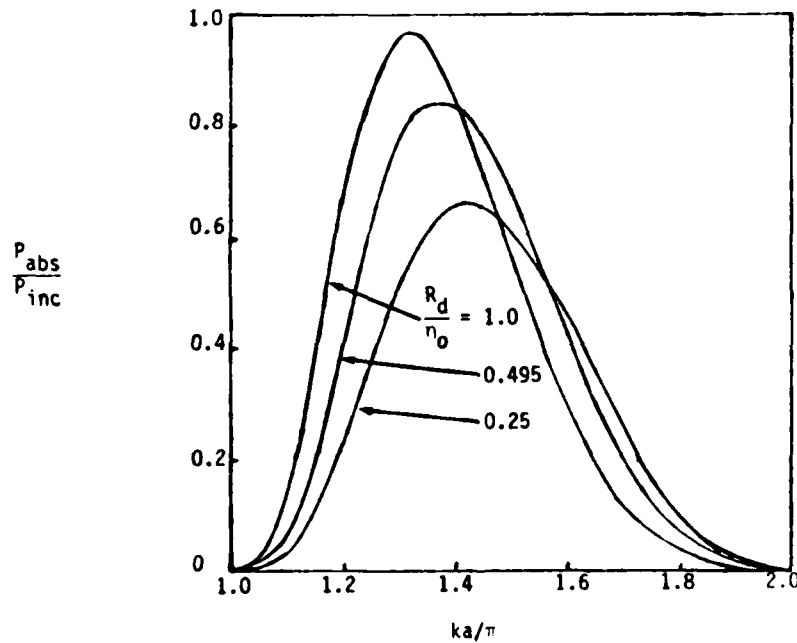
Figure 109. Normalized absorbed power vs. normalized frequency for $r/a = 0.03$; $R_d/\eta_0 = 0.25, 0.495, 1.0$.

138
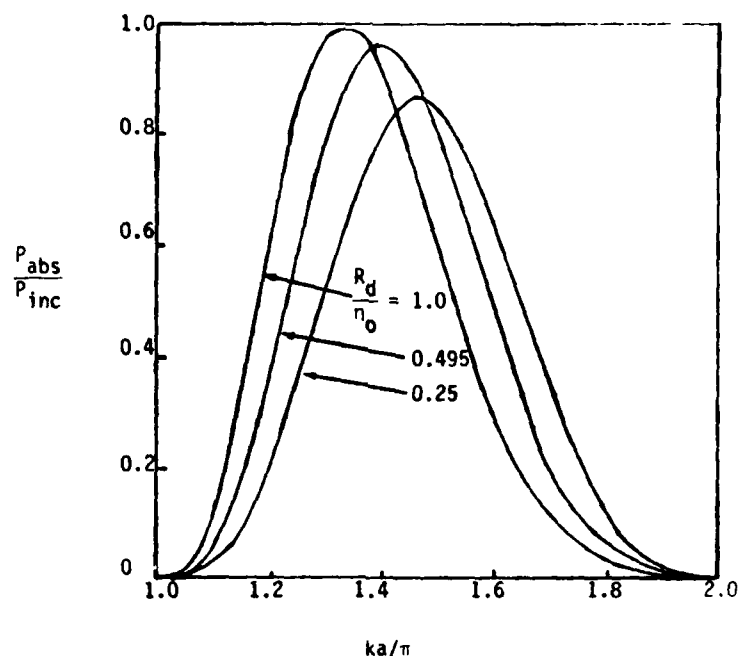
Figure 110. Normalized absorbed power vs. normalized frequency for $r/a =$ 0.1; $R_d/\eta_0 = 0.25, 0.495, 1.0$.

6.4 CONCLUDING REMARKS.

We have constructed a mathematical model for the power absorbed in a resistive load coupled to a waveguide by a thin probe extending across the short dimension of the guide cross-section. It has been assumed that at TE_{10} mode field is incident upon the probe and that the guide is terminated in a short circuit. The frequency range considered is that over which only the dominant TE_{10} mode can propagate. Representative calculations have shown that even when the probe reactance is uncompensated, a substantial fraction of the incident power is absorbed in the load. The width of the absorption curve is approximately one-half of the TE_{10} mode band for a waveguide whose cross-sectional aspect ratio is 2, a typical value.

The values of R_d, the load resistance, which were considered were in the range 100 - 400 Ω. This range includes typical small-signal diode resistances.

It is not surprising that coupling to a load in a waveguide can be so highly efficient – after all, this is the desired purpose of the configuration. From the standpoint of vulnerability modeling, however, the relatively broad-band character of the response over the frequency range associated with pure TE_{10} mode propagation

139

would lead us to conclude that in-band vulnerability of a microwave system is largely defined by the power which reaches the diode end of the system. Power which reaches this point will be absorbed.

Time has not permitted us to explore the out-of-band coupling problem. When more than one mode can propagate in the waveguide, the model of Figure 105 will contain a transformer for each propagating mode. This case can be explored using the methods employed herein, and is worthy of consideration. Other cases which might profitably be examined include that in which the probe extends only partway into the waveguide and that in which the resistive load is placed inside the waveguide itself. The analysis of both of these latter problems is straightforward.

SECTION 7
ELECTROMAGNETIC PENETRATION OF LONG SLOTS:
AN APPROXIMATE ANALYSIS

Summary: Electromagnetic penetration of an infinitely long, electrically narrow slot of arbitrary depth in a plane conductor is investigated using a relatively simple analytical technique. The quantity of interest is the total power transmitted through the slot under plane-wave illumination with magnetic field parallel to the long axis of the slot. Analytical and numerical results for this quantity are provided, as is an elementary equivalent circuit model of the problem. The analysis approach can be applied to more complicated problems.

There exists considerable need for models of various electromagnetic coupling configurations for use in the study of electromagnetic interactions with systems of many kinds. Unfortunately, only a few such configurations have been studied in detail, yet the need for models remains. At the present time, extensive numerical and experimental programs are under way whose purpose is to develop increased understanding of coupling through thick apertures, multiple apertures, loaded apertures, penetrating conductors, and other complex configurations. While these efforts have yielded useful results, these results are often not in a form which is readily usable by one responsible for making approximate coupling estimates or for quantifying hardening requirements. Analytical approaches, where they can be applied, are often the best means for obtaining relatively simple, although sometimes approximate, results for near-term use.

Our principal interest is in developing relatively simple analytical expressions for the power transmitted through a rectangular slot of arbitrary depth, illuminated by a plane wave. In this section we discuss the basis for our approach to that problem in the context of a simpler one: the case in which the slot is infinitely long. This problem has already been treated by Harrington and Auckland [16] using a slightly different method from that employed herein. The analysis and the results developed in this chapter are not new; but it is our intent to illustrate this approach for treating other more complicated problems.

The method which we shall employ herein is described in Harrington's text *Time-Harmonic Electromagnetic Fields* [17]. It consists in making reasonable assumptions concerning the tangential electric field in the aperture connecting two regions of space, calculating the electromagnetic field in each region from the assumed

141

aperture field, and then requiring that the complex power flow be continuous through the aperture. This final condition, which permits the solution for the aperture-field amplitude to be obtained, represents an approximate means for satisfying the condition that the tangential magnetic field be continuous through the aperture. This technique is ideally suited to many of the problems encountered in microwave coupling to systems via back-door paths.

We begin by considering the problem of penetration of a long, narrow slot in an infinitesimally thin conductor. This serves to illustrate the method, to demonstrate that the results are not sensitive to the form of aperture field chosen, and to show how a simple equivalent circuit can be derived which contains all the relevant features of the original problem. Then we address the deep-slot problem. We construct an equivalent circuit and present representative numerical results indicating, *inter alia*, the slot-depth resonance. The formulation of this problem includes the possibility of slot loading by a material different from free space. We also present a brief discussion of the problem of coupling to an infinitely deep slot. Certain mathematical results are given in the Appendix.

7.1 THE THIN, LONG SLOT: FORMULATION AND SOLUTION.

The geometry of the problem is shown in Figure 111. An H-polarized plane electromagnetic wave is incident at an angle θ ($\mid \theta \mid \leq \pi/2$) on a thin, perfectly conducting plane occupying the surface $z = 0$. The plane is cut by an infinitely long slot aperture in the region $\mid x \mid \leq w/2$; the center of the slot lies along the y-axis. The medium on either side of the conducting plane is free space. It is assumed that the slot is electrically thin; that is, for field time variations of the form $\exp(j\omega t)$, $kw = \omega w/c << 1$ where c denotes the speed of light. The object of the analysis is to calculate the power transmitted through the slot.

Our approximate approach to the solution of this boundary-value problem proceeds as follows: first, an electric field $E_x(x)$ of (assumed) known spatial variation but unknown amplitude is imposed across the slot and the total electromagnetic field is computed in the regions $z < 0$ and $z > 0$. Next, the fields are connected through the slot by forcing the complex power flow to be continuous there. This condition permits us to obtain the amplitude of the electric field across the slot and thus to calculate the power transmitted through the slot.

The electromagnetic field comprises components E_x, H_y, and E_z related by

$$E_x = \frac{-Z_0}{jk} \frac{\partial H_y}{\partial z}$$ (283)

$$E_z = \frac{Z_0}{jk} \frac{\partial H_z}{\partial x}$$ (284)

where

$$\left(\frac{\partial^2}{\partial x^2} + \frac{\partial^2}{\partial z^2} + k^2 \right) H_y = 0$$ (285)
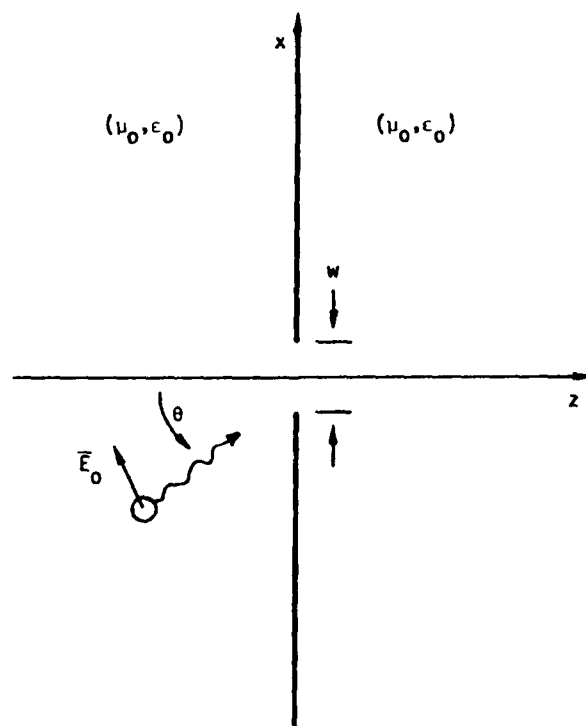
Figure 111.   Geometry of the thin-slot problem. The slot width w is assumed to be small compared to the wavelength.

143

and Z_0 denotes the intrinsic impedance of free space. Denoting by E_0 the amplitude of the incident electric field and by V_0 the total voltage across the slot

$$V_0 = -\int_{-w/2}^{w/2} E_x(x,0)dx \qquad (286)$$

we obtain the following expressions for the relevant components of the electromagnetic field:

$$z < 0: H_y = \frac{2E_0}{Z_0} e^{-jkx\sin\theta} \cos(kz\cos\theta) \qquad (287)$$

$$+ \frac{kV_0}{2\pi Z_0} \int_{-\infty}^{\infty} F(h)e^{jhx+j\sqrt{k^2-h^2}\,z} \frac{dh}{\sqrt{k^2-h^2}}$$

$$E_x = 2jE_0\cos\theta e^{-jkx\sin\theta}\sin(kz\cos\theta) \qquad (288)$$

$$- \frac{V_0}{2\pi} \int_{-\infty}^{\infty} F(h)e^{jhx+j\sqrt{k^2-h^2}\,z}dh$$

$$z > 0: H_y = \frac{-kV_0}{2\pi Z_0} \int_{-\infty}^{\infty} F(h)e^{jhx-j\sqrt{k^2-h^2}\,z}\frac{dh}{\sqrt{k^2-h^2}} \qquad (289)$$

$$E_x = \frac{-V_0}{2\pi} \int_{-\infty}^{\infty} F(h)e^{jhx-j\sqrt{k^2-h^2}\,z}dh \qquad (290)$$

The function $F(h)$ is to be determined. The field expressions given above are readily shown to satisfy Eqs. (283) and (285) as well as proper boundary conditions at $|z| \to \infty$ if

$$\Re\sqrt{k^2-h^2} \geq 0 \qquad (291)$$

$$\Im\sqrt{k^2-h^2} \leq 0 \qquad (292)$$

The electric field in the aperture plane $E_x(x,0)$ is

$$E_x(x,0) = \frac{-V_0}{2\pi} \int_{-\infty}^{\infty} F(h)e^{jhx}dh \qquad (293)$$

whence

$$F(h) = -\frac{1}{V_0} \int_{-w/2}^{w/2} E_x(x',0)e^{-jhx'}dx' \qquad (294)$$

144

and from Eq. (286), $F(0) = 1$. Thus the tangential electric field E_x is continuous at $z = 0$ and $E_x = 0$ on the conducting surface if Eq. (294) is satisfied.

An exact solution to this problem would follow from forcing continuity of H_y through the slot. This condition can be written

$$\frac{2E_0}{Z_0}e^{-jkx\sin\theta} = \frac{-kV_0}{\pi Z_0}\int_{-\infty}^{\infty}F(h)e^{jhx}\frac{dh}{\sqrt{k^2-h^2}} \quad (\mid x\mid\le w/2) \tag{295}$$

which can easily be shown to lead to an integral equation for the electric field across the slot. We shall apply a less stringent condition: multiply both sides of Eq. (295) by $(1/2)E_x^*(x,0)$ and integrate over all x. This condition makes the complex power continuous through the slot, a necessary but not sufficient condition for the satisfaction of Eq. (295). We obtain

$$\frac{1}{2}\int_{-\infty}^{\infty}dx\left(\frac{-V_0^*}{2\pi}\right)\int_{-\infty}^{\infty}F^*(h)e^{-jhx}dh\left(\frac{2E_0}{Z_0}\right)e^{-jkx\sin\theta} \tag{296}$$

$$= \frac{1}{2}\int_{-\infty}^{\infty}dx\left(\frac{-V_0^*}{2\pi}\right)\int_{-\infty}^{\infty}F^*(h)e^{-jhx}dh\left(\frac{-kV_0}{\pi Z_0}\right)\int_{-\infty}^{\infty}F(h')e^{jk'x}\frac{dh'}{\sqrt{k^2-h'^2}}$$

and making use of the result

$$\frac{1}{2\pi}\int_{-\infty}^{\infty}e^{-j\alpha\xi}d\xi = \delta(\alpha) \tag{297}$$

where $\delta(\cdot)$ denotes the Dirac delta-function, we find that Eq. (296) reduces to

$$E_0F^*(-k\sin\theta) = \frac{-kV_0}{\pi}\int_0^{\infty}\mid F(h)\mid^2\frac{dh}{\sqrt{k^2-h^2}} \tag{298}$$

Furthermore, the real power transmitted through the slot is given by

$$P_t = \frac{k\mid V_0\mid^2}{2\pi Z_0}\int_0^k\mid F(h)\mid^2\frac{dh}{\sqrt{k^2-h^2}} \tag{299}$$

Now it is evident from Eq. (294) that

$$F(-k\sin\theta) = 1 + \mathcal{O}(kw\sin\theta)^2 \tag{300}$$

Further, defining

$$\int_0^{\infty}\mid F(h)\mid^2\frac{dh}{\sqrt{k^2-h^2}} = I_r + jI_i \tag{301}$$

145

we have

$$I_r = \int_0^k \mid F(h) \mid^2 \frac{dh}{\sqrt{k^2 - h^2}} \cong \frac{\pi}{2} \quad (kw \ll 1) \tag{302}$$

$$I_i = \int_k^\infty \frac{\mid F(h) \mid^2 dh}{\sqrt{h^2 - k^2}} \tag{303}$$

so that, for $kw \ll 1$,

$$V_0 = \frac{-2E_0 w}{kw \left(1 + 2j I_i / \pi\right)} \tag{304}$$

and

$$P_t = \frac{w \mid E_0 \mid^2}{Z_0 kw \left[1 + (2I_i / \pi)^2\right]} \tag{305}$$

We may define an effective slot width w_e as

$$w_e = \frac{P_t}{S_{\text{inc}}} \tag{306}$$

where $S_{\text{inc}} = \mid E_0 \mid^2 / (2Z_0)$ denotes the power density incident on the slotted plane. We obtain

$$w_e = \frac{2w}{kw \left[1 + (2I_i / \pi)^2\right]} \tag{307}$$

whence

$$\frac{w_e}{w} = \frac{2}{kw \left[1 + (2I_i / \pi)^2\right]} \tag{308}$$

is the normalized effective slot width.

It is useful to construct an equivalent circuit describing the penetration of the slot. From Eq. (298) with $F^*(-k \sin \theta) \cong 1$, we have

$$V_0 = -J_{sx}^{sc} / (2Y') \tag{309}$$

where $J_{sx}^{sc} = 2E_0 / Z_0$ is the short-circuit current density across the slot and

$$Y' = \frac{k}{2Z_0} \left(1 + \frac{2j I_i}{\pi}\right) \tag{310}$$

is an admittance per unit length. Writing $Y' = G' + jB'$, we have

$$G' = \frac{k}{2Z_0} \tag{311}$$

$$B' = \frac{k}{Z_0 \pi} I_i \tag{312}$$

where G' and B' are respectively the slot conductance and susceptance per unit length. The equivalent circuit is shown in Figure 112.

It remains to consider the slot electric field and evaluate the integral I_i. To show that the result is not sensitive to the specific form chosen for $E_x(x,0)$ we consider two different expressions for this field:

$$E_x^{(1)}(x,0) = \frac{-V_0}{w} \tag{313}$$

$$E_x^{(2)}(x,0) = \frac{-V_0}{\pi \sqrt{(w/2)^2 - x^2}} \tag{314}$$

The first of these expressions represents a field which is constant across the slot. From Eq. (294), we obtain

$$F(h) = \text{sinc}\left(\frac{hw}{2}\right) \tag{315}$$

where $\text{sinc}(x) \equiv \sin x / x$. The second expression for $E_x(x,0)$ accounts for the singular behavior of the electric field at the edges of the slot and is an accurate representation of the field in the limit $kw \to 0$ [18]. Again from Eq. (294), for this case

$$F(h) = J_0\left(\frac{hw}{2}\right) \tag{316}$$

where $J_0(\cdot)$ is the Bessel function of order zero. Thus define

$$I_i^{(1)} = \int_1^\infty \frac{\text{sinc}^2\left(kwu/2\right) du}{\sqrt{u^2 - 1}} \tag{317}$$

$$I_i^{(2)} = \int_1^\infty \frac{J_0^2\left(kwu/2\right) du}{\sqrt{u^2 - 1}} \tag{318}$$

It is shown in the Appendix that

$$\lim_{kw \to 0} I_i^{(1)} = 3/2 + \ln\left(\frac{2}{\gamma kw}\right) \tag{319}$$

$$= \ln\left(\frac{8.963}{kw}\right)$$

$$\lim_{kw \to 0} I_i^{(2)} = 1.3863 \cdots + \ln\left(\frac{2}{\gamma kw}\right) \qquad (320)$$

$$= \ln\left(\frac{8}{\gamma kw}\right)$$

where $\gamma = 1.781 \cdots$ is the exponential of Euler's constant. It is apparent that the change produced in I_i by different choices for the slot electric field occurs only as a factor multiplying kw in the argument of a natural logarithm, a slowly varying function.

We show in Figure 113 plots of w_e/w as a function of kw/π for $I_i = I_i^{(1)}$ and $I_i = I_i^{(2)}$. One will observe that the differences are small, a result of the fact that the quantity calculated depends on the integral of the aperture field rather than on its detailed behavior. We shall use this fact to advantage in the next section, wherein we consider the effect of finite slot depth.

(illuminated side)   (shadowed side)
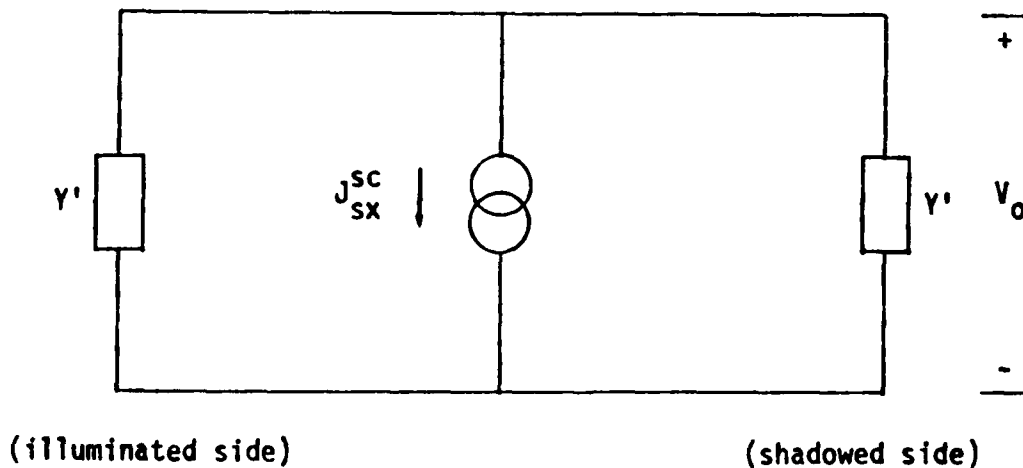
Figure 112. Equivalent circuit for the thin-slot problem. J_{sx}^{sc} is the short-circuit current density across the slot and Y' is an admittance per unit length.
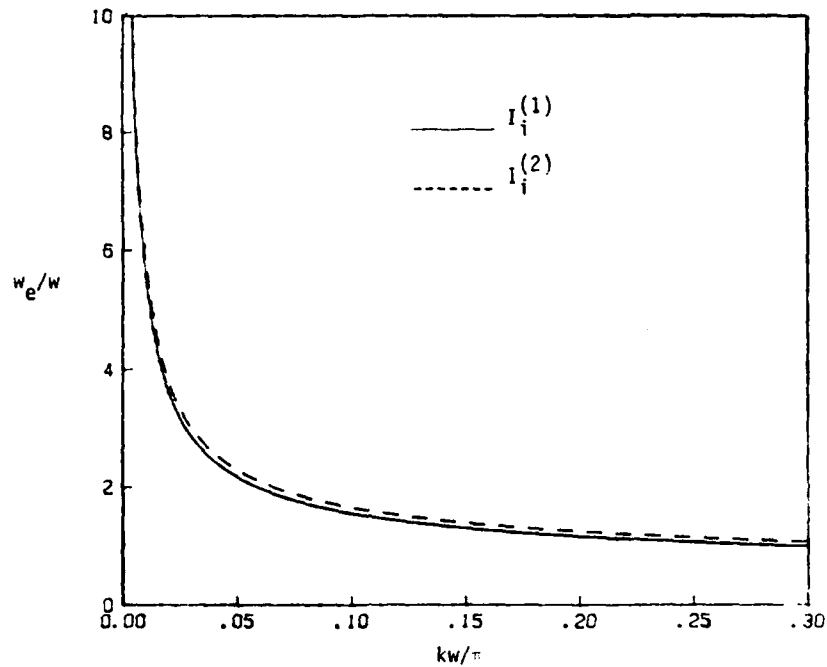
Figure 113.   Normalized effective slot width w_e/w as a function of kw/π. The solid curve results from choosing $I_i = I_i^{(1)}$ and the dashed curve from $I_i = I_i^{(2)}$.
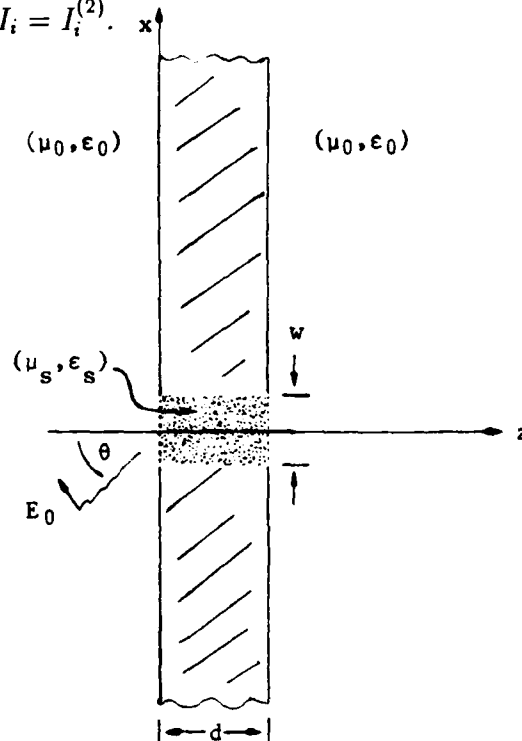
Figure 114.   Geometry of the deep-slot problem. It is assumed that $kw \ll 1$ and that kd is arbitrary. The slot may be filled with a homogeneous, isotropic medium other than free space.

149

7.2 THE DEEP, LONG SLOT: FORMULATION AND SOLUTION.

The geometry of the deep-slot problem is shown in Figure 114. The depth of the slot is d and it is assumed that this depth is not necessarily small. As in the thin-slot problem, we shall assume that the forms, but not the complex amplitudes, of the electric fields across the entrance and exit of the slot are known.

The fields in the regions outside the slot are given by

$z < 0$:

$$H_y = \frac{2E_0}{Z_0}e^{-jkx\sin\theta}\cos(kz\cos\theta) \tag{321}$$

$$+ \frac{kV_i}{2\pi Z_0}\int_{-\infty}^{\infty}F(h)e^{jkx+j\sqrt{k^2-h^2}z}\frac{dh}{\sqrt{k^2-h^2}}$$

$$E_x = -2jE_0\cos\theta e^{-jkx\sin\theta}\sin(kz\cos\theta) \tag{322}$$

$$- \frac{V_i}{2\pi}\int_{-\infty}^{\infty}F(h)e^{jhx+j\sqrt{k^2-h^2}z}dh$$

$z > d$:

$$H_y = \frac{-kV_0}{2\pi Z_0}\int_{-\infty}^{\infty}F(h)e^{jkx-j\sqrt{k^2-h^2}(z-d)}\frac{dh}{\sqrt{k^2-h^2}} \tag{323}$$

$$E_x = \frac{-V_0}{2\pi}\int_{-\infty}^{\infty}F(h)e^{jhx-j\sqrt{k^2-h^2}(z-d)}dh \tag{324}$$

where now V_i denotes the voltage across the input aperture at $z = 0$ and V_0 is the voltage across the output aperture at $z = d$. We shall assume that the slot field is uniform, so that

$$F(h) = \text{sinc}\left(\frac{hw}{2}\right) \tag{325}$$

The field in the slot itself is represented by forward-and backward-going TEM modes. In order to account for loading within the slot, we assume that the propagation constant k_s and intrinsic impedance Z_s of the medium filling the slot are not necessarily those of free space. Thus

150

$0 < z < d$:

$$E_x = Ae^{-jk_sz} + Be^{jk_sz} \qquad (\mid x \mid \leq w/2) \qquad (326)$$

$$H_y = \frac{1}{Z_s}\left(Ae^{-jk_sz} - Be^{jk_sz}\right) \qquad (\mid x \mid \leq w/2) \qquad (327)$$

where the amplitudes A and B are determined from the relations

$$A + B = \frac{-V_i}{w} \qquad (328)$$

$$Ae^{-jk_sd} + Be^{jk_sd} = \frac{-V_0}{w} \qquad (329)$$

and are given by

$$A = (2jw \sin k_s d)^{-1}(-V_i e^{jk_sd} + V_0) \qquad (330)$$

$$B = (2jw \sin k_s d)^{-1}(-V_0 + V_i e^{jk_sd}) \qquad (331)$$

As in the thin-slot problem considered in the previous section, we construct equations expressing the continuity of H_y across the slot apertures and then satisfy these conditions in an integral sense. Continuity of H_y at $z = 0$ yields the condition

$$\frac{2E_0}{Z_0}e^{-jkx\sin\theta} + \frac{kV_i}{2\pi Z_0}\int_{-\infty}^{\infty} F(h)e^{jhx}\frac{dh}{\sqrt{k^2 - h^2}} \qquad (332)$$

$$= \frac{1}{jwZ_s \sin k_s d}(-V_i \cos k_s d + V_0) \qquad (\mid x \mid < w/2)$$

Continuity of H_y at $z = d$ yields

$$\frac{-kV_0}{2\pi Z_0}\int_{-\infty}^{\infty} F(h)e^{jhx}\frac{dh}{\sqrt{k^2 - h^2}} = \frac{1}{jwZ_s \sin k_s d}(-V_i + V_0 \cos k_s d) \qquad (\mid x \mid < w/2)$$

$$(333)$$

Now multiply Eq. (332) through by $(1/2) E_x^*(x,0)$ and Eq. (333) by $(1/2)E_x^*(x,d)$ and integrate with respect to x. The result is the pair of equations

$$E_0 \quad + \quad \frac{kV_i}{4}\left(1 + \frac{2jI_i}{\pi}\right) \qquad (334)$$

$$= \frac{Z_0}{2jwZ_s \sin k_s d}(V_0 - V_i \cos k_s d)$$

151

$$\frac{-kV_0}{4}\left(1 + \frac{2jI_i}{\pi}\right) = \frac{Z_0}{2jwZ_s \sin k_s d}(V_0 \cos k_s d - V_i) \qquad (335)$$

where we have used the fact that for $kw << 1$, $F^*(-k\sin\theta) \cong 1$ and $I_r \cong \pi/2$.

Now it is a simple matter to solve Eqs. (334) and (335) for the slot voltages V_i and V_0. We obtain

$$V_i = \frac{E_0 w\left[(Z_0/2jZ_s)\cot k_s d + (kw/4)\left(1 + \frac{2j}{\pi}I_i\right)\right]}{D} \qquad (336)$$

$$V_0 = \frac{E_0 w\left[(Z_0/2jZ_s)\csc k_s d\right]}{D} \qquad (337)$$

where

$$D = \left(\frac{Z_0}{2jZ_s}\csc k_s d\right)^2 - \left[\frac{Z_0}{2jZ_s}\cot k_s d + \frac{kw}{4}\left(1 + \frac{2j}{\pi}I_i\right)\right]^2 \qquad (338)$$

As in the thin-slot case, we can construct an equivalent circuit representing the thick-slot configuration. This equivalent circuit is shown in Figure 115. The admittance Y is given by

$$Y = \frac{kw}{2Z_0}\left(1 + \frac{2j}{\pi}I_i\right) \qquad (339)$$

and the source current I_s is

$$I_s = J_{sx}^{sc}w \qquad (340)$$

This equivalent circuit yields the correct voltages at the slot apertures and at points inside the slot. Powers calculated with this circuit should be divided by the slot width w to yield power per unit length along the slot.

The normalized effective width of the slot is

$$w_e/w = \left(\frac{kw}{2}\right)\left|\frac{Z_0 \csc k_s d}{2jZ_s D}\right|^2 \qquad (341)$$
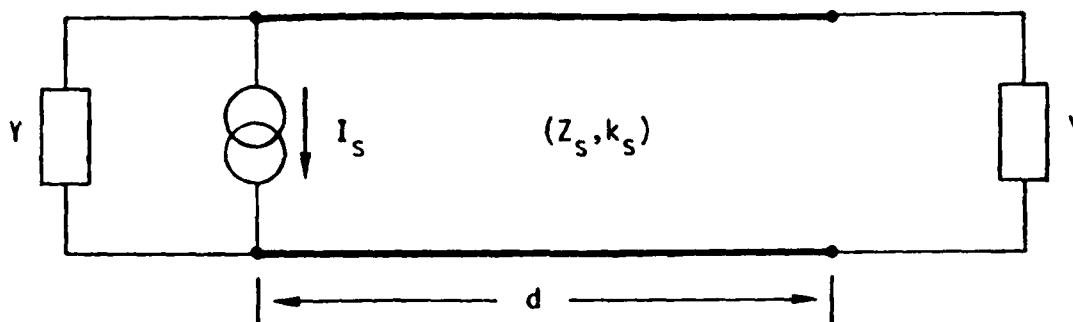
Figure 115. Equivalent circuit for the deep-slot problem.

which can be written as

$$w_e/w = \frac{2kw}{\left| j\left(Z_0/Z_s + Y^2 Z_0 Z_s\right)\sin k_s d + 2Y Z_0 \cos k_s d \right|^2} \qquad (342)$$

Note that

$$\lim_{d \to 0} \; w_e/w = \frac{2}{kw\left[1 + (2I_i/\pi)^2\right]} \qquad (343)$$

as required by Eq. (308).

Curves of $w_e(d)/w_e(0)$ are plotted in Figure 116 as a function of kd/π for fixed values of kw/π when $k_s = k$ and $Z_s = Z_0$, i.e., when the slot is unloaded. We observe an initial decrease in $w_e(d)/w_e(0)$ as kd/π is increased from zero, followed by an increase when kd/π is close to, but less than, one, and return to unity at $kd/\pi = 1$. This effect is readily understood in terms of the circuit model of Figure 115. As kd/π increases, the admittance seen looking into the entrance aperture changes. Between $kd/\pi = 0$ and 1 there will exist a condition where a conjugate match of source and apparent load admittances will most nearly occur; the transmitted power will be maximized at this point. The maximum possible

153

values of w_e/w and $w_e(d)/w_e(0)$ can be found from the maximum power-transfer theorem to be

$$w_e/w\Big|_{\text{max}} = \frac{2}{kw} \tag{344}$$

$$w_e(d)/w_e(0)\Big|_{\text{max}} = 1 + \left(\frac{2I_i}{\pi}\right)^2 \tag{345}$$

It is of potential practical interest in revealing the existence of deep-slot penetrations to consider the effective width of the entrance aperture for power scattered back into the illuminated region. This normalized effective width, denoted w'_e/w, is given by

$$w'_e/w = \left(\frac{kw}{2}\right)\left|\frac{(Z_0/2jZ_s)\cot k_s d + (kw/4)\left[1 + (2jI_i/\pi)\right]}{D}\right|^2 \tag{346}$$

Curves of $w'_e(d)/w_e(0)$ are plotted as a function of kd/π for various values of kw/π and $k_s = k$, $Z_s = Z_0$ in Figure 117. We observe that $w'_e(d)/w_e(0)$ behaves similarly to $w_e(d)/w(0)$. Thus it would appear that deep-slot resonance effects should be observable from either side of the slot.

7.3 PENETRATION OF AN INFINITELY DEEP SLOT.

If the slot is taken to be infinitely deep, the fields in the slot are of the form

$$E_x = \frac{-V_i}{w}e^{-jk_s z} \quad (\mid x \mid \leq w/2) \tag{347}$$

$$H_y = \frac{-V_i}{Z_0 w}e^{-jk_s z} \quad (\mid x \mid \leq w/2) \tag{348}$$

Continuity of H_y across the opening of the slot requires that

$$\frac{2E_0}{Z_0}e^{-jkx\sin\theta} + \frac{kV_i}{2\pi Z_0}\int_{-\infty}^{\infty} F(h)e^{jhx}\frac{dh}{\sqrt{k^2 - h^2}} = \frac{-V_i}{Z_s w} \quad (\mid x \mid < w/2) \tag{349}$$

154
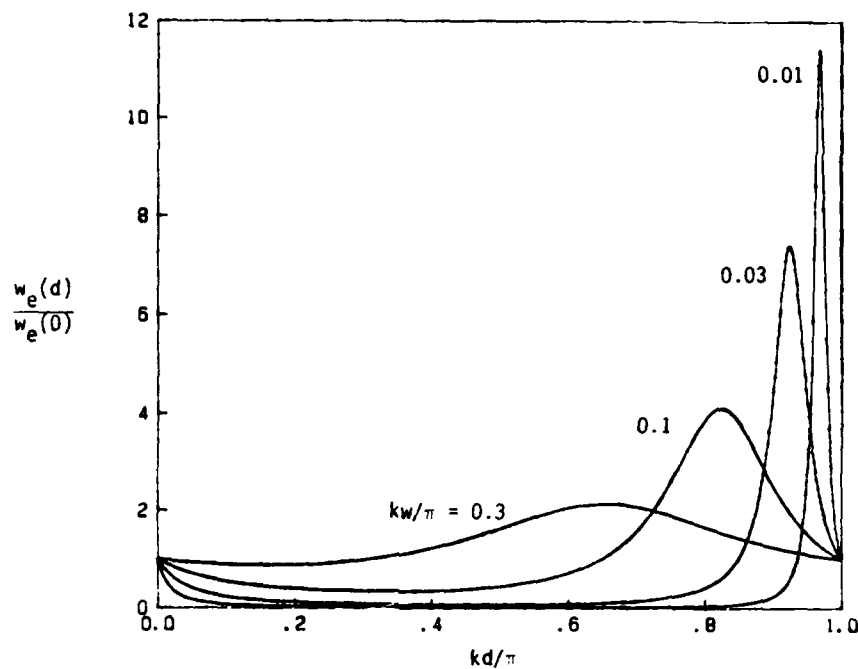
Figure 116. Normalized effective width $w_e(d)/w_e(0)$ as a function of kd/π for $kw/\pi = 0.01$, 0.03, 0.1. The slot is unloaded, i.e., $k_s = k$ and $Z_s = Z_0$.
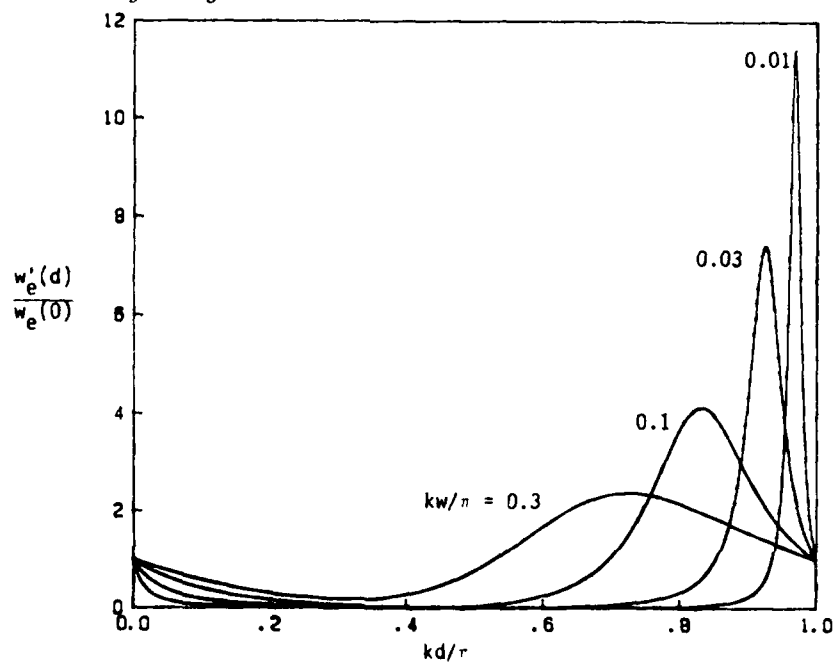
Figure 117. Normalized effective width $w'(d)/w_e(0)$ as a function of kd/π for $kw/\pi = 0.01$, 0.03, 0.1. The slot is unloaded, i.e., $k_s = k$ and $Z_s = Z_0$.

155

Enforcing this condition in the integral sense used throughout this section yields an expression for V_i:

$$V_i = \frac{-2wE_0}{Z_0/Z_s + (kw/2)(1 + 2jI_i/\pi)} \tag{350}$$

The real power entering the slot is

$$P_t = \frac{1}{2w} \mid V_i \mid^2 \Re\left(\frac{1}{Z_s}\right) \tag{351}$$

and the normalized effective slot width is

$$w_e/w = \frac{4Z_0\Re(1/Z_s)}{\mid Z_0/Z_s + (kw/2)(1 + 2jI_i/\pi)\mid^2} \tag{352}$$

A plot of w_e/w as a function of kw/π is shown in Figure 118 for the case $Z_s = Z_0$, i.e., when the slot is empty. Note that

$$\lim_{kw \to 0} w_e/w = 4\Re(Z_s)/Z_0 \tag{353}$$
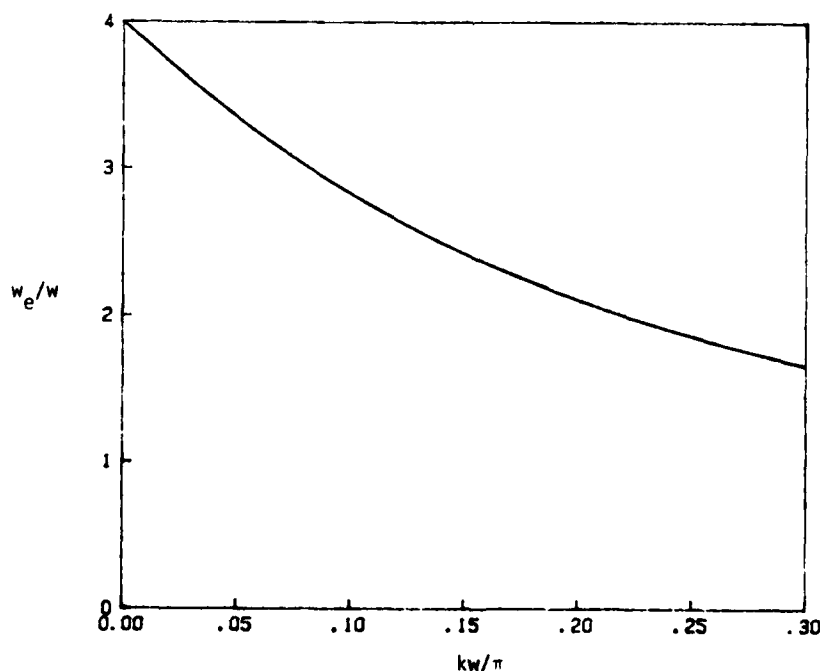
Figure 118. Normalized effective area of an infinitely deep slot as a function of kw/π. The slot is taken to be unloaded, i.e., $k_s = k$ and $Z_s = Z_0$.

156

7.4 CONCLUDING REMARKS.

We have presented some approximate analysis, equivalent circuits, and relatively simple formulas for assessing the penetration of electromagnetic fields through slot apertures which are electrically narrow (the short aperture dimension is small compared to the wavelength), infinitely long, and of arbitrary depth. We have employed a technique which can be utilized in many other related problems of interest in microwave coupling, including penetration through a slot of finite length.

We wish to stress in concluding this chapter that, while not exact, analytical methods such as those employed herein can provide useful models for many "back-door" coupling problems. They should be "bench-marked" by checking the limiting cases for which exact analytical solutions are available and/or by careful numerical modeling studies of special cases. Through this means the limitations on the validity of the simple analytical models can be established and their accuracy quantified.

SECTION 8
LIST OF REFERENCES

[1] John Ruze, "Antenna Tolerance Theory - A Review", *IEEE Trans. on Antennas and Propagation*, vol. 54, pp. 633-640, April 1966.

[2] E. Hallén, "Über die elektrischen Schwingungen in drahtförmigen Leitern," *Uppsala Univ. Årsskrift*, No. 1, pp. 1-102, 1930.

[3] E. Hallén, "Theoretical Investigations into the Transmitting and Receiving Properties of Antennae," *Nova Acta Reg. Soc. Sci. Upsaliensis*, Vol. 11, No. 4, pp. 1-44, 1938.

[4] L. Marin, "Natural Modes of Certain Thin-Wire Structures" *Interaction Notes*, Note 186, 1974.

[5] G. Bedrosian, "Stick-Model Characterization of the Natural Frequencies and Natural Modes of Aircraft," *Interaction Notes*, Note 326, 1977.

[6] K. S. H. Lee, ed., *EMP Interaction: Principles, Techniques, and Reference Data*, AFWL-TR-80-402, Air Force Weapons Laboratory, 1980, pp. 147-149.

[7] E. T. Whittaker and G. N. Watson, *A Course of Modern Analysis*, University Press, Cambridge, 1963, pp. 134-136.

[8] H. Jasik, ed., *Antenna Engineering Handbook*, McGraw-Hill, New York, 1961, p. 3-7.

[9] A. Sommerfeld, *Optics*, Academic Press, New York, 1964, pp. 118 ff.

[10] R. E. Haskell and C. T. Case, "Transient signal propagation in lossless, isotropic plasmas", *IEEE Transactions on Antennas and Propagation*, vol. AP-15, pp. 458 464, May 1967.

[11] M. Abramowitz and I. A. Steguns, eds., *Handbook of Mathematical Functions*, Dover Publications, New York, 1972, p. 297.

[12] A. Ishimaru, *Wave Propagation and Scattering in Random Media*, vol. II, Academic Press, New York, 1978, Ch. 21.

[13] M. Abramowitz and I. A. Stegun, eds., *Handbook of Mathematical Functions*, Dover Publications, New York, 1972, pp. 231-233.

[14] R. F. Harrington, *Time-Harmonic Electromagnetic Fields*, McGraw-Hill, New York, 1961, pp. 425-428.

[15] I. S. Gradshteyn and I. M. Ryzhik, *Table of Integrals, Series and Products*, Academic Press, New York, 1965, Nos. 1.421.3, 1.513.1.

[16] R. F. Harrington and D. T. Auckland, "Electromagnetic transmission through narrow slots in thick conducting screens", *IEEE Transactions on Antennas and Propagation*, vol. AP-28, pp. 616-622, September 1980.

[17] R. F. Harrington, *Time-Harmonic Electromagnetic Fields*, New York: McGraw-Hill, 1961, pp. 180 ff.

[18] K. S. H. Lee (ed.), *EMP Interaction: Principles, Techniques, and Reference Data*, AFWL-TR-79-403, p. 422, December 1979.

APPENDIX TO SECTION 7
EVALUATION OF INTEGRALS

EVALUATION OF $I_i^{(1)}$ AS $kw \to 0$

We express $\text{sinc}\,(kwu/2)$ in integral form as

$$\text{sinc}\left(\frac{kw}{2}u\right) = \frac{1}{2}\int_{-1}^{1} e^{jkwu\xi/2}d\xi \tag{354}$$

and write $I_i^{(1)}$ as

$$I_i^{(1)} = \frac{1}{4}\int_{-1}^{1}\int_{-1}^{1} d\xi\,d\eta \int_{1}^{\infty} \frac{\cos\,(kwu\,|\,\xi - \eta\,|\,/2)\,du}{\sqrt{u^2 - 1}} \tag{355}$$

$$= \frac{-\pi}{8}\int_{-1}^{1}\int_{-1}^{1} d\xi\,d\eta\,Y_0\left(\frac{kw}{2}\,|\,\xi - \eta\,|\right)$$

where $Y_0(\cdot)$ denotes the Neumann function of order zero. Since $kw \ll 1$, the argument of the Neumann function will be small over the range of integration and the function can be replaced by its small-argument approximation

$$\lim_{x \to 0} Y_0(x) = \frac{-2}{\pi}\ln\left(\frac{2}{\gamma x}\right) \tag{356}$$

where $\gamma = 1.781\cdots$ is the exponential of Euler's constant. Thus

$$\lim_{kw \to 0} I_i^{(1)} = \frac{1}{4}\int_{-1}^{1}\int_{-1}^{1}\ln\left(\frac{4}{\gamma kw\,|\,\zeta - \eta\,|}\right) d\xi\,d\eta \tag{357}$$

which is readily evaluated to yield

$$\lim_{k \to 0} I_i^{(1)} = \frac{3}{2} + \ln\frac{2}{\gamma kw} \tag{358}$$

$$= \ln\left(\frac{8.963}{\gamma kw}\right)$$

161

EVALUATION OF $I_i^{(2)}$ as $kw \to 0$

We use the integral representation of the Bessel function

$$J_0 \left(\frac{kw}{2} u \right) = \frac{1}{2\pi} \int_{-\pi}^{\pi} e^{jkwu \cos \phi / 2} d\phi \tag{359}$$

to write $I_i^{(2)F}$ in the form

$$I_i^{(2)} = \frac{1}{(2\pi)^2} \int_{-\pi}^{\pi} \int_{-\pi}^{\pi} d\phi d\psi \int_1^{\infty} \frac{\cos \left(kwu \mid \cos \phi - \cos \psi \mid /2 \right)}{\sqrt{u^2 - 1}} du \tag{360}$$

$$= -\frac{1}{8\pi} \int_{-\pi}^{\pi} \int_{-\pi}^{\pi} Y_0 \left(\frac{kw}{2} \mid \cos \phi - \cos \psi \mid \right) d\phi d\psi$$

Again using the small-argument approximation for the Neumann function, we obtain

$$\lim_{kw \to 0} I_i^{(2)} = \frac{1}{4\pi^2} \int_{-\pi}^{\pi} \int_{-\pi}^{\pi} \ln \left(\frac{4}{\gamma kw \mid \cos \phi - \cos \psi \mid} \right) d\phi d\psi \tag{361}$$

and with the help of the identity

$$\ln \left(2 \mid \cos \phi - \cos \psi \mid \right) = -2 \sum_{n=1}^{\infty} \frac{1}{n} \cos n\phi \cos n\psi \tag{362}$$

we find

$$\lim_{kw \to 0} I_i^{(2)} = \ln \frac{8}{\gamma kw} \tag{363}$$

$$= \ln \frac{2}{\gamma kw} + \ln 4$$

$$= 1.3863 + \ln \frac{2}{\gamma kw}$$

162

DISTRIBUTION LIST

DNA-TR-89-108

DEPARTMENT OF DEFENSE

ARMED FORCES STAFF COLLEGE
    ATTN: LIBRARY

ASSISTANT SEC OF DEF (C3I)
    ATTN: SPECIAL ASST FOR SATCOM

ASSISTANT TO THE SECRETARY OF DEFENSE
ATOMIC ENERGY
    ATTN: EXECUTIVE ASSISTANT

DEFENSE ADVANCED RSCH PROJ AGENCY
    ATTN: DED

DEFENSE COMMUNICATIONS AGENCY
    ATTN: CODE H396 TECH LIB

DEFENSE COMMUNICATIONS AGENCY
    ATTN: COMMANDER

DEFENSE COMMUNICATIONS ENGINEER CENTER
    ATTN: CODE R410

DEFENSE INTELLIGENCE AGENCY
    ATTN: W E THOMPSON
    ATTN: DR J COLEMAN
    ATTN: RTS-2B

DEFENSE NUCLEAR AGENCY
    ATTN: DFRA
    ATTN: OPNA
    ATTN: OPNS
    ATTN: RAAE
    ATTN: RAEE
    ATTN: RAEV
4 CYS ATTN: TITL

DEFENSE NUCLEAR AGENCY
    ATTN: TDNM
    ATTN: TDTT

DEFENSE TECHNICAL INFORMATION CENTER
2 CYS ATTN: DTIC/FDAB

DIRECTOR
    ATTN: DOCUMENT CONTROL

JOINT STRAT TGT PLANNING STAFF
    ATTN: JK (ATTN: DNA REP)
    ATTN: JKCS, STUKMILLER
    ATTN: JLWT (THREAT ANALYSIS)
    ATTN: JPEM
    ATTN: PSS

NATIONAL DEFENSE UNIVERSITY
    ATTN: NWCO

NATIONAL SECURITY AGENCY
    ATTN: CHIEF A GROUP
    ATTN: TECHNICAL LIBRARY
    ATTN: Y253 (HILTON)

STRATEGIC DEFENSE INITIATIVE ORGANIZATION
    ATTN: T/SL

THE JOINT STAFF
    ATTN: J-3 NUCLEAR CONTINGENCY BR
    ATTN: J-3/NUC OPS BR STRAT OP BR
    ATTN: J-5 NUCLEAR & CHEMICAL DIV
    ATTN: J-8/CAD

U S NATIONAL MILITARY REPRESENTATIVE
    ATTN: SACEUR

UNDER SECRETARY OF DEFENSE
    ATTN: DEP UND SEC C3I-STRAT & THT C2 SYS
    ATTN: DEP UND SEC RES & ADV TECH
    ATTN: DEP UND SEC, TAC WARFARE PROG
    ATTN: STRAT & THTR NUC FORCES

DEPARTMENT OF THE ARMY

DEP CH OF STAFF FOR OPS & PLANS
    ATTN: DAMO-ODW

HARRY DIAMOND LABORATORIES
    ATTN: SLCHD-NW
    ATTN: SLCHD-NW-E
    ATTN: SLCHD-NW-EA
    ATTN: SLCHD-NW-EC
    ATTN: SLCHD-NW-EE
    ATTN: SLCHD-NW-RA
    ATTN: SLCHD-NW-RC
    ATTN: SLCHD-NW-RE (B GARVER)
    ATTN: SLCHD-NW-RE (H BRISKER)
    ATTN: SLCHD-NW-RH (G MERKEL)
    ATTN: SLCHD-NW-RH (R GILBERT)
    ATTN: SLCHD-PM-M (G BROWN)
    ATTN: SLCIS-IM-TL (TECH LIB)

OFFICE OF ASSISTANT SECRETARY OF ARMY
    ATTN: SARD-ZCA

U S ARMY ARMAMENT RSCH & DEV CENTER
    ATTN: TECHNICAL LIBRARY

U S ARMY BALLISTIC RESEARCH LAB
    ATTN: SLCBR-SS-T (TECH LIB)
    ATTN: SLCBR-VL
    ATTN: SLCBR-VL-LD

U S ARMY BELVOIR RD & E CTR
    ATTN: TECH LIB

U S ARMY COMB ARMS COMBAT DEV ACTY
    ATTN: ATZL-CAC-A
    ATTN: ATZL-CAN-I
    ATTN: ATZL-CAP

U S ARMY COMD & GENERAL STAFF COLLEGE
    ATTN: LIBRARY

U S ARMY FOREIGN SCIENCE & TECH CTR
    ATTN: DRXST-PO T CALDWELL

U S ARMY MATERIEL SYS ANALYSIS ACTVY
    ATTN: AMXSY-CR

U S ARMY MISSILE COMMAND/AMSMI-RD-CS-R
    ATTN: AMSMI-RD-CS-R (DOCS)

U S ARMY NUCLEAR & CHEMICAL AGENCY
    ATTN: MONA-NU

U S ARMY NUCLEAR EFFECTS LABORATORY
    ATTN: DR J MEASON

U S ARMY STRATEGIC DEFENSE CMD
    ATTN: DASD-H-SAV

U S ARMY STRATEGIC DEFENSE COMMAND
    ATTN: ATC-R
    ATTN: CSSD-H-L

U S ARMY TEST AND EVALUATION COMD
    ATTN: TECHNICAL LIBRARY SI-F

U S ARMY VULNERABILITY ASSESSMENT LAB
    ATTN: SLCVA-TAC (R FLORES)

U S ARMY WAR COLLEGE
    ATTN: LIBRARY

USA SURVIVABILITY MANAGMENT OFFICE
    ATTN: SLCSM-SE J BRAND

DEPARTMENT OF THE NAVY

NAVAL AIR SYSTEMS COMMAND
    ATTN: AIR 5161
    ATTN: AIR-5164
    ATTN: AIR-5462
    ATTN: AIR-933

NAVAL OCEAN SYSTEMS CENTER
    ATTN: CODE 9642 (TECH LIB)

NAVAL POSTGRADUATE SCHOOL
    ATTN: CODE 1424 LIBRARY
    ATTN: CODE 4650 (T WEITING)

NAVAL RESEARCH LABORATORY
    ATTN: CODE 2627 (TECH LIB)
    ATTN: CODE 4000 (W ELLIS)
    ATTN: CODE 4650 (T WEITING)
    ATTN: CODE 4700.1 (W ALI)
    ATTN: CODE 4740 (W MANNHEIMER)
    ATTN: CODE 8320.1 (V FOLEN)

NAVAL SURFACE WARFARE CENTER
    ATTN: CODE R40
    ATTN: CODE R43
    ATTN: CODE 425

NAVAL SURFACE WARFARE CENTER
    ATTN: CODE H-21
    ATTN: R RICHARDSON
    ATTN: TECHNICAL LIBRARY

NAVAL TECHNICAL INTELLIGENCE CTR
    ATTN: DEOO
    ATTN: LIBRARY

NAVAL WEAPONS CENTER
    ATTN: CODE 343 (TECH SVCS)

OFC OF THE DEPUTY CHIEF OF NAVAL OPS
    ATTN: NOP 098(OFC RES-DEV-TEST & EVAL)
    ATTN: NOP 506
    ATTN: NOP 551

    ATTN: NOP 941F
    ATTN: NOP 981N1
    ATTN: NOP 982
    ATTN: NOP 987
    ATTN: NOP-956
    ATTN: OP 654 (STRAT EVAL & ANAL BR)
    ATTN: OP 981

SPACE & NAVAL WARFARE SYSTEMS CMD
    ATTN: PME 117-21
    ATTN: PMW-145
    ATTN: TECHNICAL LIBRARY

THEATER NUCLEAR WARFARE PROGRAM OFC
    ATTN: PMS 423

DEPARTMENT OF THE AIR FORCE

AERONAUTICAL SYSTEMS DIVISION
    ATTN: ASD/ENACE

AFIA
    ATTN: AFIA/INKD, MAJ COOK

AIR FORCE CTR FOR STUDIES & ANALYSIS
    ATTN: AFCSA/SAMI (R GRIFFIN)

AIR FORCE ELECTRONIC WARFARE CENTER
    ATTN: TECHNICAL LIBARY

AIR FORCE INSTITUTE OF TECHNOLOGY/EN
    ATTN: AFIT/ENP C BRIDGMAN
    ATTN: ENA/MAJ D STONE

AIR FORCE SPACE COMMAND
    ATTN: LKA

AIR UNIVERSITY LIBRARY
    ATTN: AUL-LSE

BALLISTIC SYSTEMS DIVISION
    ATTN: MYSP

DEPUTY CHIEF OF STAFF/XOX
    ATTN: AFXOXFM (PLNS FRC DEV MUN PLNS)

FOREIGN TECHNOLOGY DIVISION, AFSC
    ATTN: LIBRARY
    ATTN: SDMDA/S SPRING

ROME AIR DEVELOPMENT CENTER, AFSC
    ATTN: RBCM
    ATTN: RBCT

SECRETARY OF AF/AQQS
    ATTN: AF/RDQI

SPACE DIVISION/IN
    ATTN: IND

SPACE DIVISION/YA
    ATTN: YAR

STRATEGIC AIR COMMAND/XRFS
    ATTN: XRFS

U S RESEARCH & DEVELOPMENT COORD
    ATTN: USRADCO

USAF/LEEEU
    ATTN: LEEE

WEAPONS LABORATORY
    ATTN: AWP
    ATTN: AWPB
    ATTN: NTAA
    ATTN: NTCA (B SINGARAJU)
    ATTN: SUL

DEPARTMENT OF ENERGY

LAWRENCE LIVERMORE NATIONAL LAB
    ATTN: L-156
    ATTN: L-156 (R KING)
    ATTN: L-86 H CABAYAN

LOS ALAMOS NATIONAL LABORATORY
    ATTN: MS D408
    ATTN: MS F617
    ATTN: MS F630 (M GILLESPIE)
    ATTN: MS F635 (LTCOL J DUNN)
    ATTN: MS H827
    ATTN: MS P364 REPORT LIBRARY

SANDIA NATIONAL LABORATORIES
    ATTN: DEPT 1235 (J HOFFMAN)
    ATTN: DEPT 2230 (J RENKER)
    ATTN: DEPT 7555
    ATTN: ORG 1230 J E POWELL
    ATTN: TECH LIB 3141

OTHER GOVERNMENT

CENTRAL INTELLIGENCE AGENCY
    ATTN: OSR/SE/F
    ATTN: OSWR/NED
    ATTN: OSWR/SSD/SWB
    ATTN: OSWR/STD/MTB
    ATTN: OSWR/STD/TTB

DEPARTMENT OF DEFENSE CONTRACTORS

BATTELLE MEMORIAL INSTITUTE
    ATTN: ELEC SYS DEPT V PUGLIELLI

BDM INTERNATIONAL INC
    ATTN: E DORCHAK

BDM INTERNATIONAL INC
    ATTN: LIBRARY

BOOZ-ALLEN & HAMILTON, INC
    ATTN: L ALBRIGHT

CHARLES STARK DRAPER LAB, INC
    ATTN: TECH LIBRARY

EG&G SPECIAL PROJECTS INC
    ATTN: J GILES

ELECTRO MAGNETIC APPLICATIONS, INC
    ATTN: J BOWERS

GENERAL DYNAMICS CORP
    ATTN: TECHNICAL LIBRARY

GTE GOVERNMENT SYSTEMS CORPORATION
    ATTN: TECH LIBRARY

HONEYWELL, INC
    ATTN: LIBRARY

HONEYWELL, INC
    ATTN: SR&C LIBRARY/T CLARKIN

HUGHES AIRCRAFT CO
    ATTN: G SARAN

IIT RESEARCH INSTITUTE
    ATTN: I MINDEL

INSTITUTE FOR DEFENSE ANALYSES
    ATTN: CLASSIFIED LIBRARY
    ATTN: TECH INFO SERVICES

IRT CORP
    ATTN: B WILLIAMS
    ATTN: R W STEWART

JAYCOR
    ATTN: E WENAAS

JAYCOR
    ATTN: E WENAAS
    ATTN: M SCHULTZ, JR

JAYCOR
    ATTN: R BONN

JAYCOR
2 CYS ATTN: K F CASEY

KAMAN SCIENCES CORP
    ATTN: K LEE

KAMAN SCIENCES CORP
    ATTN: C EKLUND
    ATTN: B KINSLOW

KAMAN SCIENCES CORP
    ATTN: E CONRAD

KAMAN SCIENCES CORPORATION
    ATTN: TECHNICAL LIBRARY

KAMAN SCIENCES CORPORATION
    ATTN: DASIAC
    ATTN: R RUTHERFORD

KAMAN SCIENCES CORPORATION
    ATTN: DASIAC

LITTON SYSTEMS, INC
    ATTN: J SKAGGS

LOCKHEED MISSILES & SPACE CO, INC
    ATTN: G LUM
    ATTN: TECH INFO CTR D/COLL

METATECH CORPORATION
    ATTN: W RADASKY

MISSION RESEARCH CORP
    ATTN: EMP GROUP

MISSION RESEARCH CORP
    ATTN: D SULLIVAN

MISSION RESEARCH CORP
    ATTN: M BOLLEN

MISSION RESEARCH CORP
    ATTN: J LUBELL
    ATTN: J R CURRY

MISSION RESEARCH CORP, SAN DIEGO
    ATTN: V VAN LINT

MITRE CORPORATION
    ATTN: M FITZGERALD
    ATTN: TECHNICAL REPORT CENTER

PACIFIC-SIERRA RESEARCH CORP
    ATTN: H BRODE
    ATTN: L E JOHNSON

PHYSICS INTERNATIONAL CO
    ATTN: DOCUMENT CONTROL
    ATTN: J BENFORD

PULSE SCIENCES, INC
    ATTN: TECHNICAL LIBARY

R & D ASSOCIATES
    ATTN: C MO

R & D ASSOCIATES
    ATTN: LIBRARY

R & D ASSOCIATES
    ATTN: J P CASTILLO
    ATTN: R PARKER

RAYTHEON CO
    ATTN: H FLESCHER

RCA CORPORATION
    ATTN: G BRUCKER

ROCKWELL INTERNATIONAL CORP
    ATTN: AUTO SENSORS & ACFT DIV/TECH LIB

ROCKWELL INTERNATIONAL CORP
    ATTN: B-1 DIV TIC (BAOB)

ROCKWELL INTERNATIONAL CORP
    ATTN: AUTO STRAT SYS DIV/TECH LIB
    ATTN: G MORGAN

S-CUBED
    ATTN: A WILSON

SANDERS ASSOCIATES, INC
    ATTN: G H BOLLES

SCIENCE & ENGRG ASSOCIATES, INC
    ATTN: V JONES

SCIENCE APPLICATIONS INTL CORP
    ATTN: TECH LIBRARY
    ATTN: W CHADSEY

SCIENCE APPLICATIONS INTL CORP
    ATTN: P J DOWLING

SRI INTERNATIONAL
    ATTN: D ARNS
    ATTN: ELECTROMAG SCI LAB TECH LIB

TEXAS INSTRUMENTS, INC
    ATTN: TECHNICAL LIBRARY

TRW INC
    ATTN: LIBRARIAN

TRW INC
    ATTN: A R CARLSON
    ATTN: J PENAR
    ATTN: P BHUTA

TRW SPACE & DEFENSE SYSTEMS
    ATTN: D M LAYTON
    ATTN: A SPEHAR

UNISYS CORPORATION-DEFENSE SYSTEMS
    ATTN: TECHNICAL LIBRARY

VARIAN ASSOCIATES INC
    ATTN: TECHNICAL LIBRARY